Spins, Peptides, and Alzheimer's Disease: Solid-State Nuclear Magnetic Resonance Investigations of Amyloid Peptide Conformation

by

Philip R. Costa

B.A., Physics and Biology (1990)
Cornell University

Submitted to the Department of Chemistry
in Partial Fulfillment of the Requirements for the Degree of

Doctor of Philosophy in Physical Chemistry

at the

Massachusetts Institute of Technology

September 1996

Signature of Author:_____
Department of Chemistry
16 August 1996

Certified by:____
Robert G. Griffin
Professor of Chemistry
Thesis Supervisor

Certified by:_____
Peter T. Lansbury, Jr.
Associate Professor of Chemistry
Thesis Supervisor

Accepted by:_____
Dietmar Seyferth
Professor of Chemistry
Chairman, Departmental Committee on Graduate Students

This Doctoral thesis has been examined by a Committee of the Deparment of Chemistry as follows:

Professor James R. Williamson_____
Chairman

Professor Robert G. Griffin_____
Thesis Supervisor

Professor Peter T. Lansbury, Jr._____
Thesis Supervisor

Professor Bruce Tidor_____

Spins, Peptides, and Alzheimer's Disease: Solid-State Nuclear Magnetic Resonance Investigations of Amyloid Peptide Conformation

by

Philip R. Costa

Submitted to the Department of Chemistry on 16 August 1996
in Partial Fulfillment of the Requirements for the Degree of
Doctor of Philosophy in Physical Chemistry

ABSTRACT

In this thesis several techniques are described by which detailed structural information can be extracted from the dipolar interactions in solid compounds between neighboring low-γ, spin-1/2 nuclei. In Chapter One we list the relevant (primarily chemical shift and dipolar) nuclear spin interactions for low-γ, spin-1/2 nuclei in solids. We also introduce the concept of dipolar recoupling within the CP/MAS framework, and provide as an example a discussion of the rotational resonance (RR) effect in a homonuclear two-spin system. Novel methods for the extraction of accurate distance information using the RR technique, particularly in the presence of zero-quantum relaxation and chemical shift dispersion (CSD), are discussed. In Chapter Two, specific details of the structure of the 'ß34-42' peptide (the 9 C-terminal residues of the 42 residue variant of the ß-amyloid protein implicated in Alzheimer's disease) are examined, particularly the conformation of the central glycyl-glycyl peptide linkage (i.e. between resides 37 and 38). Experiments (both RR-based and static) designed to characterize the relative orientation of dipolar and CSA interactions demonstrate that the linkage is in the *trans* conformation. Chapter Three describes how modifications of the MAS-induced rotational resonance effect can be created by

application of a weak, continuous rf-field to a spinning solid. The RR Tickling (RRT) and ramped 2Q-HORROR experiments are described using a two-spin framework, and the concept of dipolar pulse sequences (DPS) is presented. The accuracy of the RRT technique as an alternative to standard RR in measuring internuclear distances in two-spin systems is demonstrated, and its lack of dependence on chemical shift dispersion and zero-quantum relaxation is emphasized. Chapter Four describes the application of homonuclear recoupling techniques to multiply labeled (more than 2 spin) samples, and demonstrates that non-commutation between dipolar interactions makes it difficult to extract useful internuclear distance information from highly-enriched samples using broadband recoupling techniques. The effect is sketched theoretically, and demonstrated in a model 3-spin system using both the RFDR and MELODRAMA pulse sequences. The application of more selective recoupling techniques (RRT and 2Q-HORROR), to avoid simultaneous reintroduction of a large number of dipolar interactions and hence the described "destructive" interference, is demonstrated.

Thesis Supervisor: Robert G. Griffin
Title: Professor of Chemistry
Thesis Supervisor: Peter T. Lansbury, Jr.
Title: Associate Professor of Chemistry

TABLE OF CONTENTS

ACKNOWLEDGMENTS

Boqin Sun taught me most of what I know about NMR, and many of the ideas in this thesis were greatly improved by discussions with him. Dennis Hall and John Gross also provided willing and critical ears, and again made numerous useful suggestions (Dennis also proofread as much of this thesis as he could get through, so any remaining mistakes are his fault).

The use of probes constructed by Chad Rienstra and Doug Maus was of great benefit for a significant portion of the work presented here. Peter Allen and Ajay Thakkar provided technical assistance at various stages of different experiments. Dave Ruben advised on appropriate usage of his pulse programming language, and the occasional FORTRAN problem.

All of the labeled samples used in the experiments described in Chapter Two were synthesized by Dave Kocisko. The $^{13}C_2$-labeled TEE sample used in experiments in Chapters One and Three was synthesized by Sunil Das Gupta. And although the GGV samples of Chapter Four were synthesized by me, I had a great deal of help from both Paul Weinreb and Raul Zambrano.

Chapter 1

Solid State NMR and Rotational Resonance

1.1 Introduction: Structural Biology, Solid-State NMR.

The transition from molecular to "atomic" biology, from a description based on the molecule as the fundamental unit to one in which the details of molecular structure become relevant, ultimately requires some method of determining the relevant structures at atomic resolution. The structures of proteins and nucleic acids, which form the bulk of the active machinery of the cell, were first determined at near-atomic resolution using X-ray crystallographic techniques. The earliest studies proposed general structural motifs based on data obtained from fiber-diffraction experiments combined with extensive model-building (e.g. β-sheet protein structure by Pauling and co-workers in 1951-5[1, 2]; B-form DNA by Watson, Crick, and co-workers in 1953[3]). The extraction of useful structural parameters from the fiber diffraction data depended upon the preferential alignment of one axis of the molecular assembly within the fiber, that is, macroscopic ordering of the molecules in the sample relative to one coordinate axis. Subsequent studies on single-crystals of proteins and nucleic acids, where the macroscopic ordering of the constituent molecules extends along all 3 coordinate axes, allowed extraction of more precise structural information, and hence determination of molecular structure with significantly less

dependence on model-building (first done for the protein sperm whale myoglobin by Kendrew and coworkers in 1959[4]). X-ray crystallographic determination of the structures of proteins and nucleic acids (and mixtures of the two) has since become routine, the crucial step often now being the ability to obtain high-quality single crystals of the desired compound.

During the 1980's, solution nuclear magnetic resonance (NMR) biomolecular structure-determination techniques were developed as an alternative which (i) do not require a macroscopically ordered sample, and (ii) are more sensitive to, and hence allow study of, changes in structure (i.e. molecular dynamics) on a relatively short timescale (μsec-msec). The first successful application of these techniques to a true protein (i.e. not a small peptide) was performed by several groups, including Wuthrich and coworkers in 1985 (on the protein BPTI)[5]. These techniques depend upon the rapid isotropic tumbling of the molecule in solution to average out the anisotropic (i.e. dipolar and chemical shift anisotropy (CSA)) contributions to the nuclear spin Hamiltonian. This allows acquisition of very high-resolution spectra in which many of the resonance peaks corresponding to specific nuclei within the molecule are separately identifiable. Application of J- and NOE-dependent mixing periods within a multidimensional framework then creates cross-peaks between resonances corresponding to nuclei that are in close proximity[6, 7]. Analysis of this connectivity this leads first to assignment of the resonances to their associated nuclei within the (known) primary structure, then second, to extraction of a multitude of internuclear distance and torsion angle constraints (upwards of

10-20 constraints per residue are typical[8]) which can be used to determine the 3-dimensional molecular structure. Although a more recent development than X-ray crystallography, biomolecular structure determination using solution NMR techniques has been routinely applied in recent years for small proteins where spectral overlap is not severe.

However, for systems in which the biologically relevant state is neither soluble nor crystalline (e.g. amyloid peptide aggregates, membrane peptide/proteins), or where the solubilized compound does not tumble in solution fast enough to adequately average the anisotropic nuclear interactions, some alternative method for general structure determination is needed. Given even an amorphous solid sample where some degree of microscopic order does exist, solid-state NMR (ssNMR) can provide just such an alternative. Although advances in the last two decades have greatly increased the resolution and sensitivity of ssNMR spectra of low-γ, spin-1/2 nuclei (e.g. ^{13}C, ^{15}N, ^{31}P) in organic compounds, the current state of the art does not allow acquisition of well-resolved one-dimensional (1D) spectra of moderately-sized proteins, nucleic acids, or even large, non-crystalline peptides. However, combined with specific labeling and/or liberal use of multidimensional correlation techniques, sufficiently precise separation and assignment of the resonances in such a spectrum is possible to subsequently allow a detailed study of internuclear distances and relative interaction tensor orientations.

In this thesis several techniques are described by which detailed structural information can be extracted from the dipolar interactions in solid compounds between neighboring low-γ, spin-1/2

nuclei. In Chapter One we list the relevant (primarily chemical shift and dipolar) nuclear spin interactions for low-γ, spin-1/2 nuclei in solids. We also introduce the concept of dipolar recoupling within the CP/MAS framework, and provide as an example a discussion of the rotational resonance (RR) effect[9, 10] in a homonuclear two-spin system. Novel methods for the extraction of accurate distance information using the RR technique, particularly in the presence of zero-quantum relaxation and chemical shift dispersion (CSD), are discussed. In Chapter Two, specific details of the structure of the 'ß34-42' peptide (the 9 C-terminal residues of the 42 residue variant of the ß-amyloid protein implicated in Alzheimer's disease[11]) are examined, particularly the conformation of the central glycyl-glycyl peptide linkage (i.e. between resides 37 and 38). Experiments (both RR-based and static) designed to characterize the relative orientation of dipolar and CSA interactions demonstrate that the linkage is in the *trans* conformation. Chapter Three describes how modifications of the MAS-induced rotational resonance effect can be created by application of a weak, continuous rf-field to a spinning solid. The RR Tickling (RRT) and ramped 2Q-HORROR[12, 13] experiments are described using a two-spin framework, and the concept of dipolar pulse sequences (DPS) is presented. The accuracy of the RRT technique as an alternative to standard RR in measuring internuclear distances in two-spin systems is demonstrated, and its lack of dependence on chemical shift dispersion and zero-quantum relaxation is emphasized. Chapter Four describes the application of homonuclear recoupling techniques to multiply labeled (more than 2 spin) samples, and demonstrates that non-commutation between

dipolar interactions makes it difficult to extract useful internuclear distance information from highly-enriched samples using broadband recoupling techniques. The effect is sketched theoretically, and demonstrated in a model 3-spin system using both the RFDR and MELODRAMA pulse sequences. The application of more selective recoupling techniques (RRT and 2Q-HORROR), to avoid simultaneous reintroduction of a large number of dipolar interactions and hence the described "destructive" interference, is demonstrated.

A more detailed summary of Chapter One is as follows. In the following section we list the relevant nuclear spin interactions in solids, and discuss the effectiveness of cross-polarization (CP)[14], magic-angle sample spinning (MAS)[15, 16], and high-power proton decoupling (HPPD) in obtaining high-resolution, high-sensitivity spectra of low-γ spin-1/2 nuclei in solids. In Section Three we discuss the need to interfere with MAS-induced averaging of dipolar interactions between low-γ nuclei (i.e. dipolar recoupling) to allow extraction of useful structural information, and describe as an example the RR effect (in a homonuclear 2-spin system). In Section Four we show that quantitation of the longitudinal spin-dynamics for a homonuclear spin-pair at RR can, when compared to simulated data, be used as a measure of the internuclear distance[17], and describe several versions of the pulse sequence necessary to perform such an experiment. We also discuss the importance of zero-quantum relaxation and chemical-shift dispersion (CSD) in the longitudinal magnetization exchange process, and describe how measurements of the off-resonance behavior of the spin-system can be used to quantify these parameters with the necessary precision.

1.2 The ssNMR Hamiltonian and the CP/MAS experiment.

1.2A Zeeman and Chemical Shift Interactions; Spherical Tensors.

Placing an isolated spin-1/2 nucleus in a strong magnetic field induces a splitting between the two nuclear spin energy levels. Confined to one of two quantum states corresponding classically to an orientation of the nuclear magnetic moment either along or against the field, the energy associated with each of the two states differs by an amount depending upon the strength of the moment-field interaction, that is, upon the strength of the magnetic field and the size of the magnetic dipole moment. The classical equation for the interaction energy would simply be the dot product of the field vector with the moment vector. The quantum-mechanical analog uses spin operators in place of the classical spin vector, so that the term in the nuclear spin Hamiltonian accounting for this interaction (the Zeeman interaction) is written[18]:

$$H^Z = -\gamma_I\left(\tilde{I}\bullet\tilde{B}\right) = -\gamma_I B_o I_Z \equiv \omega_o I_Z \qquad (1),$$

where $\tilde{B}(=B_o\hat{z})$ represents the magnetic field, $\tilde{I}$ represents the nuclear spin operator, γ_I (the gyromagnetic ratio for nucleus I) characterizes the size of the nuclear magnetic moment, and ω_o is defined as the nuclear Zeeman frequency.

The equation for the energy level splitting given above does not take into account the shielding effect that the electrons surrounding the nucleus have in reducing the value of the magnetic field at the nucleus. The magnitude of this shift depends upon the nature of the surrounding electron cloud, i.e. the chemical environment the nucleus is in, and hence is termed the chemical

shift. The shift is anisotropic: its magnitude depends upon the orientation of the anisotropic electron distribution relative to the external magnetic field. If the shift in the magnetic field at the nucleus due to the shielding effect is[18]:

$$\Delta\tilde{B} = -\tilde{\tilde{\sigma}} \bullet \tilde{B} \qquad (2),$$

then the chemical shift contribution to the Hamiltonian is given by:

$$H^{CS} = \gamma_I \tilde{I} \bullet \tilde{\tilde{\sigma}} \bullet \tilde{B} \qquad (3),$$

where $\tilde{\tilde{\sigma}}$ is the chemical shift interaction tensor.

Calculation of the explicit chemical shift contribution to the Hamiltonian requires expressing the chemical shift tensor in a "laboratory-fixed" coordinate frame (indicated by the superscript L), i.e. one whose orientation relative to the magnetic field is known, so that the tensor product between the chemical shift tensor and the magnetic field (in equ (3)) can be calculated. We then re-write equ (3) using Cartesian coordinates as[18]

$$H^{CS} = \gamma_I \sum_{\alpha=X,Y,Z} I_\alpha \sum_{\beta=X,Y,Z} \sigma^L_{\alpha\beta} B_\beta = \gamma_I \sum_{\alpha=X,Y,Z} \sigma^L_{\alpha Z} I_\alpha B_Z = \gamma_I \sigma^L_{ZZ} I_Z B_Z \qquad (4),$$

where the second equality assumes that the applied field points along the z-axis of the lab coordinate system, and the third makes the secular approximation (dropping terms that do not commute with the dominant Zeeman interaction). An alternative form for the expression following the first equaiity is[18]:

$$H^{CS} = \gamma_I \sum_{\alpha=X,Y,Z} I_\alpha \sum_{\beta=X,Y,Z} \sigma^L_{\alpha\beta} B_\beta = \gamma_I \sum_{\alpha,\beta=X,Y,Z} T^{CS}_{\alpha\beta} \sigma^L_{\alpha\beta} \qquad (5)$$

where we have introduced the tensor $T^{CS}_{\alpha\beta} = I_\alpha B_\beta$, the dyad product of the two vectors. In this notation, it is common to refer to the first tensor (T) as the "spin" part of the interaction, and the second tensor (here $\tilde{\tilde{\sigma}}$) as the "spatial" part of the interaction. Physical manipulations of the sample (such as magic angle spinning) will

affect the spatial part of this equation, while rf pulses will affect the spin part. This is an important distinction that we will make use in later sections.

Because the chemical shift tensor expresses the spatial dependence of the electronic shielding of the nucleus, and hence has an orientation that is fixed relative to the molecule, the most natural frame in which to initially write down the tensor components is one which also has a specific orientation relative to the molecule (a molecule-fixed, or molecular, coordinate frame). Given such a representation, the specific values of the chemical shift tensor components, when expressed in the lab frame, can be calculated by appropriate rotation of the tensor to bring the two frames into alignment. We can express the relative orientation of two coordinate frames using the standard Euler angle convention. A set of three angles (α,β,γ) relating two coordinate systems (A and B) are defined which indicate that a rotation of coordinate system A by an angle α about its z-axis (creating coordinate system A'), followed by a rotation of angle β about the y-axis of coordinate system A' (creating A''), followed by a rotation of angle γ about the z-axis of A'', will bring us to coordinate system B. This convention follows Spiess, et al.[19]

Spherical tensor notation provides an elegant means to calculate the effects of rotations on the interaction tensors in the nuclear spin Hamiltonian. Switching from Cartesian notation, the tensor product expressing the chemical shift contribution to the Hamiltonian (from equ (5)) becomes[18]:

$$H^{CS} = \gamma_I \sum_{l} \sum_{m=-l,l} (-1)^m \sigma^{L}_{l,-m} T^{CS}_{l,m} \qquad (6),$$

where for 2nd-rank tensors the sum over l is restricted to the values 0, 1, and 2. The values of these lab frame chemical shift tensor elements are calculated from those in the molecular frame according to[19]:

$$\sigma^{L}_{l,m} = \sum_{m=-l,l} D^{l}_{m',m}(\alpha,\beta,\gamma)\sigma^{M}_{l,m'} \qquad (7),$$

where the superscript M refers to tensor element values in the molecular frame, and D^l is the Wigner rotation matrix which is a function of the relative orientation of the two frames as given by (α,β,γ). The form of the Wigner rotation matrix can be more closely defined[19, 20]:

$$D^{l}_{m',m}(\alpha,\beta,\gamma) = e^{im'\alpha} d^{l}_{m',m}(\alpha,\beta,\gamma) e^{im\gamma} \qquad (8),$$

where d^l is the reduced Wigner matrix. Rotation of a spherical tensor about the z-axis (e.g. the α or γ Euler rotations) adds a phase (exp(ix) where x=mα or mγ) to each component $\sigma_{l,m}$, while rotations about the x- or y- axes (β) "mix" components.

The secular approximation, as applied to a Hamiltonian expressed in spherical tensor notation, requires dropping those terms whose spin component has m≠0. The reasoning is as follows: the secular approximation involves keeping only those terms in the Hamiltonian whose spin component commutes with the Zeeman term, which implies insensitivity to rotation about the z-axis of the lab frame (i.e. the magnetic field); only m=0 spin components (in the lab frame) are insensitive to such a rotation (only they do not gain a phase on rotation about the z-axis) and hence are not lost in the approximation. Applied to the general tensor product in equ (6) this yields:

$$H^{CS} = \gamma_I \sum_{l=0,1,2} \sigma^{L}_{l,0} T^{CS}_{l,0} \qquad (9).$$

The remaining three terms (specified by l) can be considered separately. The l=0 term is independent of orientation and is the isotropic chemical shift. The l=1 term corresponds to antisymmetric components of the chemical shift tensor, which in general do not make observable contributions to the spin dynamics and can be dropped[18]. The l=2 term corresponds to the symmetric components of the chemical shift tensor, does have a value that depends on orientation, and hence characterizes the anisotropic component of the chemical shift interaction. The final form of the Zeeman and chemical shift terms in the Hamiltonian, once these factors have been considered, is:

$$H=\left(\omega_0^I+\omega_{iso}^I+\gamma_I\sum_{m=-2,2}D_{m,0}^2(\Omega)\sigma_{2,m}^M\right)I_Z \qquad (10),$$

where we have absorbed γ_I into $\sigma_{0,0}$ to create ω_{iso}^I, and have explicitly written out the value of $\sigma_{2,0}^L$ as a function of the molecular-frame components $\{\sigma_{2,m}^M\}$ and the orientation angles $\Omega=(\alpha,\beta,\gamma)$. The distinction between the first and second terms is not always clear, and we often arbitrarily set the magnitude of the first term equal to the rf carrier frequency and, after a transformation to the standard "rotating frame", refer to the shift from the carrier frequency as the isotropic chemical shift. The third term, the chemical shift anisotropy (CSA), can be represented in a number of alternative ways depending on the purpose. We will use various representations of the CSA throughout this thesis.

1.2B Spin Dynamical Equations of Motion.

Given a system characterized by a Hamiltonian, H, the time-evolution of the system is determined according to[7]:

$$\frac{d\rho(t)}{dt} = \dot{\rho}(t) = -i[H(t),\rho(t)] \qquad (11),$$

where $\rho(t)$ is a density operator describing the state of the system at time t. From this we can derive a general form for the "equation of motion" for the spin system[7]:

$$\rho(t_2) = U(t_1,t_2)\rho(t_1)U^{-1}(t_1,t_2) \qquad (12)$$

where the general form for the propagator, U, is given by:

$$U(t_1,t_2) = \hat{T}\exp\left(-i\int_{t_1}^{t_2} H(t)dt\right) \qquad (13)$$

and $\hat{T}$ is the Dyson time-ordering operator. The value of an observable O at time t is then calculated according to:

$$\langle O\rangle_t = \mathrm{Tr}[\rho(t)O] \qquad (14).$$

The Hamiltonian (containing only chemical shift and Zeeman terms) for a spin with a specific orientation relative to the field (i.e. fixed (α,β,γ)) is a constant multiplying the z component of the spin operator:

$$H = cI_z \qquad (14)$$

(where the magnitude of the constant depends upon the molecular orientation (see equ (10)). The propagator for such a system is easily calculated:

$$U(t_1,t_2) = \hat{T}\exp\left(-i\int_{t_1}^{t_2} cI_z dt\right) = e^{-icI_z(t_2-t_1)} \qquad (15).$$

Given an initial state ($t_1 = 0$) consisting of transverse magnetization lying along the x-axis ($\rho(0) = I_x$), detectable polarization along the x-

axis evolves according to:

$$\langle I_x \rangle_t = \mathrm{Tr}[\rho(t) I_x] = \mathrm{Tr}[e^{-ic I_x t} I_x e^{+ic I_x t} I_x] \propto \cos(ct) \qquad (16).$$

The oscillation (precession) of polarization in the sample induces a detectable current in the coil surrounding the sample; Fourier transformation (FT) of the signal yields a single peak in the spectrum (assuming pure-phase detection) centered at the precession frequency, c, which is equal to the two-level energy splitting.

1.2C Powder Samples; MAS; AHT.

"Powder" samples, in the context of ssNMR, are macroscopically disordered solid samples in which all possible molecular orientations relative to the field occur with equal probability (i.e. a static, isotropic distribution of orientations). Instead of the single, narrow peak obtained, for instance, from a crystalline sample containing only one unique molecular orientation relative to the field, the spectra of powder samples (powder spectra) show very broad resonances resulting from the overlap of a series of narrow peaks over a continuous range of frequencies, each arising from a different molecular orientation and hence a different CSA contribution to the observed precession frequency. The Hamiltonian characterizing such a sample still has the form given in equ (10), but the Euler angles (α,β,γ) are no longer fixed. Calculation of the Hamiltonian-driven dynamics observed in such samples requires calculating the dynamics as a function of orientation, and then summing/integrating over all possible orientations. This procedure is often termed the "powder average". The explicit form of the integration, when

orientation is expressed using Euler angles, is[18]:

$$\frac{1}{8\pi^2}\int_0^{2\pi} d\alpha \int_0^{\pi} d\beta \int_0^{2\pi} d\gamma \left(f(\alpha,\beta,\gamma)\sin\beta \right) \qquad (17),$$

where f represents the dynamical function of interest. In some systems symmetry allows reducing the ranges over which integration is performed.

Solution spectra show very narrow resonance peaks, in part because the anisotropic contribution to the chemical shift is removed by fast isotropic (on the appropriate timescale) molecular reorientation. The fact that the motion is microscopic in nature is not critical, as it depends only on the reorientation of the spatial anisotropies of each interaction relative to the field: were we able to induce such fast, random isotropic motion on the macroscopic sample as a whole, we would observe the same effect. This suggests a mechanism by which we can average out the CSA broadening effects in spectra of solids. Clearly mechanical reproduction of "isotropic" motion would be difficult, particularly given the need for speed and the constraints of the surrounding coil; however, the 2nd-rank character of the chemical shift anistropy implies that lower-symmetry motion will suffice to average out its effects. Rotation about an axis that is inclined at the "magic angle" relative to the magnetic field, i.e. the angle that the body diagonal of a cube makes with each axis of the corners that it trisects, provides such a motion[15, 16]. Assign the edges of a cube to x-, y-, and z- axes using standard convention; rotating the cube about its body diagonal brings each of these edges, in turn, along the longitudinal axis where the field would lie. The average component of some cube-defined

anisotropy (e.g. a different value along each axis x, y, or z) along the longitudinal axis where the magnetic field would lie (the only important component, given the secular approximation) over one full rotation might then be considered as some type of average of the components along the x-, y-, and z-axes. The analogy to CSA interactions, which are often characterized by their magnitudes along three orthogonal axes (the "principal values" - see chapter 2), should be clear.

We can explicitly include the effects of rotation about the magic angle (magic-angle sample spinning, MAS) in the Hamiltonian. First we introduce a new coordinate frame, the "rotor-fixed" frame (the rotor is the object containing the sample that spins at the magic angle). This frame has a fixed (time-independent) orientation relative to each molecule in the sample (specified by the angles $(\alpha^{MR},\beta^{MR},\gamma^{MR})=\Omega^{MR}$), and hence is the orientation over which we will perform the powder average. We choose the rotor frame such that its z-axis lies along the magic-angle axis; transformation from this frame (fixed in a spinning rotor) to the lab frame requires first a time-independent magic-angle tilt, followed by a time-dependent rotation about z: $(\alpha^{RL},\beta^{RL},\gamma^{RL})=(0,\beta_{MA},\omega_r t)$, where β_{MA} represents the magic angle ($\approx$54.73°) and ω_r is the magic-angle rotation frequency. Hence we apply two rotations to each spatial tensor to transform them from their molecular frame to the lab frame: first, a time-independent (powder averaged) rotation to the rotor-fixed frame, second a time-dependent (common) rotation to the lab frame. Applying the appropriate transformations to the static Hamiltonian

in equ (10) yields:

$$H=\left(\omega_o^I+\omega_{iso}^I+\sum_{m'=-2,2}d_{0,m'}^2(\beta_{MA})e^{im'\omega_r t}\gamma_I\sum_{m=-2,2}^{m\neq 0}D_{m',m}^2(\Omega^{MR})\sigma_{2,m}^L\right)I_Z \qquad (18).$$

Combining all of the CSA parameters into a single variable multiplying the time-dependent phase yields a simpler form:

$$H=\left(\omega_o^I+\omega_{iso}^I+\sum_{m'=-2,2}\omega_{(m)}^I e^{im\omega_r t}\right)I_Z \qquad (19),$$

where we have used

$$\omega_{(m)}^I=d_{0,m}^2(\beta_{MA})\gamma_I\sum_{m'=-2,2}D_{m,m'}^2(\Omega^{MR})\sigma_{2,m'}^L \qquad (20).$$

The key feature of equ (14) for our purposes is that $\omega_{(o)}^I=0$, because $d_{0,0}^2(\beta_{MA})=0$. This implies that all components of the CSA interaction will be sinusoidally amplitude modulated at ω_r or $2\omega_r$, and so averaged out over a rotor cycle (as we demonstrate below). ^{rf} is the combination of the secular approximation - the truncation in spin space that reduces a double sum over $d_{m',m}^2(\beta_{MA})$ to the single sum over $d_{0,m}^2(\beta_{MA})$ - with magic-angle averaging (truncation in "spatial" space) that leads to the removal of anisotropic effects up to 2nd rank.

Visualizing the dynamics driven by time-dependent Hamiltonians of this type can be very difficult. Some method of calculating a simpler, time-independent effective Hamiltonian which describes similar dynamics can be very useful, particularly to increase our understanding of the dynamics (brute-force numerical integration of the equations of motion generally suffices for explicitly calculating the dynamics of any 2-spin Hamiltonian, regardless of complexity). For very fast MAS frequencies relative to the magnitudes of the Hamiltonian terms, dropping the time-dependent anisotropic terms is often an adequate accounting of the effects of the rotation. A more general approach that allows consideration of

higher-order effects when the spinning speed does not dominate is provided by the Average Hamiltonian Theory (AHT)[21], which makes use of the Magnus expansion[22]. Given a time-dependent Hamiltonian, the Magnus expansion over a specific time period yields a series of time-independent terms which, together, constitute an effective Hamiltonian that will drive the system to the identical state at the end of the time period[21]:

$$U(t_1,t_2)=\hat{T}\exp\left[-i\int_{t_1}^{t_2}H(t)dt\right]=e^{-iH_{eff}(t_2-t_1)} \qquad (21),$$

where

$$H(t)\rightarrow H_{eff}=\sum_n \overline{H}^{(n)} \qquad (22).$$

For a time-dependent Hamiltonian which is periodic, repeated application of the same time-independent effective Hamiltonian (calculated over one period) can be used to calculate the dynamics over multiples of the period, this property being particularly useful in MAS calculations.

The zero-order term in the expansion is simply the time-average of the Hamiltonian over the period[21]:

$$\overline{H}^{(0)}=\frac{1}{\tau}\int_0^{\tau}H(t)dt \qquad (21).$$

For sinusoidally-modulated terms where we define the period as equal to the length of a single oscillation, the corresponding zero-order term in the expansion is zero and hence the term can be dropped in the lowest-order approximation. The validity of this level of approximation depends on the relative magnitudes of successive terms in the expansion. The first-order term has the

form[21]:

$$\overline{H}^{(1)} = \frac{-i}{2\tau}\int_0^{\tau} dt_2 \int_0^{t_2} [H(t_2), H(t_1)]dt_1 \qquad (22),$$

and higher-order terms contain increasingly more nested commutators between the Hamiltonian and itself at different times. If the time-dependent Hamiltonian commutes with itself at all times - i.e. is inhomogeneous in the Maricq and Waugh (MW)[23] sense - then all of the higher-order terms are identically zero, and the zero-order approximation is exact, independent of the length of time over which averaging is performed. If the Hamiltonian does not commute with itself at all times (i.e. is homogeneous according to MW), then higher order terms may not all be zero, although each should be smaller than the preceding term, roughly by the ratio of the averaging frequency (the inverse of the period, $1/\tau$) to the magnitude of the Hamiltonian. This suggests that attenuating the anisotropic spatial components of homogeneous interactions requires fast spatial modulation: when the averaging frequency dominates, the series converges quickly, and the zero-order approximation is valid.

The time-dependent Hamiltonian containing Zeeman and MAS-modulated chemical shift terms (equ 19) is inhomogeneous in the MW sense, so that a zero-order approximation is valid independent of the spinning frequency. Hence we can use the following time-independent effective Hamiltonian to describe the dynamics at multiples of the rotor period ($\tau_r = 2\pi/\omega_r$):

$$H_{eff} = \overline{H}^{(0)} = (\omega_o + \omega_{iso})I_Z \qquad (23),$$

and we expect transverse evolution to yield a single, narrow resonance at the isotropic frequency. Because we often observe the

system over fractions of a rotor period (e.g. with the dwell time smaller than the rotor period) where the average Hamiltonian calculation does not hold, we obtain after FT both a narrow resonance at the isotropic frequency (the centerband), and a flanking series of narrow resonances (spinning sidebands) that are spaced at intervals equal to the sample spinning frequency. The magnitudes of the sidebands shrink with increasing spinning frequency, and when the spinning frequency is significantly larger than the size of the CSA the sidebands are no longer visible. At slower speeds the sideband pattern can be used to extract parameters characterizing the nature of the CSA interaction using well-known techniques[24].

1.2D Homo- and Heteronuclear Dipolar Interactions.

The magnetic field experienced by a nuclear spin is influenced by the magnetic fields arising from neighboring spins. The corresponding term in the Hamiltonian for this interaction is identical to the classical equation describing the interaction between two dipoles (I and S), but with spin-operators substituted for the dipolar vectors[18]:

$$H^D = b_{IS}\left[\tilde{I}\bullet\tilde{S} - 3\left(\tilde{I}\bullet\hat{r}\right)\left(\tilde{S}\bullet\hat{r}\right)\right] \qquad (24),$$

where $\hat{r}$ is a unit vector pointing along the line connecting the two nuclei, and the coupling constant b_{IS} is given by:

$$b_{IS} = \frac{\mu_o h}{8\pi^2}\frac{\gamma_I\gamma_S}{r^3} \qquad (25)$$

(r represents the internuclear distance). Van Vleck has described a separation of equ (24) into 6 terms (the dipolar alphabet)[25], only two of which remain after taking into account the secular

approximation:

$$H^D = \omega_D\left[2I_ZS_Z - (I_XS_X + I_YS_Y)\right] = \omega_D\left[2I_ZS_Z - \frac{1}{2}(I_+S_- + I_-S_+)\right] \quad (26),$$

where $I_\pm = I_X \pm iI_Y$,

$$\omega_D = \frac{b_{IS}}{2}(1 - 3\cos^2\theta) \quad (27),$$

and θ is the angle between the internuclear vector and the external magnetic field. Further simplification is possible for a heteronuclear spin pair, where the Zeeman frequencies of the two spins are significantly different, so that the flip-flop terms become non-secular (they do not commute with $(I_Z - S_Z)$):

$$H^D = \omega_D 2I_ZS_Z \quad (28).$$

The spatial anisotropy of the dipolar interaction, accounted for in these equations by the θ angle, is modulated by MAS. Spherical tensors again provide a more elegant mechanism for calculating its effects on the evolution of the system. The general form for the dipolar interaction in spherical tensor notation is[18, 26]:

$$H^D = \sum_{m=-2,2}(-1)^m R^D_{2,m}T^D_{2,m} = R^D_{2,0}T^D_{2,0} \quad (29).$$

where R represents the spatial part and T the spin part of the interaction, and the secular approximation has been made. By comparison to equ (26) we can assign $R^D_{2,0} = \omega_D$ and $T^D_{2,0} = 2I_ZS_Z - I_XS_X - I_YS_Y$ (the multiplicative constants may be re-apportioned differently). Calculation of the explicit time dependence of the spatial component of the dipolar Hamiltonian yields the dipolar equivalent of equ (20):

$$\omega_D(t) = \sum_{m=-2,2}^{m\neq 0}\omega^{IS}_{(m)}e^{im\omega_r t} \quad (30),$$

where

$$\omega_{(m)}^{IS} = \left(d_{0,m}^{2}(\beta_{MA}) \sum_{m'=-2,2} D_{m,m'}^{2}(\Omega^{MR}) R_{2,m}^{M} \right) \qquad (31),$$

If we choose a molecular frame with its z-axis along the internuclear vector, the only non-zero component of the dipolar tensor in the molecular frame is the $(l=2, m=0)$ component ($R_{2,0}^{M} = b_{IS}$), so the sum in equ. (31) simplifies to:

$$\omega_{(m)}^{IS} = b_{IS}\left(d_{0,m}^{2}(\beta_{MA}) D_{m,0}^{2}(\Omega^{MR}) \right) \qquad (32).$$

Note that $D_{0,0}^{2}(\Omega) = \frac{1}{2}\left(1 - 3\cos^{2}\beta\right)$, so that we recover (27) from (32) for a static sample.

The form of equ (30) indicates that, because no component of the dipolar interaction remains unmodulated under MAS, the interaction will be fully averaged (and hence can be dropped from the Hamiltonian) given a sufficiently fast spinning speed. The required speed depends upon whether the interaction behaves inhomogeneously or homogeneously, the former type refocussing at all spinning speeds while the latter type requires speeds significantly larger than the magnitude of the dipolar interaction (and any other non-commuting terms in the Hamiltonian - see below). Absent chemical shifts, either interaction alone behaves inhomogeneously; with chemical shifts, the heteronuclear interaction remains inhomogeneous while the homonuclear interaction become homogeneous (except in special cases). The presence of several couplings together, sharing common nuclei, leads to homogeneous behaviour (again excepting special cases).

1.2E Decoupling and the CP/MAS Experiment.

^1H nuclei in organic solids form a network of coupled spins where the strongest couplings can approach 20kHz. This is far too large to be adequately attenuated by MAS given currently obtainable spinning speeds, and efforts to perform the necessary averaging in spin space (by application of the appropriate pulse sequence, e.g. WAHUHA[27]) have so far not been highly successful. Hence high-resolution ^1H spectra, i.e. absent the effects of dipolar broadening, are not generally obtainable in rigid organic solids. However, high-resolution spectra of low-γ nuclei such as ^{13}C, ^{15}N, and ^{31}P can be obtained, provided the ^1H-(low-γ) dipolar couplings are attenuated. These couplings behave homogeneously because of the presence of the homonuclear ^1H couplings, so that MAS alone (at currently obtainable spinning speeds) is not sufficient to remove their broadening effects. High-power irradiation at the ^1H resonance frequency during evolution of the low-γ spin system has proven to be an effective way to attenuate the broadening influence of the ^1H spins. The technique is termed high-power proton decoupling (HPPD), and when combined with MAS (to attenuate CSA and low-γ/low-γ dipolar interactions), allows high-resolution spectra to be obtained. Recent modifications of basic CW decoupling have been suggested in the context of MAS, most notably the TPPM sequence[28].

HPPD (and its variants) and MAS are regularly joined with cross-polarization (CP) to form the standard CP/MAS experiment[29]. The pulse sequence is illustrated in Fig. (1-1). A 90° pulse applied to the ^1H nuclei creates transverse ^1H polarization, which is

subsequently spin-locked by application of an rf field shifted in phase by 90° from the first pulse. Simultaneous application of rf at the low-γ resonance frequency, of the appropriate magnitude, couples the two spin baths (^1H and low-γ), and leads to polarization transfer from the ^1H to the low-γ nuclei. Because of the higher Boltzmann spin polarization of ^1H relative to lower-γ nuclei at thermal equilibrium, this leads to a net increase in the polarization of the low-γ nuclei (for example by a factor approaching 4 for ^1H-^{13}C CP). Following the CP period, the low-γ polarization evolves in the transverse plane, while HPPD is applied. The experiment is repeated extensively to allow for increases in S/N due to signal averaging, at a rate limited by the T_1 of the relevant nucleus. For CP experiments, the relevant nucleus is ^1H, which has a relatively short T_1; this factor is a second (often the dominant) benefit of using CP.

Figure 1-1: CP/MAS pulse sequence. The initial 90° pulse creates transverse ^{1}H magnetization, which is subsequently spin-locked by applying a ^{1}H spin-lock pulse, shifted in phase by 90° from the initial pulse. During this period, cross-polarization (CP) to ^{13}C (or other low-γ) nuclei is performed by simultaneously applying ^{13}C rf with a magnitude appropriate to match the Hartmann-Hahn condition (suitably modified to account for MAS under fast-spinning conditions). At the end of this period (typically lasting on the order of 1-2 ms), the transverse ^{13}C polarization is allowed to precess, and the free-induction decay (FID) is detected. High-power ^{1}H rf is applied during detection to remove the broadening influences of ^{1}H nuclei.

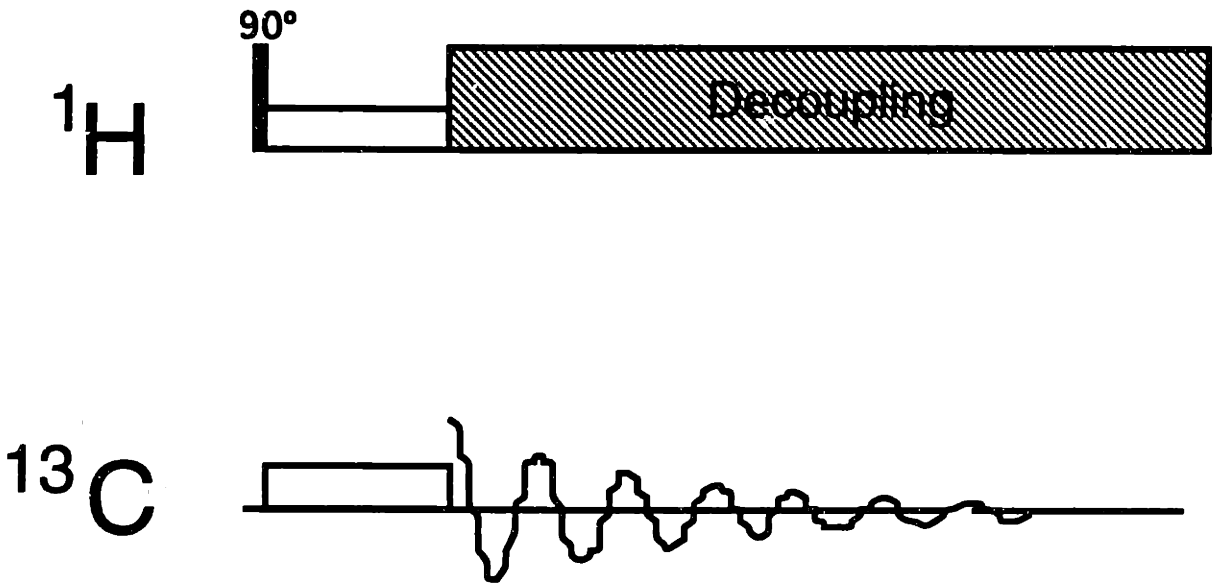
90°
^{1}H
Decoupling
^{13}C

1.3 Dipolar Recoupling: the Rotational Resonance (RR) Effect.

1.3A Dipolar Recoupling and the RR Concept.

Although we can generally predict the form of the Hamiltonian (that is, the set of interactions from which it is constructed) for any given compound based only on a superficial knowledge of its chemical composition, we usually can not determine the magnitudes of its various components (in any coordinate frame) based on such limited knowledge. This is because the nature of the local spin environment, and hence the specific nature of the various terms in the Hamiltonian, depends upon the details of the local structure in which the nuclear spin is embedded. Measurement of the behaviour of the spin system under various experimental conditions (e.g. MAS, pulse sequences, etc.) provides a means of extracting the values characterizing each interaction, and, because the interactions are so strongly determined by the local structure, extracting information about that structure.

Characterization of the chemical shift interaction for various nuclei is an obvious means of examining the local electronic environment of each nucleus, particularly in solids where both the isotropic and anisotropic components of the interaction are easily quantified[30, 31]. Because the relationship between chemical shift and electronic structure is a complex one with "non-local" character, however, that has not yet been worked out in detail, drawing unambiguous conclusions about molecular conformation based solely on chemical shift data is difficult. Comparison of measured parameters to previously published chemical shift data from similar

compounds of known conformation can provide support for loosely-drawn conclusions (e.g. assignment of secondary structure in peptides).

Characterization of the dipolar interaction provides a much more direct means of examining molecular structure. The orientation of the dipolar tensor in the molecular frame is known (it is axially symmetric, with its symmetry axis pointing along the line connected the coupled spin pair), and its magnitude is proportional to the inverse cube of the internuclear distance. Hence quantitation of either parameter (magnitude or orientation relative to some other interaction) provides unambiguous information about the local structure of the compound in which the nuclear spins are embedded. Unfortunately, because the magnitudes of the couplings (hetero- or homonuclear) between low-γ nuclei in solids are no larger a few kHz, and are often on the order of 0.1kHz or less, these couplings are effectively averaged by MAS and so generally do not have an observable effect on the spin dynamics under these conditions. Some method of reintroducing their effects, without sacrificing the high-resolution obtained by application of MAS, becomes crucial for extracting structural information from them.

Dipolar recoupling (DR) techniques reintroduce the effects of the dipolar couplings between low-γ nuclei by interfering with MAS averaging of dipolar interactions during some portion of the spin-system evolution (termed the dipolar mixing period) (reviewed in Bennett, et al.[32]). This is usually followed by a detection period in which the averaging effects of MAS are allowed to proceed unimpeded and a high-resolution spectrum is obtained (although in

some cases the two periods can be combined, the reduced resolution due to low-γ dipolar broadening still being sufficient to allow adequate identification of the resonance peaks[33]). By incrementing the length of the dipolar mixing period and observing the changes in the high-resolution spectra subsequently obtained (a two-dimensional (2D) dipolar-chemical shift experiment in which the dipolar evolution period is the "indirectly detected" dimension), one can determine the effects of the dipolar coupling on the spin dynamics during the dipolar mixing period, and hence quantify the components of the coupling. One obvious DR technique involves shifting the angle the sample rotation axis makes with the external field away from the magic angle during the dipolar mixing period[34], a method which does not so much interfere with MAS averaging as simply eliminate it for a time. Technical difficulties in designing a robust probe which remains stable during repeated switching of the rotation axis to and from the magic angle (necessary for signal averaging and multidimensional experiments) have limited the usefulness of this technique.

A more common class of DR techniques uses rf pulses to manipulate the spin system in such a way as to induce a time-dependence on the spin part of the dipolar interaction that has frequency components that match one or more of those that make up the MAS modulation of the spatial part of the interaction (ω_r and $2\omega_r$). Calculating the zero-order contribution of the dipolar interaction to the effective Hamiltonian then involves averaging over the product of the two time dependencies, and yields a non-zero result. Note that a further requirement of these techniques is that

they do not modulate the spin components of other interactions (particularly the CSA) such that the effects of those interactions are also reintroduced, and in a manner that interferes with the desired dipolar evolution. Examples of this class of DR techniques include (homonuclear:) RR[10, 35], RFDR[36], DRAMA[37], MELODRAMA[38], and C7[39]; (heteronuclear:) CP[14], REDOR[40]/TEDOR[41], and FDR[42]. The techniques vary in the nature of the recoupled dipolar interaction (for example, its magnitude, orientation dependence, and zero- or double-quantum character), and in their sensitivity to a variety of parameters including chemical shift offset, CSA, pulse imperfections, and ^{1}H decoupling power. The recent trend has been towards developing more "broadbanded" recoupling sequences, e.g. techniques that are not sensitive to chemical shift and hence can recouple spin pairs equally well across the spectrum, independent of CSA.

Rotational resonance (RR) is a MAS-based homonuclear DR technique that is unique in that it does not require application of rf pulses to drive the appropriate modulation of the spin component of the dipolar interaction and so create the recoupling effect. Instead, the technique exploits the time-dependence that chemical shift-differences in the Hamiltonian apply (in the appropriate interaction frame) to the dipolar flip-flop term: adjusting the sample spinning speed so that a frequency of the spatial modulation matches a frequency of the chemical-shift-driven spin modulation induces dipolar recoupling. An analogy can be drawn to the Nuclear Overhauser effect (NOE) in solution[43], where random motional modulations provide the energy to drive spin flip-flops, and hence

the transfer of polarization within a spin pair, depending on the spectral density of the motional correlation function at the chemical shift difference frequency. In solids undergoing MAS, the motion is coherent and under experimental control, and we can match its frequency to the appropriate chemical shift difference to reintroduce the coupling between selected spin pairs.

1.3B Derivation of the Average Hamiltonian at RR.

We proceed with an explicit demonstration of the RR recoupling effect, starting from the nuclear spin Hamiltonian (in the rotating frame, i.e. having transformed away the Zeeman term and made the secular approximation) for a homonuclear spin pair (I and S):

$$H = \omega_I I_Z + \omega_S S_Z + \omega_D(t)\left[2I_Z S_Z - \frac{1}{2}\left(I_+ S_- + I_- S_+\right)\right] \qquad (33).$$

where $\omega_I = \omega_{iso}^I$ and $\omega_S = \omega_{iso}^S$ (we are ignoring the effects of CSA for now; they are considered in more detail in the context of RR in chapter 3). Although naive reasoning along the lines of AHT immediately suggests that we can drop the coupling term when the spinning speed sufficiently exceeds its magnitude, and this property does hold over a wide range of conditions, the reasoning behind this approximation is not technically correct. Because higher order terms in the average Hamiltonian expansion will include cross terms between the dipolar and chemical shift terms in equ (33), with a magnitude proportional to the product of the two, we will require the spinning speed to be significantly greater than the magnitude of both terms to ensure that the Magnus expansion converges fast enough to allow use of the zero-order average as a valid approximation. When this condition does not hold solely because of the magnitude of the

chemical shift terms, we can transform to an interaction frame in which the chemical shift terms are reduced in magnitude such that the condition does hold. Calculation of the zero-order average Hamiltonian in this frame then indicates whether the dipolar interaction will make a significant contribution to the dynamics[10].

Before making the appropriate transformation, we split the Hamiltonian into separate blocks as follows:

$$\begin{aligned} H &= \{H_0\} + \{H_1\} \\ &= \left\{\frac{\Sigma}{2}(I_z + S_z) + \omega_D(t)\tilde{1}\right\} + \left\{\frac{\Delta}{2}(I_z - S_z) - \frac{\omega_D(t)}{2}(I_+S_- + I_-S_+) - \omega_D(t)\tilde{1}\right\} \end{aligned} \quad (34),$$

where $\tilde{1}$ represents the unit matrix, $\Sigma = \omega_I + \omega_S$, and $\Delta = \omega_I - \omega_S$. Numbering the four states that span the space of this two spin system according to $1 = |++\rangle, 2 = |+-\rangle, 3 = |-+\rangle, 4 = |--\rangle$ (using $|m_I, m_S\rangle$ notation), the first block describes dynamics in the (14) subspace and the second block in the (23) subspace. Hence $[H_0, H_1] = 0$, and we can calculate the dynamics in the two blocks separately. The first block is inhomogeneous and yields a purely chemical-shift dependent effective Hamiltonian after averaging. It is the second block, which is homogeneous, that requires transformation to an interaction frame to ensure the validity of the zero-order average as an approximation to the full Hamiltonian. We can express the second block of the Hamiltonian using the spin-1/2 operators for a fictitious spin $\tilde{J}^{(23)}$[44, 45]:

$$\begin{aligned} J_X^{(23)} &= \frac{1}{2}(I_+S_- + I_-S_+) \\ J_Y^{(23)} &= \frac{-i}{2}(I_+S_- - I_-S_+) \\ J_Z^{(23)} &= (I_z - S_z) \end{aligned} \quad (35),$$

where the (23) superscript refers to the two levels of the original system which constitute this subspace. Inserting these into the second block of the Hamiltonian yields:

$$H_1 = \Delta J_Z^{(23)} + \omega_D(t) J_X^{(23)} \qquad (36),$$

where the unit matrix term has been dropped because it makes no contribution to the dynamics.

The interaction frame transformation that we now wish to perform is defined according to:

$$U = e^{i(n\omega_r t) J_Z^{(23)}} \qquad (37),$$

where we choose the integer n to minimize the magnitude of the residual chemical shift term in the transformed Hamiltonian:

$$H_1 = (\Delta - n\omega_r) J_Z^{(23)} + \omega_D(t)\left(J_X^{(23)} \cos(n\omega_r t) + J_Y^{(23)} \sin(n\omega_r t)\right) \qquad (38),$$

(that n is an integer ensures that the time-dependence remains a multiple of the spinning speed). Inserting the explicit form of the dipolar time dependence from equ. (30) and using raising and lowering operators yields:

$$H_1 = (\Delta - n\omega_r) J_Z^{(23)} + \sum_{m=-2,2} \omega_{(m)}^{IS} \left(J_+^{(23)} e^{i(m-n)\omega_r t} + J_-^{(23)} e^{i(m+n)\omega_r t}\right) \qquad (39).$$

The time-average over one rotor-cycle is

$$\overline{H}_1^{(0)} = (\Delta - n\omega_r) J_Z^{(23)} + \sum_{m=-2,2} \omega_{(m)}^{IS} \left(J_+^{(23)} \delta_{m,n} + J_-^{(23)} \delta_{m,-n}\right) \qquad (40).$$

Our selection of n ensures that the frequency of the slowest modulation (equal to the spinning speed) is at least twice as large as the residual chemical shift terms in the transformed Hamiltonian, and so as long as the dipolar interaction is also much smaller than the spinning speed, equ (40) should be a valid approximation to the time-dependent Hamiltonian (over integer multiples of the rotor period). If n>2, there are no components of the spatial and spin modulations that are close in frequency, and no recoupling occurs

(absent CSA effects - see chapter 3). If n=1 or 2, then there are components of the spatial modulation near in frequency to those of the spin modulation, and the average Hamiltonian has a dipolar component:

$$\overline{H}_1^{(0)} = (\Delta - n\omega_r)J_Z^{(23)} + \left(J_+^{(23)}\omega_{(-n)}^{IS} + J_-^{(23)}\omega_{(n)}^{IS}\right), \qquad \text{for n=1,2} \qquad (41),$$

re-expressed as:

$$\overline{H}_1^{(0)} = (\Delta - n\omega_r)J_Z^{(23)} + \left|\omega_{(n)}^{IS}\right|\left(J_X^{(23)}\cos\gamma - J_Y^{(23)}\sin\gamma\right) \qquad (42),$$

where $\gamma = \tan^{-1}\left[\mathrm{Im}\left(\omega_{(n)}^{IS}\right)/\mathrm{Re}\left(\omega_{(n)}^{IS}\right)\right]$. This Hamiltonian can be represented as a vector in the three-dimensional (x,y,z) space of the fictitious spin-1/2, where the transverse component of the representative vector arises from the recoupled dipolar interaction, and the longitudinal component comes from the residual chemical shift terms. When resonance is precisely matched:

$$\Delta = n\omega_r \qquad \text{for n=1,2} \qquad (43),$$

and the residual chemical shift term is zero, the vector representing the average Hamiltonian has no longitudinal component, and the spin dynamics are fully determined by the recoupled dipolar interaction. Observation of the spin dynamics at this condition can therefore be used to quantify the coupling, and hence extract information about molecular structure. As one moves away from resonance the longitudinal component of the vector representing the Hamiltonian increases; far enough from resonance the longitudinal component dominates and no dipolar evolution is evident. This dependence of the recoupling effect on chemical shift difference (relative to spinning frequency) can be exploited in multispin systems to selectively recouple pairs of spins for isolated observation (see chapter 4).

1.4 Internuclear Distance Measurements using RR.

1.4A Longitudinal Magnetization Exchange.

The recoupling effect evident in the average Hamiltonian of equ. (42) can be exploited in several different ways. Given the form of the recoupled dipolar interaction, both transverse and longitudinal (difference) magnetization are alternative initial states that do not commute with the Hamiltonian, and will evolve in a dipole-dependent manner. Preparation of transverse magnetization can be performed with CP, and followed immediately by acquisition of the FID (i.e. the standard CP/MAS experiment diagrammed in Fig. (1-1A), performed at RR[33]). The dipolar and chemical shift evolution periods are combined in this experiment, the recoupled dipolar interaction broadening the resonances of the recoupled spins relative to the width they would normally have away from RR. RR broadening imparts a characteristic shape (the RR "lineshape") to the lines, and the additional width depends on the magnitude of the coupling. In weakly coupled systems (b_{IS}<0.1kHz), T_2-type linebroadening effects (homogeneous or inhomogeneous) on transverse evolution of the magnetization closely mimic the broadening effects of the recoupled dipolar interaction, making it difficult to extract an accurate value for the magnitude of the dipolar effect, and placing (in most systems) a relatively restrictive upper limit on the magnitude of the internuclear interaction whose effects can be detected.

Longitudinal mixing experiments require separate dipolar mixing and detection periods, and hence at least a two-dimensional framework. Because these experiments have proven to be more sensitive to the effects of weak couplings, however, they have been used much more extensively in RR-based structural studies of biological compounds[17, 35]. Unlike transverse experiments where the initial condition commutes with part of the recoupled dipolar interaction and hence evolves at a slower rate, longitudinal experiments make use of the full recoupled dipolar Hamiltonian. Furthermore, decay of the initial state occurs (absent T_1 relaxation) only in the presence of a recoupled interaction, avoiding the need to subtract out the effects of other decay processes to uncover the dipolar-driven effect (although the rate of dipole-driven decay can be strongly influenced by relaxation effects - see below).

Longitudinal polarization in a two spin system, represented by the density operator $aI_z + bS_z$ where a and b are constants indicating the polarization level of each spin, can be separated into sum and difference components:

$$\rho = (a+b)(I_z + S_z)/2 + (a-b)(I_z - S_z)/2 = (a+b)J_z^{(14)} + (a-b)J_z^{(23)} \qquad (43).$$

Sum and difference polarization states are represented by longitudinal vectors in the (14) and (23) subspaces, respectively. Evolution of the system then occurs as a rotation of the vector representing the initial state about the vector representing the effective Hamiltonian in each subspace. In the (14) subspace, the Hamiltonian is purely longitudinal even at RR, and the vector representing longitudinal sum polarization does not rotate. In the (23) subspace, we have already described that at RR the effective

Hamiltonian is purely dipolar and is represented by a transverse vector; hence the longitudinal vector representing difference polarization will precess about the effective Hamiltonian at a rate determined by the magnitude of the recoupled interaction. The explicit calculation is as follows:

$$\begin{aligned}\rho(t) &= e^{-i\bar{H}^{(0)}t}\rho(0)e^{+i\bar{H}^{(0)}t} \\ &= \exp\left[-i\left|\omega_{(n)}^{IS}\right|t\left(J_X^{(23)}\cos\gamma + J_Y^{(23)}\cos\gamma\right)\right]\left(J_Z^{(23)}\right)\exp[+i...] \\ &= J_Z^{(23)}\cos\left(\left|\omega_{(n)}^{IS}\right|t\right) - \left(J_X^{(23)}\sin\gamma + J_Y^{(23)}\cos\gamma\right)\sin\left(\left|\omega_{(n)}^{IS}\right|t\right)\end{aligned} \qquad (44),$$

where we have assumed that the initial state consists purely of difference polarization. This describes a sinusoidal oscillation between longitudinal difference polarization and 2Q-coherence. We detect difference polarization:

$$\begin{aligned}\langle I_Z - S_Z\rangle_t &= \mathrm{Tr}\left[\rho(t)J_Z^{(23)}\right] \\ &= \cos\left(\left|\omega_{(n)}^{IS}\right|t\right)\end{aligned} \qquad (45).$$

In a powder sample, there is a distribution of recoupled interaction strengths due to the orientation dependence of the parameter $\omega_{(n)}^{IS}$. Calculating the observed signal requires a powder average over equ (45):

$$\langle I_Z - S_Z\rangle_t = \frac{1}{8\pi^2}\int_0^{2\pi} d\alpha \int_0^{\pi} d\beta \int_0^{2\pi} d\gamma\left(\cos\left(\left|\omega_{(n)}^{IS}\right|t\right)\sin\beta\right) \qquad (46).$$

For the n=1 resonance,

$$\left|\omega_{(1)}^{IS}\right| = b_{IS}\left|d_{0,1}^2(\beta_{MA})D_{1,0}^2\left(\Omega^{MR}\right)\right| = b_{IS}\frac{\sqrt{2}}{4}\sin(2\beta) \qquad (47),$$

and equ (46) describes the damped oscillatory decay in Fig. (1-2A). The FT of this curve (the recoupled dipolar powder pattern), is shown in Fig. (1-2B). Note several features of these plots. First, the recoupled powder pattern (1-2B) has a different shape than the static equivalent (a Pake pattern[46]), and a width that is approximately 35% of the static width (measured peak-to-peak).

Figure 1-2: Details of the longitudinal magnetization exchange process at the n=1 rotational resonance (absent CSA and relaxation effects):

(A) Magnetization exchange curve plotted vs. a dipolar constant-defined time scale. Maximum inversion of difference polarization occurs at $t \approx 1.8/b_{IS}$, with a level of -0.46 corresponding to a maximum polarization transfer efficiency of 73%. At longer times the value oscillates about, and eventually approaches, 0.0, corresponding to a long-time transfer efficiency of 50%.

(B) Recoupled dipolar powder spectrum, obtained by FT of time-dependent oscillations in (A). The outer edges of the pattern occur at ±35% of the dipolar coupling constant. The presence of a distribution of frequencies corresponds to the distribution of the magnitude of the recoupled dipolar interaction across the powder sample.

(A)

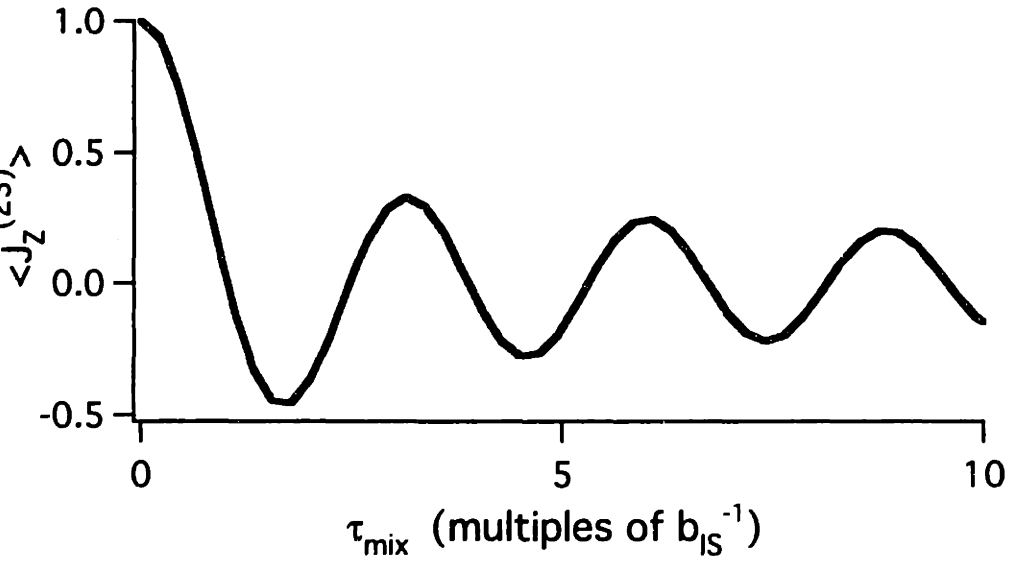
1.0
0.5
0.0
-0.5
$\langle J_Z^{(23)} \rangle$
0
5
10
τ_{mix} (multiples of b_{IS}^{-1})

(B)

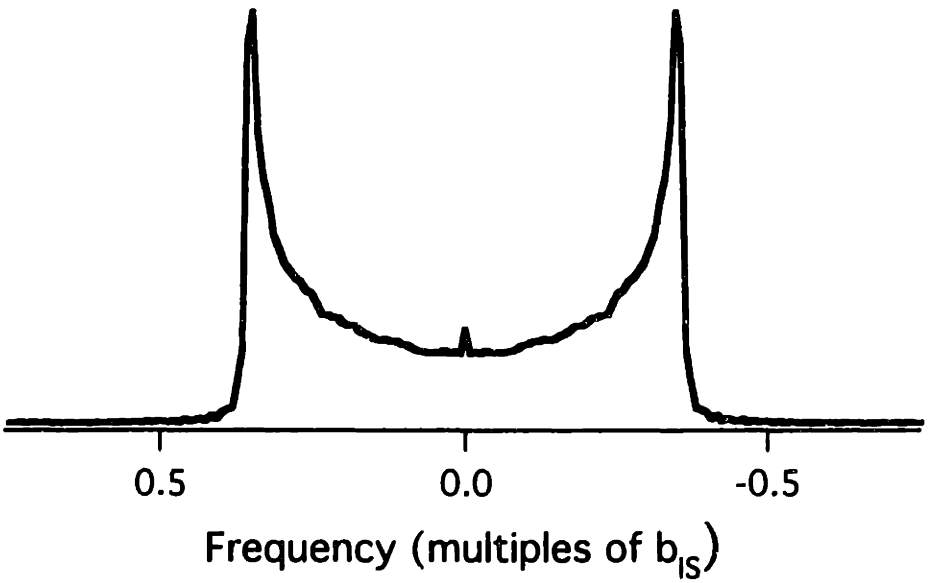
0.5
0.0
-0.5
Frequency (multiples of b_{IS})

Second, the maximum polarization transfer one can achieve in this type of experiment is approximately 73% (1-2A), and requires a mixing time tuned to the particular coupling constant ($t_{mix} \approx 2b_{IS}^{-1}$). Finally, at long times the equilibrium transfer efficiency is 50%.

Pulse sequences for dipolar mixing of longitudinal difference polarization are diagrammed in Fig. (1-3). They have 4 distinct periods: (i) the standard CP sequence is applied to transfer polarization from the ^{1}H reservoir to the low-γ nucleus of interest; (ii) after CP, an inversion sequence is used to create longitudinal difference polarization; (iii) longitudinal dipolar mixing ensues for a time τ_{mix}; (iv) a 90° pulse is applied and the resulting FID is detected. HPPD is applied throughout the final three periods as diagrammed. An exchange curve of the type shown in Fig. (1-2A) is determined by obtaining FID's and measuring the residual difference polarization as a function of the mixing time. Because increases in mixing time lead to longer periods of decoupling and hence probe heating effects that may cause changes in the detected signal independent of the spin dynamics, a period of (otherwise useless) decoupling is applied at the end of the experiment to ensure that the overall decoupling time remains constant[47]. As the mixing period is increased, the length of this extra decoupling period is decreased by a compensating amount. Placing the additional decoupling before the experiment may better control for heating effects, but placing it after the experiment is easier, and we found that this was sufficient to eliminate decoupling-time dependent changes in detected signal intensity.

Figure 1-3: Pulse sequences for performing longitudinal mixing experiments. All three sequences have four basic features in common:: (i) cross-polarization from ^1H to ^{13}C (or other low-γ nucleus) to increase S/N (directly and indirectly, through shorter ^1H T_1's), (ii) a preparation period during which longitudinal difference polarization is created; (iii) a dipolar mixing period; and (iv) a detection period in which a 90° pulse is applied to create transverse polarization, followed by pure-phase detection of the resulting FID. High-power ^1H decoupling is applied through the final three periods, and an optional "dummy" decoupling period after detection is often applied to keep the overall power input into the probe constant during experiments in which the mixing time is incrementally increased. The preparation periods in each case are as follows:

(A) A 90° pulse is applied after CP to create longitudinal sum polarization. This is followed by application of a weak rf-field (typically 1-2kHz) at (or very near) the resonance frequency of one spin, selectively inverting its polarization.

(B) The long, low-power, CW selective inversion pulse of (A) is broken up into a series of high-power bursts separated by periods of free evolution. This DANTE sequence has selective inversion properties similar to those of the longer CW pulse.

(C) A modified form of the n=2 DANTE sequence, where the CP period creates transverse polarization and so substitutes for the 1^{st} pulse of the two-pulse DANTE. The speed of this inversion technique is beneficial in many 2-spin applications (see text).

^{1}H:


90°
Decoupling

^{13}C:

(A)

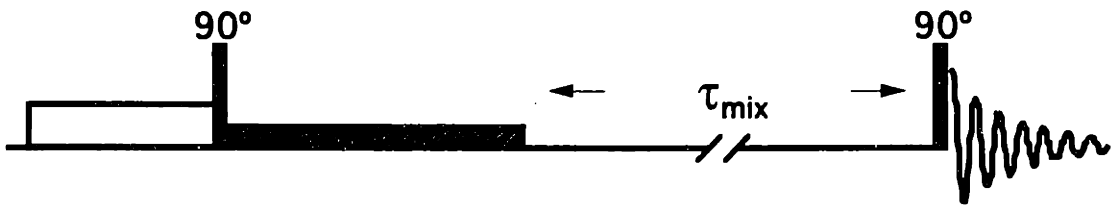
90°
90°
τ_{mix}

(B)

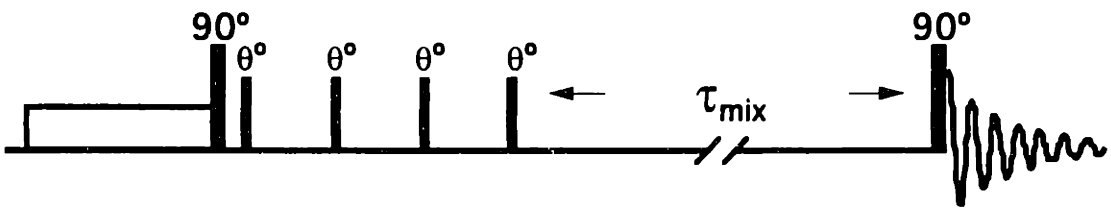
90°
θ°
θ°
θ°
θ°
90°
τ_{mix}

(C)

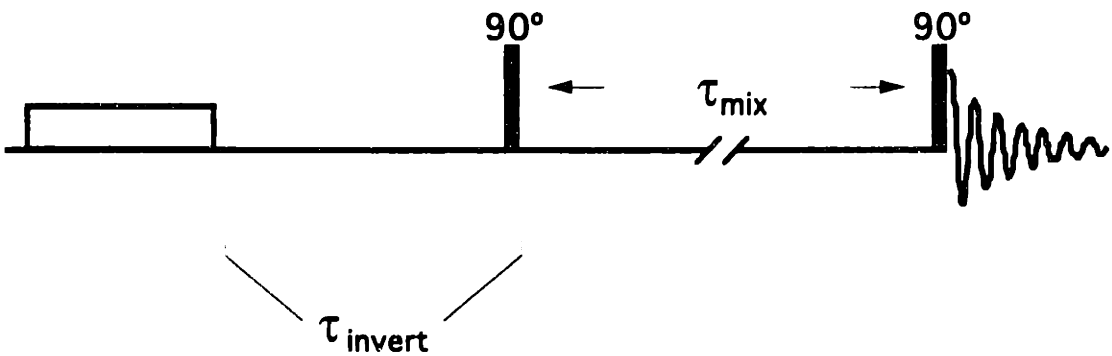
90°
90°
τ_{mix}
τ_{invert}

Three different inversion methods are illustrated in Fig. (1-3). In the first (1-3A), a 90° pulse is applied after CP to rotate the magnetization along the z-axis. This creates longitudinal sum polarization. Following this, a weak rf field is applied at the frequency of the resonance whose inversion is desired. To ensure selectivity in the inversion process, the strength of the rf field should be significantly less than the chemical shift offset of resonance(s) whose inversion is not desired. Typically the rf field magnitude is set such that a 0.2-0.5ms inversion period (i.e. 180° pulse length) is required (corresponding to 1-2kHz field strengths). A DANTE[48] inversion of the type indicated in Fig. (1-3B) provides a high-power alternative. Splitting the weak, CW, selective inversion pulse into a series of short, high-power bursts (separated by free evolution) such that the overall rotation induced by the rf remains constant, leads to very similar inversion behaviour (although the character of the inversion sidebands is different). For n short, equal-length bursts, the length of each burst is selected to induce a (180/n)° rotation.

The final sequence (1-3C) shows a modification of the n=2 DANTE sequence derived from (1-3B), where CP performs the action of the first 90° pulse. With the carrier placed directly between two resonances with a chemical shift difference Δ, the delay between CP and the first 90° pulse required for inversion is $1/2\Delta$. Given the speed of the inversion, this sequence (CPDELAY for inversion) has advantages over the previous ones, particularly in systems where the couplings are large and can have a significant effect on 10^2 μsec timescales. These effects include both a reduction in initial signal intensity, and a shift in the time-axis of the measured exchange

curve because of dipolar evolution during the inversion process. The latter effect is illustrated by a series of simulations in Fig. (1-4) for a model system with a 0.5kHz coupling (the parameters are identical to those for 1-α2, ^{13}C-labeled glycylglycine, given in chapter 3). The solid curve traces out the evolution of difference polarization expected after an instantaneous (i.e. ideal) inversion. Overlapping this curve is the one obtained by explicitly calculating the effects of a CPDELAY inversion (delay approximately 0.045ms). The dotted and dashed lines show the calculated dynamics including the effects of either a weak selective inversion pulse or a standard DANTE sequence. These curves reach their first minimum $\approx$0.2-0.3ms before the ideal curve. Corrections for effects of this type were necessary for the RR data obtained in chapter 3. In more strongly-coupled systems, the exchange that occurs during the longer inversions can also make it difficult to normalize the exchange curve appropriately (one must project back to estimate the initial intensity). In weakly coupled systems effects of this type are negligible.

1.4B Zero-Quantum Relaxation.

Relaxation during dipolar mixing can have a significant effect on the observed spin dynamics when the rate of relaxation is comparable to (or exceeds) the relevant dipolar couplings, and its effects must be included in calculations in these cases if accurate distance information is to be extracted from experimental data. The density matrix representing the state of the system during dipolar mixing (equ (44)) has two components which we expect to relax differently. Longitudinal difference polarization relaxes according to

Figure 1-4: Time-delay artifacts in n=1 RR exchange curves due to inversion method. Simulations performed for a 2-spin system with a 0.5kHz coupling, a 10kHz isotropic chemical shift difference, and typical CSA parameters. The solid line shows result expected after an ideal (instantaneous) inversion; the simulated result using the CPDELAY sequence (50μs inversion period) overlays this one. The dotted lines show the results using either a selective inversion (^{13}C rf=2.5kHz, inversion time=200μs) or a n=4 DANTE with 2.5μs pulses (^{13}C rf=50kHz) and 50μs interpulse spacings (peaks at 0 and 10kHz relative to the carrier). These curves lag the ideal curve by approximately 240μs. The dashed line shows the simulated result for an N=4 DANTE equivalent to the previous, but with the interpulse spacing set at 150μs (peaks at -3.3 and +6.7kHz relative to the carrier). This curve lags ideal by 340μs. The inset shows the curves plotted with the appropriate corrections to the timescales in each case; the match with the ideal curve is in this case much improved.

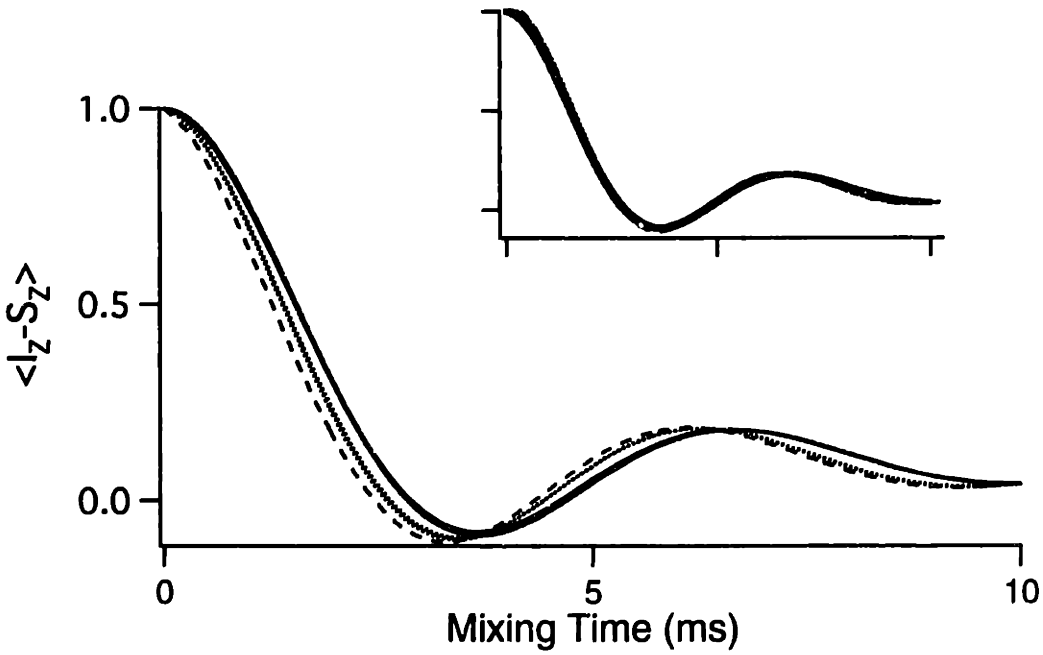
1.0
0.5
0.0
<I_z-S_z>
0
5
10
Mixing Time (ms)

T_1, which is usually on the order of seconds (or longer) for low-γ nuclei in rigid solids, while we generally use mixing times of 100ms or less. Hence under most experimental conditions we can ignore this type of relaxation; observed changes in the amount of difference polarization during mixing then must be attributed to the creation of 2Q coherence. Relaxation of the 2Q coherences, however, which is driven by T_2-dependent processes and can be significant on the timescale of typical experiments (msec), affects the rate at which difference polarization rotates into 2Q coherence, and hence on the observed dynamics.

Calculation of the modified dynamics is complicated by the different relaxation rates of the two components of the density matrix. Here we list the results from Levitt, et. al.[10] (they do not include the powder average). In strongly coupled systems, e.g. where the magnitude of the recoupled interaction is much larger than the 2Q-coherence relaxation rate, the density matrix oscillates between the two components several times before relaxation has an appreciable effect, and the modified dynamics do not show evidence of different relaxation rates for the two components[10]:

$$\langle I_z - S_z \rangle_t = e^{-rt/2} \cos\left(\left|\omega^{IS}_{(n)}\right| t\right) \qquad \text{for } r << \left|\omega^{IS}_{(n)}\right| \tag{48},$$

where r represents the rate of 2Q-coherence relaxation (multiplication of the dynamics absent relaxation (equ. (45)) by the appropriate exponential is what we would expect if both components of the density matrix relaxed identically). In weakly-coupled systems the modified dynamics are more complicated[10]:

$$\langle I_z - S_z \rangle_t = e^{-rt/2}\left[\cosh(Rt/2) + \frac{r}{R}\sinh(Rt/2)\right] \tag{49},$$

where $R^2 = r^2 - 4|\omega_{(n)}^{IS}| > 0$. When the dephasing rate becomes much larger than the magnitude of the recoupled interaction, equ (49) reduces to[10]:

$$\langle I_z - S_z \rangle_t = \exp\left[-\frac{|\omega_{(n)}^{IS}|^2}{r} t \right] \qquad (50),$$

and the decay of difference polarization is exponential, with a time constant that is inversely proportional to the 2Q-coherence relaxation rate (r). That the dynamics, particularly in the weakly-coupled case, are so strongly dependent on r makes it difficult to extract accurate distance information from the observed dynamics without an accurate estimate of this parameter. This is demonstrated in Fig. (1-5). The top plot (1-5A) shows the exchange curves we would expect to obtain from spin pairs at n=1 RR with 4.7, 5.0, and 5.3 Å internuclear distances, and otherwise identical parameters (r= 0.3kHz; these simulations include the powder average). The middle plot (1-5B) shows that if we hold the distance constant (5.0Å), and instead vary the 2Q-relaxation rate (r=0.4, 0.3, 0.2kHz), we obtain similar variations in the exchange curves. This illustrates that the dependence of the shape of the exchange curve on r and the internuclear distance is very similar. Hence if we change both the internuclear distance and the 2Q-relaxation rate in a compensating manner, we can, as shown in the bottom plot (1-5C), obtain almost overlapping exchange curves. We have two parameters to extract, but effectively only one experimental variable.

Estimation of the 2Q-relaxation rate from other information will allow us to fit experimental longitudinal exchange curves solely as a function of the internuclear distance (subject to uncertainty in

Figure 1-5: Comparison of the dependence of n=1 RR exchange curves on the 2Q-relaxation rate (r) and the dipolar coupling constant (b_{IS}). Simulations were performed for a 2-spin ^{13}C-^{13}C system with standard CSA values and a 10kHz isotropic chemical shift difference.

(A) At constant r (91Hz, corresponding to a zero-quantum T_2 of 3.5ms), the curves clearly show a strong dependence on the dipolar coupling constant and hence the internuclear distance. This is the effect that allows the extraction of internuclear distance information from RR magnetization exchange data.

(B) At constant b_{IS} (61Hz, corresponding to an internuclear distance of 5.0Å), the exchange curves show a similar dependence on r. Hence without an accurate estimate of the 2Q-relaxation rate, it is not possible to extract accurate distance information.

(C) Compensating changes in b_{IS} and r can produce nearly overlapping exchange curves (in the parameter regime we examine here). This illustrates the point that accurate estimates of r are necessary to extract accurate distance information form these data.

(A)

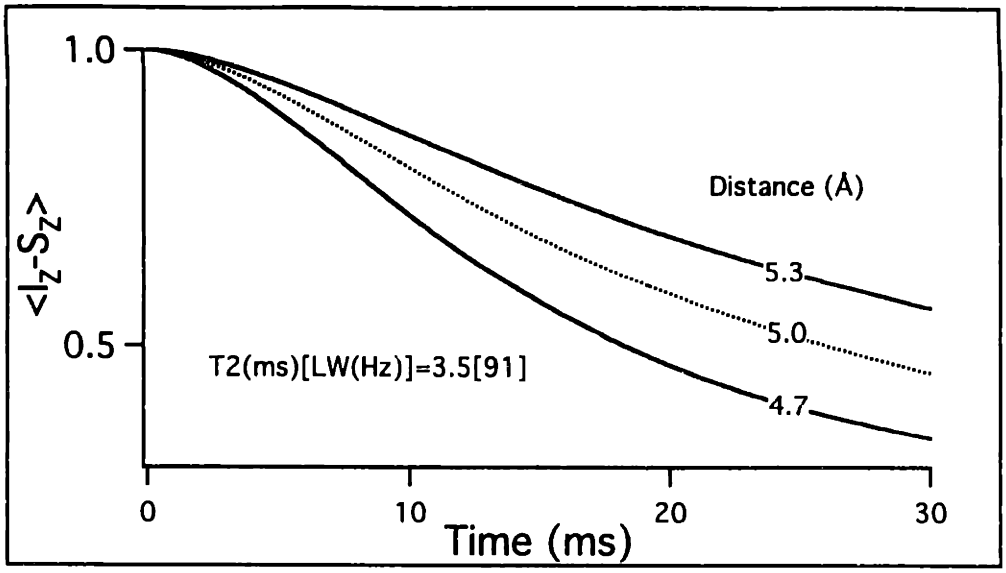
1.0
0.5
<Iz-Sz>
Distance (Å)
5.3
5.0
4.7
T2(ms)[LW(Hz)]=3.5[91]
0
10
20
30
Time (ms)

(B)

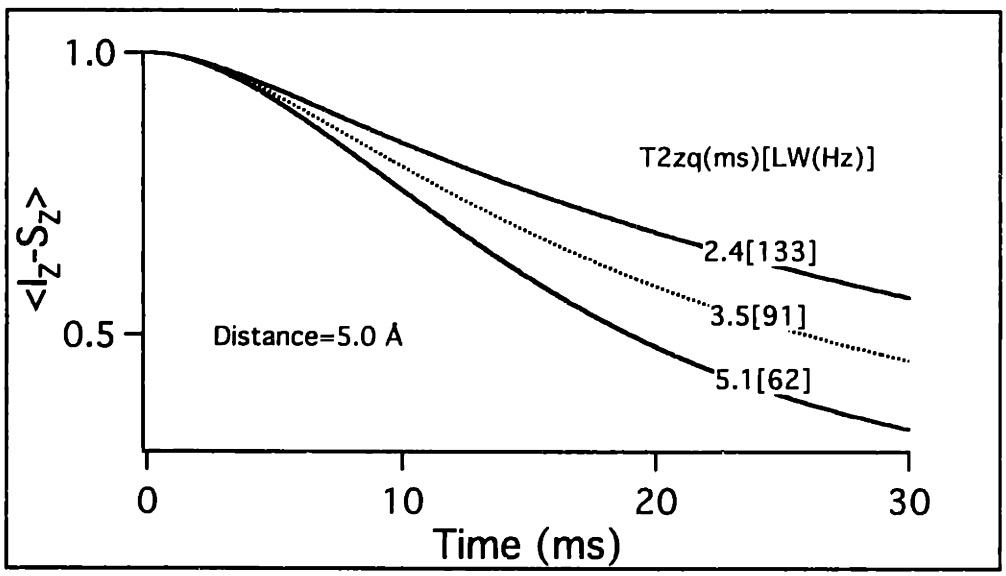
1.0
0.5
<Iz-Sz>
T2zq(ms)[LW(Hz)]
2.4[133]
3.5[91]
5.1[62]
Distance=5.0 Å
0
10
20
30
Time (ms)

(C)

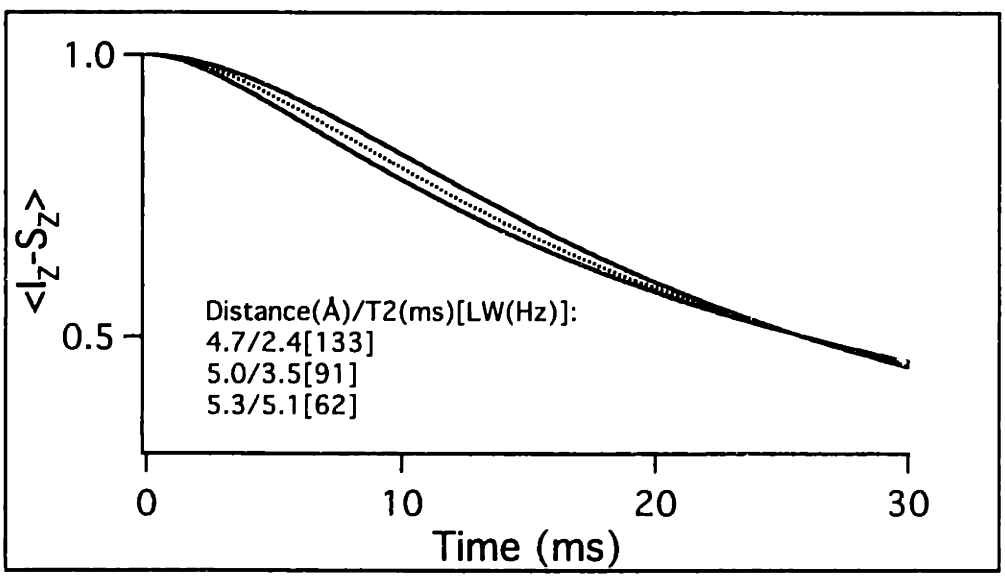
1.0
0.5
<Iz-Sz>
Distance(Å)/T2(ms)[LW(Hz)]:
4.7/2.4[133]
5.0/3.5[91]
5.3/5.1[62]
0
10
20
30
Time (ms)

all of the relevant spin system parameters, particularly r itself). Kubo and McDowell[49] have shown that the 2Q-relaxation rate is equal to the sum of the transverse relaxation rates of the relevant single quantum coherences (r_{1Q}^{x}):

$$r = r_{1Q}^{I} + r_{1Q}^{S} \qquad (51),$$

using a model in which relaxation is driven by random fluctuating fields at each nucleus, and assuming that the random fluctuations at the two nuclei are uncorrelated. Absent a significant inhomogeneous contribution to the linewidth, the single-quantum transverse relaxation rates can be calculated directly from the observed width away from RR (FWHM multiplied by π). When inhomogeneous broadening is present, single π-pulse Hahn-echo experiments[50] (again, performed away from RR) allow separation of homogeneous and inhomogeneous contributions to the linewidth, and only the former is used in equ. (51). When the inhomogeneous contribution is significant, however, its effects on the exchange must also be taken into account, as described in the following sections.

1.4C Chemical Shift Dispersion.

The analysis of RR spin dynamics that we have performed to this point assumes that each of the spins, I and S, has a single distinct isotropic chemical shift across the macroscopic sample, and any linewidth evident in the spectrum arises solely from homogeneous effects. Even in well-characterized, polycrystalline samples, known (by other methods, e.g. x-ray crystallography) to be composed of molecules in a single conformation, there often is a distribution in the isotropic chemical shift exhibited by each distinct nucleus in the

molecule. We attribute this effect (termed chemical shift dispersion, CSD), at least in part, to slight variations in molecular conformation and intermolecular packing across the macroscopic sample which do not change on the NMR timescale[51] (in solution NMR, motion among similar conformations is often fast on this timescale, so that broadening effects of this type are not evident even if analogous conformational heterogeneity is present).

Because the distribution in isotropic shifts at each site (termed chemical shift dispersion, or CSD) translates into a distribution of isotropic chemical shift differences between pairs of nuclei in the sample, this has implications for RR experiments that extend beyond the obvious reduction in spectral resolution. It becomes impossible to precisely match the RR condition for all copies of a two-spin system in a macroscopic sample where this effect is present. The longitudinal exchange dynamics observed by performing experiments with the spinning speed placed at the approximate center of the distribution (or a submultiple of it, for RR experiments of order greater than one) are modified according to the nature of the CSD broadening, the modification becoming significant when the width of the distribution is comparable to (or exceeds) the magnitude of the relevant dipolar coupling(s). Given a model for the difference distribution, inclusion of its effects in the calculation of the spin dynamics is straightforward. Several calculations of the dynamics are performed at a series of chemical shift differences spanning the difference distribution, and the results are summed in a weighted fashion determined by the shape of the difference distribution. The

resulting curve should accurately model the observed dynamics under these conditions.

The difficult step in this process is the determination of the chemical shift difference distribution. Assuming the single π-pulse echo experiments (performed away from RR) that we described in the previous section are accurate, we can quantify the homogeneous contribution to the linewidth at each site, and remove it from the spectrum by appropriate exponential multiplication (i.e. by a negative value) of the FID before FT (we assume in this process that the homogeneous contribution is lorentzian - hence the echo data is fit using an exponential, etc.). We also assume that the inhomogeneous lineshape at each site thus uncovered is dominated by CSD, and hence can be interpreted as the probability distribution of the isotropic chemical shift for the relevant nucleus in the sample. Calculation of the chemical shift difference distribution from the separate, single-spin chemical shift distributions then requires some determination of the nature of the chemical shift correlation between the two sites - e.g. when spin I has a particular chemical shift, does the corresponding spin S in the same molecule have a particular chemical shift (or a particular probability distribution of shifts that differs from the overall S-spin chemical shift distribution?). Contributions to the inhomogeneous linewidth from factors such as magnet inhomogeneity should be correlated between two sites in the same molecule, and so will not contribute additional breadth to the difference distribution. Variations in chemical shift at the two sites that are related to variations in molecular structure or packing, however, may or may not be correlated between the two sites,

perhaps depending on both the magnitude of the heterogeneity and the distance between the two sites. For the relatively crystalline model compounds we are considering here, we assume that the limited conformation heterogeneity implied by the relatively small inhomogeneous components of the resonances are uncorrelated for weakly coupled spins (e.g. separated by 3 or more bonds), so that, given a particular chemical shift for I, the probability of having various chemical shifts at S is given directly by the overall inhomogeneous distribution. (Determining the chemical shift difference distribution with sufficient resolution to extract accurate distance information when correlation is present is discussed in later sections).

The shape of the difference distribution follows directly after the "uncorrelated chemical shift" assumption: it is given by the convolution of the distribution at one site with the mirror image of the second site. Such a convolution can be calculated directly from the FID of the two-spin system (obtained away from RR to eliminate (homonuclear) dipolar broadening) in the obvious manner, listed here to ensure clarity (see Fig. 1-6): (i) invert the imaginary part of one copy of the FID; (ii) multiply (in complex fashion) the unmodified FID with the modified FID from (i); (iii) reverse exponentially multiply by the sum of the two homogeneous linewidths to remove homogeneous broadening (and correlated contributions to the linewidth). The Fourier transformed result will have peaks at the chemical shift differences of all peak pairs in the spectrum (a peak at zero-frequency appears due to convolution of peaks with themselves). The shape of each resonance in this

Figure 1-6: Sketch of the procedure by which the isotropic chemical shift difference distribution can be calculated from the FID obtained under typical CP/MAS conditions. The top plot shows the spectrum of a typical two-spin, weakly-coupled sample ((2-^{13}C)Glycyl(1-^{13}C)glycine•HCl, diluted 1:10 in natural abundance) spinning near the n=1 RR condition (ω_r=13.2kHz). Creating a copy of the corresponding FID with an inverted imaginary component, and multiplying (in complex fashion) this copy by the original FID, yields the FID of the mirror-convoluted spectrum (see text). Reverse exponential multiplication can be used at this stage to remove the homogeneous contribution to the linewidths (obtained, for example, from standard echo experiments). FT of the convolution FID yields a spectrum with peaks at the difference frequency of all resonance pairs in the original spectrum, in this case at 12.88kHz and 0kHz (the latter arising from convolution of the peaks with themselves). An expanded view of the difference distribution is also included.

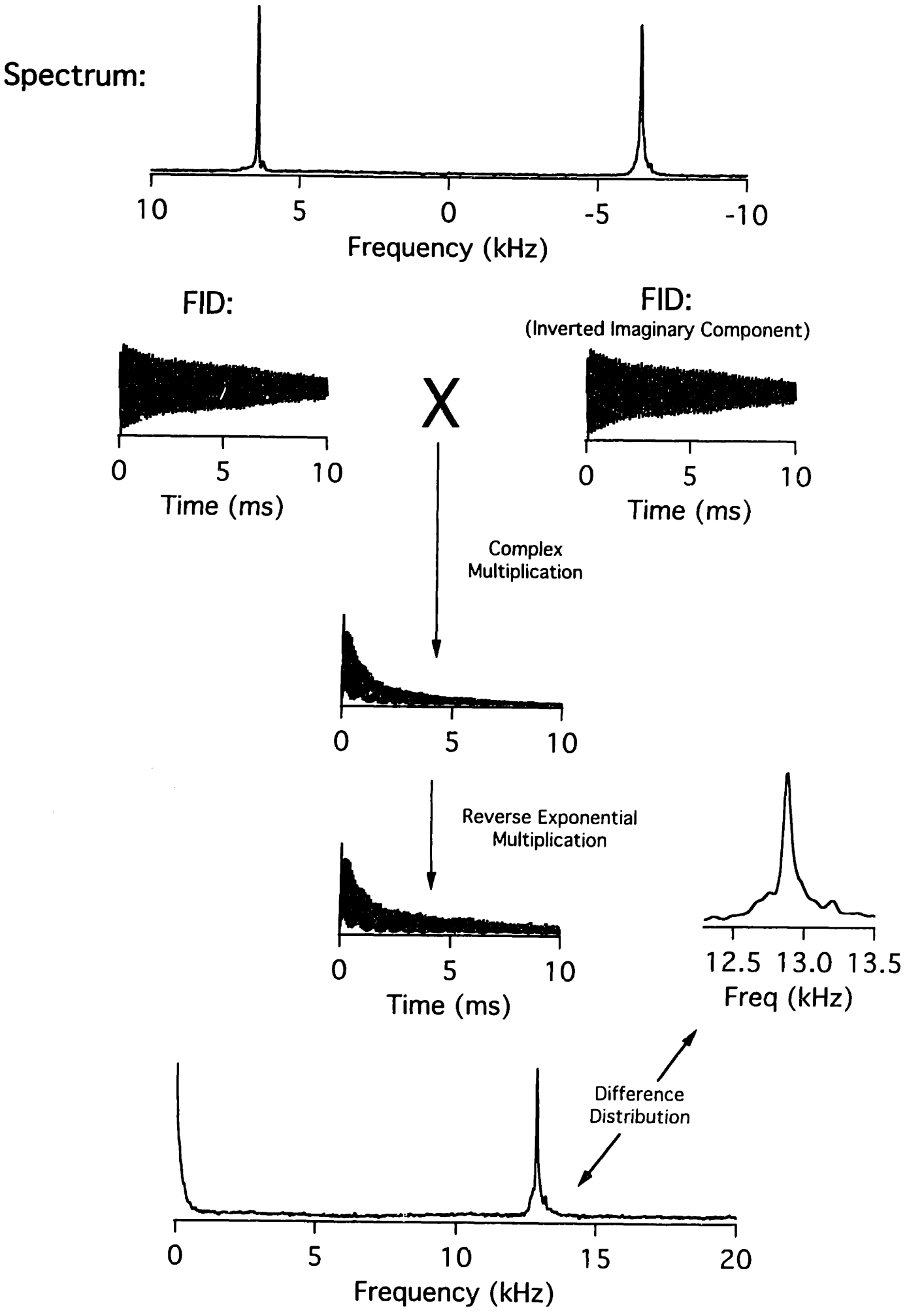
Spectrum:
10
5
0
-5
-10
Frequency (kHz)
FID:
0
5
10
Time (ms)
X
FID:
(Inverted Imaginary Component)
0
5
10
Time (ms)
Complex
Multiplication
0
5
10
Reverse Exponential
Multiplication
0
5
10
Time (ms)
12.5
13.0
13.5
Freq (kHz)
Difference
Distribution
0
5
10
15
20
Frequency (kHz)

spectrum outlines the chemical shift difference distribution for the relevant spin pair. This distribution can be used directly in calculating the expected spin dynamics (as detailed above), or it can be fit using standard models (e.g. gaussian or lorentzian lineshapes), with the appropriate lineshape parameters then fed into the simulation program. We have primarily used the second method in the calculations described here and in subsequent chapters.

1.4D Rotational Resonance Shape.

Accurate calculation of spin dynamics at RR requires, as we detailed in the previous two sections, inclusion of zero-quantum lineshape parameters: the magnitude of the homogeneous component (characterized by $r=\frac{1}{T_2^{ZQ}}$, and assumed to be lorentzian in shape), and the magnitude and shape of the inhomogeneous component (arising from CSD). Estimation of both of these parameters is possible based on appropriate measurements of the relevant single-spin lineshape parameters (as described), but the accuracy of the estimation depends in both cases on assumptions about possible correlations (for either relaxation processes or CSD) between the two sites (or, more generally, on the validity of our models for these two effects, from which our arguments on correlation are based). Methods do exist for independently measuring the zero-quantum relaxation rate and the nature of the chemical shift correlation between sites (using standard 2D chemical shift correlation spectroscopy - see chapter two), but these methods are either not highly accurate, or can not easily be applied to the weakly-coupled systems which are of the most interest in structural studies. Here we describe techniques for

extracting, or at least constraining, the zero-quantum lineshape parameters directly from RR-induced spin dynamics - from the near-resonance behaviour of the spin system.

1.4D.1 RR shape absent 2Q-relaxation.

Longitudinal magnetization exchange is generally maximized when a RR condition is matched, and decreases monotonically as one moves away from resonance (the monotonic property of the decrease as a function of mismatch does not necessarily hold for certain short mixing times in strongly coupled systems). The "RR shape" that this defines is a function of mixing time, and can be measured as follows: set the mixing time to a fixed value (t), and measure the extent of magnetization exchange as a function of spinning speed, incrementing the speed from one side of the resonance condition to the other (Fig. 1-7). Absent relaxation, the shape of the RR for a single spin-pair is given by:

$$\langle I_Z - S_Z \rangle_{\omega_r} = \frac{(\omega_r - \Delta)^2 + |\omega_{(n)}^{IS}|^2 \cos\left(\sqrt{|\omega_{(n)}^{IS}|^2 + \Delta^2}\, t\right)}{(\omega_r - \Delta)^2 + |\omega_{(n)}^{IS}|^2} = 1 - \frac{1 - \cos\left(\sqrt{|\omega_{(n)}^{IS}|^2 + \Delta^2}\, t\right)}{\left((\omega_r - \Delta)^2 / |\omega_{(n)}^{IS}|^2\right) + 1} \quad (52).$$

The shape that this describes near the n=1 rotational resonance is illustrated in Fig 1-7 for a particular mixing time ($t=0.9/b_{IS}$): it has a minimum on-resonance (equal to $\cos\left(\sqrt{|\omega_{(n)}^{IS}|^2 + \Delta^2}\, t\right)$) and a width (FWHM) of approximately (b_{IS}). After powder averaging, the time-dependent shape becomes more complex, partly because the magnitude of the contributions of various crystallites to the overall shape oscillates. As a general conclusion, however, we expect increases in the dipolar coupling constant to both increase the depth

Figure 1-7: Shape of the n=1 rotational resonance (exchange as a function of spinning speed away from exact resonance) for a 2-spin system with typical CSA parameters and a 60Hz dipolar coupling constant. Relaxation and difference distribution effects have not been included. The resonance "peak" can be characterized by its width and depth (or height) as shown.

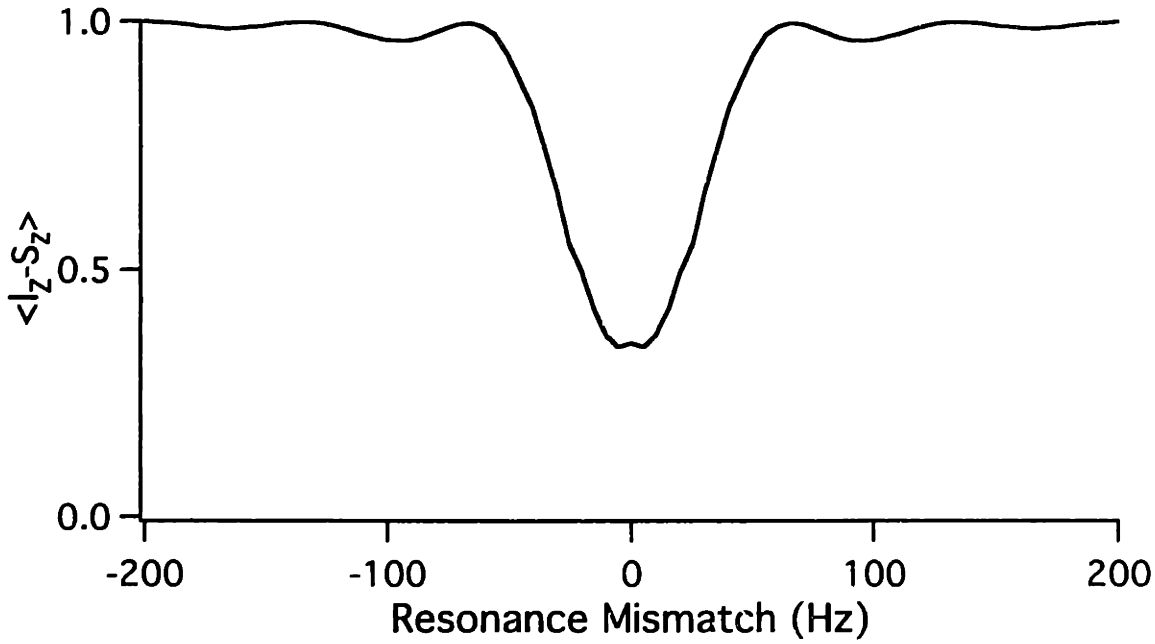
1.0
0.5
0.0
<I_z-S_z>
-200
-100
0
100
200
Resonance Mismatch (Hz)

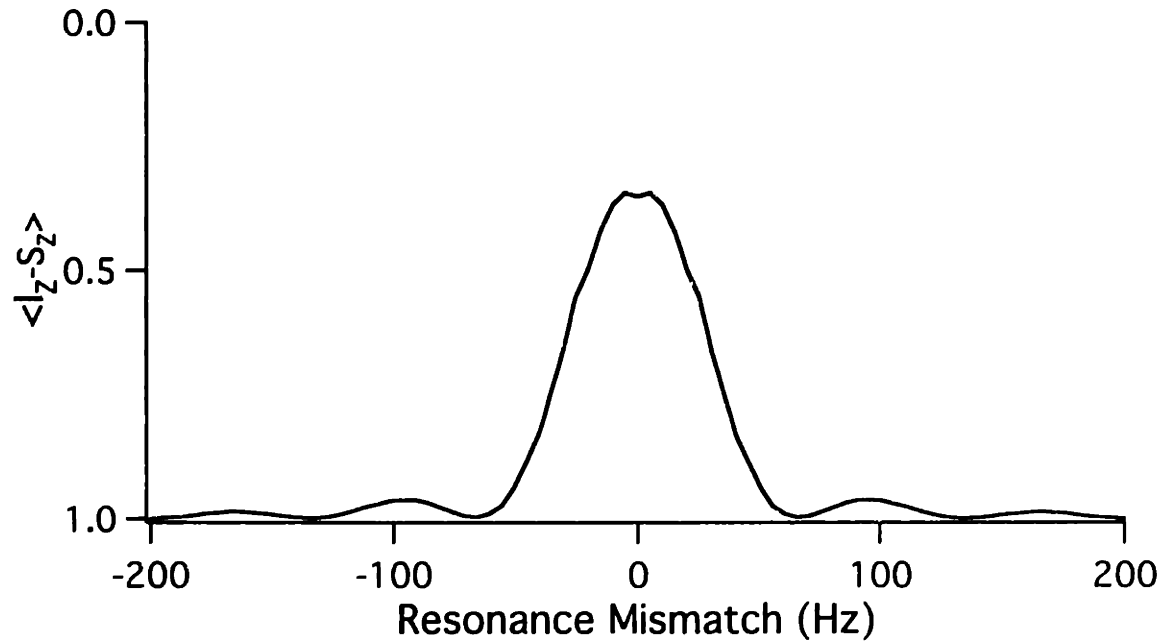
0.0
0.5
1.0
<I_z-S_z>
-200
-100
0
100
200
Resonance Mismatch (Hz)

and the width of the RR shape at all mixing times. Numerical simulations of the resonance shape at 20 ms, absent relaxation and using two different coupling constants, illustrate the effect in Fig. (1-8A).

1.4D.2 RR shape in the presence of 2Q-relaxation.

When 2Q-coherence relaxation is present, the modified form of equ (52) is difficult to calculate explicitly for the general case, and in any event a powder-average is required. If 2Q-relaxation dominates ($r >> b_{IS}$), the resonance shape approaches a lorentzian with a width determined by r (FWHM=r/π). The shape has no dependence on either the powder average or the mixing time (although its magnitude does increase over time). Increases (decreases) in r increase (decrease) the width of the resonance, with a concomitant decrease (increase) in the resonance peak. This is illustrated in Fig. (1-8B). When 2Q-relaxation does not clearly dominate, numerical simulation allows calculation of the resonance shape in the absence of an analytic formulation. These calculations show that the effect of relaxation to decrease the level of exchange measured on resonance at a specific mixing time, and increase the level of exchange measured off resonance, is maintained even when r does not clearly dominate. (Hence for systems with levels of inhomogeneous broadening that are comparable to or exceed the magnitude of the recoupled interaction, this implies that appropriate tuning of the relaxation rate (by changing the ^1H decoupling power) will maximize the level of magnetization transfer. Minimizing the 2Q-relaxation rate (by, for instance, application of maximum decoupling power)

Figure 1-8: Dependence of the rotational resonance shape on the dipolar coupling constant (b_{IS}) and 2Q-relaxation (r):

(A) Increasing the coupling constant from 60Hz to 80Hz (r=100Hz) increases both the width and height of the resonance peak, as shown. Both on- and off-resonance exchange is increased.

(B) Decreasing the 2Q-relaxation rate from 400Hz to 200Hz (b_{IS}=60Hz) increases the height and decreases the width of the resonance peak. On-resonance exchange is increased, but sufficiently off-resonance exchange is decreased.

(A)

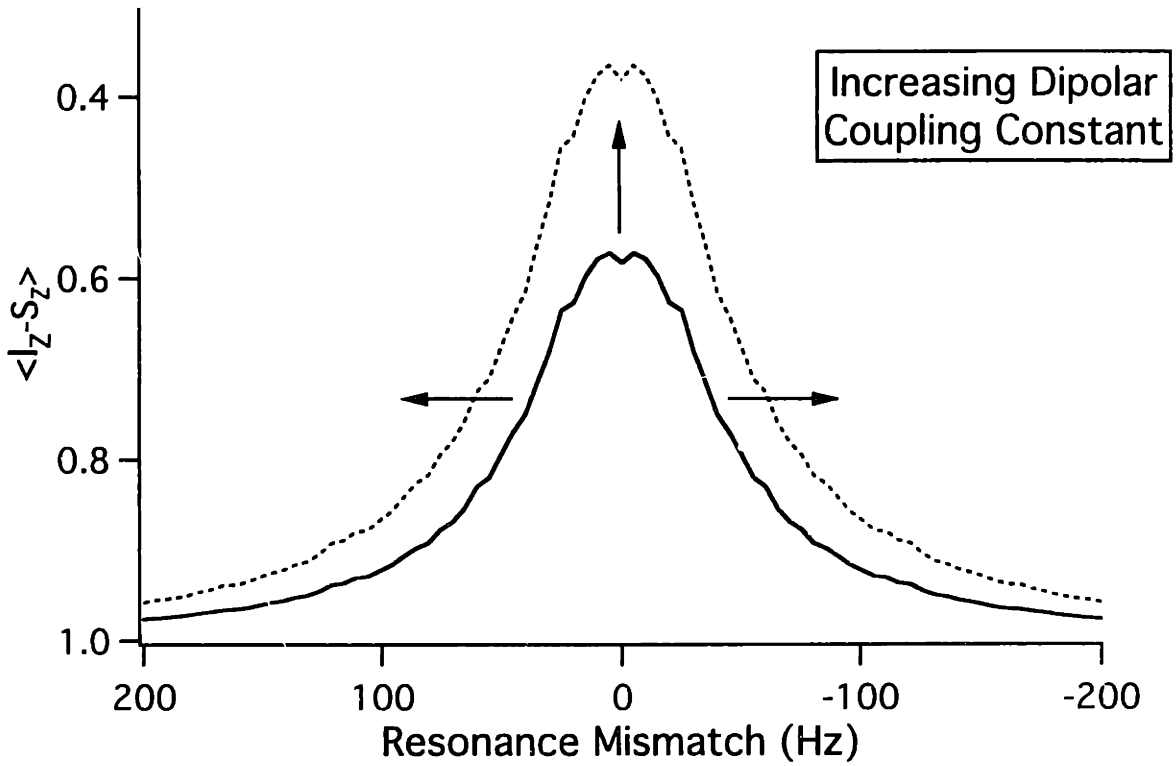
Increasing Dipolar Coupling Constant
0.4
0.6
0.8
1.0
<I_z-S_z>
200
100
0
-100
-200
Resonance Mismatch (Hz)

(B)

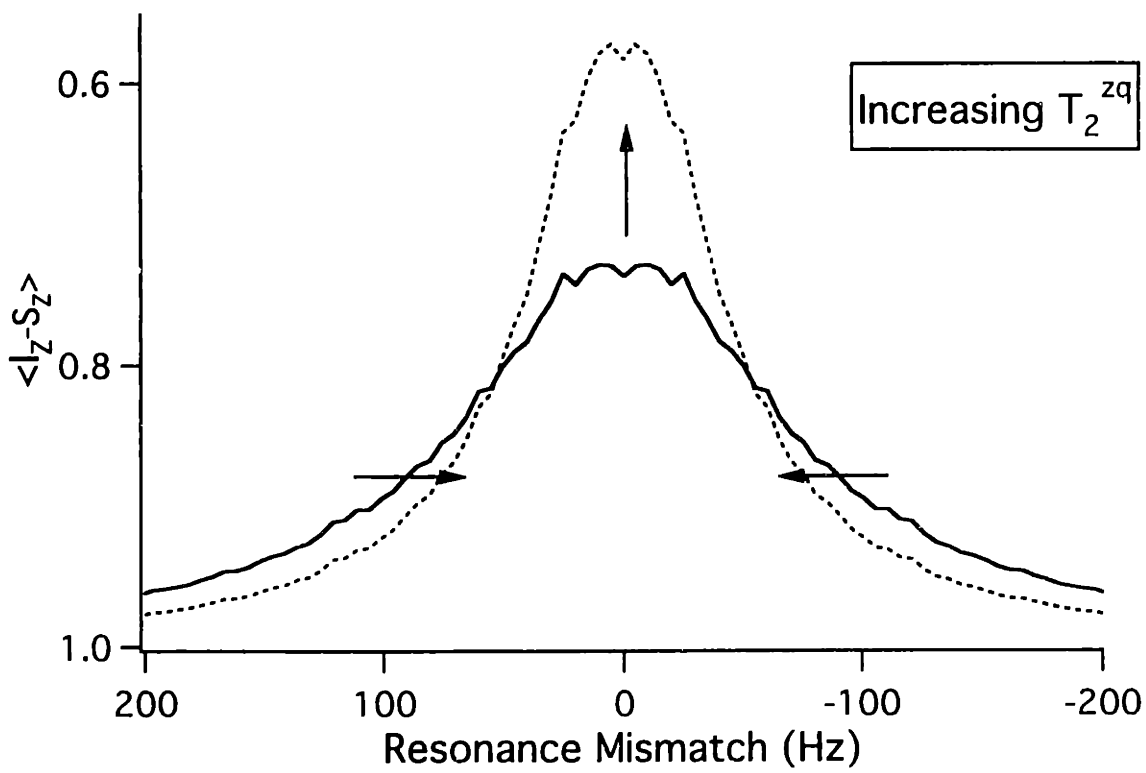
Increasing T2zq
0.6
0.8
1.0
<I_z-S_z>
200
100
0
-100
-200
Resonance Mismatch (Hz)

may lead to reduced levels of polarization transfer in some systems.)

Because the RR shape has distinctly different dependencies on r and b_{IS} (compare figures 1-8A,B), we can use measurements of the shape to extract both parameters directly from the RR dynamics without independently estimating the 2Q-coherence relaxation rate. This is illustrated in Fig. (1-9). The top plot (1-9A) shows the change in the resonance shape for internuclear distances of 4.7, 5.0, and 5.3Å. The parameters used in these calculations were identical to those used for Fig. (1-5). The middle plot (1-9B) shows the change in the resonance shape due to changes in r, with b_{IS} held constant. Clearly the changes in (1-9A) and (1-9B) are distinguishable, and the bottom plot (1-9C) illustrates that measurement of the RR shape can resolve the problem of extracting distance information independent of T_2^{zq}, evident in Fig. (1-5C).

1.4D.3 RR shape including 2Q-relaxation and CSD effects.

The shape of the rotational resonance in the presence of a distribution of chemical shift differences is determined by the convolution of that difference distribution with the resonance shape expected for a system with a single, well-defined shift difference (calculated as described in the previous sections). Because of this additional contribution to the RR shape, extraction of the dipolar coupling constant from measurements of the shape is no longer as straightforward as what was detailed in the previous section. At a minimum, however, measurements of the resonance shape will place constraints on the 2Q-quantum relaxation rate and chemical shift difference distribution that can be useful in reducing the error in RR

Figure 1-9: Comparison of the dependence of n=1 RR shape on the 2Q-relaxation rate (r) and the dipolar coupling constant (b_{IS}). Because the shapes are symmetric, only one half is displayed. Simulations were performed using the same parameters described in Fig. (1-5).

(A) At constant r (91Hz, corresponding to a zero-quantum T_2 of 3.5ms), the curves clearly show a strong dependence on the dipolar coupling constant and hence the internuclear distance. Both the height and width of the shape increase with the coupling constant.

(B) At constant b_{IS} (61Hz, corresponding to an internuclear distance of 5.0Å), the exchange curves show a different dependence on r. The height decreases with increasing r, but the width increases. This suggests that r and b_{IS} can be extracted separately from measurements of the resonance shape.

(C) Compensating changes in b_{IS} and r relative to exchange curve shapes (see Fig. (1-5)) produce different resonance shapes from which both b_{IS} and r can simultaneously be extracted.

(A)

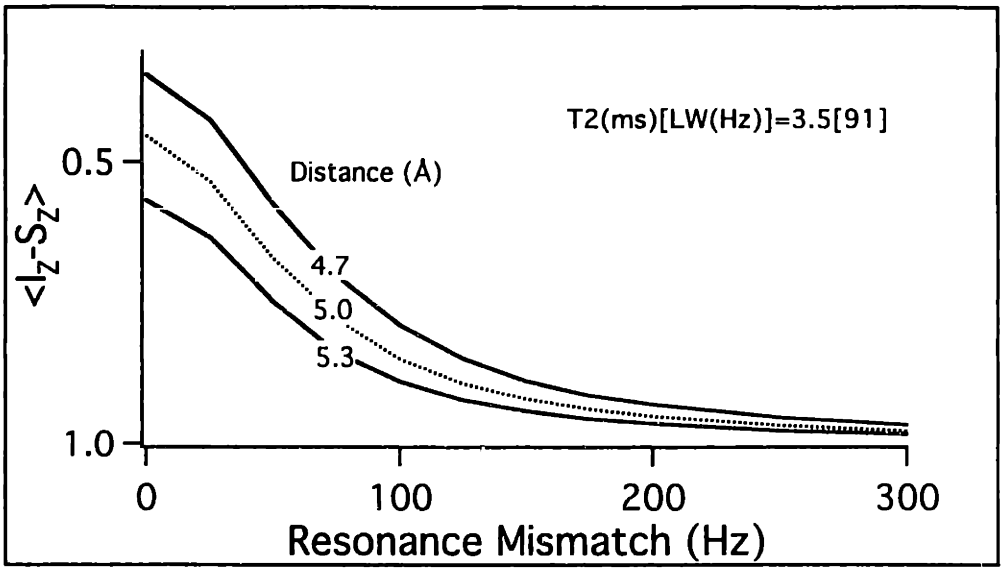
T2(ms)[LW(Hz)]=3.5[91]
Distance (Å)
4.7
5.0
5.3
0.5
1.0
<Iz-Sz>
0
100
200
300
Resonance Mismatch (Hz)

(B)

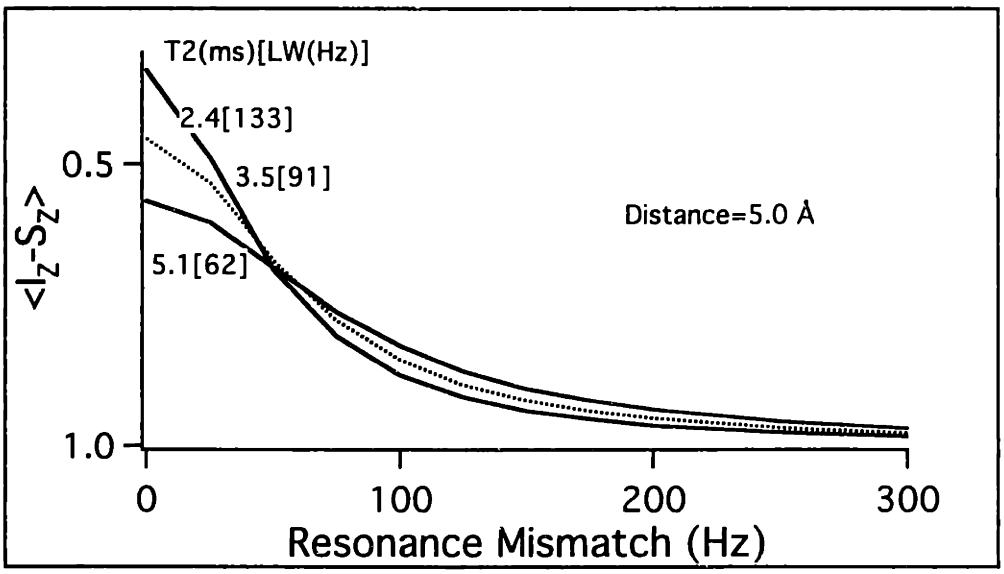
T2(ms)[LW(Hz)]
2.4[133]
3.5[91]
5.1[62]
Distance=5.0 Å
0.5
1.0
<Iz-Sz>
0
100
200
300
Resonance Mismatch (Hz)

(C)

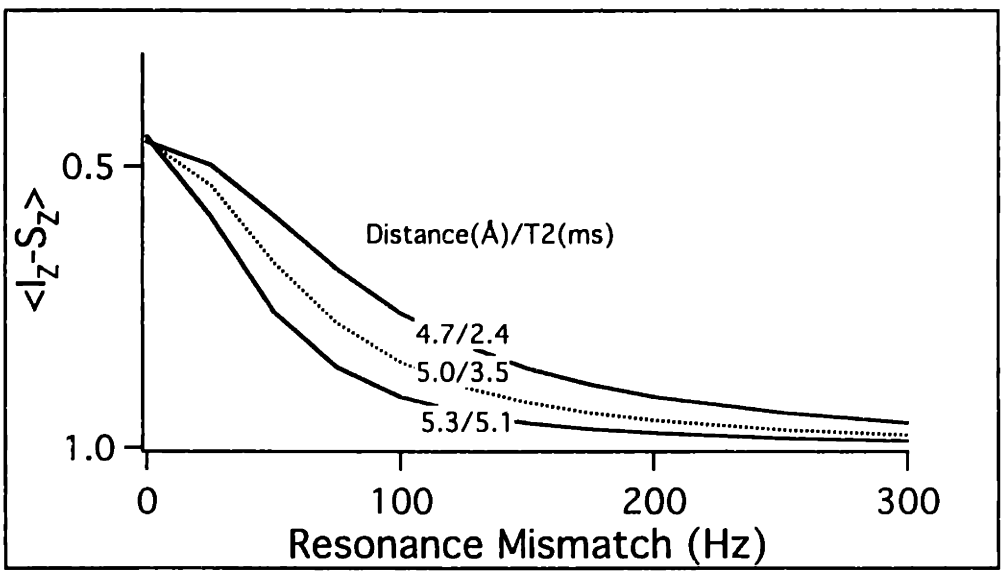
Distance(Å)/T2(ms)
4.7/2.4
5.0/3.5
5.3/5.1
0.5
1.0
<Iz-Sz>
0
100
200
300
Resonance Mismatch (Hz)

distance measurements due to uncertainties in these two variables. Given a value for b_{IS} and r, the difference distribution consistent with both these values and the measured shape of the RR resonance will be fixed. Estimation of r and the difference distribution using "no-correlation" assumptions can provide starting points for both parameters, and fitting of the resonance lineshape can then be used to refine these estimates (particularly to detect the presence of significant correlation in either parameter).

It may possible, at least in principle, and certainly under some experimental conditions, to determine both the 2Q-relaxation rate and the shift difference distribution from the RR shape with sufficient accuracy to extract an accurate value for the dipolar coupling constant. Here we describe fitting procedures for two different regimes: (i) when the relaxation rate dominates ($r>>b_{IS}$), and (ii) when the relaxation rate does not dominate ($r\leq b_{IS}$):

(i) $r>>b_{IS}$.

Under these conditions, we expect the RR shape to be independent of mixing time, determined by a convolution of the difference distribution with a lorentzian of width$\approx r/\pi$. Separation of the two contributions to the measured shape is not possible without additional information, however such a separation is not generally needed. Fig. (1-10A) shows the exchange curve calculated for a system with a 1.0kHz 2Q-relaxation rate and a single chemical shift difference. The RR shape measured in such a system would be lorentzian, with a width of approximately 0.32kHz (Fig. 1-10B). Were we to measure this RR shape we would, as stated, not be able to determine what contributions from 2Q-relaxation and difference

Figure 1-10: Extraction of 2Q-lineshape parameters when the 2Q-relaxation rate (r) is much larger than the coupling constant (b_{IS}). In such a case, the measured resonance shape will have a time-independent width (FWHM) of r/π. Separation of this width into homogeneous and inhomogeneous components is not clear, but is not necessary to accurately simulate the longitudinal magnetization exchange dynamics. Bottom figure shows the simulated resonance shape at 3 different mixing times for a 2-spin system near n=1 RR with a 60Hz coupling and a 2Q-relaxation rate of 1kHz. The shape at all times is identical; the width is slightly larger than expected solely from r because of a small contribution due to the magnitude of the coupling itself. Simulations of the exchange dynamics where the 2Q-linewidth has been divided between homogeneous (2Q-relaxation) and inhomogeneous (difference distribution) components are shown in the top plot (2Q-relaxation rate/difference distribution width=1.0kHz/0, 0.84kHz/50Hz, .69kHz/100Hz, 0.53kHz/150Hz, 0.37kHz/200Hz; lorentzian lineshape used for difference distribution). Clearly the exchange dynamics are not sensitive to the details of the separation in this regime.

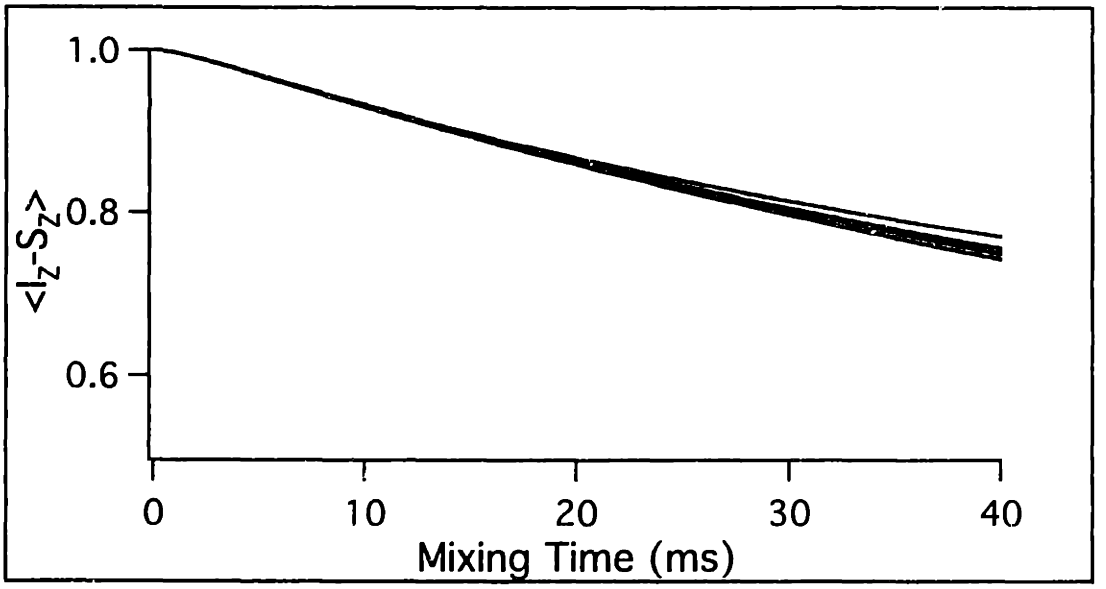
1.0
0.8
0.6
<I_z-S_z>
0
10
20
30
40
Mixing Time (ms)

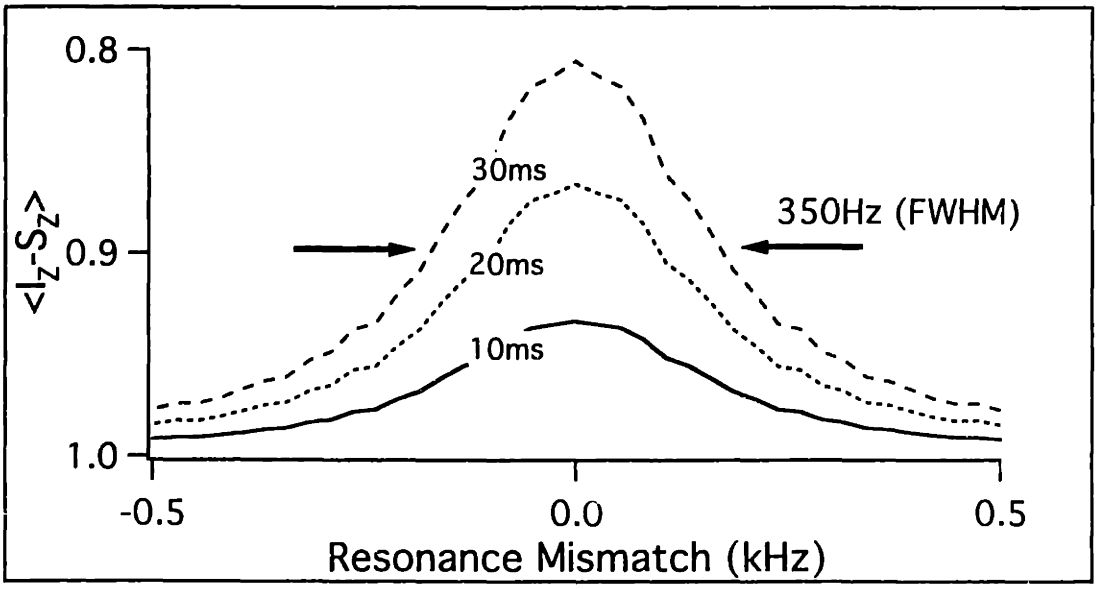
0.8
0.9
1.0
<I_z-S_z>
30ms
20ms
10ms
350Hz (FWHM)
-0.5
0.0
0.5
Resonance Mismatch (kHz)

distribution were present (although the estimates derived from "no-correlation" assumptions would be starting points). Simulations using a series of different 2Q-relaxation rates, each with its associated difference distribution determined from the constraint that the combined width equal 0.32kHz, yield essentially identical exchange curves over a wide range of parameters. (Because the convolution of two lorentzians with widths a and b is a lorentzian with width a+b, we can in this case simply divide the measure RR width into two parts, for instance 0.1kHz to difference distribution (with lorentzian shape) and the remaining 0.22kHz to 2Q-relaxation (resulting in $r=0.22kHz*\pi=0.69kHz$).) Only when we begin to assign most of the width to difference distribution, and the residual width to 2Q-relaxation, do significant differences appear among the exchange curves, but this is because r no longer satisfies the condition $r>>b_{IS}$.

(ii) $r \leq b_{IS}$.

Under these conditions, we expect the measured RR shape to be time-dependent. Because the contribution of the difference distribution to the RR shape is time-independent, measurement of the shape at different mixing times should in principle allow separation of the two components. When the coupling constant greatly exceeds the relaxation rate the change in RR shape with time is most distinct, and such a separation is easiest. In the intermediate regime where the rate r is comparable to the coupling constant, the change in shape is modest and can be washed out by a sufficiently broad difference distribution. In these cases, measurement of the resonance width is best used as a constraint on r and the difference

distribution, rather than a method to determine them with sufficient accuracy to extract the coupling.

1.4E Example: Longitudinal Exchange Dynamics at n=1 RR in $^{13}C_2$-Labeled TEE.

Tyrosine ethyl ester (TEE) crystallizes in a "scorpion-like" conformation, with the ethyl "tail" bending back over the tyrosyl ring[52]. The distance between the -CH_2- carbon nucleus of the ester moiety and the 4'-OH aromatic carbon nucleus is 5.05Å, as calculated from the x-ray crystal structure coordinates (Fig. (1-11A)). The MAS spectrum (ω_r=8kHz) of a $^{13}C_2$-labeled version of this compound (diluted 1:10 in natural abundance material), with the labels placed at the named carbons, is shown in Fig. (1-11B). The aromatic and methylene linewidths are approximately 27 and 20 Hz, respectively, in a 7.4T magnetic field (79.9MHz for ^{13}C). The isotropic chemical shift difference at this field strength is 7.501kHz, in the range to allow for an n=1 RR longitudinal exchange experiment. Because the shift difference does not significantly exceed the magnitude of the CSA's of both nuclei (aromatic carbon δ=-7.19kHz, η=0.91; methylene δ=-3.20kHz, η=0.05; determined by fitting the sideband patterns in several slow-spinning (2-3kHz) spectra using the SPEEDYFIT fitting routine), evident in the presence of visible sidebands in the spectrum at ω_r=8kHz, the dynamics even at n=1 RR will have some dependence on the relative orientations of the dipolar and CSA tensors (the reasons for this dependence are discussed in chapter two). The relative orientations can be calculated from the x-ray coordinates given some assignment of the CSA tensor axes in the molecular frame. Previous work in the literature indicates that the σ_{22} axis of

Figure 1-11: (Top) Structure of the doubly-$^{13}C_2$ labeled tyrosine ethyl ester (TEE) used in experiments in this these, with principal axes of the CSA tensors of the labeled carbon atoms as indicated. (Bottom) ^{13}C CP/MAS spectrum of the doubly-labeled sample dilute 1:10 in natural abundance material (w_r=8kHz). The chemical shift difference at this field strength (7.4T) is 7.501kHz, as indicated. At 8kHz, visible sidebands (labeled "sb") from the aromatic resonance appear in the spectrum, suggesting that the exchange dynamics even at the n=1 RR will show some dependence on the relative orientation of the dipolar and CSA tensors.

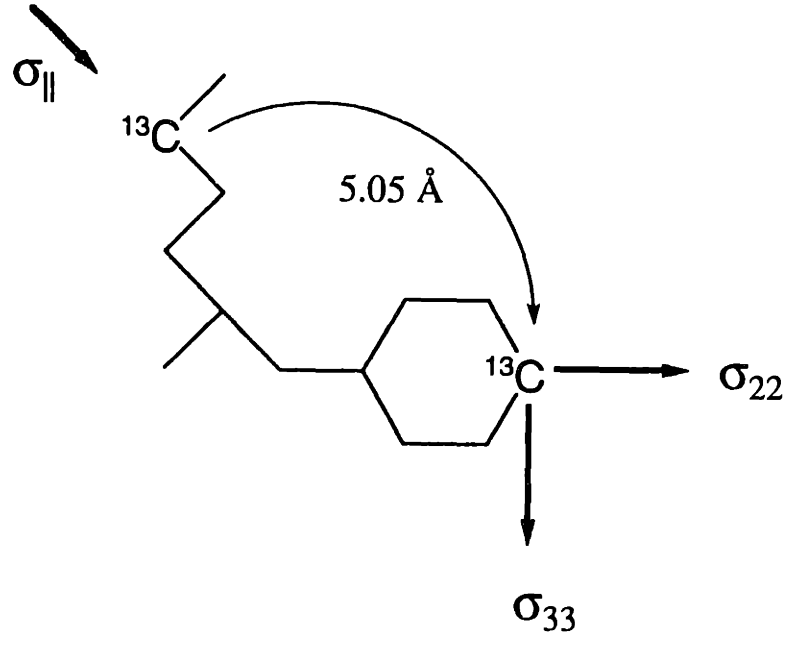
σ||
13C
5.05 Å
13C
σ22
σ33

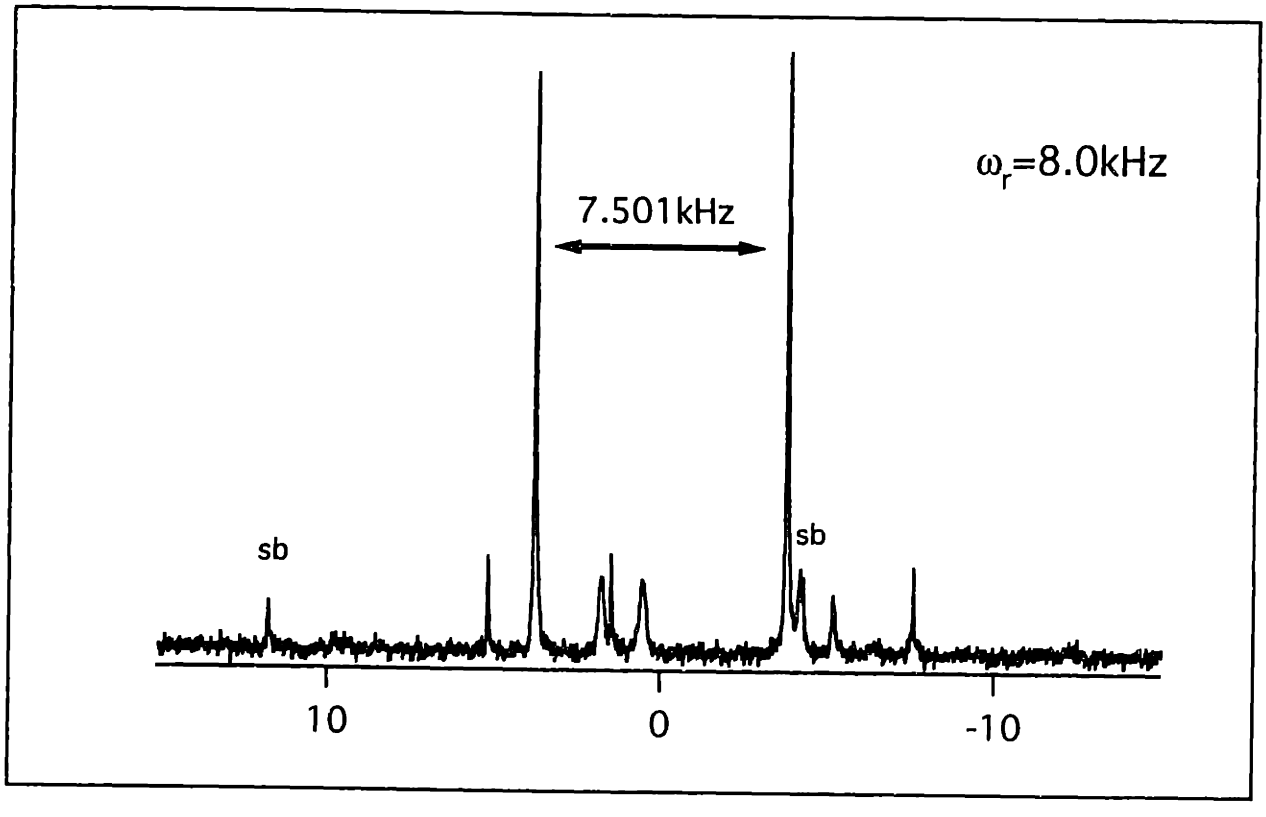
ωr=8.0kHz
7.501kHz
sb
sb
10
0
-10

the aromatic carbon CSA tensor generally points perpendicular to the tyrosyl ring, while the σ_{33} axis points along the C-OH bond; the σ_{11} axis direction is then defined as perpendicular to those two directions[17]. The assignment of the methylene tensor is not as straightforward, but its axially symmetric character suggests that the unique (symmetry) axis points along the O-C ester bond. Based on these assignments, the Euler angles describing the relative orientations of the CSA and dipolar tensors are as follows: the dipolar tensor z-axis is chosen as the z-axis of the common frame relative to which all 3 tensor orientations will be described, yielding the Euler angles (α=0°,β=0°,γ=0°). The aromatic carbon CSA tensor orientation is then given by (0°,55°,37°), and the methylene tensor orientation by (0°,66°,-136°). These values were calculated according to the Euler angle convention in Spiess[19], and described earlier in this chapter.

The n=1 RR exchange curve, Fig. (1-12A), was obtained using the CPDELAY pulse sequence from Fig. (1-3C), with a 2ms CP mixing time and at a ^{1}H decoupling power (CW) of ≈81kHz. Integrated peak intensities were used to characterize the polarization level of each peak at each time point. The time between successive acquisitions was set equal to 3sec, which is not sufficient to allow for full recovery of the longitudinal ^{1}H magnetization (which has T_1>10sec). Several dummy shots (3-5) were taken at the start of each acquisition to account for this (and experiments with longer recycle delays did not give results significantly different from those shown here). An amount equal to 10% of the intensity of the t=0ms point was subtracted from each point to account for the contribution from

Figure 1-12: Experimental n=1 RR exchange curves and associated data for determining the intramolecular, internuclear distance in $^{13}C_2$-labeled TEE (1:10 diluted sample, 80kHz ^1H decoupling field):

(A) n=1 RR exchange data (open circles) and calculated curves (solid line includes both T_2^{zq} (14.1ms) and CSD (27Hz lorentzian) effects; dotted line includes only T_2^{zq} (6.8ms, as determined directly from single-quantum linewidths)). The coupling constant was set to 59Hz (equivalent to a 5.05Å ^{13}C-^{13}C distance, as measured from the x-ray derived molecular coordinates).

(B) Single-π pulse echo data from experiments performed with each peak near resonance and w_r=8kHz. Curves show results of exponential fit to each data set, and result in 11.5Hz and 11Hz homogeneous linewidths for the aromatic and methylene carbons, respectively. This yields a T_2^{zq} value of 14ms.

(C) Isotropic chemical shift difference distribution calculated from the spectrum using the previously described method (thick line) and fit with a 27Hz lorentzian lineshape (thin line).

(A)

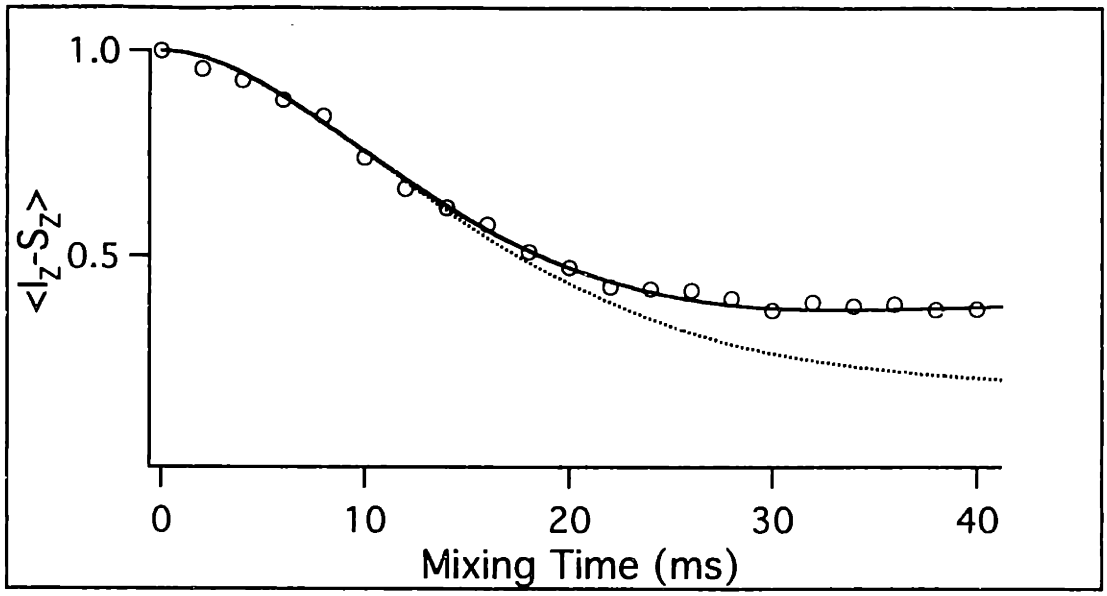
1.0
0.5
$\langle I_z - S_z \rangle$
0
10
20
30
40
Mixing Time (ms)

(B)

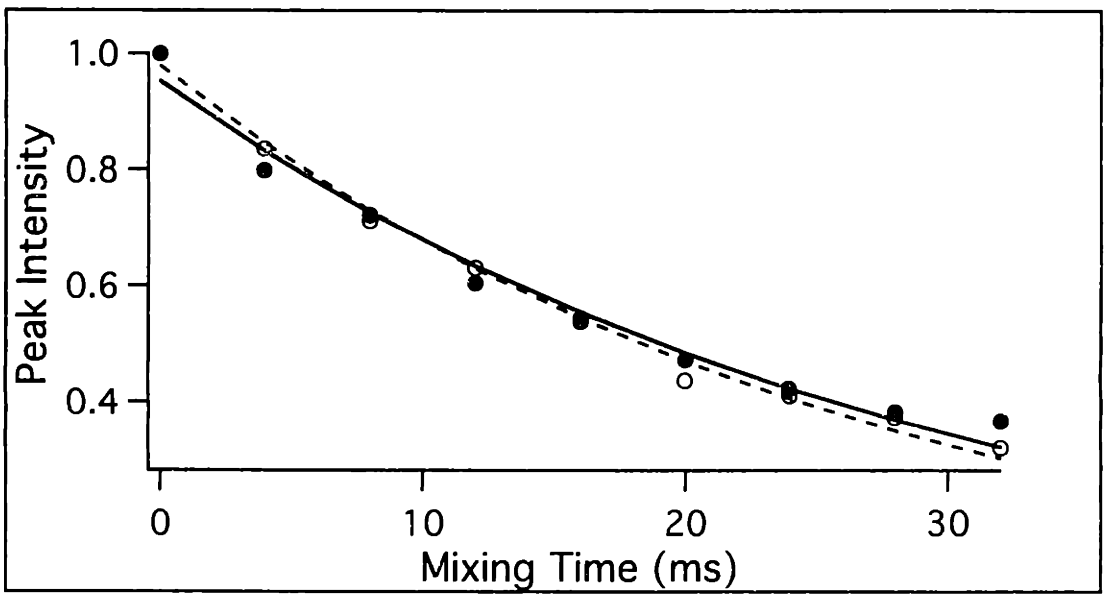
1.0
0.8
0.6
0.4
Peak Intensity
0
10
20
30
Mixing Time (ms)

(C)

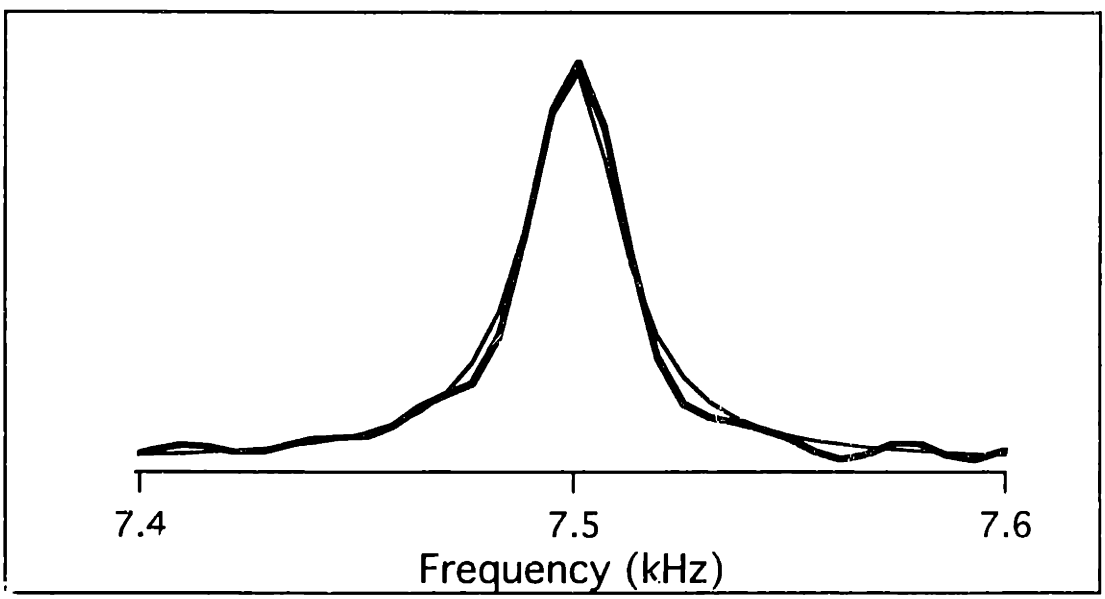
7.4
7.5
7.6
Frequency (kHz)

natural abundance background signal (the 1:10 dilution level was estimated based on the relative intensities of the labeled and unlabeled peaks, and the natural abundance signal is assumed not to change during the experiment). Fitting the signal intensity decay in single-π pulse Hahn echo experiments (data and fit in Fig. (1-12B)) yields 11 and 11.5Hz homogeneous linewidths for the aromatic and methylene nuclei, respectively (ω_r=8kHz; ^{13}C 180° pulse of 8.4μs; separate experiments were performed with each peak near (within 1kHz of) resonance). The 2Q-relaxation rate calculated from these values is 71Hz (T_2^{zq}=14.1ms), as compared to the 148Hz rate (T_2^{zq}=6.8ms) calculated directly from the observed linewidths. Calculation of the appropriate "mirror" convolution of the two lines (as described in a previous section and using -22.5Hz of exponential linebroadening) yields the difference distribution shown in Fig. (1-12C), which is approximately fit by a 27Hz wide lorentzian lineshape (note that no accounting of magnet inhomogeneity was made in this calculation). Simulations using either the 14.1ms T_2^{zq} value and including the effects of the 27Hz lorentzian chemical shift difference distribution, or just the 6.8ms T_2^{zq} value calculated directly from the linewidths, (and a 59Hz coupling constant corresponding to a 5.05Å internuclear ^{13}C-^{13}C distance) are shown in Fig. (1-12A). Both simulations fit well at early time points, but at later time points the former simulation, which distinguishes between inhomogeneous and homogeneous components of the 2Q-lineshape - clearly fits better.

Measurements of the RR shape were also made at τ_{mix}=20ms , and are shown in Fig. (1-13). Fitting the shape assuming no difference distribution yields an 17ms value for T_2^{zq}; however the

Figure 1-13: Measured RR shape for $^{13}C_2$-labeled TEE (1:10 dilute) at t_{mix}=20ms:

(A) Experimental data (solid circles) are fit assuming that the lineshape has only a homogeneous component. Fitting yields a value for T_2^{zq} of 7ms.

(B) Experimental data (solid circles) are fit assuming that the lineshape has both homogeneous and inhomogeneous components, with the "sum" constrained by the resonance shape. Division into the two components used the previous echo and difference distribution calculations as a guide, but variations around this do not lead to significantly different fits to the shape, or the exchange curve itself (data not shown).

(A)

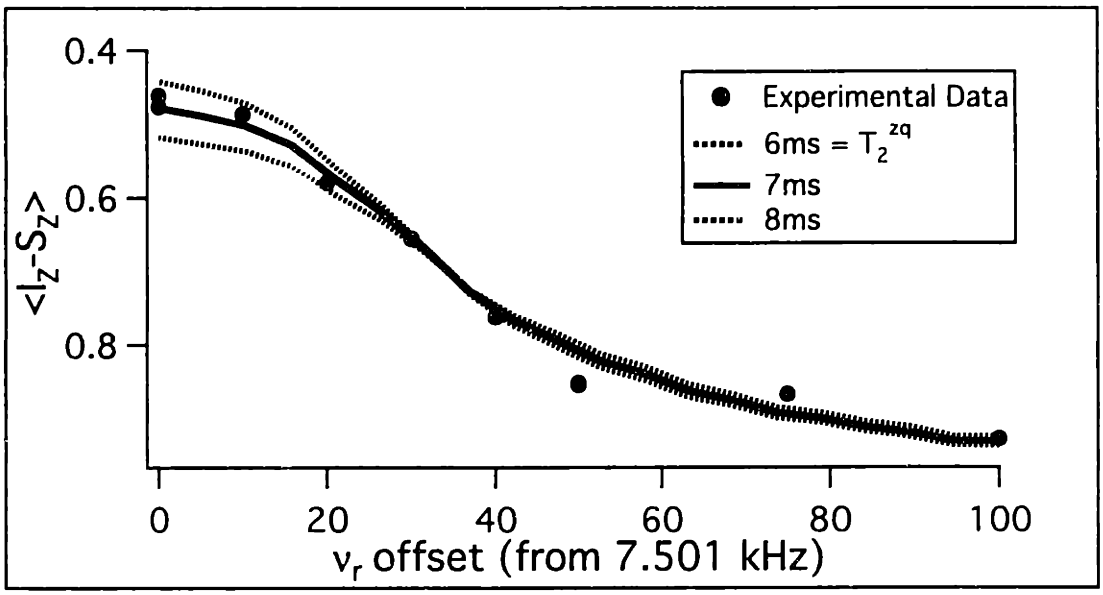
0.4
0.6
0.8
<I_Z-S_Z>
Experimental Data
6ms = T2zq
7ms
8ms
0
20
40
60
80
100
ν_r offset (from 7.501 kHz)

(B)

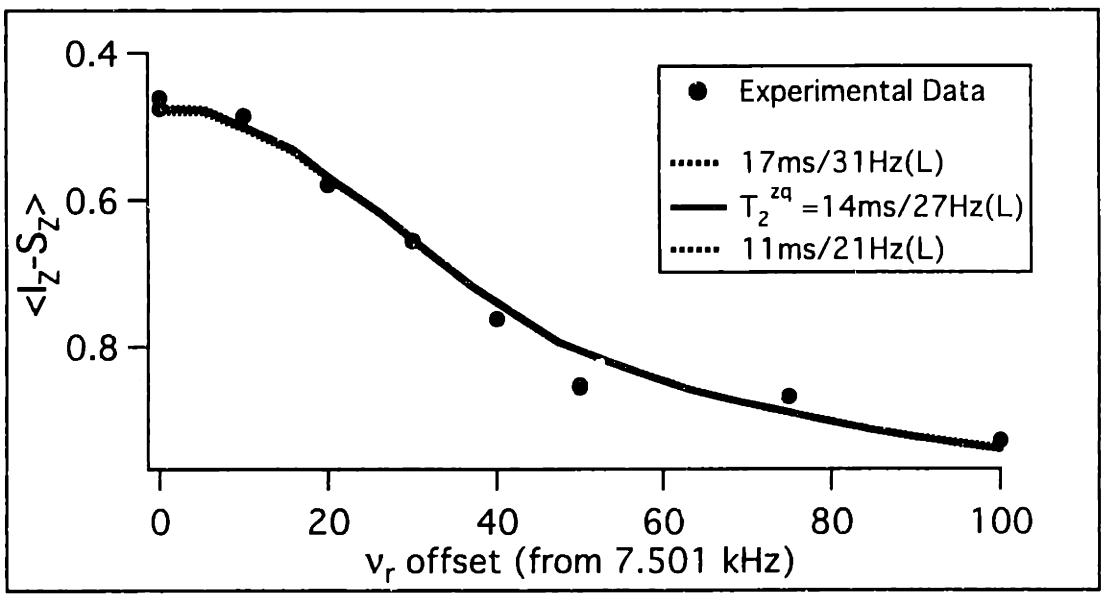
0.4
0.6
0.8
<I_Z-S_Z>
Experimental Data
17ms/31Hz(L)
T2zq =14ms/27Hz(L)
11ms/21Hz(L)
0
20
40
60
80
100
ν_r offset (from 7.501 kHz)

combination of a 14ms T_2^{zq} with a 27Hz (lorentzian, L) difference distribution (based on the single-quantum measurements) also fits well. The shape observed at 40ms (not shown) fits the14ms/27Hz(L) parameters somewhat better than the 7ms/0Hz ones, although the distinction is not sharp. Because we are in an intermediate regime (r not much greater or lesser than b_{IS}), accurate separation of the two components of the zero quantum lineshape is not expected to be straightforward by RR shape-based methods, but is crucial in accurately simulating the observed on-resonance exchange dynamics. Having used the estimates of T_2^{zq} and the difference distribution calculated from single-quantum measurements (14ms and 27Hz(L) from echo experiments and mirror convolution, respectively) and the no-correlation assumption as starting points for the RR shape fit in Fig. (1-13B), the measured RR shape confirms that these two values are consistent with the observed dynamics (i.e. the no-correlation assumption seems valid), which is particularly useful given the uncertainty in the contribution of magnet inhomogeneity to the calculated chemical shift difference distribution. Clearly (Fig. (1-12A)) these parameters provide a much better fit to the experimental exchange curve (note that small deviations around the estimated zero-quantum lineshape parameters, as long as they are changed in a compensating manner that keeps the fit to the resonance shape, lead to very similar simulated on-resonance dynamics).

If we reduce the decoupling power in the experiment sufficiently so that the zero-quantum relaxation rate r grows large enough to dominate the dipolar coupling, we can enter the regime

where extraction of the zero-quantum lineshape parameters can be performed with adequate accuracy directly from the RR shape. The on-resonance exchange data for such an experiment (^1H decoupling power=45kHz) is shown in Fig (1-14B). The resonance shape, shown in Fig. (1-14A), has a near-lorentzian shape from which the value of 0.4kHz. for r, and 0.056Hz for the dipolar coupling constant (b_{IS}), is extracted (the latter equivalent to a 5.15Å internuclear distance). Using these parameters to simulate the on-resonance dynamics (CSD contributions set to zero) yields the results shown in Fig. (1-14B), an accurate match between simulation and experiment, and in this case without the need to estimate zero-quantum relaxation and CSD from other sources. That a smaller value for the dipolar coupling constant is necessary to accurately fit the dynamics in this case may be due to experimental error, or to an increased sensitivity in this experiment (given the reduced number of fitting parameters) to the size of a coupling constant which may effectively have a value less than that measured from the x-ray data due to molecular motion. Results from chapter 3 using rotational resonance tickling (RRT) to measure the distance independent of CSD (and nearly independent of T_2^{zq}) suggest that the true explanation is a combination of both of these.

1.4F Additional RR Comments.

Several final comments relevant to the application of RR techniques in biological solids:

(1) In the limit of a 2Q-relaxation rate much larger than the dipolar coupling constant, the method of mapping out the resonance shape

Figure 1-14: Measured RR shape (top) and on-resonance exchange curve data (bottom) for $^{13}C_2$-labeled TEE (1:10 dilute) at 45kHz ^1H decoupling power:

(A) Values for both the dipolar coupling (b_{IS}) and a 'pseudo'-zero-quantum relaxation rate (which includes CSD effects) can be extracted from the experimentally-determined resonance shape (solid circles; τ_{mix}=45ms), as described in the text. The best fit in this case requires a value of 0.4kHz for r and of 0.056Hz for b_{IS}, 3 Hz smaller that the value calculated from the x-ray structure.

(B) Exchange curve data (open circles) closely matches the simulation using the known spin system parameters (see text) and the zero-quantum relaxation rate (r) and dipolar coupling constant (b_{IS}) determined from the resonance shape. No CSD effects were included, although previous experiments indicate that there is a CSD component to the zero-quantum linewidth. As stated in the text, in this parameter regime (zero quantum relaxation rate much larger than the coupling), separation of the zero-quantum lineshape into homogeneous and inhomogeneous components is not necessary for accurate simulation of RR dynamics.

(A)

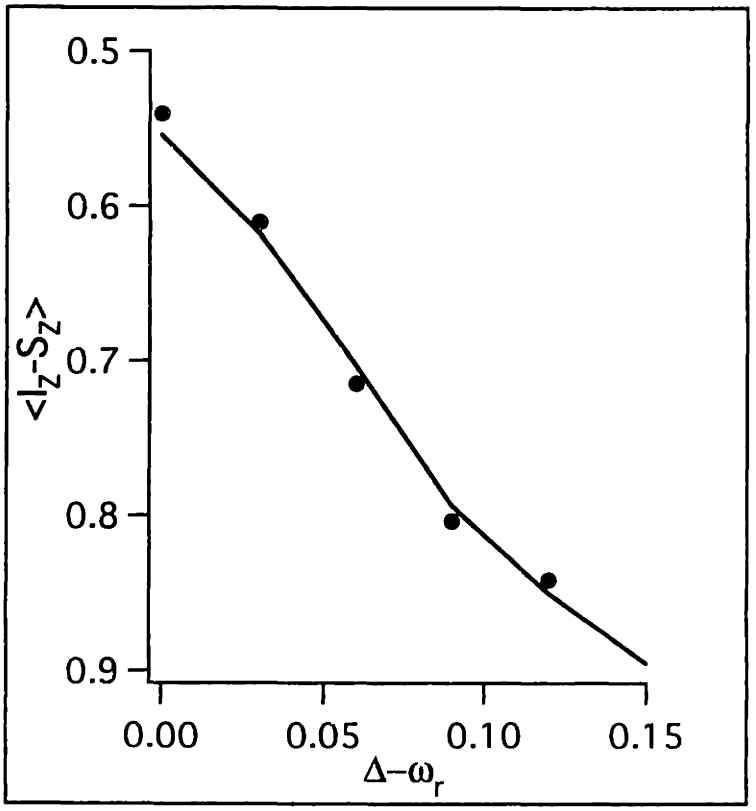
0.5
0.6
0.7
0.8
0.9
<I_z-S_z>
0.00
0.05
0.10
0.15
Δ−ω$_r$

(B)

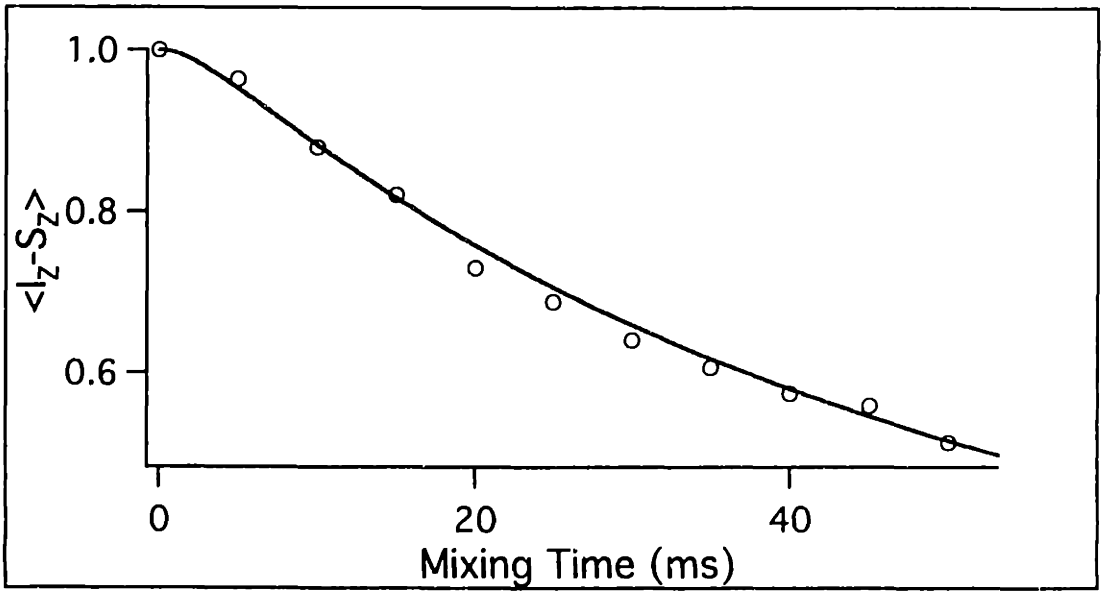
1.0
0.8
0.6
<I_z-S_z>
0
20
40
Mixing Time (ms)

described above has close analogies to lineshape measurements using CW magnetic resonance techniques.

(2) Measurements of the RR shape, particularly as a function of mixing time, provide an additional method of characterizing RR dynamics, and one that may be sensitive to errors in the model that is currently used (described in Levitt, et. al.[10]) to simulate the dynamics. In particular, errors in assumptions about zero-quantum relaxation behaviour (assumptions of orientation independence and a lorentzian zero-quantum homogeneous lineshape, for instance), may lead to incorrect predictions of near-resonance behaviour.

(3) The experiments described here (and in chapter 3), which allow for extraction of dipolar coupling constants with reduced dependence on estimates of zero-quantum lineshape parameters based on single-quantum measurements, may also be used to investigate the validity of the "no-correlation" assumption in making such estimates. This would be particularly useful in investigating whether the presence of correlation that has been identified in strongly-coupled systems[53] (1.5-2.5Å internuclear distance) also occurs in more weakly coupled systems (given that we expect correlations to reduce as the distance between the atom pair grows). Preliminary results confirm correlation for strongly-coupled pairs, and indicate that the correlation disappears (within experimental error) for more distant (>4-5Å internuclear distance) spins.

1.5 References.

1. Pauling, L., R.B. Corey. *Proc. Nat. Acad. Sci.* **37**, 729-740 (1951).
2. Marsh, R.E., R.B. Corey, and L. Pauling. *Biochimica et Biophysica Acta* **16**, 1-34 (1955).
3. Watson, J.D., F.H.C. Crick. *Nature* **171**, (1953).
4. Kendrew, J.C., R.E. Dickerson, B.E. Strandberg, R.G. Hart, D.R. Davies, D.C. Phillips, and V.C. Shore. *Nature* **185**, 422-427 (1960).
5. Williamson, M.P., T.F. Havel, K. Wuthrich. *J. Mol. Biol.* **182**, 179 (1985).
6. Wuthrich, K. *NMR of Proteins and Nucleic Acids* (John Wiley and Sons, New York, 1986).
7. Ernst, R.R., G. Bodenhausen, A. Wokaun. *Principles of Nuclear Magnetic Resonance in One and Two Dimensions* (Oxford University Press, Oxford, 1987).
8. Clore, G.M., A.M. Gronenborn. *Science* **252**, 1390-1399 (1991).
9. Andrew, E.R., A. Bradbury, R.G. Eades, V.T. Wynn. *Phys. Lett.* **4**, 99 (1963).
10. Levitt, M.H., D.P. Raleigh, F. Creuzet, R.G. Griffin. *J. Chem. Phys.* **92**, 6347-6364 (1990).
11. Halverson, K.J., P.E. Fraser, D.A. Kirschner, P.T. Lansbury, Jr. *Biochemistry* **29**, 2639 (1990).
12. Nielsen, N.C., H. Bildsoe, H.J. Jakobsen. *J. Chem. Phys.* **101**, 1805-1812 (1994).
13. Takegoshi, K., K. Nomura, T. Terao. *Chem. Phys. Lett.* **232**, 424 (1995).

14. Pines, A., M.G. Gibby, J.S. Waugh. *J. Chem. Phys.* **59**, 569-590 (1973).

15. Andrew, E.R., A. Bradbury, R.G. Eades. *Nature* **182**, 1659 (1958).

16. Lowe, I.J. *Phys. Rev. Lett.* **2**, 285 (1959).

17. Raleigh, D.P., F. Creuzet, S.K. Das Gupta, M.H. Levitt, R.G. Griffin. *J. Amer. Chem. Soc.* **111**, 4502-4503 (1989).

18. Haeberlen, U. *High Resolution NMR in Solids* (Academic Press, New York, 1976).

19. Spiess, H.W. in *Dynamic NMR Spectroscopy* (eds. Diehl, P., E. Fluck, R. Kosfeld) 58-214 (Springer-Verlag, Berlin, 1978).

20. Sakurai, J.J. *Modern Quantum Mechanics* (Addison-Wesley Publishing Company, Inc., Redwood City, 1985).

21. Waugh, J.S., U. Haeberlen. *Phys. Rev.* **175**, 453-467 (1968).

22. Magnus, W. *Commun. Pure Appl. Math* **7**, 649 (1954).

23. Maricq, M.M., and J.S. Waugh. *J. Chem. Phys.* **70**, 3300 (1979).

24. Herzfeld, J., A.E. Berger. *J. Chem. Phys.* **73**, 6021-6030 (1980).

25. Van Vleck, J.H. *Phys. Rev.* **74**, 1168 (1948).

26. Mehring, M. *Principles of High Resolution NMR in Solids* (Springer-Verlag, Berlin, 1983).

27. Waugh, J.S., L.M. Huber, U. Haeberlen. *Phys. Rev. Lett.* **20**, 180 (1968).

28. Bennett, A.E., C.M. Rienstra, M. Auger, K.V. Lakshmi, R.G. Griffin. *J. Chem. Phys.* **103**, 6951-6958 (1995).

29. Schaefer, J., E.O. Stejskal. *J. Amer. Chem. Soc.* **98**, 1030 (1976).

30. Saito, H. *Magn. Res. Chem.* **24**, 835-852 (1986).

31. Ando, I., Shigeki Kuroki. in *Encyclopedia of NMR* (eds. Grant, D.M., R.K. Harris) (John Wiley and Sons, New York, 1996).

32. Bennett, A.E., R.G. Griffin, S. Vega. in *NMR Basic Principles and Progress* (eds. Diehl, P., E. Fluck, H. Gunther, R. Kosfeld, J. Seelig) 1-77 (Springer-Verlag, Berlin, 1994).

33. Verdegem, P.J.E., M. Helmle, J. Lugtenburg, and H.J.M de Groot. *submitted* (1996).

34. Tomaselli, M., B.H. Meier, M. Baldus, J. Eisenegger, R.R. Ernst. *Chem. Phys. Lett.* **225**, 131-139 (1994).

35. Raleigh, D.P., M.H. Levitt, R.G. Griffin. *Chem. Phys. Lett.* **146**, 71-76 (1988).

36. Bennett, A.E., J.H. Ok, R.G. Griffin. *J. Chem. Phys.* **96**, 8624-8627 (1992).

37. Tycko, R., G. Dabbagh. *Chem. Phys. Lett.* **173**, 461 (1990).

38. Sun, B.-Q., P.R. Costa, D. Kocisko, P.T. Lansbury, Jr., R.G. Griffin. *J. Chem. Phys.* **102**, 702 (1995).

39. Lee, Y.K., N.D. Kurur, M. Helmle, O.G. Johannessen, N.C. Nielsen, M.H. Levitt. *Chem. Phys. Lett.* **242**, 304-309 (1995).

40. Gullion, T., J. Schaefer. *J. Magn. Res.* **81**, 196 (1989).

41. Hing, A., S. Vega, J. Schaefer. *J. Magn. Res.* **96**, (1992).

42. Bennett, A.E., L.R. Becerra, R.G. Griffin. *J. Chem. Phys.* **100**, 812-814 (1994).

43. Williamson, M.P., D. Neuhaus. *The Nuclear Overhauser Effect in Structural and Conformational Analysis* (VCH Publishers, Inc., New York, 1989).

44. Wokaun, A., R.R. Ernst. *J. Chem. Phys.* **67**, (1977).

45. Vega, S. *J. Chem. Phys.* **68**, 5518 (1978).

46. Pake, G.E. *J. Chem. Phys.* **16**, 327-336 (1948).

47. Sun, B.Q. .

48. Morris, G.A., R. Freeman. *J. Magn. Res.* **29**, 433-462 (1977).

49. Kubo, A., C.A. McDowell. *J. Chem. Soc., Faraday Trans. 1* **84**, 3713-3730 (1988).

50. Hahn, E.L. *Phys. Rev.* **80**, 580 (1950).

51. VanderHart, D.L., W.L. Earl, A.N. Garroway. *J. Magn. Res.* **44**, 361-401 (1981).

52. Pieret, P.A., F. Durant, M. Griffe, G. Germain, T. Dehaerdemacker. *Acta Cryst.* **B26**, 2117-2124 (1970).

53. Tomita, Y., A. McDermott. *Submitted* (1995).

Chapter 2

Cis vs. *Trans* : Conformation of the central glycylglycyl region of the 9mer

2.1 RR experiments initially suggested that the G(37)-G(38) peptide bond may be in the *cis* conformation.

Given the assumption that the bond lengths and angles in a peptide are fixed, the distance between any two atoms in the molecule is solely a function of the dihedral angles about each of the bonds between them (excepting the intervening bonds that include either of the atoms themselves). For measurements between the alpha carbon (C_α) of one residue (labeled '1') and the carbonyl carbon ($C_{=O}$) of the next (labeled '2'; this is the standard 'α1-2' distance measurement), the internuclear distance depends upon the torsion about two bonds: the N-$C_{=O}$ (peptide) bond between residues 1 and 2 (whose torsion angle is denoted $\omega_{1,2}$); and the $C_{=O}$-C_α bond of residue 2 (ϕ_2). The conformation about the peptide bond is constrained by its double-bond character - maximizing overlap of the π orbitals of the N and $C_{=O}$ atoms requires either a *trans* ($\omega_{1,2} \approx 180°$) or *cis* ($\omega_{1,2} \approx 0°$) conformation[1]. This restriction segregates the α1-2 distances into two classes: when the intervening peptide bond is *trans*, the measurement can range from approximately 4.2 to 4.8 Å (depending upon the value of ϕ_2); when it is *cis*, this range is 2.1 to 4.3 Å (this calculation ignores steric overlap, but assumes standard values for

the bond lengths and angles[2]). Steric interactions between adjacent residues in a peptide backbone are significantly more favorable in the *trans* conformation, and hence this conformation is far more prevalent in known peptide and protein structures (when the i^{th} residue is proline, however, it is not uncommon to find the (i)-(i+1) peptide bond in the *cis* conformation)[1, 3]. Thus there was some surprise when the initial measurement of the distance between the C_α of glycine 37 and the $C_{=O}$ of glycine 38 in the 9mer yielded a value of 4.0 ± 0.2 Å (determined from 1:5 and 1:10 dilutions of labeled sample in unlabeled sample, to attenuate intermolecular effects)[4]. This value strongly suggested that the intervening peptide bond was either in the unusual *cis* conformation, or in a highly strained (and hence also unusual) *trans* conformation. When *cis* conformations do occur absent proline, the one of the more likely locations is between two glycine residues[3]; hence there was some reason for accepting the possibility of a *cis* conformation. The high (local) energetic costs of such a conformation at this bond would need to be compensated for by favorable interactions in other parts of the molecule, or by access to favorable packing arrangements in the aggregate. In light of the unusually high propensity of this molecule to aggregate under many conditions where most other peptides are soluble[5], it was thought that such an unusual conformation at the central glycylglycyl linkage might be part of an overall unusual structure that would explain the molecule's extreme insolubility.

The adoption of a new simulation method for extracting distance information from R^2 magnetization exchange data, one that explicitly included the effects of inhomogeneous broadening, led to a

re-evaluation of the α37-38 distance measurement. Application of the new simulation method to the old data suggested a distance in the 4.3-4.5 Å range, and so called into question the possibility of a *cis* conformation at the intervening peptide bond. To investigate the issue further, the sample was re-synthesized and the R^2 magnetization exchange experiments were repeated. Fig. (2-1A) details the results. First, we see an unusually large "dilution effect" in terms of the greater amount of exchange that occurs in the undiluted vs. the 1:5 diluted (labeled:unlabeled) sample. This is in stark contrast to the previous data (where no dilution effect was seen), but agrees with the large dilution effect observed in the 37-α39 distance measurement, which straddles this one. Second, "exact" numerical simulations of the exchange process (based on measured spin system parameters and using a series of dipolar couplings spanning the range of possible internuclear distances) are unable to accurately fit the exchange curve obtained from the 1:5 diluted sample. At early time points, the data is fit well by simulations based on relatively short distances (4.1-4.3 Å), while at later points it is fit better by simulations using longer distances (4.4-4.6 Å). One explanation for the poor fit is the continued presence of appreciable intermolecular interactions, an explanation that is supported by the large dilution effect observed, and by the proximity and orientation of the spin pairs on adjacent molecules in the proposed antiparallel ß-sheet structure[6].

To better isolate the desired intramolecular interaction, the experiments were repeated on a 1:10 diluted sample (data shown in Fig. (2-1B)). Due to S/N limitations, the exchange curve was not

Figure 2-1: On-resonance n=1 RR exchange data for G(37)C_α-G(38)$C_{=O}$ $^{13}C_2$-labeled 9mer at a series of dilution levels:

(A) Undilute (solid circles) and 1:5 dilute (open circles) data, acquired in a 9.4T magnet (100MHz for ^{13}C). There is a large reduction in the magnetization exchange rate upon dilution, indicating the presence of significant intermolecular dipolar interactions in the undilute sample. The dilute data matches simulations using a larger coupling (corresponding to a shorter distance, <4.2Å) at early times, and the longer-distance simulation (4.4-4.6Å) at longer times. The lack of a good fit may be due to residual intermolecular effects.

(B) Undilute (solid circles) and 1:10 dilute (open circles) data, acquired in a 7.4T magnet (79.9MHz for ^{13}C), again showing the dilution effect. Fewer time points were acquired of the 1:10 dilute sample due to S/N constraints. Comparison to simulation suggests a distance in the 4.6-4.8Å range. The inset shows the experimental chemical shift difference distribution (solid line), calculated using the methods described in chapter one, and a 210Hz lorentzian fit (dashed line).

(A)

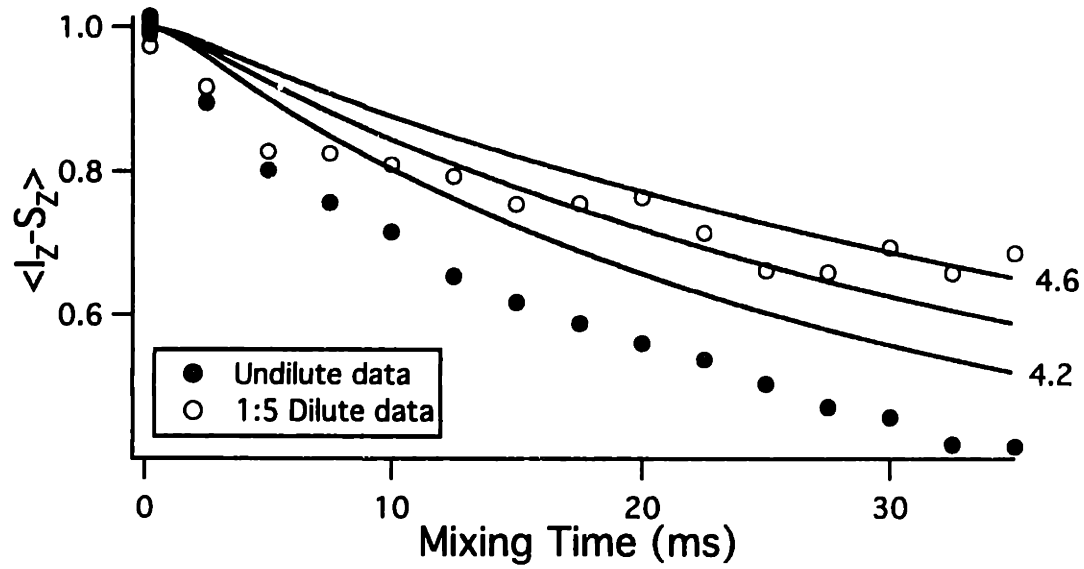
1.0
0.8
0.6
<I_z-S_z>
Undilute data
1:5 Dilute data
4.6
4.2
0
10
20
30
Mixing Time (ms)

(B)

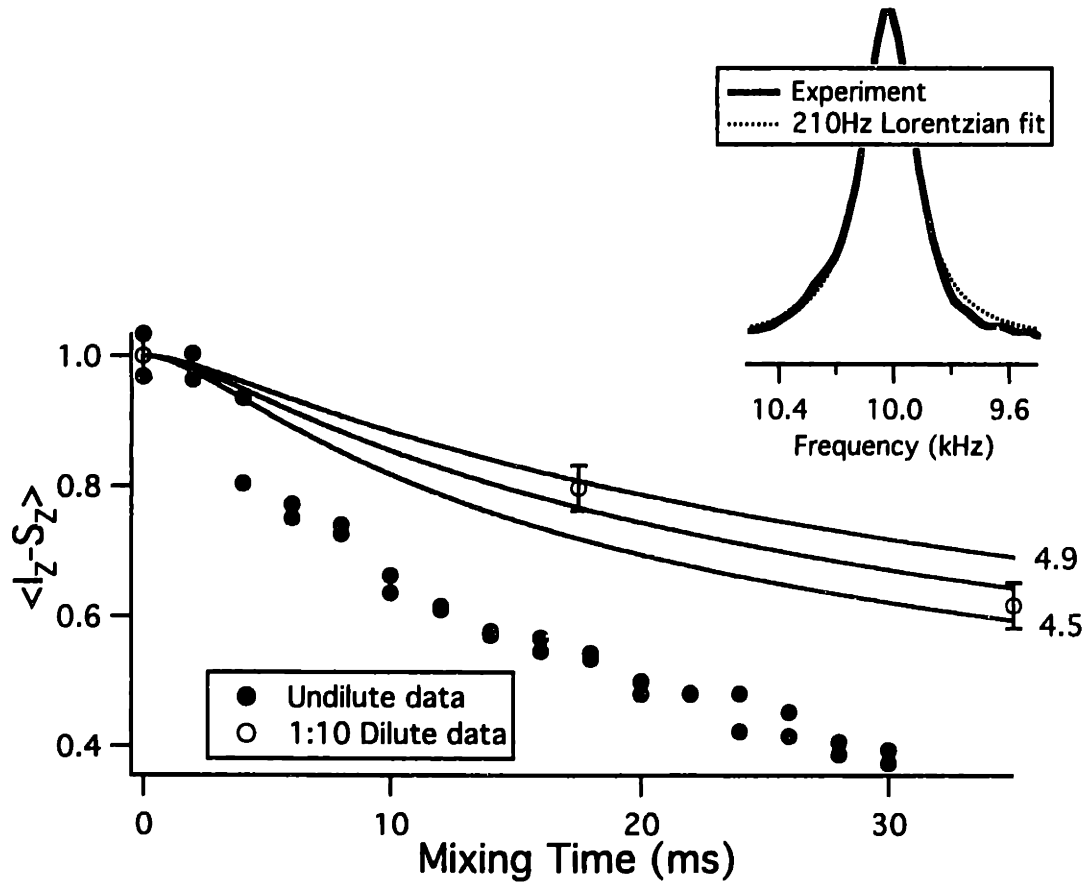
Experiment
210Hz Lorentzian fit
10.4
10.0
9.6
Frequency (kHz)
1.0
0.8
0.6
0.4
<I_z-S_z>
Undilute data
1:10 Dilute data
4.9
4.5
0
10
20
30
Mixing Time (ms)

mapped out in sufficient detail at this dilution level to determine whether the poor fit present in the 1:5 experiment remains (and hence is attributable to something other than intermolecular dipolar interactions). However, the time points that were obtained (15 and 30 ms) show that a further dilution effect has occurred, where the data is now consistent with an intramolecular distance in the 4.6-4.8 Å range. This range represents our best estimate of the $\alpha 37\text{-}38$ distance.

Although this value rules out the possibility of a *cis* conformation, the uncertainty raised by earlier experiments, and the fact that much of the analysis just described was not made until the latter stages of our efforts, led us to attempt a series of experiments to directly examine the conformation of this peptide bond. These experiments are detailed here. In the following section we present chemical shift data for the carbonyl carbons in glycylglycine•HCl (gg•HCl), diketopiperazine (DKP) - *trans* and *cis* model compounds, respectively - and for $36V_{=O}$ and $37G_{=O}$ labeled versions of the 9mer (the former as a control, the latter as an indicator of the conformation of the peptide bond in question). This data does not provide unambiguous information about the conformation of the peptide bond each carbonyl is involved in. The following section describes the use of a static echo experiment in $1\text{-}\alpha 2$ labeled peptides to isolate dipolar evolution and allow determination of the orientation of the dipolar tensor relative to the carbonyl CSA tensor (whose orientation in the molecular frame is known). That this technique can easily differentiate between *cis* and *trans* conformations is demonstrated by application to appropriately-

labeled versions of gg•HCl and DKP. The next section details the results for the 9mer compounds, indicating that both are *trans*. The effects of some motional process are also evident in room-temperature static spectra. Section 2-5 demonstrates the application of n=2 RR experiments to all four of these compounds, showing that such an experiment can distinguish between *cis* and *trans* conformations, and confirming that both 9mer compounds have the *trans* conformation at the relevant peptide bond. The following section (2-6) briefly describes the general CSA/dipole orientation dependence of RR experiments, and then focuses on the details of the n=2 experiment applied to $C_{=O}/CH_n$ labeled compounds.

Experimental: The n=1 RR Experiments on $37G_{=O}$-$38G_{\alpha}$ were performed on undilute, 1:5 dilute, and 1:10 dilute samples (labeled:unlabeled). The undilute and 1:5 dilute experiments were performed at 9.4T (100MHz ^{13}C) using a home-built probe with a 5mm Doty spinning assembly. The ^{1}H and ^{13}C pulse lengths were approximately 3.5ms and 4.5ms, respectively. The 1:10 dilute experiments were performed at 7.4T (79.9MHz ^{13}C) using a similar probe, with ^{1}H and ^{13}C pulse lengths of 2.5ms and 4.5ms. The experimental data was obtained using the methods outlined in chapter one, with only minor modifications. The simulations include the effects of CSD (a typical difference distribution is shown as an inset in Fig. (2-1B)) and 2Q-relaxation, as described in the previous chapter.

2.2 Carbonyl chemical shift parameters provide qualitative information about local molecular structure but do not clearly distinguish between *cis* and *trans* conformations.

The electron cloud surrounding a nucleus acts to shield the nucleus from the effects of an applied magnetic field; in so doing it gives rise to the chemical shift interaction[7, 8]. Just as the electron distribution about the nucleus is anisotropic, so too is this shielding effect. That is, the particular frequency at which a nucleus resonates in a given magnetic field - the degree to which it is shielded - depends upon the orientation of the shape of its surrounding electron cloud relative to the applied magnetic field. For a polycrystalline (or "powder") sample (defined in ch. 1 as containing the nucleus of interest in an equal distribution of all possible orientations), the sum of the signals from all possible orientations results in a broad, static (i.e. non-MAS) spectrum with a distinct shape characterized by three features: a downfield edge (labeled σ_{11}), a central peak (σ_{22}), and an upfield edge (σ_{33}) (Fig. (2-2))[7, 8]. Absent extraordinary effects (e.g. motional averaging), the parameter set $\{\sigma_{ii};i=1,2,3\}$, consisting of the frequencies at which these three distinct features occur, suffices to fully characterize both the static spectrum itself, and more generally provides information about the "magnitude" (as opposed to the "orientation" - see below) of the spatial dependence of the chemical shift interaction as manifested in most NMR experiments. In MAS spectra, where one observes a centerband at the isotropic frequency ($\sigma_{iso}=[\sigma_{11}+\sigma_{22}+\sigma_{33}]/3$), and the anisotropic nature of the chemical shift manifests itself as a series of sidebands, a more natural set includes

Figure 2-2: CSA-dependent powder pattern spectra:

(A) $\eta=1$ (axially asymmetric) case. The elements $\sigma_{11}, \sigma_{22}, \sigma_{33}$ are assigned downfield to upfield, as shown.

(B) $\eta=0$ (axially symmetric) case. The elements $\sigma_{11}, \sigma_{22}, \sigma_{33}$ are again assigned downfield to upfield; in this case the two initial elements have identical values (hence the symmetry). Note that there is a continuum from $\eta=0$ to $\eta=1$, these spectra representing the extremes.

(A) $\eta \approx 1$

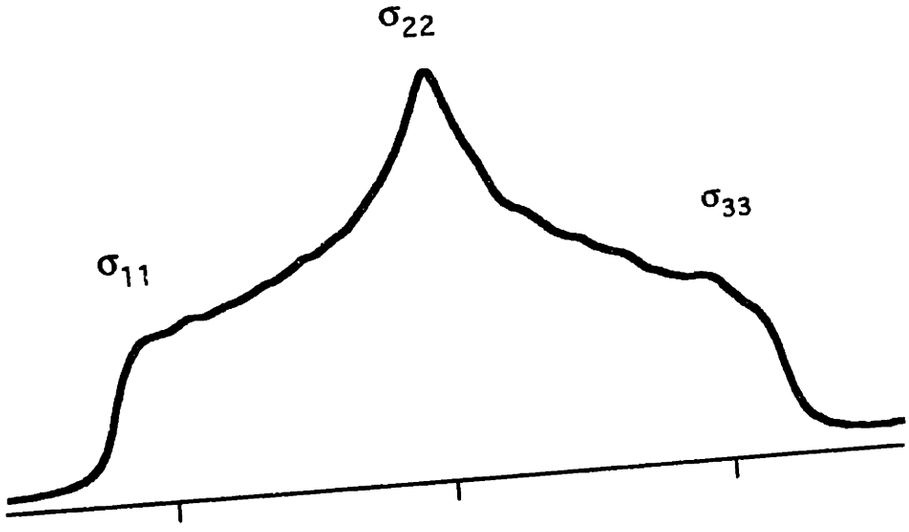

(B) $\eta \approx 0$

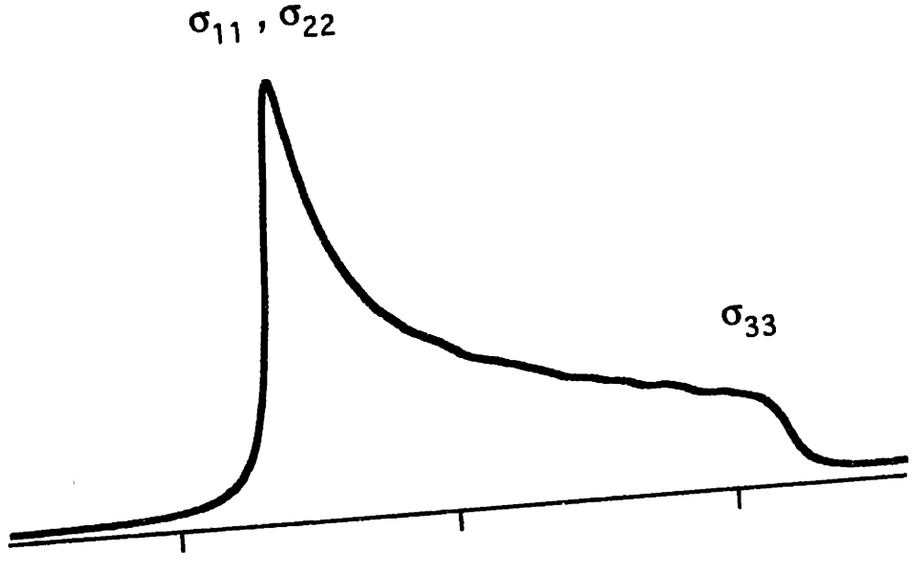

σ_{iso} and the parameters δ and η[8],

$$\delta = \sigma_{zz} - \sigma_{iso}$$
$$\eta = (\sigma_{xx} - \sigma_{yy})/\delta \qquad (1),$$

(where the assignments {x,y,z} are made to {1,2,3} such that $|\sigma_{zz} - \sigma_{iso}| \geq |\sigma_{xx} - \sigma_{iso}| \geq |\sigma_{yy} - \sigma_{iso}|$, and a right-handed coordinate system results). These values characterize the size and symmetry of the anisotropic component of the chemical shift interaction, and can be extracted from sideband intensities in slow-spinning MAS spectra ($\omega_r \leq \delta$) using standard methods[9]. (More recently the pair of parameters Ω and κ, termed span and skew respectively, have been suggested. They more naturally separate the width and symmetry of the powder pattern into two parameters and are given by[10]:

$$\Omega = \sigma_{33} - \sigma_{11}$$
$$\kappa = (2\sigma_{22} - \sigma_{11} - \sigma_{33})/\Omega \qquad (2).$$

All three sets are equivalent in the sense that any one can be derived from the other two, but the latter two parameter sets allow a more direct comparison of the nature of the anisotropic component of the chemical shift interaction between various nuclei.)

The parameter set $\{\sigma_{ii}\}$ describes the range over which the chemical shift varies as the molecule in which the nucleus of interest is embedded is rotated among various orientations relative to the applied magnetic field (the magnitude of the spatial dependence of the chemical shift). The manner in which this variation takes place - that is, the form of the functional dependence of the chemical shift

upon the molecular orientation in the field - is determined by the tensorial character (2^{nd} rank, symmetric) of relevant components of the chemical shift interaction. Given the nature of the interaction tensor, we can postulate the presence of a set of 3 orthogonal axes $\{\sigma_{ii}\}$ (the principal axis system, or PAS) corresponding to the principal components $\{\sigma_{ii}\}$[8]. The reasoning is as follows. The chemical shift interaction can be represented by a second-rank Cartesian tensor (a 3x3 matrix) which, when multiplied into the vector representing the magnetic field direction, results in a vector describing the magnetic field experienced by the nucleus (i.e. the field after shielding has been taken into account). Because of the symmetries inherent in the system, the antisymmetric component of the chemical shift tensor can be ignored in almost all NMR experiments[8]. This reduces the number of parameters necessary to characterize the effects of the interaction from the nine necessary to characterize a general second-rank tensor (the nine elements of the original matrix) to six (the six independent elements of a symmetric matrix). The particular values these six elements take on depend upon the coordinate system in which the interaction is described. For any symmetric tensor one can find a coordinate system (the principal axis system, or PAS) in which its representative matrix is diagonal (i.e. the off-diagonal elements are zero and there are three independent elements). The diagonal elements of the matrix in this coordinate system are termed the "principal components" of the tensor, and correspond directly to the three parameters $\{\sigma_{ii}\}$ described above. Each element σ_{ii} describes the shielding along a corresponding axis (labeled σ_{ii}). If the molecule is oriented such that

the magnetic field points along the σ_{ii} axis, the observed chemical shift is given by the value of the parameter σ_{ii}. The chemical shift (σ_{cs}) observed for magnetic field orientations which do not lie directly along any of the three principal axes are easily calculated by applying the appropriate rotation to the system; the general result is expressed as

$$\sigma_{cs} = \sigma_{11}(\sin^2\theta\cos^2\phi) + \sigma_{22}(\sin^2\theta\sin^2\phi) + \sigma_{33}(\cos^2\theta) \qquad (3),$$

(where θ is the angle between the magnetic field and σ_{33}, and ϕ is the angle between the projection of the magnetic field in the σ_{11}-σ_{22} plane and the σ_{11} axis; these correspond to the standard polar and azimuthal angles in a coordinate system where the $\{\sigma_{11},\sigma_{22},\sigma_{33}\}$ axes have been labeled $\{\mathbf{x},\mathbf{y},\mathbf{z}\}$, respectively).

Note that our selection of the PAS coordinate system is not unique. The chemical shift parameters $\{\sigma_{ii}\}$ describe the magnitude of the shift along perpendicular axes $\{\sigma_{ii}\}$, but the shift is identical for magnetic field orientations pointing in either sense (parallel or antiparallel) relative to the axes. This is the nature of a symmetric tensor. Given this degeneracy in the selection of the direction of the coordinate system basis vectors, there are 8 possible combinations (2^3); restricting ourselves to right-handed coordinate systems for convenience (assuming some assignment of $\{\mathbf{x},\mathbf{y},\mathbf{z}\}$ to $\{\sigma_{11},\sigma_{22},\sigma_{33}\}$ like the one detailed above in the definitions of δ and η) eliminates half of the possibilities, yielding 4 equivalent PAS systems, related to each other by 180° rotations about the axes.

What remains to be determined is the orientation of the PAS relative to some molecule-fixed coordinate system (e.g. the molecular frame). That is, we can extract the parameter set $\{\sigma_{ii}\}$ directly from

powder spectra, and we can postulate the presence of a PAS, and with it describe the functional form of the orientation dependence of the chemical shift such that we know, for instance, that the chemical shift "along" the σ_{ii} axis (i.e. with the magnetic field pointing along that direction) is given by σ_{ii}; we can not, however, determine which axis in the molecular frame corresponds to the σ_{ii} axis, and so more generally which molecular orientation corresponds to which chemical shift. Such information is not generally evident in chemical shift spectra obtain from powder samples (MAS or static), in part because all orientations are present so that the system is insensitive to the specific orientation of the PAS in the molecular frame. Given additional information, for instance from symmetry arguments, or the use of a single crystal where the molecular orientation(s) relative to the field is known, or from the introduction of a second interaction tensor into the molecular system, one often can extract this information. This topic will be discussed in some detail in the next section.

The lack of routinely available information about the orientation of the PAS in the molecular frame has forced most studies of the conformational dependence of the chemical shift to focus solely on the magnitude of the principal components[11, 12], and often these studies focus on the isotropic chemical shift alone[13]. Such studies are generally empirical in nature: they involve tabulating the chemical shift parameters for a range of compounds about which at least some structural information is known (ideally the crystal structure at high resolution), and then attempt to identify trends in the chemical shift data that correlate

with identifiable changes in conformation[14]. Theoretical calculations are often performed in addition, to provide supporting evidence for the postulated correlations[12, 13]. Until recently these calculations have focused on relatively simple models of the system, although now systems as complex as proteins are under investigation[15].

Given that we are interested in the conformation about the G(37)-G(38) peptide bond, a close examination of the conformation dependence of the chemical shift of the glycine (37) carbonyl, as discussed in the literature, may prove useful. It has a relative large chemical shift interaction (i.e. a broad powder pattern), which might more obviously bear the imprint of its conformation. Several papers have been published examining the conformational dependence of glycine $C_{=O}$'s in various peptide and protein (poly-aa's, at least) structures[11, 13]. The authors have found that the chemical shift components of glycine $C_{=O}$'s in a series of gly-containing poly-amino acids lie in the following ranges: σ_{11}(242-244), σ_{22}(171/174/178-179), σ_{33}(88/93-95). Within these ranges, they have identified one clear trend: an increase in the isotropic chemical shift (measured in ppm, i.e. a downfield shift) for $C_{=O}$'s involved in shorter hydrogen bonds. This shift is primarily driven by a downfield shift of the σ_{22} component of the chemical shift tensor; the other two elements are either insensitive (σ_{33}) or shift weakly in the opposite direction (σ_{11}).

Here we are interested in the structure of the peptide bond between residues G(37) and G(38) in the 9mer. We choose the $C_{=O}$ involved in this bond (^{1}G(37)) as a probe of conformation because it has a relatively large chemical shift interaction (i.e. a broad powder

pattern), which might more obviously bear the imprint of its conformation. As a control, we also examined the chemical shift parameters of the $C_{=O}$ involved in the preceding peptide bond in the 9mer (^{1}V(36)), where n=1 RR experiments have clearly identified a *trans* conformation (α1-2 dist ≈ 4.9 Å). The valine $C_{=O}$ chemical shift parameters will be sensitive to the presence of the valine sidechain, so that attributing any differences directly to the conformation of their respective peptide bonds is not possible. Finally, carbonyl carbons in trans and cis model compounds (glycylglycine•HCl and diketopiperazine, respectively) were also examined during the course of this work to provide standards for comparison.

The observed chemical shift parameters for each compound are displayed in Fig. (2-3). Although the DKP and gg•HCl patterns are distinctly different, it is not clear whether this difference (or what fraction of it) is due to the conformation of the peptide bond, and what is due to other considerations such as intermolecular packing. Hence it is not possible to extract unambiguous information about the conformation of the peptide bond in which the various carbonyls are involved.

Experimental: Several (at least 4) slow-spinning (1-4 kHz) MAS spectra of each sample [100% labeled at the appropriate $C_{=O}$] were obtained on 7.4 and 9.4 T magnets (79.9 and 100.0 MHz for ^{13}C, respectively) using home-built probes equipped with Doty 5mm high-speed spinning assemblies. ^{1}H pulse lengths varied

Figure 2-3: Chemical shift parameters for ^{13}C-labeled carbonyl atoms in the indicated compounds (units in ppm). Isotropic shifts were taken directly from peak position in MAS spectra; CSA parameters were extracted by fitting the sideband pattern for slow-spinning MAS spectra using standard techniques:

Left: The values of the chemical shift tensor components $\{\sigma_{ii}\}$ are indicated by thick lines (with numerical values listed underneath each bar); isotropic shifts are indicated by thin lines (with numerical values above the appropriate bar). The uncertainty in the measurements is given by the width of the appropriate indicating line (±1.5 ppm for tensor components, ±0.5 ppm for isotropic shifts).

Right: δ and η are related to the $\{\sigma_{ii}\}$ parameters according to: $\delta = (\sigma_{iso} - \sigma_{33}), \quad \eta = (\sigma_{11} - \sigma_{22})/\delta.$

Carbonyl Chemical Shift Parameters

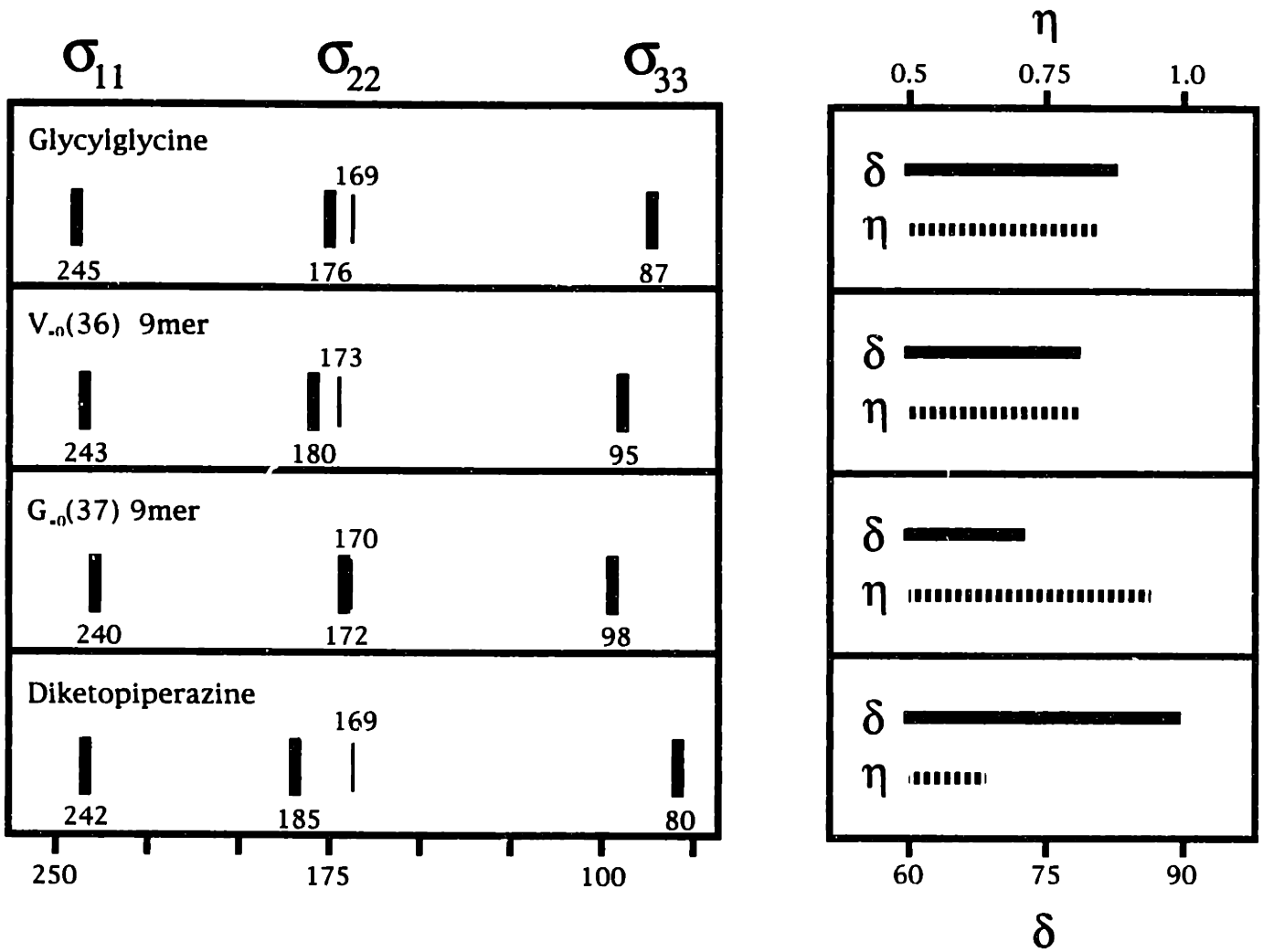

(Units are PPM)

from 2.5-3.8μs; ^{13}C pulse lengths were 4-5μs. Isotropic shifts (in kHz) were read directly from centerband positions. CSA parameters were extracted from sideband intensities using the standard method, implemented by the program SPEEDYFIT. Results from the series of measurements in each case were averaged. Calculation of parameters in ppm units was made using the ^{13}C carboxyl resonance of glycine as a reference (at 177 ppm).

2.3 Static echo experiments applied to (1-α2) labeled peptides can distinguish between *cis* and *trans* in model compounds.

The nature of a powdered sample - the presence of an isotropic distribution of molecular orientations relative to the magnetic field - makes it difficult to extract directly from chemical shift spectra (static or MAS) the orientation of the chemical shift PAS relative to the molecular frame. Given that we can extract the magnitudes of the shielding effect along each of three orthogonal axes, often a reasonable argument can be made for an approximate alignment of these axes within the molecular frame based on an estimate of the local electronic structure. Such arguments are most convincing when they can take advantage of symmetries in the molecular structure that are reflected in the observed spatial dependence of the chemical shift interaction; clearly, in these cases, the symmetry elements in the molecular frame and the chemical shift PAS are aligned. One can forgo such arguments, and measure the orientation of the PAS directly, by obtaining spectra of crystalline (as opposed to polycrystalline, i.e. powdered) material, where the orientation of the crystal axes relative to the magnetic field are known (this assumes that the molecular structure is known relative to the crystal axes, information that is routinely determined in x-ray structural analysis)[8]. Such a sample contains the molecule of interest in only one (or a few) orientations; assuming for simplicity a single orientation, chemical shift spectra show a single, relatively narrow, line at the chemical shift corresponding to the chosen molecular orientation relative to the field. By varying the crystal (and hence

the molecular) orientation in the magnet, one can directly observe the change in chemical shift that occurs as a function of orientation and thereby determine the orientation of the chemical shift PAS relative to the molecular frame. Such an experiment has been performed for glycylglycine (crystallized as the HCl salt), and the results are diagrammed in Fig. (2-4A)[16]. The most-shielded axis, σ_{33} (not shown; points directly into the page), is aligned approximately along the long axis of the π orbital (nearly perpendicular to the peptide plane); the σ_{11} and σ_{22} axes lie in the peptide plane, with the σ_{22} axis pointing approximately along the $C_{=O}$ bond (shifted to one side by 13° as shown). Since these experiments require a large single crystal (weighing ≈10's of mg or more), they can not be performed routinely. There are no other published reports of such a direct measurement of the PAS/molecular frame orientation for a carbonyl carbon in a peptide (at least that I can find). Because of this, the results from glycylglycine are often referenced as the model for carbonyl CSA orientation.

In 1987, Oas and coworkers attempted to crystallize a series of dipeptides with the sequence Ac-Gly-X-NH_2 (X=Gly, Ala, Tyr, Phe) to examine the sequence- and conformation- dependence of the canonical result just described (the uncapped glycylglycine•HCl peptide was also synthesized as a control)[17]. Because they were unable to grow crystals of sufficient size to permit a single-crystal study of each compound, they were forced to use a less direct method to assign the PAS in the molecular frame. Their approach involved obtaining ^{13}C powder spectra of a (^{13}C, ^{15}N) labeled version of each peptide, where the labels were located at the carbonyl carbon

Figure 2-4: Orientation of the carbonyl chemical shift tensor and the (1-α2) dipolar tensor in the molecular frame.

(A) Schematic drawing of a peptide backbone with tensor components drawn in. The orientation of the carbonyl chemical shift tensor elements (thick vectors) is not strongly conformation dependent (not shown: σ_{33} points directly into the page). The orientation of the (1-α2) dipolar vector (dashed vectors) depends upon the peptide conformation (*cis* or *trans*) as indicated.

(B) Relative orientation of the tensors, characterized by the angle α. Given a "flat" peptide plane (formed by C_α and $C_{=O}$ of first residue, N and C_α of second) perpendicular to the σ_{33} element, the relative orientation of the two tensors is fully characterized by the angle α. Single-crystal studies indicate α=19° for glycylglycine•HCl; studies on a series of G-X dipeptides show a range from α=9° to 19° (indicated by bracket). Results detailed here yield α=65° for our *cis* model, diketopiperazine.

(A)

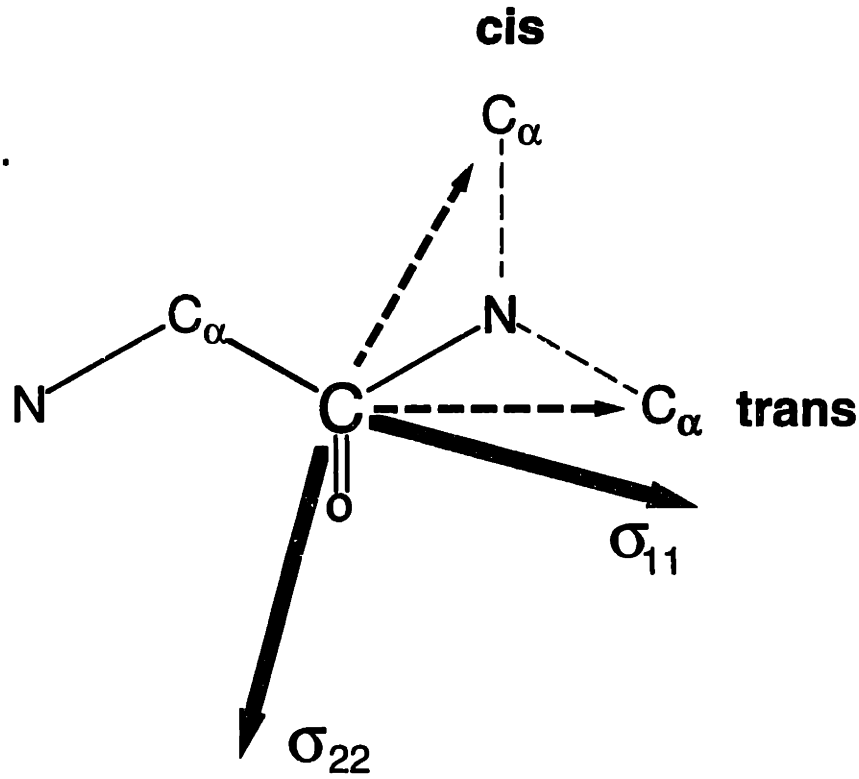
cis
C_α
N
C_α
N
C
C_α
trans
O
σ_{11}
σ_{22}

(B)

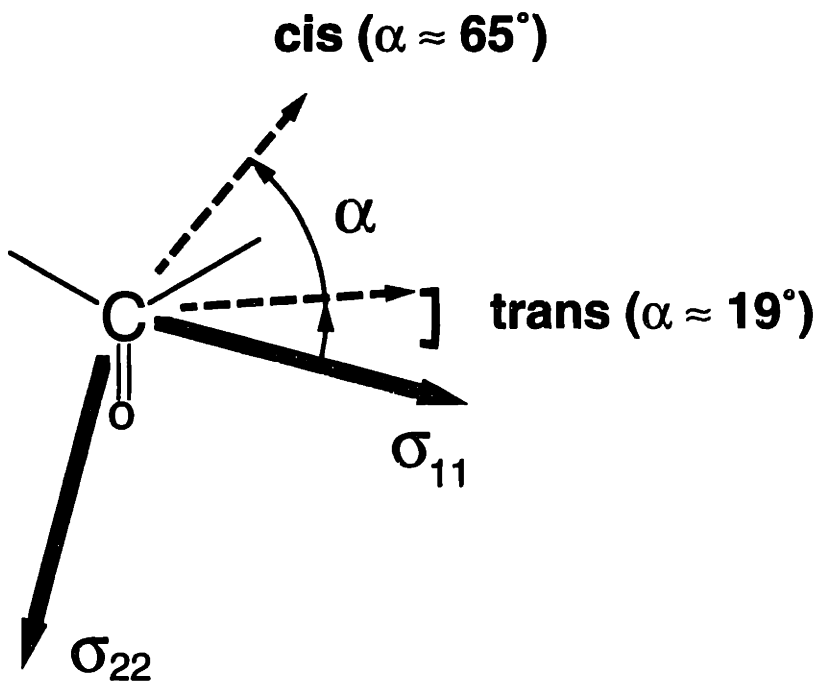
cis ($\alpha \approx 65^\circ$)
α
C
trans ($\alpha \approx 19^\circ$)
O
σ_{11}
σ_{22}

and amide nitrogen involved in the central peptide bond in each dipeptide. The ^{13}C spectra were dominated by the carbonyl chemical shift, and showed the characteristic powder pattern. There were distortions present, however, that were induced by the presence of the ^{13}C-^{15}N coupling, distortions that were dependent upon the relative orientation of the $^{13}C_{=O}$ chemical shift PAS and the ^{13}C-^{15}N dipolar vector. This is best explained by first considering a single crystallite where there is only one molecular orientation relative to the field. Absent the coupling, the spectrum will consist of a single narrow resonance at a frequency dependent upon the orientation of the $C_{=O}$ PAS relative to the field. With the coupling, a pair of resonances occur, symmetrically placed about the original. The size of the induced splitting depends both on the size the coupling constant (b_{IS}, a distance-dependent parameter, in this case ≈ 1.05 kHz), and the orientation of the C-N dipolar vector relative to the magnetic field. The orientation dependence is given by

$$splitting = 2 \times \omega_d(b_{IS}, \theta_d) = \frac{b_{is}}{2}\left(3\cos^2\theta_d - 1\right) \qquad (4),$$

where θ_d denotes the angle between the dipolar vector and the magnetic field. Now we can consider the static ^{13}C spectrum obtained from the entire powder sample, and focus on one feature, the σ_{11} edge. This feature arises from crystallites with a common orientation, such that the magnetic field points approximately along the σ_{11} axis. In these crystallites, the dipolar vector has a single orientation relative to the field (as described by the angle θ_d, defined above), so that they all experience approximately the same splitting

in its presence. We therefore observe two σ_{11} "edges" in the spectrum of the doubly labeled compound, where the size of the splitting between the two depends upon the angle between the dipolar vector and the σ_{11} axis in the manner defined above. Similar arguments can be made for the σ_{22} and σ_{33} features. The authors of the study used this fact to determine the angle of the dipolar vector relative to each of the axes of the $^{13}C_{=O}$ PAS in turn, thus defining the relative orientation of the two interactions (they used derivative spectra, where the three features show up as absorptive or dispersive "spikes" and the splittings are therefore clearly delineated). Because the dipolar vector has an obvious assignment in the molecular frame (it points along the axis connecting the pair of dipolar-coupled atoms), this served to partially fix the $^{13}C_{=O}$ PAS within the molecular frame.

The $^{13}C_{=O}$ PAS is only partially fixed in the molecular frame because of the symmetry of the situation. We know the orientation of the $^{13}C_{=O}$ PAS relative to the dipolar vector, and we know the orientation of the dipolar vector relative to the molecule. If we picture the dipolar vector as pointing along some direction within the $^{13}C_{=O}$ PAS, and then appropriately superimpose the molecular structure on the dipolar vector, we see the orientation of the molecule relative to the $^{13}C_{=O}$ PAS. However, if we rotate the molecule about the dipolar axis, we do not change either of the known orientations (the $^{13}C_{=O}$ PAS relative to the dipolar vector, or that vector relative to the molecule), but we do change the orientation of the $^{13}C_{=O}$ PAS relative to the molecule. Thus we have

only assigned the $^{13}C_{=O}$ PAS within the molecular frame up to a rotation about the dipolar vector.

The authors got around this point by assuming that the σ_{33} axis points perpendicular to the peptide plane, as is nearly the case for gg•HCl (within 1°-2°). Given this assumption, we are merely determining the orientation of the σ_{11} and σ_{22} vectors within the peptide plane. This orientation can be described by a single angle measured in the peptide plane, for instance the angle between the σ_{11} element and the $C_{=O}(1)$-$C_{\alpha}(2)$ dipolar vector (termed 'α', and chosen for reasons that will become apparent shortly). Note that there are still degeneracies in the system due to the symmetric nature of the chemical shift interaction. Selection of one of the equivalent $^{13}C_{=O}$ PAS's (discussed previously) does not change the relative orientation of the tensors, but results in a new value for α. These degeneracies in α can be expressed by two transformations [$\alpha \Rightarrow (180°+\alpha)$, $\alpha \Rightarrow (180°-\alpha)$], with the result that α describes a unique relative orientation only over the range (0°-90°). The results of the Oas, et. al. experiments are detailed in Fig. (2-4B). The angle α for the 5 dipeptides examined varies from approximately 9° to 19°, the latter being the value for gg•HCl, equal to that calculated from the single-crystal results. This range is indicated in the figure by a bracket.

Because these experiments are insensitive to rotations about the peptide bond, they are clearly unable to distinguish between *cis* and *trans* conformers. We can perform a similar experiment which is sensitive to this difference by choosing a pair of atoms whose inter-nuclear vector does not lie nearly along the peptide bond (preferably

with a large dipolar coupling, to maximize our ability to detect its effects). One such selection is the $C_{=O}$ of the peptide bond in question and the C_α of the following residue (the '1-α2' labeling scheme). Given such a choice, the approximate dipolar-chemical shift PAS orientation is diagrammed in Figs. (2-4A) and (2-4B) for both *cis* and *trans* conformations. In Fig. (2-4A), we have assumed that we can derive the chemical shift and dipolar tensor assignments in the *cis* conformation from those in the *trans* conformation (calculated from the single crystal and dipeptide studies) by a simple 180° rotation about the peptide bond. This results in an α angle of approximately $75°\pm5°$ for the *cis* conformer. The strain of adopting the *cis* configuration may induce changes in the local electronic structure and molecular conformation that make this approximation less than exact (such an effect may be evident in the chemical shift parameters given for DKP in section 2-2). Experiments conducted on our *cis* model (DKP), discussed in detail in what follows, indicate that $\alpha \approx 65°\pm10°$ is more representative of the *cis* structure. This is indicated in Fig. (2-4B).

The selection of a homonuclear spin pair, and the application of these experiments to 9mer samples, force several changes in the manner in which the experiment is performed. The static 1D spectra obtained by Oas, et al, were dominated by the $^{13}C_{=O}$ chemical shift, but there was sufficient inherent resolution (determined by the width of the signal from a single crystallite) to observe the effects of the only other interaction of significance, the 1.05 kHz ^{13}C-^{15}N dipolar coupling. The spin pair we are considering has a smaller coupling (≈0.5 kHz), and we expect the resolution to be somewhat

reduced in the 9mer samples, by as much as 4 ppm (300-400 Hz at our field strengths) due to the presence of chemical shift dispersion. Furthermore, there are additional interactions of significance in the system, specifically the coupling of the central amide ^{14}N (99.6% natural abundance) to both the $^{13}C_{=O}$ and the $^{13}C_{\alpha}$ (≈0.6 kHz coupling in both cases). Because of these two effects, it is difficult to determine the relative orientation of the $^{13}C_{=O}$-$^{13}C_{\alpha}$ dipolar tensor relative to the $^{13}C_{=O}$ chemical shift tensor from static 1D spectra in the manner used by Oas et al.

The standard separated local field (SLF) experiment provides an alternative approach that avoids many of the stated problems[18-20]. An appropriate pulse sequence for this experiment in our system is shown in Fig. (2-5). After CP from ^{1}H's, the transverse ^{13}C magnetization evolves for a period t_d (the 'dipolar mixing period'), with a π pulse placed in the center of the period. The pulse refocusses the chemical shift and heteronuclear dipolar interactions, so that the only interaction of significance driving the evolution during this period is the $^{13}C_{=O}$-$^{13}C_{\alpha}$ dipolar coupling. Using I to denote the $^{13}C_{=O}$ spin and S to denote the $^{13}C_{\alpha}$, the initial state $\rho(0)=I_x+S_x$ evolves under the coupling as

$$\rho'(0) = I_x \xrightarrow{2\omega_d I_z S_z} \rho'(t_d) = I_x \cos(\omega_d t_d) + I_y S_z \sin(\omega_d t_d) \qquad (5),$$

(the S-spin magnetization evolves in an identical fashion, derived simply by transposing I and S in the above equation). Focusing on the carbonyl (I) magnetization, we see that the evolution consists of an oscillation between detectable transverse magnetization and

Figure 2-5: Standard echo sequence used to induce a period of purely (homonuclear) dipolar evolution in static experiments. After standard cross-polarization from ^{1}H to ^{13}C, CW ^{1}H decoupling is applied on the ^{1}H channel. On the ^{13}C channel, a π pulse is applied in the center of the dipolar mixing period (of length t_d) to refocus chemical shift and heteronuclear interactions; the dominant remaining interaction (in (1-α2) labeled peptides) is the homonuclear dipolar interaction. The refocussed FID is acquired at the end of the evolution period.

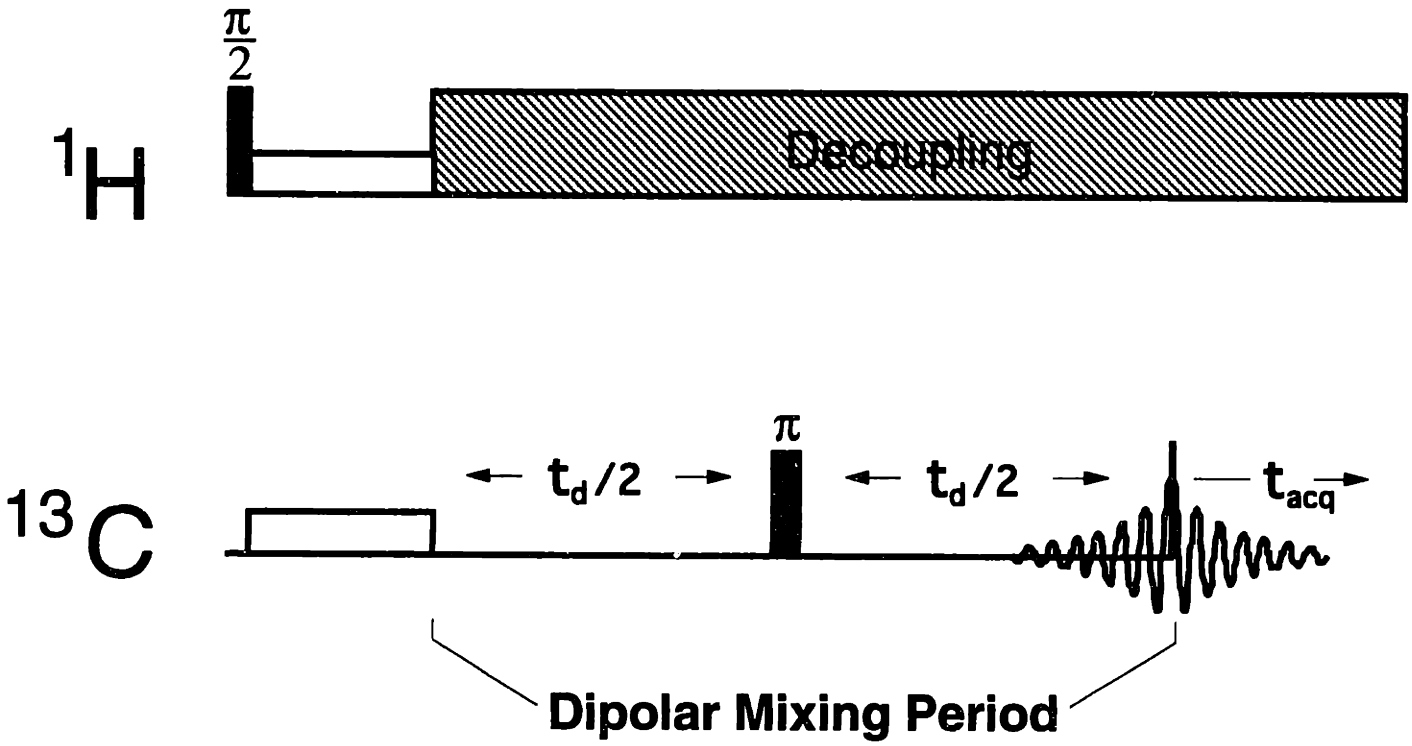
π/2
1H
Decoupling
13C
π
← td/2 →
← td/2 →
tacq
Dipolar Mixing Period

undetectable antiphase magnetization, with a frequency depending upon the orientation of the (1-α2) dipolar axis relative to the magnetic field (implicit in ω_d, as given above). Upon acquisition of the signal at the end of the dipolar mixing period, we find that the observed powder pattern has been distorted by the preceding dipolar evolution. There has been a loss of detectable polarization across the pattern, maximized where the molecular orientation is such that the product ($\omega_d t_d$) approaches an odd multiple of $\pi/2$ (i.e. when $\omega_d t_d=(n+1)\pi/2$, n=0,1,2,3...). Note that experimentally we choose the shortest values of t_d which will induce significant signal decay, so that the effects of relaxation and intermolecular couplings are minimized. Such a choice for our system (0.5 kHz coupling constant) lies between 0.5 and 1 ms, corresponding to near-full conversion to undetectable antiphase magnetization for orientations where the coupling is maximized ($\omega_d t_d \approx$ (0.5kHz*500μs) $\approx \pi/2$). (Note that longer periods might lead to an inverted powder pattern absent relaxation effects.) Clearly the shape of the acquired powder spectrum after dipolar evolution will depend to some extent upon the relative orientation of the dipolar tensor and the chemical shift PAS. The extent to which this is so for our system is shown in Fig. (2-6), where t_d has been set to 750μs and α is varied from 0° to 90°. Here we display the t_d='0' powder pattern as a solid line, and the difference between the t_d='0' and the t_d=750μs pattern as a dotted line. Because we display difference spectra, greater signal loss after mixing is indicated by greater signal intensity in the dotted spectra. When $\alpha \approx 90°$, the dipolar vector points nearly along the σ_{22} axis. Therefore, in crystallites where the magnetic field points along σ_{22}

Figure 2-6: Simulated dependence of static-echo powder spectra on relative tensor orientation (units are ppm). The solid line in each plot indicates the powder spectrum obtained with essentially no dipolar mixing (t_d=50ms); the dotted line indicates the difference between that spectrum and the one obtained after t_d=750ms of dipolar mixing (i.e. greater intensity at a particular frequency indicates greater signal loss due to dipolar evolution). The simulations explicitly included finite pulse effects (^{13}C rf power was set at 40 kHz) and the presence of the amide ^{14}N coupling. An average over 10,000 randomly selected crystallite orientations was performed, and the resulting FID's were processed using 0.75 kHz of exponential line broadening. The spin system parameters were those appropriate for (1-α2) labeled glycylglycine•HCl (see text), with the orientation angle α (defined in Fig (2-4)) varying from plot to plot as indicated.

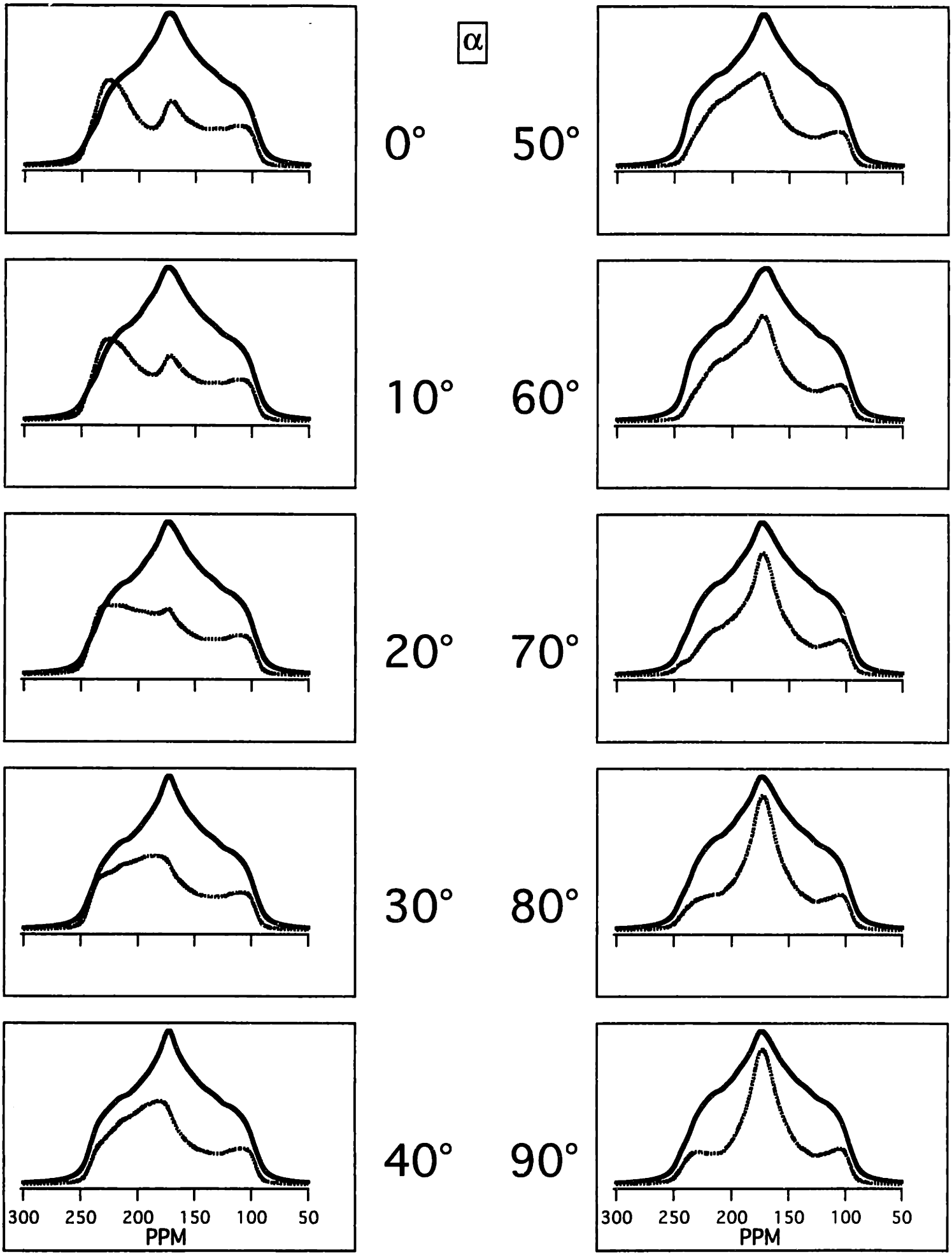
α
0°
50°
10°
60°
20°
70°
30°
80°
40°
90°
300 250 200 150 100 50
PPM
300 250 200 150 100 50
PPM

(signal from which appears in the center of the t_d='0' pattern), $\theta_d \approx 0°$ and the dipolar coupling is at its maximum. This is indicated in difference spectra by the presence of a large peak (signifying a great deal of signal loss during dipolar mixing) near the center of the spectrum. As α decreases towards 0°, the dipolar vector moves from along the σ_{22} axis to the σ_{11} axis. This is signified by an increase in the signal intensity of the difference spectrum at the σ_{11} edge, and by a decrease in the signal intensity at the σ_{22} peak. There is no change with α in the orientation of the dipolar vector relative to the σ_{33} axis, and this is reflected in the fact that this feature does not change in the difference spectra. These spectra clearly demonstrate that the technique can distinguish between *cis* and *trans* conformers.

Experimental: The simulated spectra were calculated by numerical integration of the equations of motion derived from the following 3-spin Hamiltonian that includes the four dominant interactions:

$$H = H^I_{CS} + H^S_{CS} + H^{IS}_D + H^{IN}_D \qquad (6),$$

(where superscripts I and S denote the labeled carbon atoms as described previously, N denotes the central amide ^{14}N; subscripts CS and D denote chemical shift and dipolar interactions, respectively). The SN dipolar coupling and the N quadrupolar and chemical shift interactions have been disregarded because their secular terms commute with the observable and the rest of the Hamiltonian. The validity of the secular approximation for the ^{14}N quadrupolar interaction has been shown to be acceptable at the field strengths we will be considering here[21, 22].

These simulations required specifying the magnitude and orientation of all four interactions. The magnitude of the chemical shift interactions (the first two terms) was set equal to those measured for glycylglycine•HCl (CSA parameters extracted by fitting the sideband pattern of slow-spinning MAS spectra) in a 7.4T magnetic field (79.9 MHz for ^{13}C), with the $^{13}C_{=O}$ isotropic shift placed on resonance. The magnitude of the dipolar tensors (the final two interactions) and the orientation of the $^{13}C_{=O}$ chemical shift and the $^{13}C_{=O}$-^{14}N dipolar interaction were calculated from both the published crystal structure and the associated single-crystal study of gg•HCl. The orientation of the $^{13}C_{=O}$-$^{13}C_{\alpha}$ dipolar tensor, lying in the peptide plane with a phase relative to the σ_{11} axis characterized by α, was varied as indicated in the plots. The relative orientation of the C_{α} chemical shift tensor was arbitrarily chosen and did not change in the various simulations (the experiment is insensitive to this parameter, as confirmed by a series of simulations (not shown)). The values are compiled in the following table (Table 2-1):

TABLE 2-1: Simulation parameters for static echo experiments

Interaction	Magnitude (kHz)	Orientation
$^{13}C_{=O}$ chemical shift	ν_{11}=6.1 ν_{22}=0.56 ν_{33}=-6.56	(0°,0°,0°)
$^{13}C_{\alpha}$ chemical shift	ν_{11}=-8.47 ν_{22}=-10.02 ν_{33}=-10.57	(0°,0°,0°)
$^{13}C_{=O}$-$^{13}C_{\alpha}$ dipolar coupling	b_{is}=0.50	(0°,-90°,α)
$^{13}C_{=O}$-^{14}N dipolar coupling	b_{is}=0.63	(0°,-90°,49°)

Orientations are given using the standard euler convention. Evolution during the ^{13}C π pulse was explicitly calculated using a 40 kHz ^{13}C rf field strength. Residual proton couplings were modeled using orientation-independent relaxation parameters estimated from experiments applied to natural abundance gg•HCl; the $^{13}C_{=O}$ single-quantum T_2 was set at 4 ms, the $^{13}C_{\alpha}$ at 1.5 ms (^{14}N relaxation was ignored). T_1 in all cases was assumed to be zero.

The simulations that were performed using these parameters involved averaging over a random sampling of molecular orientations (10,000) for t_d=50μs (this is denoted t_d='0'; very little dipolar evolution occurs during 50μs, and the use of a finite delay is useful in the experiment- see below) and t_d=750μs. The resulting FID's were processed using 0.75 kHz of exponential line-broadening. The solid line corresponds to the FT of the t_d='0'μs FID, and the dotted line corresponds to the FT of the difference between the t_d='0'μs and t_d=750μs FID's.

A series of simulations (not shown) was performed to examine the sensitivity of the shape of the final powder spectrum to errors in the input parameters. Essentially no observable change in the result was observed when these parameters were varied within a range encompassing the estimated range of precision for each. The experiment is extremely insensitive to the $^{13}C_{\alpha}$ and $^{13}C_{=O}$-^{14}N dipolar interactions: neglecting them completely had almost no observable effect on the result.

The experiment was applied to *trans* and *cis* model compounds, gg•HCl and DKP, respectively, in part to experimentally verify its ability to distinguish between the two conformations. Fig. (2-7) gives the results. The glycylglycine data (Fig. (2-7A), left) compares favorably with the simulation using the parameters listed in Table 2-1, with α=19° (the rise on the right edge of the experimental spectrum is the signal from the $^{13}C_{\alpha}$). For the DKP sample, we do not have independent information establishing the orientation of the $^{13}C_{=O}$ chemical shift tensor within the molecular frame, so a series of simulations was performed (using the information in Table 2-1, suitably modified to use the $^{13}C_{=O}$ chemical shift parameters for DKP given in Fig. (2-3)) to determine this orientation, starting with the initial guess of α=75° described earlier. The best fit was obtained with a value of α=65°, as shown; the estimated error is on the order of ±5°. Note that this process assumed σ_{33} was perpendicular to the peptide plane, just as in Oas, et al. Given the 10° variation seen in the α value for the series of trans peptides examined by Oas, et, al, we propose an estimate of 65° ±10° to describe the likely orientation

Figure 2-7: Comparison of experimental and simulated static echo spectra for (1-α2) labeled (A) glycylglycine•HCl (*trans* model), and (B) diketopiperazine (*cis* model). Simulation method follows that described in Figure (2-6) unless otherwise noted; the simulation parameters and experimental details for each compound are described in the text. The solid line in each plot shows the powder spectrum obtained after t=50μs of dipolar mixing, while the dotted line shows the t=750μs difference spectrum. The rising edge on the right side of both experimental data sets is the signal from the $^{13}C_{\alpha}$. The glycylglycine data is compared with a simulation using a as calculated from the x-ray structure and the results of a single-crystal NMR study (α = 19°)., while the diketopiperazine data is shown next to the best-fit simulation (α = 65° ±5°).

Experiment

Simulation

(A)

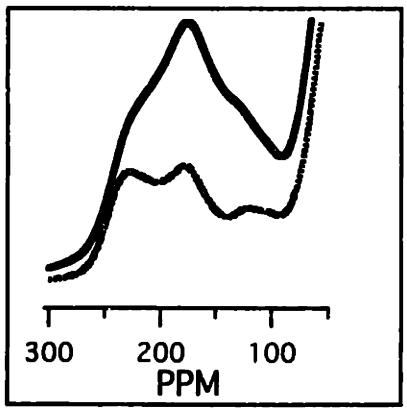

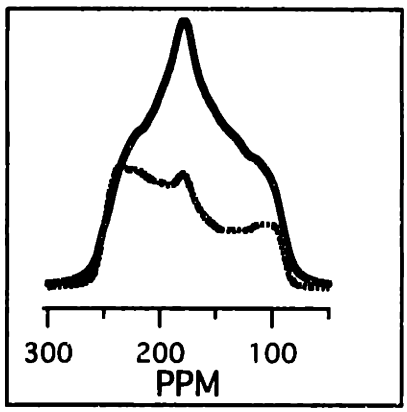

Glycylglycine

(α=19°)

(B)

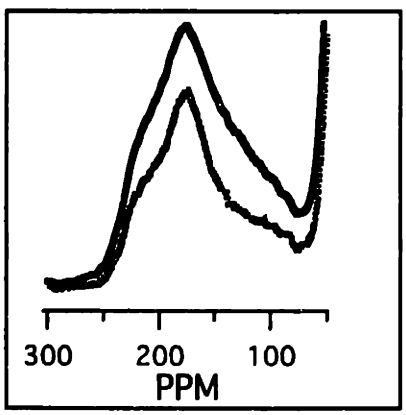

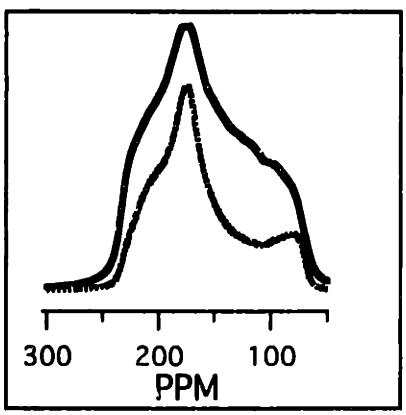

Diketopiperazine

(α=65°)

of the $^{13}C_{=O}$ chemical shift PAS within the molecular frame for *cis* conformers.

Experimental: The experimental data was obtained on a 7.4 T magnet (79.9 MHz for ^{13}C), using a MAS probe w/ a 5mm Doty spinning assembly with the spinning gas off (the coil remained at the magic angle). The ^{1}H CW decoupling power was approximately 70 kHz, and the ^{13}C 180° echo pulse length was approximately 10μs. The carrier frequency was placed near the center of the carbonyl powder pattern. t_d='0' spectra were obtained using a short (50μs) echo period, so that ringdown effects were minimized. A 16-step phase cycle (CYCLOPS and temperature inversion[23], coupled with an inversion of the phase of the 180° pulse) cycle was used, and 1000 - 5000 FID's were obtained for each spectrum. The time between acquisitions (rd) was set as short as 1 sec. This did not allow for full relaxation of the magnetization in DKP (where the relaxation time is longer than 1 minute); a series of experiments using progressively longer rd's up to 1 minute showed no dependence on this parameter. Both samples were fully labeled (i.e. there was no dilution in natural abundance). The likely effect of intermolecular spin-spin couplings is small because of the short length of the mixing period and the relatively small size of these couplings (<0.15 kHz). Simulations (not shown) explicitly including the effect of the closest intermolecular interaction in gg•HCl showed that the additional interaction had no significant effect. The differences between simulation and experiment that are present in the gg•HCl sample, where the orientations of the tensors is well

known, may be due to several factors including: orientation-dependent relaxation, and cumulative effects of intermolecular couplings over longer ranges than considered here.

2.4 Static echo experiments applied to (1-α2) labeled 9mer compounds indicate a *trans* conformation at successive peptide bonds, and suggest the presence of significant motional processes along the peptide backbone.

The results detailed in the previous section demonstrate that static echo experiments can distinguish between *cis* and *trans* conformers in model compounds. We have applied these experiments to appropriately labeled versions of the 9mer (^{1}G(37)-^{2}G(38) flanking the peptide bond in question, and ^{1}V(36)-^{2}G(37) flanking the preceding peptide bond (known to be *trans*) as a control). The experimental results are displayed in the central column of Fig. (2-8). Simulations for *cis* and *trans* conformers (defined by α=65° and 19°, respectively) are shown in the outer columns (the parameters for these simulations were identical to those described in the previous section, with modification to use the $^{13}C_{=O}$ chemical shift parameters appropriate for each compound, given in Fig. (2-3)). The experimental data for the control 9mer (Fig. (2-8A)) closely mimics the *trans* simulation to the left; what differences there are between the two also appear in the gg•HCl experiment-to-simulation comparison.

The data for the G(37)-G(38) peptide bond (Fig. (2-8B)) also shows more similarity to the *trans* simulation, however the central peak is somewhat higher than expected. This feature might be due to a conformation where α is closer to 30°, but the concomitant decrease in the σ_{11} shoulder of the difference spectrum (see Fig (2-6)) does not occur. A more reasonable explanation of this feature depends upon the temperature at which the data in Fig. (2-8) was

Figure 2-8: Comparison of experimental and simulated static echo spectra for (A) ^{1}V(36)-^{2}G(37) and (B) ^{1}G(37)-^{2}G(38) labeled 9mer. Simulation method and processing parameters follow that described in Figure 2-6 unless otherwise noted; simulation parameters and experimental details for each compound are described in the text. The solid line in each plot shows the powder spectrum obtained after t=50μs of dipolar mixing, while the dotted line shows the t=750μs difference spectrum. The simulations in the left (*trans* column) used α=19° to describe the relative orientation of the carbonyl chemical shift and (1-α2) dipolar tensors, while those on the right (*cis*) column used α=65°. The experimental data was obtained at low temperature (T=-155 °C in (A), -117 °C in (B)) for reasons described in the text. The slightly elevated central peak in the experimental difference spectrum in (B) may be due to insufficiently low temperature (see text).

trans Experiment *cis*

(A)

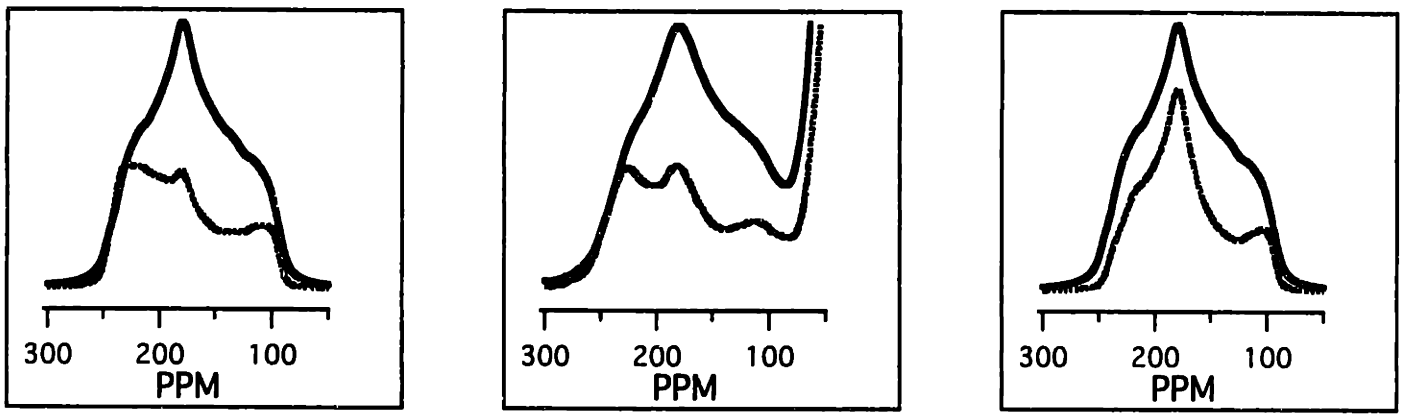

$^{1}V(36)$-$^{2}G(37)$

(B)

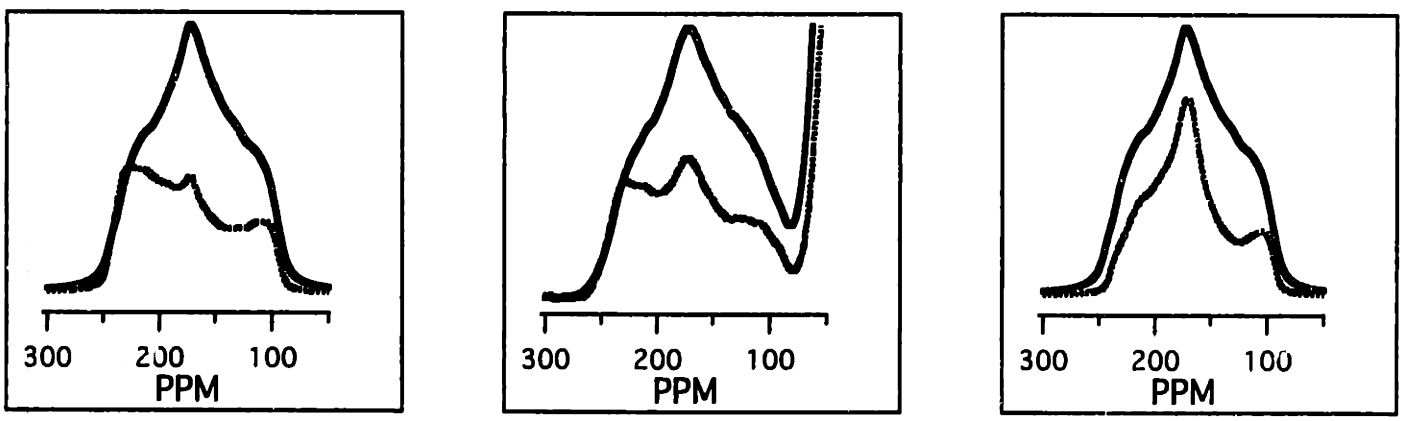

$^{1}G(37)$-$^{2}G(38)$

acquired. The data in Fig. (2-8A) (the control peptide bond) was acquired at T=-155 °C, while for Fig. (2-8B), T=-117°C. Experimentally one finds that at room temperature (T≈25°C) the difference spectra obtained from both samples show elevated central peaks with no associated drop in the σ_{11} shoulder. This is shown in Fig. (2-9), where the solid lines in A and B show the difference spectra at low-temperature, and the dotted lines show the corresponding spectra at room temperature. Given the clear temperature dependence of the difference spectra, it may be that the G(37)-G(38) data was not collected at low enough temperature to fully remove the effect causing the elevated central peak.

Temperature-dependent changes in the spectral features suggest the presence of motion in the sample that freezes out at low temperature. Whether it is the motion itself, or the associated access to at least two different conformations, that leads to the effect is not always clear. We will consider explanations of the latter type first, where motion allows access to both *cis* and *trans* conformations. The motion between two such distinctly different conformations cannot be in the intermediate or fast exchange limit, for this would induce significant distortions in the static powder spectrum that are clearly not present. Motion between the two that was in the slow-exchange limit could explain the static data (with a population distribution, approximately equal at room temperature, that shifts towards *trans* at lower temperature), but is not consistent with room temperature MAS spectra. In such spectra one would expect to see a splitting in the isotropic chemical shift resonance frequency corresponding to the two different conformations, but this does not occur at any of the

Figure 2-9: Temperature dependence of static echo spectra obtained from (1-α2) labeled versions of the 9mer. At room temperature, the t=750μs difference spectra obtained from either 9mer compound (dotted lines, compounds in (A) and (B) as indicated) do not match the simulated spectra (Figure (2-6)) for any reasonable relative orientation of chemical shift and dipolar tensors. In the corresponding spectra obtained at low temperature (indicated by solid lines), the central peak decreases and the resulting shape more closely matches that expected for a compound in the *trans* conformation. Experimental details described in the text.

Temperature Dependence of
Static-Echo Spectra

(A)

$^{1}V(36)$-$^{2}G(37)$

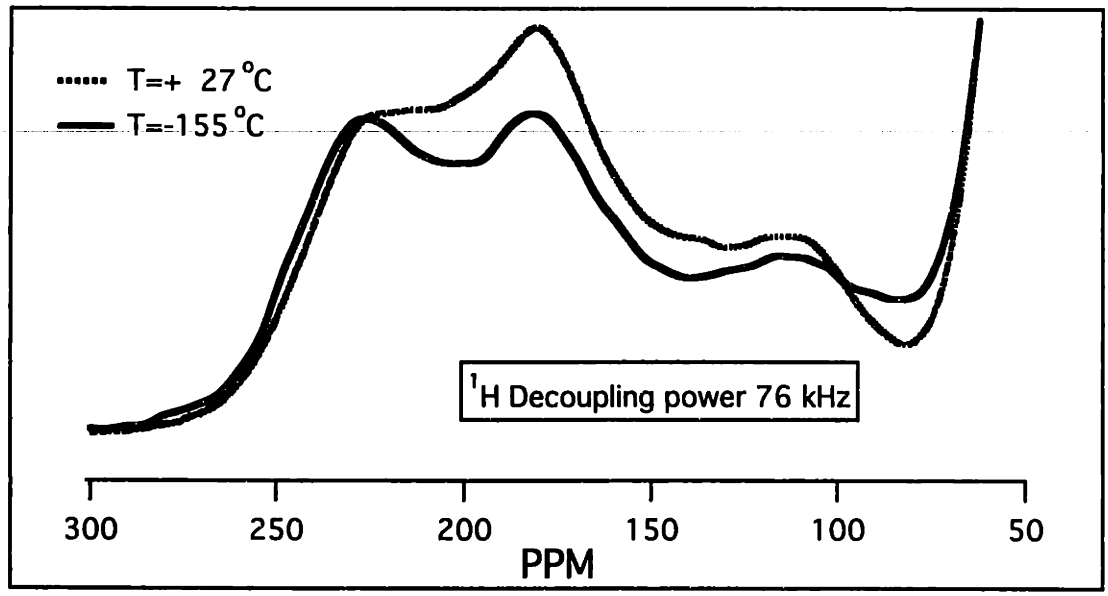

(B)

$^{1}G(37)$-$^{2}G(38)$

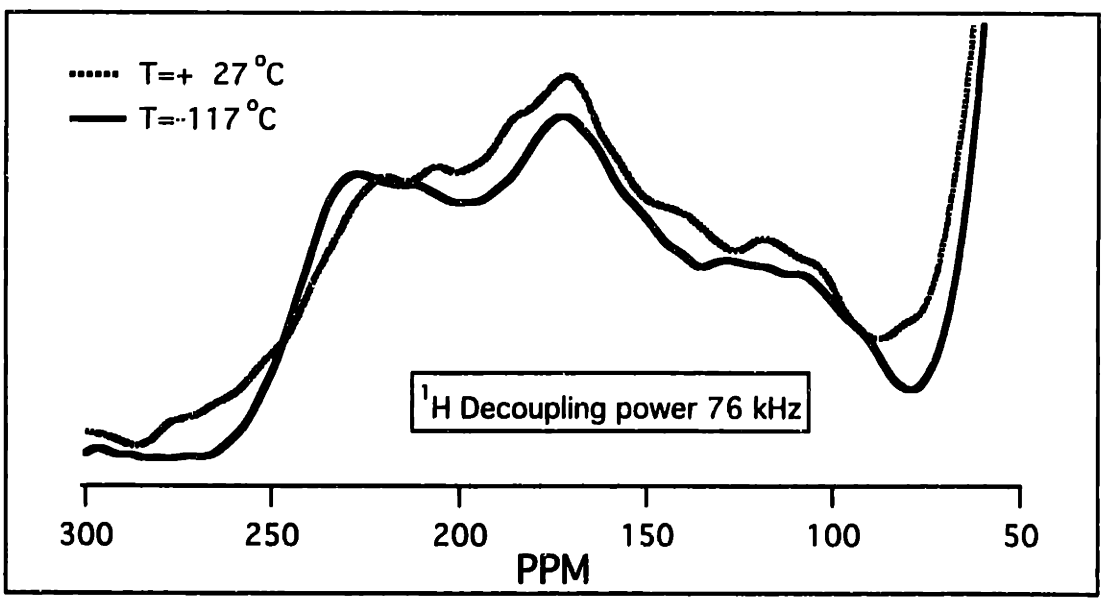

backbone resonances surrounding the bond in question (although some evidence of minor splitting has appeared in some samples). This makes it unlikely that there are two such different conformations at the G(37)-G(38) peptide bond at any temperature.

The second type of explanation involves interference between a motional process and some other modulation of the system. Motional processes affect the spin system by inducing modulations of the magnitude and/or orientation dependence of various interactions (primarily dipolar and chemical shift). If these modulations interfere with some other modulation of the system, they may introduce effects into the spectrum that would otherwise be absent[24, 25]. One example involves the chemical shift. Small fluctuations of the $C_{=O}$ chemical shift tensor may interfere with averaging of its effects. If such a motion had significant spectral density near 0.5 - 1.0 kHz, it would interfere with the π-pulse averaging of the chemical shift interaction during the dipolar mixing period of our echo experiment, and so lead to increased signal loss as observed. Such a motion would have to contain little spectral density at higher frequencies up to 10-15 kHz, because this would interfere with MAS averaging of the interaction at these spinning speeds and lead to homogeneous broadening in room-temperature MAS spectra that does not seem to be present. Experiments in which the MAS spinning speed was reduced to low values (0.5-1 kHz) would be sensitive to the postulated effect (we would expect linebroadening on the order of 500 Hz in these spectra to explain the magnitude of the increased signal loss observed in the static echo experiments), and such experiments were performed (data not shown). Although there is

significant linebroadening at slow spinning speeds, this is a common effect in many samples that is attributed to reduced ^1H decoupling efficiency; there was no clearly observable broadening beyond this. These results do not rule out this effect, but they do make it seem unlikely.

The final explanation that we will consider here involves motion that interferes with ^1H decoupling[24, 25]. Room temperature MAS spectra do not show evidence of any motion interfering with decoupling: the homogeneous linewidths of various carbons in the 9mer are similar to those measured for model compounds. If we postulate the presence of weak dipolar couplings between the $C_{=O}$ and surrounding protons, couplings which are averaged by MAS, then motional processes which interfere with the decoupling of these interactions would not be evident in MAS spectra. In static experiments, however, where these interactions are no longer averaged by MAS, motional processes with significant spectral density at the decoupling frequency would introduce additional homogeneous broadening that would cause the increased signal loss observed in our static echo experiments. We would expect such effects to show dependence upon both the temperature and the decoupling field strength; Fig. (2-10) shows the results of such experiments on the 9mer control sample. At room temperature, there is significant decoupling field dependence, evident in (A). The highest decoupling fields achievable are not sufficient to reduce the pattern to the ideal trans pattern expected, and as the decoupling field is reduced the distortion increases. At low temperature, where

Figure 2-10: ^{1}H Decoupling power dependence of static echo spectra obtained from $^{1}V(36)$-$^{2}G(37)$ 9mer (t=750μs difference spectra are displayed). (Note that the listed values for the ^{1}H decoupling power are based on calibration measurements made at room temperature; an increase on the order of 5-10 kHz may have occurred upon going to low temperature (see text).)

(A) At room temperature, decreasing the decoupling power leads to an increase in the size of the central peak and a decrease in the height of the left shoulder.

(B) At low temperature (T=-155 °C), varying the decoupling power over a wide range has little or no effect on the shape of the resulting dipolar-dephased powder pattern.

Decoupling Power Dependence of
Static-Echo Spectra

(A)

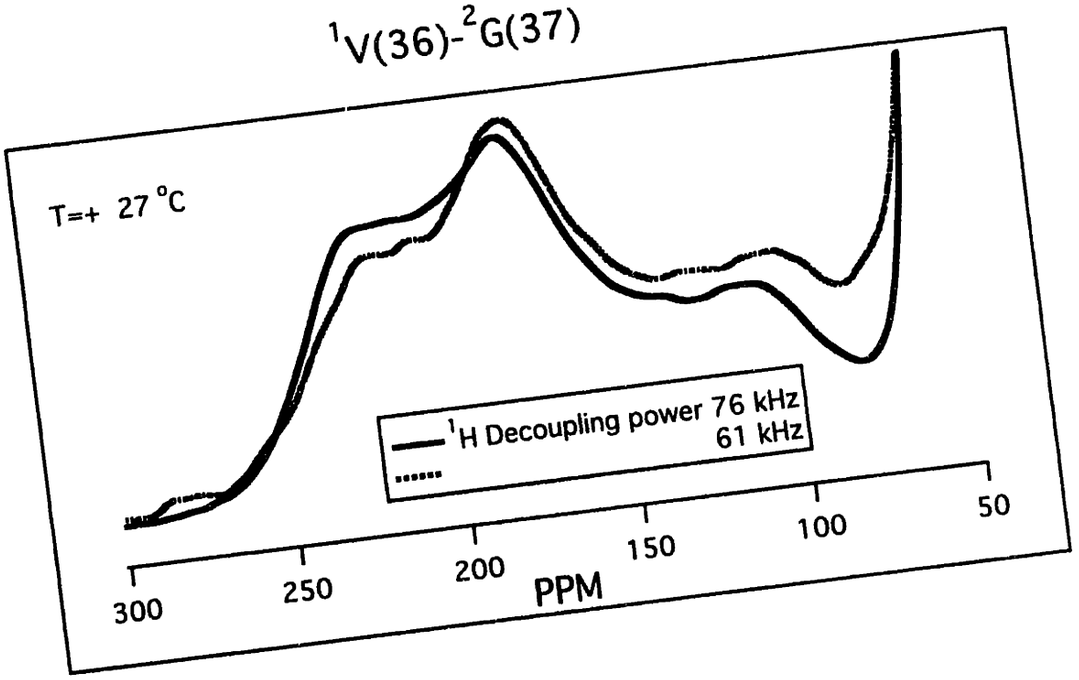

(B)

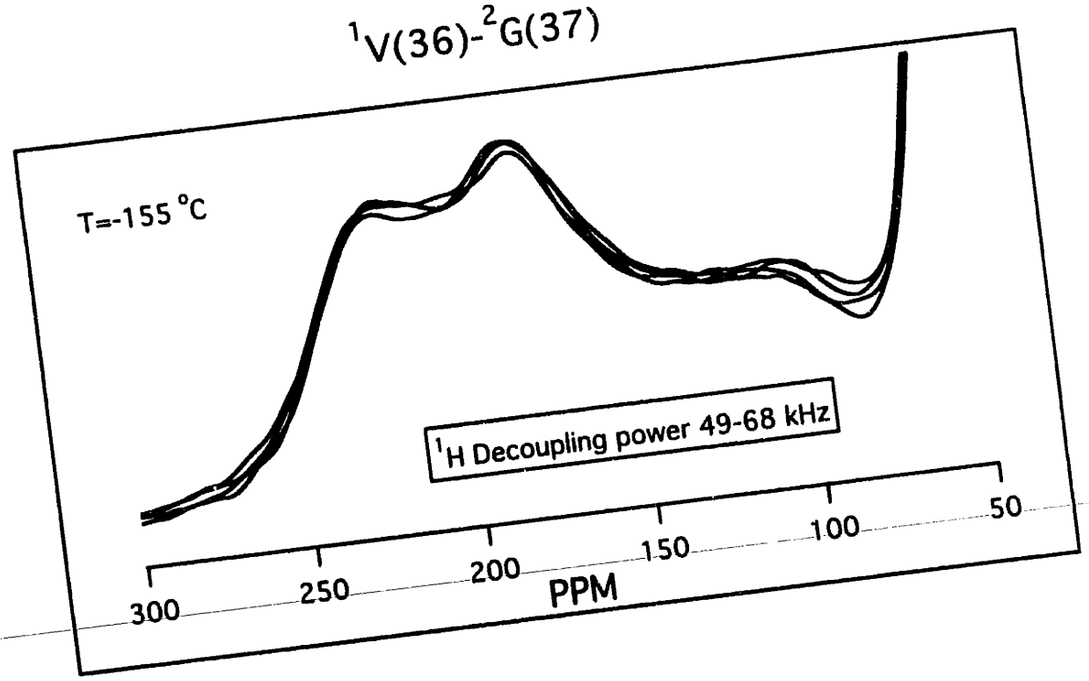

we hope that motional effects have been frozen out, there is little dependence upon the decoupling field strength.

Experimental: The experimental data was obtained on a 7.4 T magnet (79.9 MHz for ^{13}C), using a MAS probe w/ a 7mm Doty spinning assembly (the coil remained at the magic angle). Spinning gas was used to cool the sample to required temperature, but the rotor was placed into the probe such that it did not spin. The ^{1}H CW decoupling power was varied as indicated in the plots. Note that the indicated decoupling strengths are based on measurements made at room temperature. The efficiency of this probe (named the 'VT' probe) is known to increase slightly at low temperature, probably corresponding to an increase in 5-10 kHz in decoupling field above the value measured a room temperature (given the same power input). The listed decoupling values have not been adjusted for this effect. The ^{13}C 180° echo pulse length was approximately 10μs. The ^{13}C carrier frequency was placed near the center of the carbonyl powder pattern. t_d='0' spectra were obtained using a short (50μs) echo period, so that ringdown effects were minimized. A 16-step phase cycle (CYCLOPS and temperature inversion, coupled with an inversion of the phase of the 180° pulse) cycle was used, and 1000 - 5000 FID's were obtained for each spectrum. The time between acquisitions (rd) was set as short as 1 sec. Both samples were fully labeled (i.e. there was no dilution in natural abundance); the issue of intermolecular interactions was discussed in the previous section, and likely can be ignored.

2.5 n=2 RR experiments applied to (1-α2) labeled peptides can distinguish between *cis* and *trans* in model compounds, and confirm *trans* in 9mer.

The rotational resonance experiment has been discussed in detail in the previous chapter. It involves matching some multiple (n) of the spinning speed to the isotropic chemical shift difference between a pair of spins, the order of the resonance corresponding to the value of n. Viewed in the appropriate interaction frame, what occurs during this process is an interference between the MAS-induced modulation of the spatial part, and the chemical-shift induced modulation of the spin part of the flip-flop term in the dipolar Hamiltonian[26]. Either modulation separately is sufficient to attenuate the specified component of the dipolar interaction; occurring together, however, they interfere in a manner that blocks its averaging, and hence its effects are seen in the evolution of the spin system.

In systems with significant chemical shift anisotropy, the CSA component of the chemical shift interaction can be viewed (in the appropriate interaction frame - see next section) as modifying the modulations imposed on the spin part of the dipolar coupling by MAS[26]. The magnitude, and hence significance, of the modification depends upon the ratio of the spinning speed to the size of the chemical shift anisotropy. When the former term dominates (i.e. at high spinning speeds) the modification is small and can be neglected; when the latter dominates (i.e. at spinning speeds lower than or comparable to the size of the CSA) the modulation is significant and must be taken into account. One empirical measure of this effect is

the presence or absence of sidebands in the chemical shift spectrum near the appropriate spinning speed: when sidebands of significant size are present, the CSA modulation of the dipolar interaction must be taken into account.

Consider as a model system a pair of spins (I and S) with a chemical shift difference on the order of 110ppm, and where I has a sizable CSA (δ=50ppm and η=1.0) and S has none. This system is a limiting case of the standard ($C_{=O}$,C_α) spin pair used in many R^2 experiments, where the C_α CSA has been ignored, and this model will be considered at length in the next section. At the n=1 resonance, the spinning speed is significantly larger than the I spin CSA, and one finds that the dipolar evolution of the system has little dependence on the CSA parameters. At the n=2 resonance, however, one finds that there is significant dependence, both on the size of the I spin CSA and on its orientation relative to the $C_{=O}$-C_α dipolar coupling. The empirical result that one finds in these cases is that, given a set value for the size of the CSA, the rate of polarization exchange in longitudinal R^2 mixing experiments increases as the chemical shift along the axis defined by the dipolar orientation within the chemical shift PAS decreases. That is, if the dipolar vector points along σ_{11} (where chemical shift is a maximum), the rate of exchange is minimized, while if it points along σ_{33} (chemical shift minimum), the rate of exchange is maximized. Orientations in between these extremes follow the basic trend, that is, the relationship between shielding along the dipolar axis and rate of exchange is approximately monotonic (for this model, at least). An explanation for this behaviour is presented in the following section.

This result suggests that longitudinal exchange experiments at the n=2 RR on 1-α2 labeled compounds should be able to distinguish between *cis* and *trans* conformers, where we would expect more exchange for the *cis* conformation (dipole approximately along σ_{11}) than for *trans* (dipole along σ_{22}). Performing these experiments on the four compounds considered here leads to the results shown in Fig. (2-11). In each plot, the solid circles indicate the experimental data, the solid lines indicate trans simulations, and the dotted lines indicate cis simulations. A series of three simulations was necessary for each conformer (the set of three solid and dotted lines in each plot) to take into account the range of possible orientations of the C_α chemical shift tensor (unlike the static echo experiment, this experiment is somewhat sensitive to the orientation of this tensor). The results clearly agree with those from the static experiments: the *cis* and *trans* model compounds give the expected results, and both 9mer compounds give results consistent with a *trans*, not a *cis*, conformation.

Experimental: The model compound experiments (neither sample was diluted in natural abundance) were performed at 9.4 T (100MHz for ^{13}C), using home-built MAS probes with Doty 5mm high-speed spinning systems. The compounds were packed into the rotors with spacers on either (axial) side, so that the sample consisted of a central slice approximately 5mm thick. The ^{1}H and ^{13}C pulse lengths were 3.3μs and 4.4μs, respectively. The 9mer experiments (also using samples undiluted in natural abundance) were performed at 7.4 T (79.9kHz for ^{13}C), again with home-built 5mm MAS probes,

Figure 2-11: Comparison of experimental and simulated n=2 R^2 exchange curves for the indicated compounds. The simulation parameters for each system are described in the text. Each graph shows a set of three *trans* simulations (solid lines), where the $C_{=O}$-to-dipole orientation was set according to α=19°, and the $C_{=O}$-to-C_α orientation was varied among {(α,β,γ)=(0,0,0), (0,90,0), and (90,90,0)}. The three *cis* simulations (dashed lines) in each graph were obtained in a similar manner, setting the $C_{=O}$-to-dipole orientation according to α=65°. The top three compounds clearly exhibit exchange dynamics consistent with a *trans* conformation, the bottom compound with *cis*.

(1-α2) N=2 Rotational Resonance
Magnetization Exchange Experiments

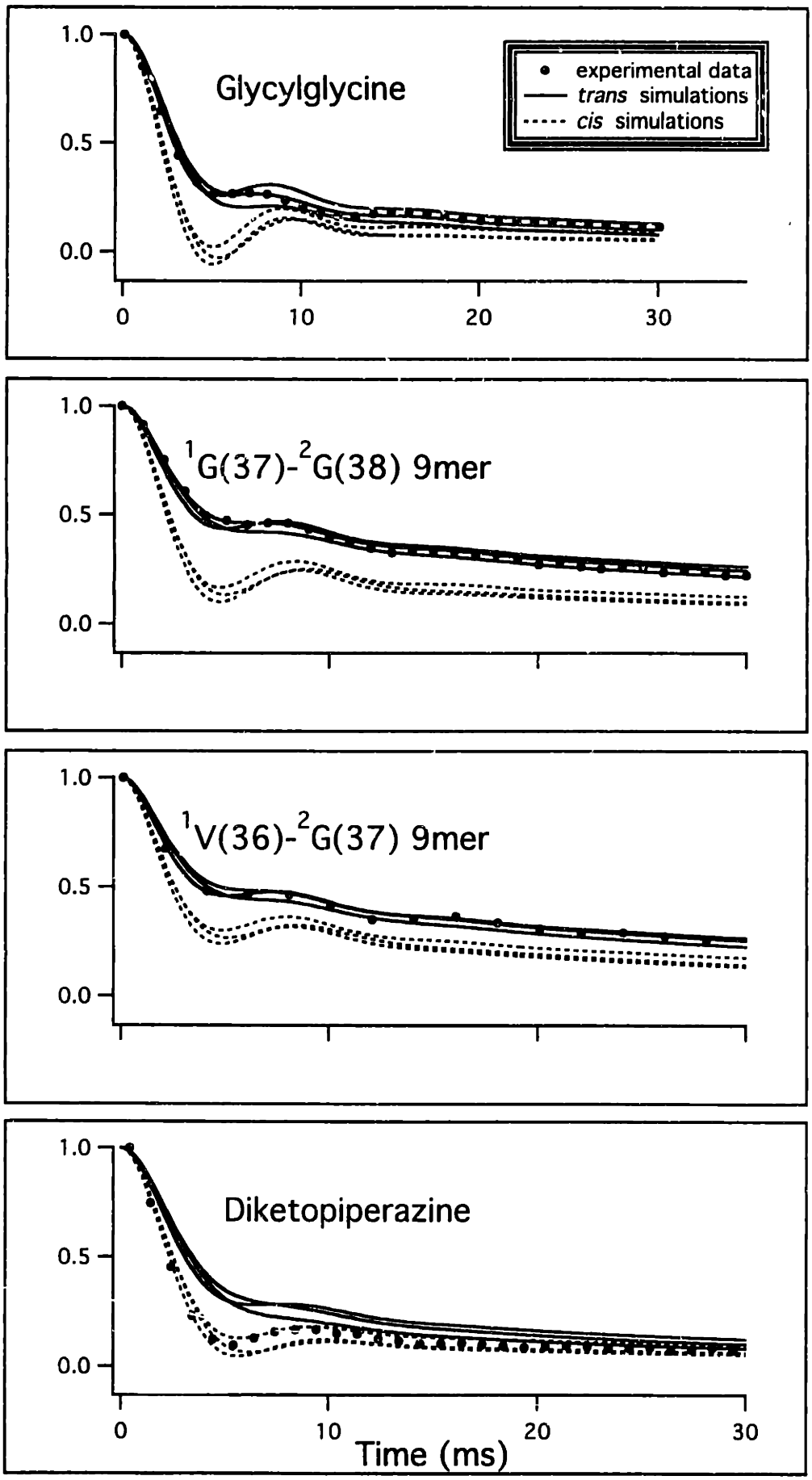

with the samples occupying the entire rotor. The ^{1}H and ^{13}C pulse lengths were 2.6μs and 4-5μs, respectively. The spinning speed in each experiment was set to the value determined by the n=2 RR relation (based on the chemical shift differences given in Table 2-2 below); fluctuations from this were on the order of ±2Hz.

Single π-pulse echo experiments were performed (away from RR) to determine the homogeneous contribution to the linewidth, as described in the previous chapter; the results, along with the calculated T_{zq}^{2} values, are summarized in Table 2-2 below. The residual linewidth (minus 20 Hz for magnet inhomogeneity) was assumed to be chemical shift dispersion, and was modeled as described in the previous chapter using either a gaussian or a lorentzian fit (listed in Table 2-2). The remaining parameters for the simulations were identical to those listed in Table (2-1), modified for the appropriate carbonyl parameters from Fig. (2-3) (and for the appropriate magnetic field strength, where necessary). The orientation of the $^{13}C_{\alpha}$ chemical shift, which has an observable effect on the simulations, was set to three extreme orientations (described by euler angles (0,0,0), (0,90,0), and (90,90,0)), corresponding to the set of three curves for each *cis* and *trans* simulation. The 3 curves approximately span the region over which the exchange curve varies as a function of the $^{13}C_{\alpha}$ chemical shift tensor orientation. Note that the ^{14}N interactions were not included in these simulations; they are averaged out by MAS. The simulations were performed by numerically integrating the equations of motion derived from the block-diagonalized Hamiltonian described by Levitt, et al[26], and involved a random sampling over 1000 crystallite orientations.

TABLE 2-2: Compilation of simulation parameters for n=2 R^2 experiments, *cis* vs. *trans* compounds.

Compound	Δ_{iso} (kHz)	Obs LW (Hz)	HomLW (Hz)	T_{zq}^2 (ms)	CSD (Hz)	Fit (G/L)
gg•HCl	12.74	115($C_{=O}$)	30	2.9	75	G
		130(C_α)	80		40	G
DKP	12.43	115($C_{=O}$)	45	1.9	60	G
		145(C_α)	125		10	G
^{1}V(36)-^{2}G(37)	10.33	140($C_{=O}$)	30	3.2	90	L
		215(C_α)	70		125	L
^{1}G(37)-^{2}G(38)	10.022	130($C_{=O}$)	35	3.35	75	L
		150(C_α)	60		70	L

Two corrections were made to the raw data. First, the natural abundance background signal, which is of appreciable magnitude in the 9mers given the inherent "dilution" due to the size of the molecule, was corrected for in the 9mer data sets by an arbitrary 5% subtraction [x $\Rightarrow$ (x-0.05)/0.95]. Second, the time axes for the raw data were adjusted by 0-400μs based on the inversion method used (0μs for G(37)-G(38), 100 for V(36)-G(37) and glycylglycine, and 400 for DKP (the data moved to the right)). These corrections are based on explicit simulations of the effects of the inversion sequence in each case (the need for this correction is discussed in chapter one).

2.6 Effects of CSA on spin dynamics at RR.

Explicit calculation of the effects that CSA has on the spin dynamics at RR begins with modifying equ (36) from chapter one to include terms representing the CSA interaction. Restating that equation:

$$H_1 = \Delta_{iso} J_Z^{(23)} + \omega_D(t) J_X^{(23)} \qquad (7),$$

we divide the dipolar term into two components according to:

$$\tilde{H}_1 = \Delta_{iso} J_Z^{(23)} + \sum_{m=-2,2} \omega_{(m)}^{IS} \left(J_+^{(23)} e^{im\omega_r t} \right) + \sum_{m=-2,2} \left(\omega_{(m)}^{IS} \right)^* \left(J_-^{(23)} e^{-im\omega_r t} \right) \qquad (8).$$

We insert terms representing the CSA interaction:

$$\tilde{H}_1 = \Delta_{iso} J_Z^{(23)} + \Delta_{CSA}(t) J_Z^{(23)} + \sum_{m=-2,2} \omega_{(m)}^{IS} \left(J_+^{(23)} e^{im\omega_r t} \right) + \sum_{m=-2,2} \left(\omega_{(m)}^{IS} \right)^* \left(J_-^{(23)} e^{-im\omega_r t} \right) \qquad (9),$$

where

$$\Delta_{CSA}(t) = \sum_{m=-2,2} \left(\omega_{(m)}^{I} - \omega_{(m)}^{S} \right) e^{im\omega_r t} \qquad (10).$$

Levitt, et. al.[26], have shown that we can recover the form of equ (8) by transferring to an interaction frame defined by the CSA term:

$$\tilde{H}_1 = UHU^{-1} \qquad (9),$$

where

$$U = \exp\left[-iJ_Z^{(23)} \left(\int_0^t \Delta_{CSA}(t') dt' \right) \right] \qquad (10).$$

This yields:

$$\tilde{H}_1 = \Delta_{iso} J_Z^{(23)} + \sum_{m=-2,2} \omega_{(m)}^{IS} \left(J_+^{(23)} e^{i(\phi(t) + m\omega_r t)} \right) + \sum_{m=-2,2} \left(\omega_{(m)}^{IS} \right)^* \left(J_-^{(23)} e^{-i(\phi(t) + m\omega_r t)} \right) \qquad (11),$$

where

$$\phi(t) = \int_0^t \Delta_{CSA}(t') dt' = \sum_{m=-2,2} \int_0^t \left(\omega_{(m)}^{I} - \omega_{(m)}^{S} \right) e^{im\omega_r t'} dt' \qquad (12).$$

We recover the form of (8) by making the substitution $\omega_D(t) \rightarrow \tilde{\omega}_D(t)$

with

$$\tilde{\omega}_D(t) = \sum_{m=-2,2} \tilde{\omega}^{IS}_{(m)} e^{im\omega_r t} \qquad (13),$$

and

$$\tilde{\omega}^{IS}_{(n)} = \sum_{m=-2,2} \omega^{IS}_{(m)} \Delta^{CSA}_{(n-m)} \qquad (14).$$

Calculation of the recoupled Hamiltonian can now proceed along the lines described in chapter one for the CSA-independent case, leading to a similar final result with the following changes: (i) the magnitude of the recoupled interaction for the n^{th} RR is given by $\tilde{\omega}^{IS}_{(n)}$ rather than $\omega^{IS}_{(n)}$; and (ii) resonance orders greater than n=2 are now possible. The extent to which the substitution in (i) modifies the dynamics, and the strength of n>2 RR effects, depends on the magnitude of the Fourier coefficients of the time-dependent CSA phase function:

$$e^{i\phi(t)} = \sum_{k=-\infty,\infty} \Delta^{CSA}_{(k)} e^{ik\omega_r t} \qquad (15).$$

When terms with $|k|>0$ have negligible magnitude, the sum in (14) yields the original dipolar coefficients, and CSA-induced effects are minimal. Because the expansion in equ (15) is similar to that derived for CSA-dependent chemical shift spectra of spinning solids[9], where the Fourier coefficients correspond to the intensities of the various sidebands, the condition that the $|k|>0$ terms have negligible magnitude implies that there is little sideband intensity in the chemical shift spectrum of the sample at the appropriate spinning frequency. For n=1 RR measurements between $C_{=O}$ and CH_n nuclei in peptides, where the necessary spinning speed is determined by a chemical shift difference on the order of 100ppm and is much larger than the size of either CSA tensor ($\delta \approx 20$-60ppm), this is generally the case. For n=2 and higher, however, where the appropriate spinning

speed is equivalent to approximately 50ppm or less, there is easily observable sideband intensity in the spectrum, and CSA-induced effects can be significant.

Here we examine the longitudinal exchange dynamics at n=2 RR of a model 2-spin system, where the dipolar coupling has been set at 0.5kHz (≈2.5Å ^{13}C-^{13}C distance), the chemical shift difference to 10kHz, the parameters for one CSA have been set to $\delta=\pm 6.0$kHz, ($\eta=0$ or 1), and for the other CSA, to zero (the zero-quantum relaxation rate was set at 0.4kHz). These chemical shift parameters (with $\eta=1$) are roughly what one might expect for a $C_{=O}/CH_n$ spin pair at ≈8T, where the (usually) small CH_n CSA tensor has been dropped. Because the one significant CSA tensor has a magnitude comparable to the spinning speed, there will be sideband intensity in the chemical shift spectrum, and we expect the dynamics to show some dependence of the relative orientation of the dipolar and CSA tensors. This is demonstrated in Fig. (2-12), with $\eta=0$. Because both tensors (dipolar and CSA) are axially symmetric in this case, we can characterize their relative orientation with a single parameter, the angle between their symmetry axes. For the $\delta=+6$kHz case (left), we observe substantially faster exchange when the tensors are aligned (0°) than when their symmetry axes are perpendicular (90°), while for the $\delta=-6$kHz case (right) we observe the opposite (the thicker line in both plots shows the result with no CSA for comparison). In both cases, we observe increasing levels of exchange as the CSA shielding along the dipolar axis increases. That this holds for intermediate orientations has been verified by further simulations (data not shown). Furthermore, comparison of the two plots indicates that the

Figure 2-12: "Idealized" static spectra (top row) and n=2 RR longitudinal magnetization exchange curves (bottom row) for a two spin system with a chemical shift difference of 10kHz, a dipolar coupling constant of 0.5kHz, and a single significant CSA tensor with η=0 and δ=+6kHz (left column) or -6kHz (right). Exchange curves are given as a function of dipole/CSA tensor orientation; because both interactions are axially symmetric, their relative orientation can be described solely by the angle between the symmetry axis for each tensor. On the left (δ=+6kHz), the exchange rate is maximized when the tensors are aligned (0°) and decreases as the angle between them increases (up to 90°). On the right, the opposite trend is observed. In both cases, the exchange rate increases as the CSA-determined chemical shift along the axis defined by the dipolar vector decreases. This is sketched in the top row. Note that the trend also holds to some extent for comparisons between the plots. Thick lines in both exchange curve plots show the results absent CSA.

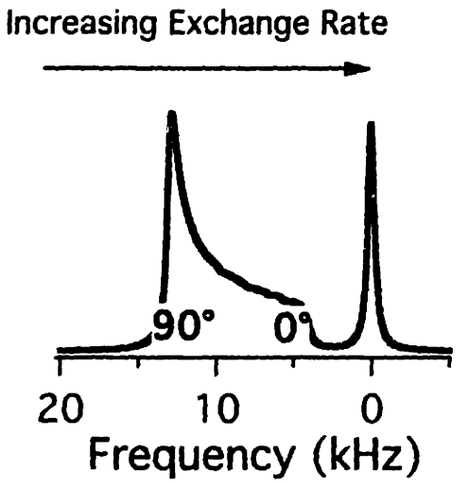
Increasing Exchange Rate
90°
0°
20
10
0
Frequency (kHz)

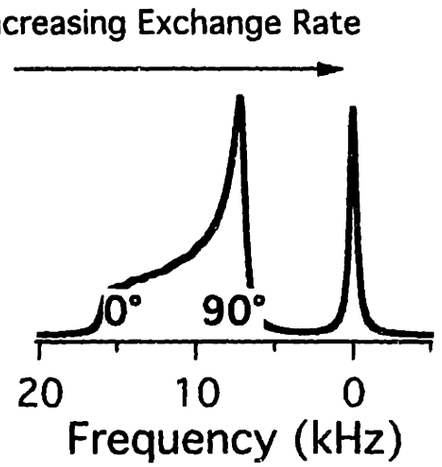
Increasing Exchange Rate
0°
90°
20
10
0
Frequency (kHz)

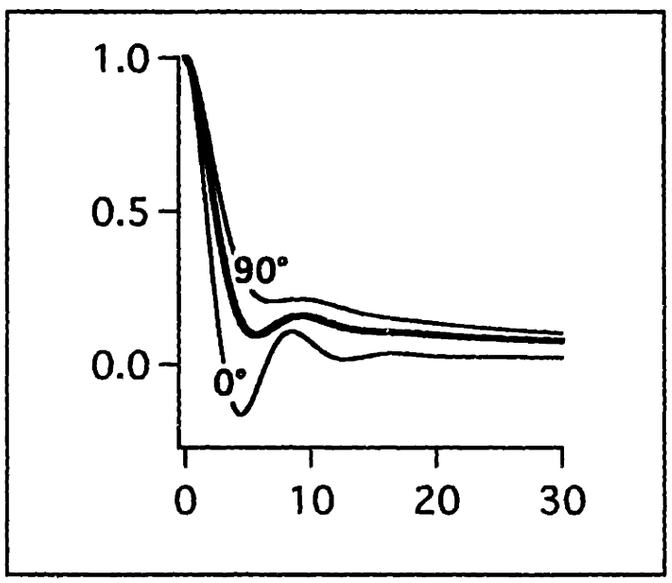
1.0
0.5
0.0
90°
0°
0
10
20
30

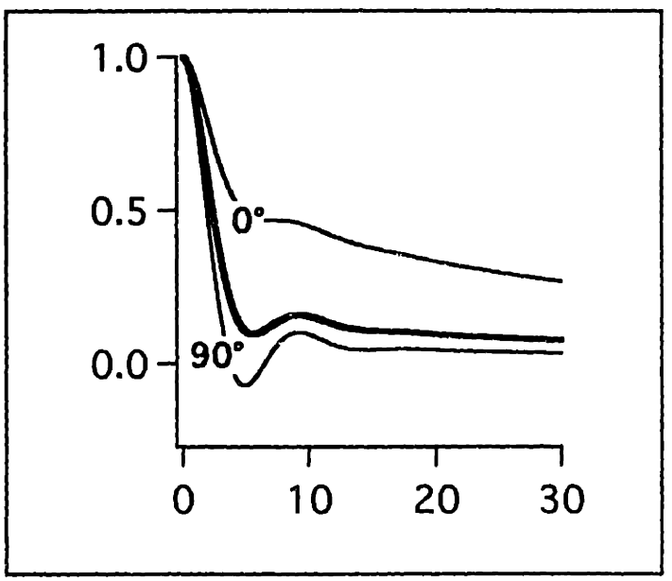
1.0
0.5
0.0
0°
90°
0
10
20
30

trend within each plot also holds (at least approximately) between the two: the 0° edge of the δ=+6kHz system is more shielded, and the corresponding dipole/CSA orientation shows more exchange, than the 90° edge of the δ=-6kHz system; and conversely the 0° edge of the δ=-6kHz system is less shielded and shows less exchange than the 90° edge of the δ=+6kHz system.

Fig. (2-13) shows the results for η=1. Again, when the dipolar vector points along the least-shielded axis of the CSA tensor (X), the slowest rate of exchange is observed, and when it points along the most shielded axis (Z), the fastest rate is observed. At the middle feature (Y), an intermediate exchange rate is observed. That the relationship is approximately monotonic has been demonstrated by simulations at a series of intermediate orientations (data not shown). (Note that switching the sign of the chemical shift should reverse the trend in both cases.)

Note several features of these effects. First, we expect these trends to hold independent of the magnitude of the dipolar interaction, assuming that relaxation effects do not wash out the differences (and to reverse given a chemical shift difference of opposite sign, i.e. switched peak positions in the 2-spin spectrum). Second, inclusion of the CH_n tensor, whose orientation is often poorly known, will introduce some uncertainty in real systems. This is clear in the plots for the previous section where these effects have been included. Third, from a more spin-physics point of view, CSA effects in many cases can increase the overall rate and transfer efficiency in longitudinal exchange experiments at RR. For simulations in which zero-quantum relaxation is neglected, appropriate alignment of the

Figure 2-13: "Idealized" static spectrum (top) and n=2 RR longitudinal magnetization exchange curves (bottom) for a two spin system with a chemical shift difference of 10kHz, a dipolar coupling constant of 0.5kHz, and a single significant CSA tensor with δ=+6kHz and η=1. Exchange curves are given as a function of dipole/CSA tensor orientation, here identified according to which distinct axis of the CSA tensor (X, Y, or Z) the dipolar vector points along. Again, the exchange rate increases as the CSA-determined chemical shift along the axis defined by the dipolar vector decreases (sketched in top figure). The single thick line in the exchange curve plots illustrates the result absent CSA. Note that the presence of the CSA interaction can significantly increase the exchange rate, given the appropriate orientation relative to the dipolar vector.

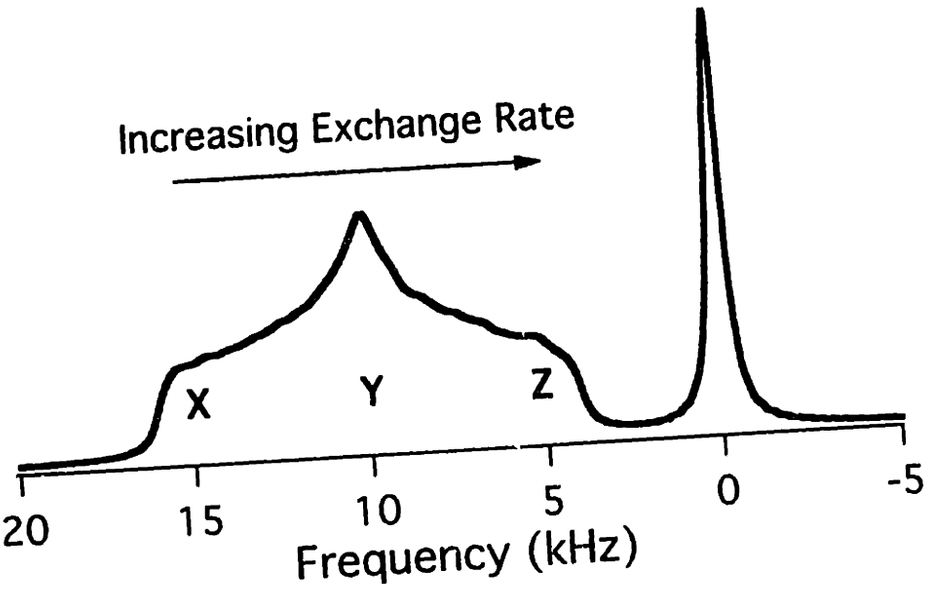
Increasing Exchange Rate
X
Y
Z
20
15
10
5
0
-5
Frequency (kHz)

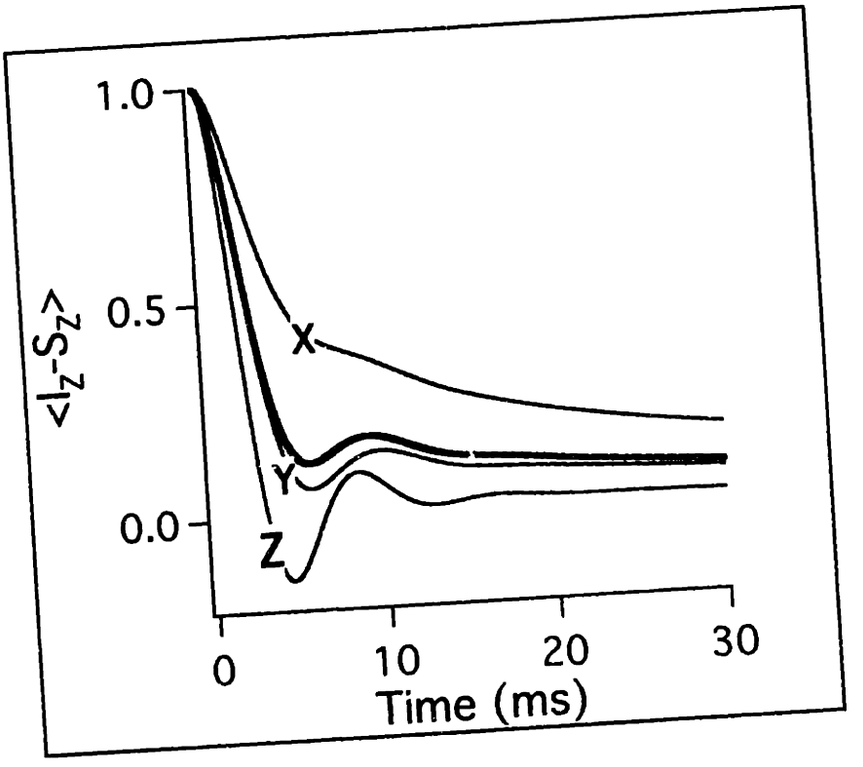
1.0
0.5
0.0
$\langle I_z - S_z \rangle$
X
Y
Z
0
10
20
30
Time (ms)

dipolar and CSA tensors can lead to maximum polarization transfer efficiencies of greater than 90% (data not shown). As we detail below, the additional efficiency arises from constructive addition of the recoupled m=1 and m=2 components of the dipolar tensor, leading to effective recoupling over a much broader distribution of crystallite orientations. Finding some manipulation of the spin system that mimics this effect might provide a pathway for increasing the speed and efficiency with which polarization transfer in spinning solids occurs.

Although calculation of CSA-induced effects directly from (14) will generally be more time-consuming than numerical simulation, such an approach is useful in attempting to explain the origin of the just-described effect. We start with the equation (from (14) for the recoupled interaction at n=2 RR:

$$\tilde{\omega}^{IS}_{(2)} = \omega^{IS}_{(2)}\Delta_{(0)} + \omega^{IS}_{(1)}\Delta_{(1)} + \omega^{IS}_{(-1)}\Delta_{(3)} + \omega^{IS}_{(-2)}\Delta_{(4)} \qquad (16).$$

Because the dipolar tensor has no m=0 component (ω^{IS}_0), there is a clear break in equ (16) between the first two terms and the last two. At spinning speeds which are not much smaller than the size of the CSA's, we expect the intensity of the centerband and first order sidebands to be much larger than that of the 3rd and 4th order sidebands. Dropping the last two terms is a valid approximation under these conditions, yielding:

$$\tilde{\omega}^{IS}_{(2)} = \omega^{IS}_{(2)}\Delta^{I}_{(0)} + \omega^{IS}_{(1)}\Delta^{I}_{(1)} \qquad (17),$$

The explicit form of the two dipolar components in this equation is:

$$\omega^{IS}_{(1)} = b_{IS}\frac{\sqrt{2}}{4}\sin(2\beta_D)e^{im\gamma_{II}} = b_{IS}c_1(\beta_D)e^{im\gamma_{II}} \qquad (18)$$

and

$$\omega_{(2)}^{IS} = b_{IS}\frac{1}{4}\sin^2(\beta_D)e^{im\gamma_D} = b_{IS}c_2(\beta_D)e^{im\gamma_D} \qquad (19),$$

where β_D and γ_D refer to the euler angles describing the orientation of the dipolar tensor relative to the rotor-fixed frame, as defined in chapter one, and c_1 and c_2 are defined as shown.

Determination of the CSA components is more difficult. Herzfeld and Berger[9] provide a general form for the intensity of the n^{th} sideband using Bessel functions[27]:

$$I_n \propto e^{in\gamma_{CSA}} \sum_{k=-\infty,\infty} J_{(-n-2k)}\left(-\frac{\delta c_1(\beta_{CSA})}{\omega_r}\right) J_{(k)}\left(-\frac{\delta c_2(\beta_{CSA})}{\omega_r}\right) \qquad (20)$$

(we have assumed η=0; β_{CSA} and γ_{CSA} refer to the CSA orientation in the rotor-fixed frame) which corresponds to $\Delta_{(n)}$ when only one CSA interaction is present (the proportionality can be made an equality by dividing through by a sum over the absolute value of all sideband intensities). The form for the centerband follows directly:

$$I_{(0)} = \Delta_{(0)} \propto J_{(0)}\left(-\frac{\delta c_1(\beta_{CSA})}{\omega_r}\right) J_{(0)}\left(-\frac{\delta c_2(\beta_{CSA})}{\omega_r}\right) \qquad (21).$$

The intensity of the 1st-order sideband does not simplify so easily, and here we truncate the sum in (20) at a certain point, yielding:

$$I_1 = \Delta_{(1)} \propto e^{i\gamma_D}\left(-J_1J_0 - J_1J_1 - J_3J_1 + J_3J_2 + O(c_n{}^5/4000)\right) \qquad (22)$$

where the first Bessel function in each pair is a function of $-\delta c_1(\beta_{CSA})/\omega_r$, and the second, of $-\delta c_2(\beta_{CSA})/\omega_r$ (the dropped terms have values that are 0.1% or less than the 1st term for $\delta/\omega_r \leq 1.5$).

These functions (at γ=0, for reasons explained below) are plotted in Fig. (2-14). The upper right plot shows the distribution of $\omega_{(2)}^{IS}$ as a function of ß. Absent CSA, crystallites whose dipolar vector makes an angle ß with respect to the rotor axis will have a recoupled interaction at n=2 RR given by the corresponding value in this plot.

Figure 2-14: Variables (as a function of ß, the angle between the MAS spinning axis and the dipolar/CSA symmetry axes) that contribute to the magnitude of the recoupled dipolar interaction across the powder sample for n=2 RR experiments in systems identical to those described for Fig. (3-12) ($\delta<0$ results indicated by dotted line). Absent CSA, the magnitude of the recoupled interaction in various crystallites is solely determined by the magnitude of the $\omega_{(2)}$ component of the modulated dipolar interaction, plotted on the upper right. This distribution of magnitudes as a function of dipolar (and hence crystallite) orientation leads to damped exchange curves of the type shown in the previous two figures (thick lines - i.e. absent CSA). When CSA is present, the $\omega_{(2)}$ (top right) and $\omega_{(1)}$ (top left) components of the dipolar interaction must be multiplied by the $\Delta_{(0)}$ (2^{nd} row, right) and $\Delta_{(1)}$ (left) components of the CSA interaction, respectively. If we assume the dipolar and CSA ($\eta=0$) tensors are aligned, then their ß values in each crystal are identical and we can directly multiply the top row with the second row to obtain the 3^{rd} row (see text). The observed powder distribution of the recoupled interaction magnitude is then given by the sum of these plots, shown on the bottom of the figure. If $\delta>0$ (solid lines in left column and bottom), then the effect is to broaden the distribution (as compared to result absent CSA, i.e. upper left) and faster exchange is observed. If $\delta<0$, the distribution narrows and slower exchange is observed. Both of these effects depend on the "synchronicity" of the oscillations in the $\omega_{(1)}$ and $\Delta_{(1)}$ plots. When the CSA and dipolar tensors do not align, this is spoiled, and the large deviations from the CSA-independent evolution decrease (see text).

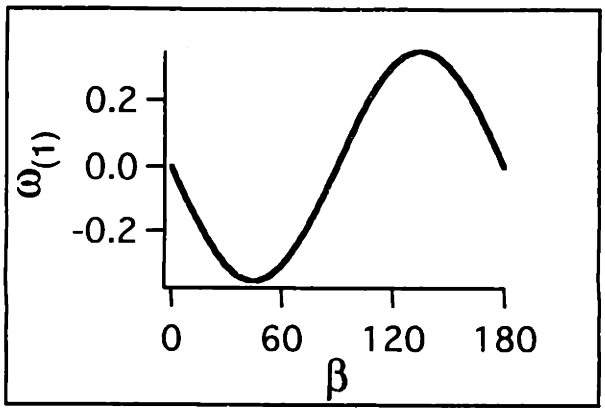
0.2
0.0
-0.2
$\omega_{(1)}$
0
60
120
180
β

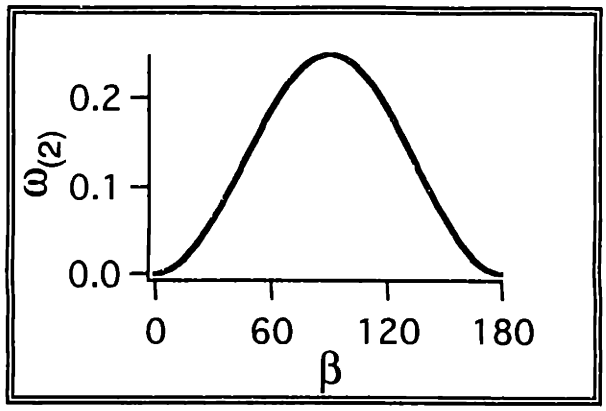
0.2
0.1
0.0
$\omega_{(2)}$
0
60
120
180
β

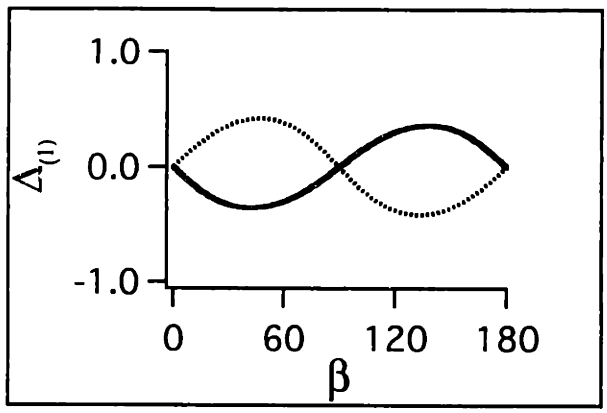
1.0
0.0
-1.0
$\Delta_{(1)}$
0
60
120
180
β

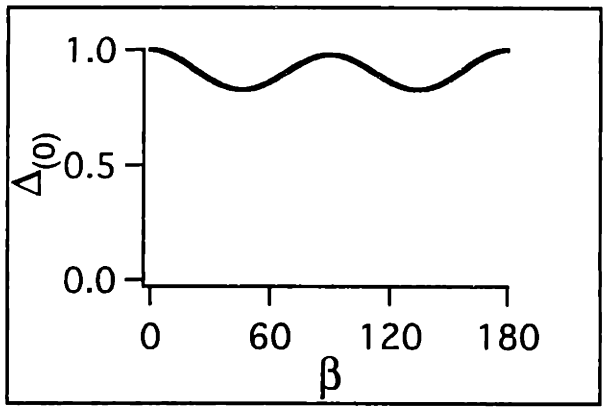
1.0
0.5
0.0
$\Delta_{(0)}$
0
60
120
180
β

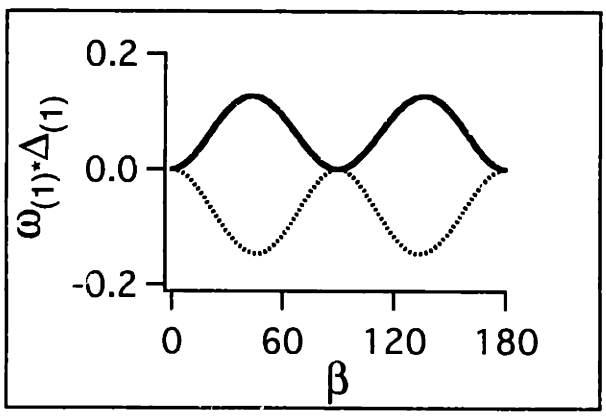
0.2
0.0
-0.2
$\omega_{(1)}*\Delta_{(1)}$
0
60
120
180
β

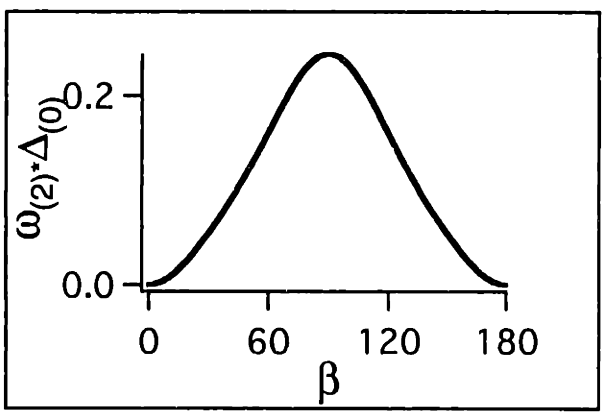
0.2
0.0
$\omega_{(2)}*\Delta_{(0)}$
0
60
120
180
β

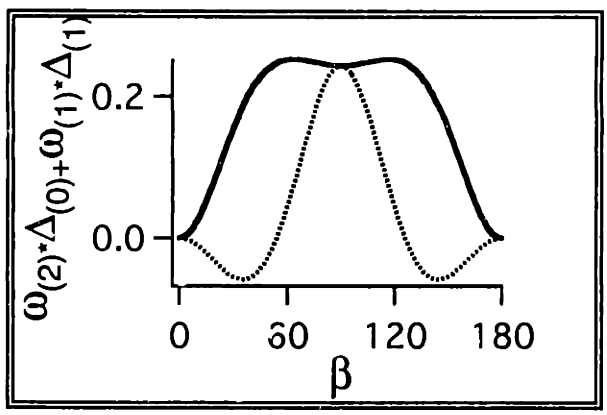
0.2
0.0
$\omega_{(2)}*\Delta_{(0)}+\omega_{(1)}*\Delta_{(1)}$
0
60
120
180
β

This distribution as a function of dipolar orientation is responsible for the shape of the time-dependent evolution. If CSA is present, then calculation of the recoupled interaction requires calculation of the terms in equ (17). Let us first consider the case in which the dipolar and CSA tensors are aligned, and hence their orientation in the rotor-fixed frame can be described by a single angle ß. The second row in Fig. (2-14) shows the +1 sideband (left) and centerband (right) intensities as a function of ß (the dotted line in the +1 sideband plot shows the result for a negative value of δ). Because both dipolar and CSA tensors have the same ß, we can calculate each of the products in (17) simply by multiplying the appropriate two plots on the left side ($\omega^{IS}_{(1)} * \Delta_{(1)}$) and the right side ($\omega^{IS}_{(2)} * \Delta_{(0)}$) to obtain the ß-dependent functions show below (third row; again dotted line in left plot shows results for negative δ). Adding these two curves together results in the final plot at the bottom, which shows the distribution of recoupled interaction strengths $\tilde{\omega}^{IS}_{(2)}$ as a function of ß once the CSA effect has been considered, for the case when the dipolar and CSA tensors are aligned. For positive δ, the distribution is much broader than the CSA-independent distribution (upper right plot in figure), and we expect faster (and more efficient transfer) - and this is what we observe for the 0° simulation with δ=+6kHz in Fig. (2-12, left). Conversely, the distribution is much narrower when δ is negative, leading to the much lower rate (and efficiency) of transfer in the 0° simulation for δ=-6kHz.

That the dynamics in this system are only a function of ß, and not of γ (and hence can be calculated for γ=0 where all 4 functions are purely real) is determined as follows. A rotation of the dipolar and

CSA tensors about the z-axis by an angle γ induces an identical change in the phase of each term in equ (17), according to the γ-dependencies listed in equs (18,19,21,22). This overall phase change simply changes the orientation of the vector representing the recoupled interaction in the fictitious spin-1/2 subspace, without changing its magnitude. Hence longitudinal exchange dynamics, as observed through the evolution of difference polarization, are unchanged. Because of this property, we can eliminate the γ part of the powder average. This holds true even in systems in which the dipolar and CSA tensors are not aligned. (There are implications for multiple-quantum filtering and other experiments, which are discussed in more detail in chapter three.)

Calculation of the recoupled interaction including CSA effects using this framework is not as straightforward by this method when the CSA and dipolar tensors are not aligned. Now we must powder average over two orientations, dipolar and CSA, in a manner that takes account of their fixed relative orientation (characterized by an angle β_D; we are still considering only η=0 CSA tensors). One way to perform this average is in a two-step process. First, consider a specific dipolar orientation characterized by the angle β (γ dependence can be ignored for the reasons given above). Associated with this dipolar orientation are a range of CSA orientations, each rotated from it by β_D in different directions, forming a cone with the dipolar vector at the center. If we average the recoupled interaction over this cone, and calculate that average as a function of dipolar orientation, we will recover the equivalent of the bottom plot in

Fig (2-14). Explicitly stated, this average is as follows:

$$\tilde{\omega}_{(2)}^{IS} = \omega_{(2)}^{IS}\Delta_{(0)}^{I} + \omega_{(1)}^{IS}\Delta_{(1)}^{I} = \left(\omega_{(2)}^{IS}\int_0^{2\pi}\Delta_{(0)}^{I}(\beta_{CSA})d\chi\right) + \left(\omega_{(1)}^{IS}\int_0^{2\pi}\Delta_{(1)}^{I}(\beta_{CSA})e^{i\gamma_{CSA}}d\chi\right) \qquad (23),$$

where we have defined the variable χ as the rotation of the CSA vector about the cone, and we must calculate the dependence of β_{CSA} and γ_{CSA} on this variable. The result is as follows:

$$\beta_{CSA} = \cos^{-1}(\cos\beta\cos\beta_D - \sin\beta\cos\chi\sin\beta_D) \qquad (24),$$

and

$$\gamma = \tan^{-1}\left(\frac{\sin\chi\sin\beta_D}{\cos\beta\cos\chi\sin\beta_D + \sin\beta\cos\beta_D}\right) \qquad (25),$$

where β_D is the angle between the dipolar and CSA tensors (fixed), and β describes the dipolar orientation (powder averaged).

Calculation of the resulting integration in (23) is difficult, but we can characterize the effects of the result. The large increase or decrease in the amount of exchange seen when the CSA and dipolar tensors are aligned depends on the synchronicity between the ß-dependent oscillations of the m=1 dipolar ($\omega_{(1)}^{IS}$) and 1st-order sideband terms ($\Delta_{(1)}$). Because the product of these two terms ($\omega_{(1)}^{IS} * \Delta_{(1)}$) has significant magnitude and constant phase relative to the m=2 dipolar/centerband term ($\omega_{(2)}^{IS} * \Delta_{(0)}$) independent of ß, its effects across the powder distribution add up to a large observable effect. When the dipolar and CSA tensors are not aligned and the averaging described by equ (23) is necessary, the phase of the m=1 dipolar/+1 sideband term ($\omega_{(1)}^{IS} * \Delta_{(1)}$) is no longer constant relative to the other term ($\omega_{(2)}^{IS} * \Delta_{(0)}$) after averaging. The result is that, as the angle between the CSA and dipolar tensors increases, the effects of the m=1 dipolar/+1 sideband term ($\omega_{(1)}^{IS} * \Delta_{(1)}$) begin to cancel out over the CSA-averaged cone and we begin to recover the CSA-

independent result. This is clear in both RR plots in Fig (2-12). In one case we start with a significant increase in exchange due to the CSA when the tensors are aligned, and see reduced exchange as the relative angle between the tensors increases. In the second case we initially have reduced exchange, and see increases towards the CSA-independent result as the angle increases. This reasoning extends to the $\eta=1$ case when one considers that alignment on the dipole along the Z- or X- axes of the CSA (characterized by a specific set of euler angles) is interchangeable by reversing the sign of δ.

2.7 References.

1. Schulz, G.E., R.H. Schirmer. *Principles of Protein Structure* (Springer-Verlag, Berlin, 1978).
2. Voet, D., J.G. Voet. *Biochemistry* (John Wiley and Sons, New York, 1990).
3. Stewart, D.E., A. Sarkar, J.E. Wampler. *J. Mol. Biol.* **214**, 253-260 (1990).
4. Spencer, R.G.S., K.H. Halverson, M. Auger, A. McDermott, R.G. Griffin, P.T. Lansbury, Jr. *Biochemistry* **30**, 10382 (1991).
5. Halverson, K.J., P.E. Fraser, D.A. Kirschner, P.T. Lansbury, Jr. *Biochemistry* **29**, 2639 (1990).
6. Lansbury, P.T.J., P.R. Costa, J.M. Griffiths, E.J. Simon, M. Auger, K.J. Halverson, D.A. Kocisko, Z.S. Hendsch, T.T. Ashburn, R.G.S. Spencer, B. Tidor, R.G. Griffin. *Nature Structural Biology* **2**, 990-998 (1995).
7. Mehring, M. *Principles of High Resolution NMR in Solids* (Springer-Verlag, Berlin, 1983).
8. Haeberlen, U. *High Resolution NMR in Solids* (Academic Press, New York, 1976).
9. Herzfeld, J., A.E. Berger. *J. Chem. Phys.* **73**, 6021-6030 (1980).
10. Herzfeld, J. .
11. Ando, S., T. Yamanobe, I. Ando, A. Shoji, T. Ozaki, R. Tabeta, H. Saito. *J. Amer. Chem. Soc.* **107**, 7648-7652 (1985).
12. Asakawa, N., S. Kuroki, H. Kurosu, I. Ando, A. Shoji, T. Ozaki. *J. Amer. Chem. Soc.* **114**, 3261-3265 (1992).

13. Ando, S., I. Ando, A. Shoji, T, Ozaki. *J. Amer. Chem. Soc.* **110**, 3380-3386 (1988).

14. Saito, H. *Magn. Res. Chem.* **24**, 835-852 (1986).

15. de Dios, A.C., J.G. Pearson, E. Oldfield. *Science* **260**, 1491-1496 (1993).

16. Stark, R.E., L.W. Jelinski, D.J. Ruben, D.A. Torchia, R.G. Griffin. *J. Magn. Res.* **55**, 266-273 (1983).

17. Oas, T.G., C.J. Hartzell, T.J. McMahon, G.P. Drobny, F.W. Dahlquist. *J. Amer. Chem. Soc.* **109**, 5956-5962 (1987).

18. Stoll, M.E., A.J. Vega, R.W. Vaughn. *J. Chem. Phys.* **65**, 4093 (1976).

19. Hester, R.K., J.L. Ackerman, B.L. Neff, J.S. Waugh. *Phys. Rev. Lett.* **36**, 1081 (1976).

20. Munowitz, M., T.-H. Huang, R.G. Griffin. *J. Chem. Phys.* **86**, 4362-4368 (1987).

21. Haberkorn, R.A., R.E. Stark, H. van Willigen, R.G. Griffin. *J. Amer. Chem. Soc.* **103**, 2534-2539 (1981).

22. Stoll, M.E., R.W. Vaughn, R.B. Saillant, T. Cole. *J. Chem. Phys.* **61**, 2896-2899 (1974).

23. Stejskal, E.O., J. Schaefer. *J. Magn. Res.* **18**, 560-563 (1975).

24. Long, J.R., B.Q. Sun, A. Bowen, R.G. Griffin. *J. Amer. Chem. Soc.* **116**, 11950-11956 (1994).

25. Maus, D.C., V. Copie, B.Q. Sun, J.M. Griffiths, R.G. Griffin, S. Luo, R.R. Schrock, A.H. Liu, S.W. Seidel, W.M. Davis, A. Grohmann. *J. Amer. Chem. Soc.* **118**, 5665-5671 (1996).

26. Levitt, M.H., D.P. Raleigh, F. Creuzet, R.G. Griffin. *J. Chem. Phys.* **92**, 6347-6364 (1990).

27. Arfken, G. *Mathematical Methods for Physicists* (Academic Press, Inc., San Diego, 1985).

Chapter 3

Modification of MAS-Induced Rotational Resonances by Application of a Weak RF Field: RR Tickling, Ramped 2Q-HORROR, and Dipolar Pulse Sequences.

3.1 Introduction.

Accurate distance measurement in homonuclear two-spin systems requires application of experimental techniques which induce observable dipolar-driven spin-dynamics that (i) are a strong function of the dipolar coupling constant, and (ii) do not have a strong dependence on other, hard to quantify parameters. Using the rotational resonance technique as an example, the time-course of longitudinal magnetization exchange at RR clearly shows the strong dependence on the magnitude of the dipolar coupling constant (see Chapter One) required by (i)[1]. However, relevant to (ii), the dependence of the evolution on hard-to quantify 2Q-relaxation and chemical shift difference distribution parameters limits its accuracy, and hence its effectiveness in determining biomolecular structure, except n cases in which these parameters either can be determined accurately, or where the dependence on them is minimized[2].

A series of homonuclear dipolar recoupling techniques have been proposed since the introduction of RR which induce dipolar-driven dynamics that do not have a significant dependence on chemical shift over some useful range ("broadband" recoupling techniques)[3]. In general,

however, the dynamics under these sequences are still expected to show dependence on the relaxation rate of the relevant 2-spin coherence created during mixing. Furthermore, because these techniques rely on vigorous, rotor-synchronized, rf-driven manipulations of the low-γ spin polarization to induce recoupling independent of chemical shift, the dynamics will additionally be dependent on rf imperfections including rf power instability, rf inhomogeneity, and on signal loss due to reduced ^{1}H decoupling efficiency upon simultaneous application of low-γ and ^{1}H rf. This latter effect has been of particular importance, because signal loss during mixing limits how long the dipolar recoupling sequence can effectively be applied, in some cases to the point where quantifiable dipolar evolution between nuclei separated by structurally interesting distances (e.g. >3Å) does not occur. And even when such evolution is observable, the need to factor out these "non-ideal" effects to uncover the coupling-dependent dynamics can introduce uncertainties which reduce the accuracy of the overall measurement.

In this chapter we describe a class of homonuclear dipolar recoupling techniques that are derived from the rotational resonance effect. These techniques involve the application of a relatively weak, CW rf field to the homonuclear spin system to modify the magnitude of the effective field (vector sum of rf field and chemical shift offset) of each spin. When the magnitude of the applied rf is selected such that the magnitude of the resulting effective fields satisfy a resonance condition (derived part A of Section Two, i.e. 3.2A), a recoupling effect very similar to rotational resonance occurs. Exploited appropriately (for instance, in the framework of the equivalent of a longitudinal mixing experiment - see 3.2C), the effect can be used to induce RR-analogous dynamics, with similar strong

dependence on the magnitude of the coupling, 2Q-relaxation, and effective field inhomogeneity (the latter including contributions from both chemical shift and rf inhomogeneity); and, in most cases, without significant signal loss during mixing due to the problems that have plagued other recoupling techniques. When the rf magnitude is much smaller than the chemical shift offsets, the experiment most closely approaches the standard RR experiment and we term the modified technique "rotational resonance tickling" (RRT); when the applied rf magnitude dominates the chemical shifts the experiment approaches the limit of the ideal "2Q-HORROR" experiment proposed by Nielsen and co-workers[4, 5]. The utility of these experiments primarily derives from the control over matching of the resonance condition on short (μsec) timescales afforded by the rf component of the effective fields. As described in Section 3.3A and demonstrated in 3.3B/C, ramping the rf magnitude so that the system passes completely through the resonance condition eliminates the dependence on the chemical shift difference distribution (and analogous rf-inhomogeneity dependence), and furthermore reduces the dependence of the dynamics on 2Q-relaxation, while maintaining a strong dependence on the magnitude of the dipolar coupling constant. As we illustrate, this technique provides improved accuracy in distance determination experiments, where applicable. And in cases where the magnitudes of the coupling constants dominate relaxation rates, we show that nearly adiabatic polarization transfer is possible.

In the final section (3.4) of this chapter, the phase-dependence of the recoupled dipolar interaction is considered. This phase dependence is a common feature of MAS-resonant recoupling techniques including RR and the experiments described here, and the heteronuclear CP[6] and rotary

resonance[7] techniques. Because evolution of two-spin sum or difference polarization about the recoupled dipolar interaction in these experiments proceeds in a manner identical to the evolution of single-spin polarization about an rf field when viewed in the appropriate fictitious spin-1/2 interaction frame (see Chapter One), control over the phase of the recoupled dipolar interaction allows implementation of rf-like dipolar pulse sequences (within the framework of any of these techniques) that may be useful in inducing a variety of different dipolar-driven effects. We describe two different methods for controlling dipolar phase, and illustrate their application separately in (i) inducing rotational resonance echos; and (ii) overcoming rf-inhomogeneity in 2Q-HORROR.

3.2 Theoretical Considerations.

3.2A Resonance Conditions and Average Hamiltonian.

Our initial goal is to determine the important features of the spin dynamics of a dipolar-coupled homonuclear spin pair (I and S) evolving under the combined effects of MAS and a weak rf-field. The Hamiltonian in the rotating frame for such a system is:

$$H = \omega_I I_z + \omega_S S_z + \omega_1 (I_x + S_x) + H_{IS}(t) \qquad (1),$$

where

$$H_{IS}(t) = \omega_D(t)\left(3I_zS_z - \tilde{I} \bullet \tilde{S}\right) \qquad (2),$$

ω_X (X=I or S) represents the isotropic chemical shift offset of each spin (effects of CSA will be considered in a later section), ω_1 represents the rf field magnitude, and $\omega_D(t)$ represents the MAS-modulated spatial part of the dipolar interaction. We can calculate the explicit time-dependence of the last term using spherical tensor notation. Rewriting equ (2) in this notation for a non-spinning sample yields

$$H_{IS} = A_{20}^{IS} T_{20}^{IS} \qquad (3),$$

($\tilde{\tilde{A}}^{IS}$ is the spatial tensor and $\tilde{\tilde{T}}^{IS}$ the spin tensor, represented in a spherical coordinate system where the symmetry axis lies along the magnetic field - hence the secular approximation leaves only the m=0 components of the tensor product). The time-dependence imposed on the spatial part of the dipolar interaction by MAS follows by a straightforward rotation about the Euler angles $(\alpha = 0, \beta_{MA}, \gamma = \omega_r t)$, which we demonstrate here to set-up

notation for what follows:

$$A_{20}^{\prime(IS)}(t) \quad = \omega_D(t) \quad = \sum_{m=-2}^{2} D_{m0}^{2}(0,\beta_{MA},\omega_r t) A_{20}^{(IS)}$$
$$= \sum_{m=-2}^{2} d_{m0}^{2}(\beta_{MA}) A_{20}^{(IS)} e^{im\omega_r t} \qquad (4),$$
$$= \sum_{m=-2}^{2} \omega_m^{(IS)} e^{im\omega_r t}$$

($D^2_{m,m'}(\alpha,\beta,\gamma)$ and $d^2_{m,m'}(\beta)$ represent the 2nd-rank Wigner and reduced Wigner matrices, respectively, following the conventions given in Spiess[8], β_{MA} is the magic angle, ω_r is the spinning frequency, and we have defined $\omega_m^{(IS)}$ as shown (following Levitt, et. al.[1]) for convenience). Note that $\omega_0^{(IS)} = 0$ for the dipolar interaction; that is, there is no component of the dipolar interaction that is not sinusoidally modulated by MAS.

Given a spinning speed significantly larger than the magnitude of the dipolar interaction, naive reasoning along the lines of Average Hamiltonian Theory (AHT)[9] (e.g. calculation of the zero-order average Hamiltonian) would suggest that the system will evolve in a manner largely independent of the effects of the coupling. This is the expected averaging effect of MAS on the 2nd rank components of anisotropic interactions, and it is effective over a wide range of system parameters. As described in Chapter One, however, under certain conditions this behaviour does not hold. Accurately estimating the dynamics under all conditions, and particularly in the presence of significant chemical shift terms (or their equivalents), requires transformation to an interaction frame in which large non-commuting terms in the Hamiltonian are appropriately minimized. The approach we follow here is similar to that described in Chapter One in the context of RR[1].

The first step in the transformation process involves moving to a doubly-tilted frame in which the effective fields (defined by the vector sum

of the rf field and chemical shift offset of each spin) lie along the z-axis. This necessitates a rotation about the y-axis in the spin space of each spin by the angle

$$\theta_X = \tan^{-1}(\omega_1/\omega_X) \qquad (5).$$

(given different chemical shift offsets each spin will undergo a different tilt, so that the coordinate systems of the two spin spaces (I and S) will no longer align). Subsequently we will transform to an interaction frame by applying a time-dependent rotation about the effective field axis (see below). The pair of rotations, tilt about y followed by time-dependent rotation about z, can be described using the Euler angles $(\alpha = 0, \beta = \theta_X, \gamma = \omega_X^{int} t)$ (where ω_X^{int} represents the magnitude of the interaction-frame transformation). This is analogous to the MAS transformation described above (but acting on the spin part of the dipolar Hamiltonian), and can be calculated using identical techniques. However, because we are allowing for the possibility of significant chemical shift offset, the rotations in the I- and S- spin spaces may be different, so that their contributions to the overall spin tensor $\tilde{\tilde{T}}$ must be manipulated separately. We can effect separate manipulations by first expressing $\tilde{\tilde{T}}$ in the untilted frame as a product of the first-rank, I and S single-spin tensors:

$$T_{20}^{(IS)} = 3\left(T_{10}^{(I)} T_{10}^{(S)}\right) + \sum_{m=-1}^{1} (-1)^m T_{1m}^{(I)} T_{1-m}^{(S)} \qquad (6).$$

The tilting transformation (a rotation in each spin-space about the y-axis by an angle θ_X) then yields the following expressions for the single-spin tensor elements:

$$T_{1,m}'^{(X)} = \sum_{m'=-1}^{1} d_{0m'}^{1}(\theta_X) T_{1,m}^{(X)} \qquad (7).$$

(The single-spin tensor elements are

$$\begin{aligned} T^{(1)}_{1,1} &= -\frac{1}{\sqrt{2}}\left(I_x + iI_y\right) &&= -\frac{1}{\sqrt{2}} I_+ \\ T^{(1)}_{1,0} &&&= I_z \\ T^{(1)}_{1,-1} &= \frac{1}{\sqrt{2}}\left(I_x - iI_y\right) &&= \frac{1}{\sqrt{2}} I_- \end{aligned} \tag{8}$$

(Mehring[10] p. 288), and the reduced Wigner matrix elements $d^1_{m,m'}(\beta)$ are

1	0	−1	m/m'
$\frac{1+\cos\beta}{2}$	$\frac{-\sin\beta}{\sqrt{2}}$	$\frac{1-\cos\beta}{2}$	1
$\frac{\sin\beta}{\sqrt{2}}$	$\cos\beta$	$\frac{-\sin\beta}{\sqrt{2}}$	0
$\frac{1-\cos\beta}{2}$	$\frac{\sin\beta}{\sqrt{2}}$	$\frac{1+\cos\beta}{2}$	−1

(9)

(Spiess[8] p. 203 - note the missing (-) sign in Spiess).) Applying a similar rotation to the chemical-shift offset and rf-field contributions to the Hamiltonian and gathering terms finishes the transformation to the doubly-tilted rotating frame:

$$H^T = \omega^e_I I_Z + \omega^e_S S_Z + \sum_{m=-2}^{2} \omega^{(IS)}_m e^{im\omega_r t} \sum_{m',m''=-1}^{1} C_{m',m''} T'^{(I)}_{m'} T'^{(S)}_{m''} \tag{10}$$

where

$$C_{m',m''}(\theta_I,\theta_S) = 3d^1_{0,m'}(\theta_I) d^1_{0,m''}(\theta_S) - \sum_{m'''=-1}^{1} d^1_{m',m'''}(\theta_I) d^1_{m'',m'''}(\theta_S) \tag{11},$$

and

$$\omega^e_X = \sqrt{\omega_1^2 + \omega_X^2} \tag{12}.$$

The next step, transforming to an interaction frame defined by the effective fields, will induce a time-dependence on the spin part of the dipolar terms in the Hamiltonian, while simultaneously reducing the magnitude of the effective field terms that give rise to significant higher-order terms in the AHT expansion. When some dipolar spin component (characterized by the values (m',m'') - see equ (10)) has a time dependence that matches that imposed by MAS on a spatial component (characterized

by m), the averaged dipolar interaction will no longer be zero. This is the essence of the rotational resonance effect - interference between chemical shift induced- and MAS-induced attenuation of the coupling. Because the series of dipolar components (m',m'') have different transformation properties with respect to the effective fields, there are a series of conditions under which resonance occurs, one for each distinctly manipulated dipolar component. We define an alternative dipolar alphabet in the tilted frame based on the effective-field induced time-dependence of the constituent terms:

$$\sum_{m',m''=-1}^{1} C_{m',m''} T_{m'}^{\prime(I)} T_{m''}^{\prime(S)} = \sum_{X} C_X T^X \qquad (13),$$

where

$X =$	$C_X =$	$T^X =$	$e^{-i(\omega_I^\zeta I_z + \omega_S^\zeta S_z)t} T^X e^{\cdots} =$
Σ	$C_{1,1}$	$T_1^I T_1^S + T_{-1}^I T_{-1}^S$	$T_1^I T_1^S e^{i\omega_\Sigma^\zeta t} + T_{-1}^I T_{-1}^S e^{-i\omega_\Sigma^\zeta t}$
Δ	$C_{1,-1}$	$T_1^I T_{-1}^S + T_{-1}^I T_1^S$	$T_1^I T_{-1}^S e^{i\omega_\Delta^\zeta t} + T_{-1}^I T_1^S e^{-i\omega_\Delta^\zeta t}$
I	$C_{1,0}$	$T_1^I T_0^S + T_{-1}^I T_0^S$	$T_1^I T_0^S e^{i\omega_I^\zeta t} + T_{-1}^I T_0^S e^{-i\omega_I^\zeta t}$
S	$C_{0,1}$	$T_0^I T_1^S + T_0^I T_{-1}^S$	$T_0^I T_1^S e^{i\omega_S^\zeta t} + T_0^I T_{-1}^S e^{-i\omega_S^\zeta t}$
Z	$C_{0,0}$	$T_0^I T_0^S$	$T_0^I T_0^S$

and $\omega_\Sigma^\zeta = \omega_I^\zeta + \omega_S^\zeta, \omega_\Delta^\zeta = \omega_I^\zeta - \omega_S^\zeta$. The component that commutes with the effective fields (T^Z) can not be recoupled under these conditions, regardless of the effective field strengths. The remaining terms are recoupled when their associated resonance condition is fulfilled:

$$\omega_X^\zeta = n\omega_r \qquad (14)$$

(with $X = \Sigma, \Delta, I, S$ and $n = 1,2$). For systems with small or identical chemical shifts, the effective fields of the two spins are approximately equal and hence the zero-quantum (Δ) condition is precluded at reasonable spinning speeds.

A demonstration of the resonance effect is shown in Fig. (3-1). Preparation of spin-locked sum polarization followed by mixing at various rf field strengths and detection of the residual polarization is used to map out the "recoupling" spectrum of the system at a given carrier frequency and sample spinning speed (the details of the pulse sequence are described below). Here ω_r=9 kHz and the carrier was placed approximately on resonance (hence the effective fields are transverse and equal in magnitude to the rf field). Absent relaxation, we expect no evolution of the spin-locked magnetization unless recoupling of some interaction occurs. When a recoupling effect does occur, evolution under the recoupled interaction leads to a reduction of the spin-locked polarization, and hence a "dip" in the recoupling spectrum. Here the resonance spectrum was mapped out for both 100%-^{13}COOH labeled (filled circles) and natural abundance (open circles) glycine samples (in the former sample, significant intermolecular dipolar interactions exist; the latter sample serves as a control) with a 25 ms mixing period. The decay of polarization in the 100% labeled sample at $\omega_{rf}\approx$5 kHz, without corresponding decay in the natural abundance control, indicates recoupling of the double-quantum dipolar term characterized by (n=1, Σ) in equ (14). This is expected with an effective field strength of approximately half the spinning speed (the up-field shift from the predicted value of ω_{rf}=4.5 kHz is probably induced by the CSA interaction; see below). Note that the (n=1, Σ) resonance condition illustrated here is the one that is exploited in both 2Q-HORROR and n=1 RR experiments (we are near 2Q-HORROR here).

A larger dip in the resonance spectrum of both samples occurs as the rf power approaches the spinning speed. The presence of the dip in both samples indicates that it does not arise solely from recoupled dipolar

Figure 3-1: Resonance spectra of 100% ^{13}COOH (filled circles) and natural abundance (open circles) glycine. The spinning speed was set to 9kHz, and the rf carrier frequency was placed approximately on resonance. Plotted is the residual sum polarization after 30ms of mixing along the applied rf field, as a function of the rf field magnitude. When the rf field was approximately equal to half the spinning speed ($\omega_1=\omega_r/2$), selective decay of sum polarization in the labeled sample was driven by intermolecular dipolar couplings. When the rf field magnitude approached the spinning speed ($\omega_1=\omega_r$), similar decay occurred in both samples, driven primarily by the recoupled CSA interaction. The presence of a dipolar contribution to the decay in the labeled sample at this latter resonance condition is obscured by the dominant CSA-driven evolution.

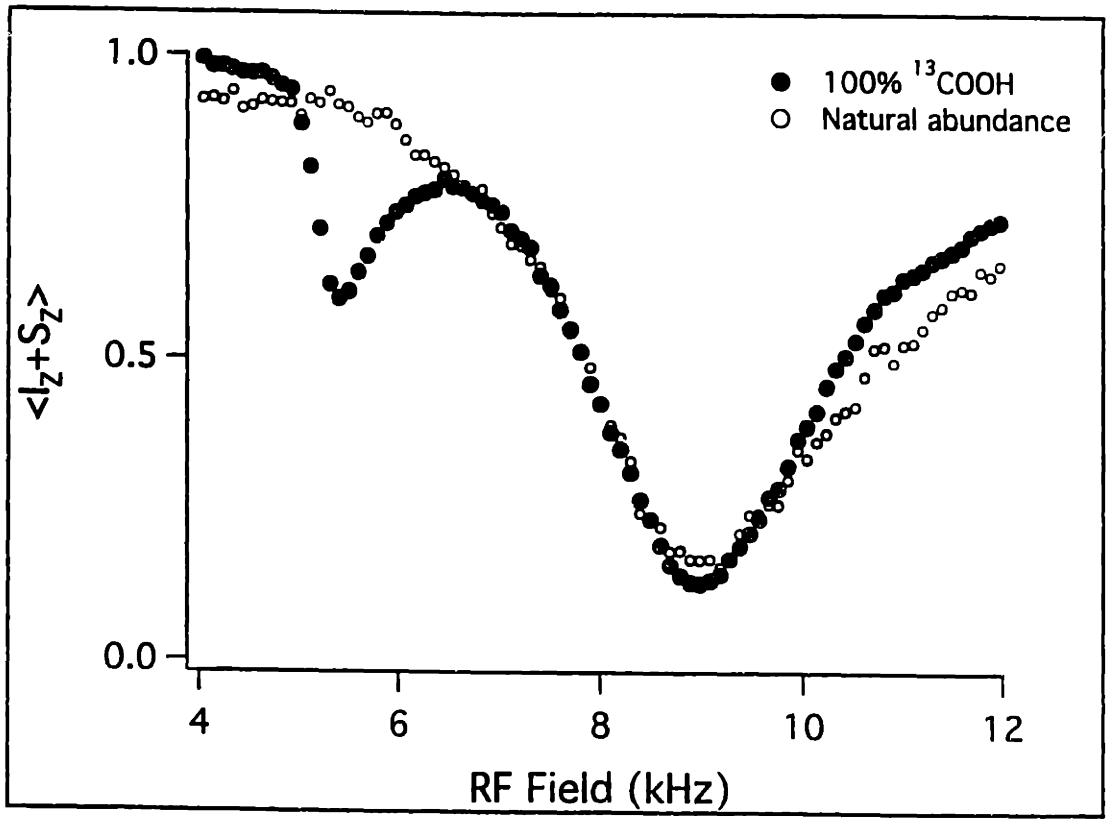
1.0
0.5
0.0
$\langle I_z+S_z \rangle$
100% ^{13}COOH
Natural abundance
4
6
8
10
12
RF Field (kHz)

interactions. Instead, the CSA interaction is recoupled and so dominates the dynamics at this rf field strength[11]. The spin term of the CSA interaction has a time-dependence in the interaction frame identical to the I and S dipolar spin terms, and so is recoupled under the same conditions (i.e. $\omega_x^c = n\omega_r$). Although in the labeled sample the (n=2, Σ) and (n=1, I and S) dipolar terms are also recoupled when the rf power approaches the spinning speed, their presence is masked by the CSA interaction. This is a general problem: experiments directed at observing dipolar-driven dynamics must avoid recoupling the often dominant CSA interactions. Hence use of the I and S dipolar resonances is precluded in most systems. In samples with small chemical shift differences (or a symmetrically placed carrier) where the effective field strengths are approximately equal, the (n=2, Σ) condition is also precluded for the same reason. Note that in systems with significant chemical shift differences, asymmetric placement of the carrier can allow access to both (n=1,2, Δ) and (n=2, Σ) dipolar resonance conditions without recoupling CSA interactions, for a variety of effects. These issues are discussed in more detail in section 3.2F.

Here we will focus on the (n=1, Σ) condition that gives rise to both n=1 RR and 2Q-HORROR effects, and is never precluded by CSA when the spinning speed is set sufficiently high. The specific form of the interaction transformation that takes us to this resonance frame depends on the placement of the carrier frequency in the 2-spin spectrum; here we will assume a symmetric placement (i.e. directly between the two resonances). Appropriate minimization of the effective field terms in the Hamiltonian requires transforming according to:

$$U = e^{-i(I_z + S_z)n\omega_r t/2} \qquad (15),$$

where n is an integer selected to minimize the magnitude of the residual effective field terms in the transformed Hamiltonian (see Chapter One). If the appropriate value for n is 1, then recoupling at the (n=1, Σ) condition is possible, and applied to the tilted Hamiltonian in equ (10) the transformation yields:

$$H^T = (\omega_\Sigma^e - \omega_r)(I_Z + S_Z) + \sum_{m=-2}^{2} \sum_{m',m''=-1}^{1} C_{m',m''} \omega_m^{(IS)} T_{m'}^{(I)} T_{m''}^{(S)} e^{i(2m+m'+m'')\omega_r t/2} \qquad (16).$$

Averaging over the cycle time ($2\tau_r = 4\pi/\omega_r$) gives the following zero-order average Hamiltonian:

$$\bar{\tilde{H}}^{(0)T} = (\omega_\Sigma^e - \omega_r)(I_Z + S_Z) + C_\Sigma(\omega_1^{(IS)} T_1^{(I)} T_1^{(S)} + \omega_{-1}^{(IS)} T_{-1}^{(I)} T_{-1}^{(S)}) \qquad (17).$$

The zero-order average Hamiltonian is block-diagonal when represented in the $|\pm\pm\rangle$ basis, with the only off-diagonal element connecting the states $|1\rangle = |++\rangle, |4\rangle = |--\rangle$. Using the standard fictitious spin-1/2 operator formalism we can consider the dynamics in a fictitious two-level system, where the average Hamiltonian becomes:

$$\bar{H}^{14} = (\omega_\Sigma^e - \omega_r) J_Z^{14} + C_\Sigma(\mathrm{Re}(\omega_1^{(IS)}) J_X^{14} + \mathrm{Im}(\omega_1^{(IS)}) J_Y^{14}) \qquad (18),$$

($\tilde{J}^{14}$ represents the fictitious spin operator, and we have used $\omega_m^{(IS)} = (\omega_{-m}^{(IS)})^*$). As in RR, the longitudinal term (J_Z^{14}) represents residual effective fields and has significant magnitude only away from resonance. The transverse term (J_X^{14} / J_Y^{14}) represents the recoupled dipolar interaction, and has double-quantum character. Hence it is sum polarization that evolves about the recoupled interaction on resonance, while difference polarization is expected not to evolve.

Similar average Hamiltonians have been derived for many recoupling experiments, including RFDR[12], MELODRAMA[13], and heteronuclear CP under fast MAS[14]. Although in some cases the relevant spin dynamics occur in the (2,3) subspace, the overall picture remains the

same: the Hamiltonian in the appropriate fictitious spin-1/2 subspace can be represented by a 3-dimensional vector, with a transverse component determined by the phase and magnitude of the recoupled dipolar interaction. The longitudinal component is determined by the matching condition; precisely on resonance this component is zero and the spin dynamics are driven solely by the recoupled dipolar interaction. Sum or difference polarization (depending on the (2,3) or (1,4) nature of the recoupled interaction) rotates about the effective Hamiltonian in the fictitious subspace exactly as single-spin magnetization evolves about an applied rf field in the standard rotating frame.

3.2B The n=1 RR to 2Q-HORROR Continuum; Defining Rotational Resonance Tickling.

We will sketch the spin dynamics in more detail in the following section. Here we focus on the connection between n=1 RR and 2Q-HORROR. The derivation of the average Hamiltonian (equs (17/18)) for the (n=1, Σ) condition which gives rise to both of these effects indicates a recoupled dipolar interaction of double quantum character when the resonance condition is matched:

$$\omega_I^e + \omega_S^e = \omega_r \qquad (19).$$

The derivation is valid over a range of chemical shift offsets, with the magnitude of the effective fields always positive and varying, as given in equ (12), as a function of chemical shift offset. When the offsets are zero, the effective fields are determined solely by the applied rf and we recover the "idealized" 2Q-HORROR resonance condition $\omega_1 = \omega_r/2$[4]. When offsets are present this resonance condition is modified to one containing the effective field magnitudes ($\sqrt{\omega_I^2 + \omega_1^2} + \sqrt{\omega_S^2 + \omega_1^2} = \omega_r$). The AHT derivation is valid right up to the limit where the rf field goes to zero and

the effective fields are determined solely by the chemical shift offsets, i.e. the RR effect. Analyzed in a rotating frame with the imaginary carrier frequency between the two resonances (imaginary because the rf magnitude is zero), the tilting transformation for a RR experiment rotates one spin coordinate space by 180° so that its tilted z-axis points opposite the rotating frame z-axis. It is this tilt that accounts for (1) the double-quantum nature of the n=1 RR effect in the interaction frame we use here; and (2) the effective field magnitudes both being positive. This last fact makes the connection between the standard n=1 RR condition ($\omega_I - \omega_S = \omega_r$) and the generalized (n=1, Σ) dipolar resonance condition (equ (19)).

That the spin dynamics at n=1 RR and 2Q-HORROR are, in the appropriate interaction frame, described by an identical average Hamiltonian (corresponding to that for the (n=1, Σ) resonance we have defined) suggests that they share several features in common. These features include the form of the generalized resonance condition (recast in terms of effective fields), the double quantum nature of the recoupled interaction in the interaction frame, and the dependence of the recoupling effect on the orientation of the dipolar axis in a powder sample. This orientation dependence is implicit in the $\omega_1^{(IS)}$ coefficient of the recoupled dipolar interaction of equ (17). Hence both n=1 RR and 2Q-HORROR have the same dependence on this parameter, the claims of Nielsen et. al. notwithstanding[4]. We discuss this issue, and its implications for fine control of the phase of the recoupled dipolar interaction, in a later section.

The n=1 RR and 2Q-HORROR experiments represent extremes of a continuum (see Fig. (3-2)). In samples with significant chemical shift differences, spinning precisely at a chemical shift difference matches the n=1 RR condition. Spinning at higher speeds necessitates the application of

an rf field to match resonance; the magnitude of the field increasing with the spinning speed (and with a concomitant change in effective field direction). When the spinning speed greatly exceeds the chemical shift difference. the rf field contribution to the resonance condition will overwhelm the chemical shift offset contribution, and one has reached the 2Q-HORROR limit. Thus selection of the spinning speed relative to the chemical shift difference allows control over where along the continuum the recoupling experiment is performed. In systems with little or no chemical shift difference, one is limited by the lowest reasonable value of the spinning speed to the 2Q-HORROR limit. Given a significant chemical shift difference (one that would allow application of the n=1 RR experiment), however, the "RR tickling" (RRT) regime, where the spinning speed is set slightly higher than the standard n=1 RR value and a small rf field is applied to match resonance, is accessible. The RRT experiment maintains many of the benefits of the standard n=1 RR technique (including selective recoupling, minimal manipulation of the spin system, and T_1-dominated relaxation of polarization during mixing) while allowing rf control over the resonance condition on short (μs) timescales. The benefits that this control affords in inducing relaxation- and inhomogeneity-independent spin dynamics are discussed in detail in the following sections.

3.2C Pulse Sequences and Spin Dynamics for Longitudinal Mixing.

The recoupling effect evident in the average Hamiltonian (17) can be exploited in several different ways. Measurement of the rate of decay of "transverse" polarization (where the polarization of the spins is prepared perpendicular to the effective fields) due the creation of two-spin

Figure 3-2: n=1 RR to 2Q-HORROR continuum. Given a two-spin spectrum, setting the spinning speed equal to the chemical shift difference induces dipolar recoupling; this is the n=1 RR effect. If we spin slightly faster than the chemical shift difference, a weak rf field applied to the spin system scales up the effective fields, and can reproduce the n=1 RR dipolar resonance effect, although with the effective fields rotated slightly away from longitudinal as indicated. If the spinning speed is set much larger than the chemical shift difference, the magnitude of the rf needed to match resonance will be much large than the chemical shift offsets of the two spins, and the effective fields will be approximately transverse. In all cases, however, the dynamics can be described with a single average Hamiltonian (suitably scaled), as shown in the text.

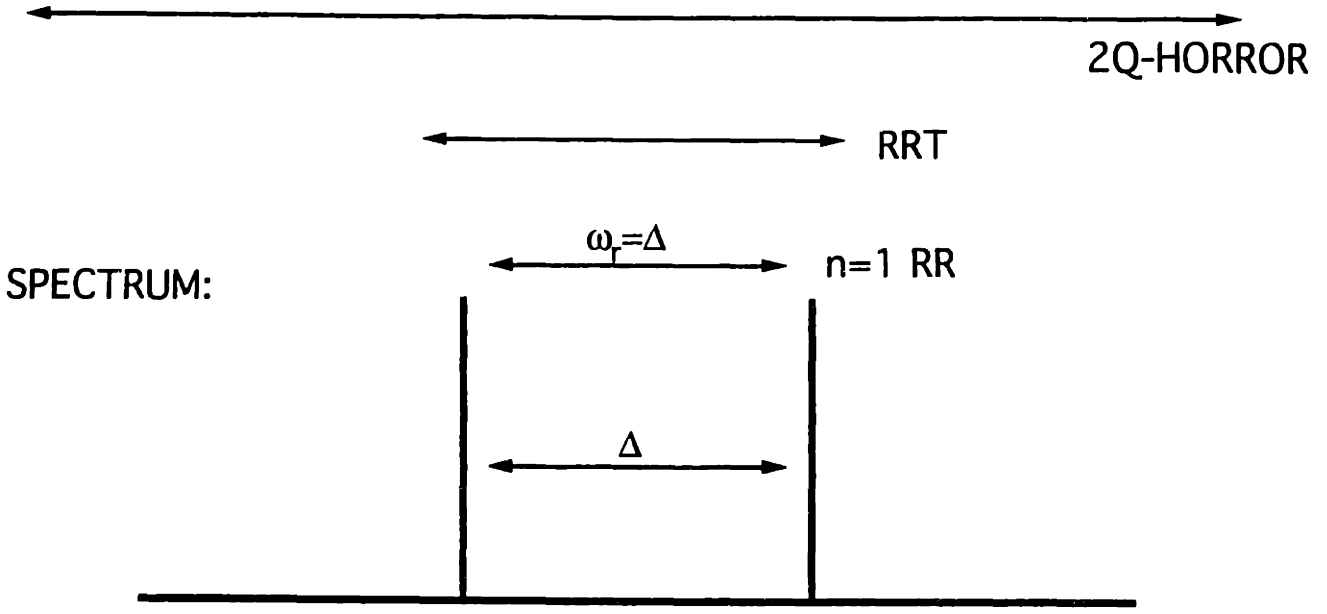
2Q-HORROR
RRT
SPECTRUM:
$\omega_r=\Delta$
n=1 RR
Δ

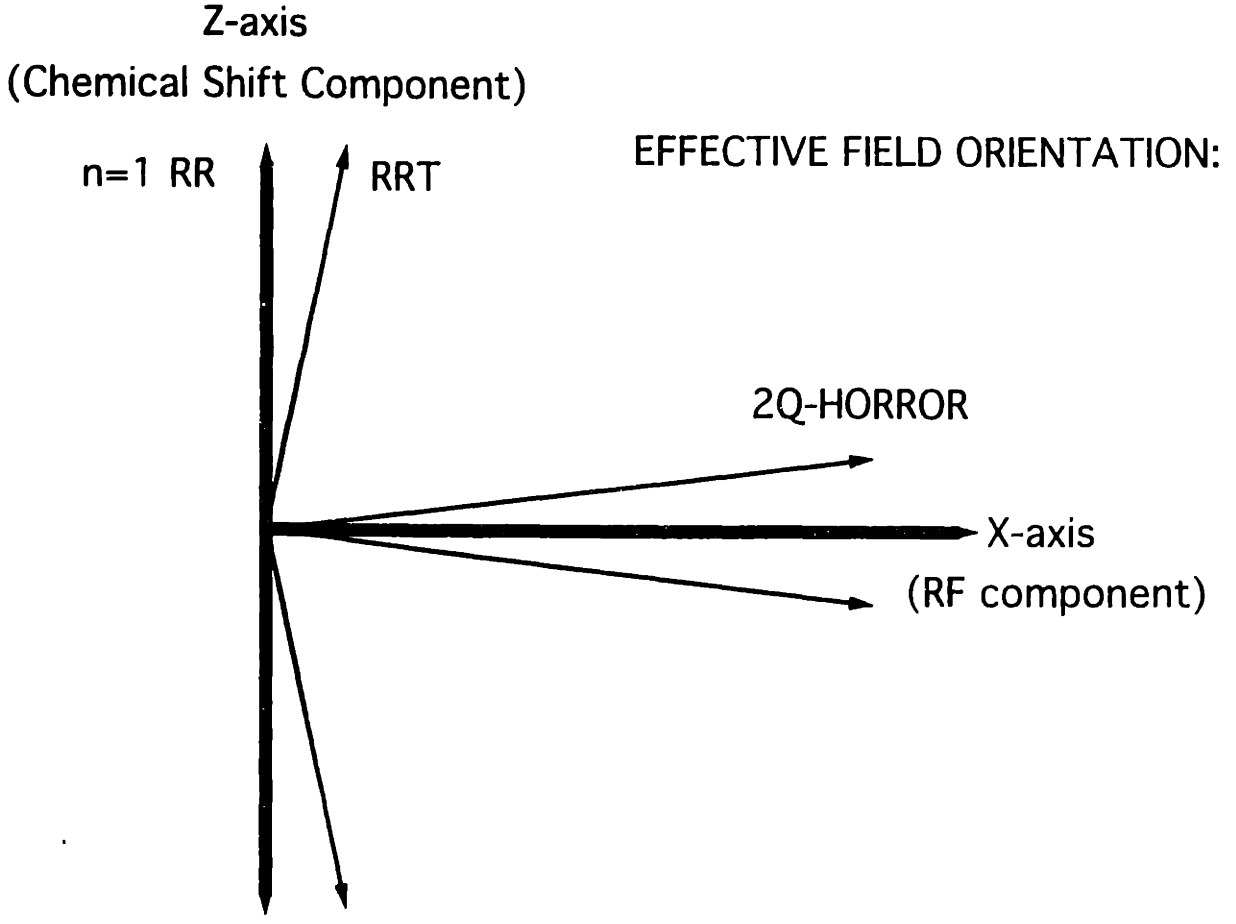
Z-axis
(Chemical Shift Component)
EFFECTIVE FIELD ORIENTATION:
n=1 RR
RRT
2Q-HORROR
X-axis
(RF component)

coherence is useful in quantifying the dipolar coupling constant (e.g. the SEDRA effect[15]; note that T_2 (or $T_{2\rho}$) decay must be taken into account). Alternatively, INEPT-style polarization transfers[16] or multiple-quantum filtering experiments[17] can be performed in this context. Such an approach is most straightforward when the effective fields are either longitudinal or transverse. "Longitudinal" mixing experiments, where the polarization of the spins is prepared along the effective fields, have been used more extensively. Unlike transverse experiments where the initial condition often commutes with part of the recoupled dipolar interaction and hence evolves at a slower rate, longitudinal experiments make use of the full recoupled dipolar Hamiltonian. Again, the rate of decay of the initial state (due to the creation of 2-spin coherence) can be used to quantify the dipolar coupling constant (this is the standard approach in experiments exploiting the RR[18] and RFDR[12] recoupling techniques). In longitudinal experiments, however, the decay of one spin's polarization depends on the polarization state of the other spin. Sequential experiments performed first with sum and then with difference polarization along the effective fields provide (i) a measure of the polarization transfer rate and (ii) a control which evolves essentially independently of the recoupled dipolar interaction. Furthermore, signal loss during mixing of the types we have described previously is minimized in these experiments due to the effective-field spin-lock. The lack of such loss is often evident in the lack of observable decay in the control mixing experiment.

Fig. (3-3) illustrates the pulse sequences that can be used to perform these experiments. The sequence for experiments near the n=1 RR condition (the RRT regime) is shown in (3-3A). The effective fields lie approximately along the +z and -z axes of the rotating frame when the

carrier is placed between the two resonances. Hence after CP we want to prepare approximately longitudinal (relative to the rotating frame) sum or difference polarization (the latter to measure dipolar-driven evolution; the former as a control). For difference polarization, we place the carrier frequency precisely between the two resonances and use a period of transverse chemical shift evolution ($\tau_{inv}=8\pi/(\omega_I-\omega_S)$) to invert, followed by a 90° pulse to create longitudinal magnetization (for sum polarization the inversion period is omitted). This inversion sequence is formally identical to an N=2 DANTE[19] sequence, where the action of the first 90° pulse of the 2-pulse DANTE sequence is performed by CP. It is effective for creating population differences between two well-separated regions of the spectrum. Following the (optional) inversion, a ramp-in (RI) pulse is used to adiabatically rotate the polarization from the longitudinal axis to the appropriate near-longitudinal effective-field axis for mixing. During the ensuing dipolar mixing period, the recoupled dipolar interaction drives zero-quantum polarization transfer between the spin pair at a rate determined in large part by the magnitude of the dipolar coupling. Note that this is zero-quantum relative to the rotating frame, but double-quantum relative to the interaction frame we have defined. Thus "longitudinal difference polarization" as created by the inversion delay corresponds to sum polarization in our interaction frame, and is the initial state (J_Z^{I4}; see below) that undergoes dipolar evolution. After mixing, a ramp-out (RO) pulse is used to adiabatically rotate the polarization back to the z-axis and a 90° pulse is applied to create transverse polarization for detection.

The equivalent pulse sequence for experiments near the HORROR regime is shown in Fig (3-3B). Here, the effective fields lie in the

Figure 3-3: Pulse sequences for dipolar mixing with polarization locked along the effective fields. Both sequences include standard cross-polarization and CPDELAY inversion periods, and high-power ^1H decoupling (additional decoupling power applied after the end of the acquisition period can be applied to eliminate differential probe heating effects - see Chapter One).

(A) RRT sequence: After the inversion period, a 90° pulse is applied to create longitudinal difference polarization. A ramp-in pulse then adiabatically rotates the polarization away from the longitudinal axis to the appropriate effective-field orientation for mixing. During mixing, the rf field may be held constant or ramped to pass through resonance. After mixing a ramp-out pulse adiabatically rotates the polarization back to the longitudinal axis; a final 90° pulse sequence creates transverse polarization for detection.

(B) 2Q-HORROR sequence: After inversion, a ramp-in sequence adiabatically rotates the polarization from the transverse plane to the appropriate near-transverse effective field orientation. Mixing can then occur either at a constant or ramped field strength. Following mixing, a ramp-out pulse rotates the polarization back to the transverse plane for detection.

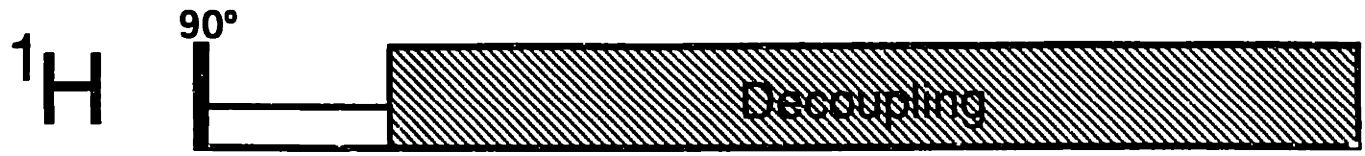
^{1}H
90°
Decoupling

^{13}C:

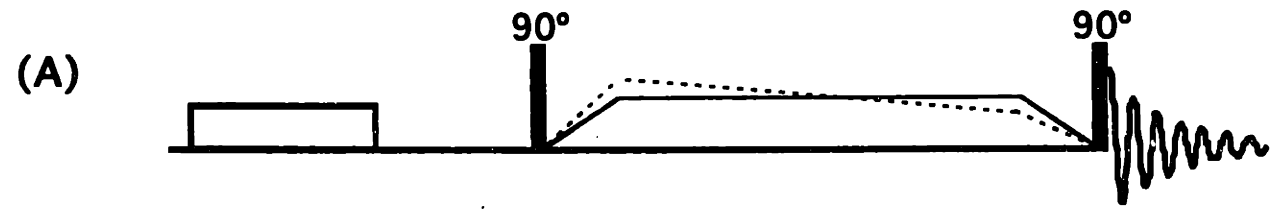
(A)
90°
90°

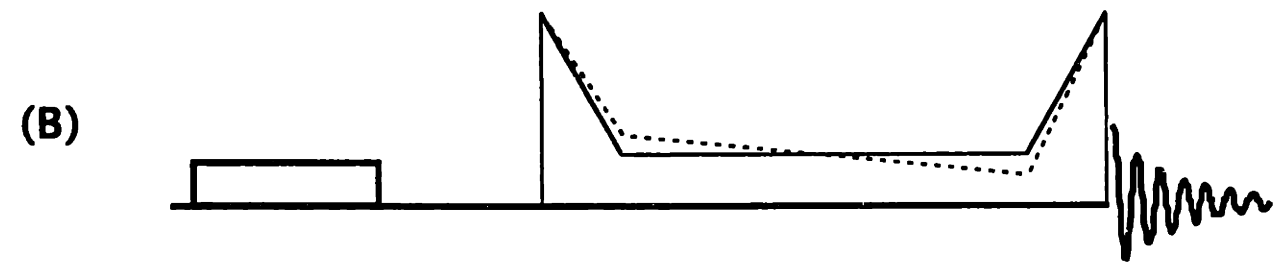
(B)

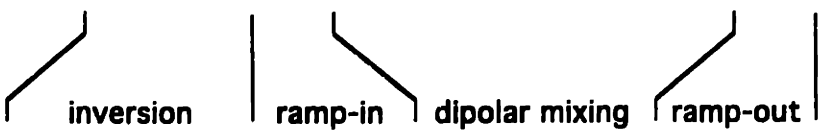
inversion
ramp-in
dipolar mixing
ramp-out

transverse plane (or near it, in the case of residual offsets); mixing along the effective fields translates into transverse, spin-locked magnetization. After CP and a delay for inversion, a modified RI pulse is applied to adiabatically rotate the polarization from the transverse plane to the appropriate near-transverse effective field for mixing. The recoupled dipolar interaction during the subsequent mixing period has double-quantum character relative to the rotating frame, hence in these experiments sum polarization evolves under the coupling and difference polarization provides the control. After mixing a modified RO pulse is applied, the rf field is turned off and transverse magnetization is detected.

The initial condition created by the RI pulses in each sequence corresponds to a vector along the z-axis in the appropriate fictitious spin-1/2 subspace:

$$\rho(t=0) = J_z^{14} \text{ or } J_z^{23} \tag{20}$$

(the first corresponding to sum and the latter to difference polarization, defined relative to the interaction frame). The latter term commutes with the zero-order average Hamiltonian for (n=1, Σ) experiments, and so should not evolve during mixing. Decay of (interaction frame) difference polarization during mixing thus provides a control by which dipolar-independent processes can be observed and quantified. If there is no decay of difference polarization during the control experiment, then one can be relatively certain that any decay of sum polarization that is observed is due to the recoupled dipolar interaction. If there is decay of difference polarization, however, it is not always clear whether this decay is due to single-spin effects (e.g. relaxation or residual CSA effects) that will identically affect the sum polarization evolution (and hence can be factored out), or whether the decay is due to zero-quantum flip-flop interactions

(e.g. from ^{1}H-driven spin diffusion or J-couplings (see below)) that will not necessarily affect the sum polarization evolution in an identical fashion and hence can not easily be factored out. We provide examples of both cases below.

Evolution of sum polarization during mixing is calculated directly from the average Hamiltonian (ignoring relaxation effects):

$$\rho(t) = e^{-i\bar{H}^{14}t} J_Z^{14} e^{i\bar{H}^{14}t} \qquad (21).$$

For a system precisely on-resonance ($\omega_\Sigma = \omega_r$), the evolution of the density operator in a single crystallite is a simple oscillation between sum polarization and double-quantum coherence:

$$\rho(t) = J_Z^{14}\cos\left(C_\Sigma\left|\tilde{\omega}_1^{(IS)}\right|t\right) + \left(\mathrm{Im}\left(\tilde{\omega}_1^{(IS)}\right)J_X^{14} - \mathrm{Re}\left(\tilde{\omega}_1^{(IS)}\right)J_Y^{14}\right)\sin\left(C_\Sigma\left|\tilde{\omega}_1^{(IS)}\right|t\right) \qquad (22).$$

The oscillation frequency depends on the magnitude and orientation of the dipolar coupling relative to the magnetic field (implicit in $\omega_1^{(IS)}$), and furthermore on the orientation of the effective field vectors in the rotating frame (implicit in C_Σ). The latter parameter can be calculated given the magnitudes of the chemical shift offset and rf field terms using equs (5) and (11). For experiments near the 2Q-HORROR regime the C_Σ parameter is maximized at 0.75, and as one proceeds along the continuum towards n=1 RR it drops to a minimum of 0.50. Hence experiments near the HORROR extreme of the continuum reintroduce the coupling with 50% greater efficiency than at the n=1 RR extreme. The dipolar orientation dependence of the oscillation frequency necessitates calculation of a powder average to determine the observed sum polarization signal:

$$\left\langle J_Z^{14}\right\rangle = \int\sin(\beta)d\beta\int d\gamma\cos\left(C_\Sigma\left|\omega_1^{(IS)}\right|t\right) \qquad (23).$$

This equation describes a damped oscillation with a minimum at -50% of the initial sum polarization and a long-time equilibrium of zero sum-polarization. In polarization transfer experiments, this corresponds to a

maximum and equilibrium transfer efficiency of 75% and 50%, respectively (assuming no evolution in the 2,3 subspace). Note that these values hold across the continuum, from (and including) n=1 RR to 2Q-HORROR.

Relaxation effects can significantly alter the spin dynamics. Relaxation of the effective-field locked sum (or difference) polarization (the first term in equ (22)) is often slow or absent, particularly in the RRT regime where the relevant relaxation time is dominated by T_1 (often on the order of seconds for low-γ nuclei in rigid solids at room temperature). Relaxation of the 2-spin coherence created during polarization transfer (the second term in equ (22)), however, is dominated by T_2-dependent processes and often has a significant effect on the spin dynamics[1]. When this relaxation rate approaches or exceeds the magnitude of the recoupled dipolar interaction, the evolution of sum polarization is damped, in the relaxation-dominated case being described by an exponential decay with a time constant proportional to the square of the coupling divided by the 2-spin coherence relaxation rate[1]. This reduces polarization transfer and 2-spin coherence creation efficiency, and, because the relaxation rate of 2-spin coherence is often difficult to measure directly, makes it difficult to extract accurate internuclear distance information from data obtained under these conditions (this is the generalization of the 2Q-relaxation problem in extracting accurate distance information from on-resonance RR data, described in Chapter One). We demonstrate below that ramping through the resonance condition (by ramping the magnitude of the applied rf field) induces spin dynamics that are less dependent on MQ relaxation, and hence allow more accurate extraction of distance information.

3.2D Isotropic Chemical Shift and RF-Homogeneity Dependence of the Matching Condition

Residual effective field terms remain in the average Hamiltonian when the resonance condition is not precisely matched (the first terms in equs (17/18)). In the fictitious spin-1/2 frame, these terms correspond to a longitudinal component of the average Hamiltonian vector which serves to truncate evolution about the "rf-like", transverse dipolar component of the average Hamiltonian. Far enough from resonance, the residual effective field terms in the interaction frame dominate the dynamics and no detectable dipolar evolution occurs. For RR, where the effective fields correspond directly to the chemical shift offsets of the spins, this implies what we term "strong" chemical shift selectivity of the recoupling effect. Differences in chemical shift that do not precisely match the spinning speed map directly into residual effective fields that truncate dipolar evolution. This has several implications. First, the RR effect is particularly useful for inducing observable effects between coupled spin pairs within a multispin network (where the additional spins may be due to natural abundance or multiple labeling). The simultaneous reintroduction of multiple couplings that occurs upon application of broadband recoupling sequences to multiply labeled samples can make it difficult to observe the dynamics between particular spin pairs, for several reasons which we describe in the following chapter. Given a favorable distribution of chemical shifts, the RR effect can be used to selectively reintroduce the coupling between the spin pair of interest, maximizing the through-space polarization transfer rate and simplifying the analysis (needed to extract an estimate of the internuclear distance).

The strong chemical shift selectivity of the RR effect is a drawback in some applications, particularly when the couplings are small. In one-dimensional mixing experiments applied to macroscopically disordered peptides, the broadening of the resonance lines due to (what is presumed to be minor) conformational heterogeneity in the sample leads to a broadened resonance condition for each spin pair that precludes simultaneous matching of the resonance condition for all members of the selected spin pair population in the sample. When the magnitude of the chemical shift broadening approaches that of the recoupled dipolar interaction, the size of the resulting mismatch for various spin pairs in the sample leads to a reduction in overall transfer efficiency, and furthermore to spin dynamics that are strongly dependent on the precise nature of the chemical shift broadening. It is then difficult to extract accurate distance information from the observed dynamics (although we have recently proposed a method to simplify the problem, described in Chapter One). Furthermore, the narrowband nature of the RR technique limits its utility in multidimensional correlation experiments, where one wishes to observe the effects of dipole-driven polarization transfer as cross-peaks between multiple pairs of resonances over some significant spectral bandwidth.

The effects of resonance mismatch, just described for RR, generalize across the continuum of experiments we are discussing here, however with the discussion restated in terms of effective fields. Hence when experiments are performed in the RRT limit and the effective fields are primarily chemical shift, we expect behaviour similar to that observed for RR: namely, chemical shift selectivity and a sensitivity to CSD. We do not expect the experiment to be strongly sensitive to rf-inhomogeneity, because the rf field makes up such a small part of the overall effective field. The

change in the effective field strength (and hence the size of the resulting mismatch) due to a change in the rf field magnitude of one spin is proportional to the parameter α_{RF}^{X} where:

$$\alpha_{RF}^{X} = \frac{d\omega_X^e}{d\omega_1} = \frac{\omega_1}{\sqrt{\omega_X^2 + \omega_1^2}} \qquad (24).$$

Near RRT this parameter approaches zero, as expected. We can perform the identical calculation for chemical shift, yielding the almost identical equation for the parameter α_{CS}^{X}:

$$\alpha_{CS}^{X} = \frac{d\omega_X^e}{d\omega_X} = \frac{\omega_X}{\sqrt{\omega_X^2 + \omega_1^2}} \qquad (25).$$

This parameter approaches 1 for RRT, confirming its chemical shift selectivity. (Note that $\alpha_{CS}^{X} \geq 0.9$ (i.e. high chemical shift selectivity) is maintained when the applied rf field is small enough such that the condition $\omega_X \geq 2\omega_1$ is satisfied.)

Near the HORROR limit, when the effective fields are transverse, α_{RF}^{X} approaches 1 while α_{CS}^{X} approaches zero. This implies that experiments performed in this regime will be (i) sensitive to rf-inhomogeneity (in a manner similar to the CSD-sensitivity of RR), and (ii) insensitive (over some range) to chemical shift variation.

At points in between these two extremes, the behaviour will show some sensitivity to both parameters, as described by equs (24) and (25).

3.2E CSA Effects.

The anisotropic components of the chemical shift interaction are rendered time-dependent by application of MAS, and hence can be recoupled by application of rf of the appropriate magnitude just as the various components of the dipolar coupling are. This often precludes the use of certain dipolar resonance conditions, as we have discussed, and can

force the use of relatively large spinning speeds in experiments near the HORROR condition to reduce the overlap between the (n=1, Σ) dipolar resonance at $\omega_1=\omega_r/2$ and the first CSA resonance at $\omega_1=\omega_r$ (evident in Fig. (3-1)). Even when this is done, however, the CSA (if large enough) can still have a measurable effect on the recoupled dipolar spin dynamics. Consider the CSA Hamiltonian for a single spin (I) in the tilted frame:

$$H^{CSA} = \omega^I_{CSA}(t)I_Z\cos(\theta_I) + \omega^I_{CSA}(t)I_X\sin(\theta_I) \qquad (26).$$

In the tilted frame the CSA interaction divides into two components, one parallel to the effective field (the z-axis) and one perpendicular to it. The parallel component commutes with the effective field and hence can not be recoupled in the standard manner. However, it does induce higher-order modulations of the dipolar interaction in 2-spin systems that can significantly affect the spin dynamics when the sample spinning speed does not sufficiently exceed the size of this component of the CSA interaction. This effect is described in detail in the context of RR by Levitt, et al.[1], and at the end of Chapter Two of this thesis.

The perpendicular component of the CSA interaction can have several effects. The strongest of these is the recoupling effect (that occurs when $\omega^e_I = n\omega_r$ (n=1,2)) that we have discussed[11]. (Note that the strength of the recoupled CSA interaction is maximized near the HORROR limit where the perpendicular component of the CSA is largest, and is minimized near RR.) Even away from the CSA resonance, however, higher-order terms arising from the CSA modulation can still have an appreciable effect. Here we focus on the Bloch-Siegert like shift[20] the perpendicular components of the CSA induce on the frequency at which magnetization precesses about an applied rf field.

The Hamiltonian in the tilted rotating frame for a single spin (I) evolving under the combined effects of an MAS-modulated CSA interaction and a weak, on resonance rf field is given by:

$$H = \omega_1 I_Z + \omega_I^{CSA}(t) I_X \qquad (27).$$

Clearly the zero-order average Hamiltonian has no CSA contribution ($\overline{H}^{(0)} = \omega_1 I_Z$) far enough away from the CSA recoupling condition. Higher order effects are significant under certain conditions, however, and can be calculated either by AHT or by application of non-degenerate perturbation theory to the Floquet Hamiltonian[21, 22]. To first order both methods yield the same result:

$$\overline{H}^{(1)} = (\Delta\omega_1) I_Z \qquad (28),$$

where

$$\Delta\omega_1 = \frac{\omega_1}{2}\left(\sum_{m=1}^{2} \frac{\left|\omega_m^{(1)}\right|^2}{\omega_1^2 - (m\omega_r^2)}\right) \qquad (29).$$

At high rf powers and typical spinning speeds (ω_1>10 kHz, ω_r>5 kHz), the size of the shift is negligible for typical CSA parameters (δ<8 kHz). At the low rf powers we propose to use here ($\omega_1 \approx$1-10 kHz), however, the shift can be of significant magnitude. The shift has two important properties: first, it is orientation dependent, so that spins in different crystallites will experience different shifts; second, it is always negative in the parameter regime considered here. Hence we expect to observe a broad distribution of nutation frequencies about an applied rf field, with the center of the distribution shifted down in frequency from the magnitude of the applied field.

We demonstrate the shift and broadening in natural abundance glycine spinning at 9 kHz (Fig. (3-4)). Application of the standard 2D nutation experiment[23] at a constant rf power ($\approx$5 kHz), first with the

alpha carbon on resonance and then with the carboxyl, yields the rf-field distributions shown in Fig. (3-4A). The distribution obtained from the nutation of the alpha carbon is clearly narrower, and of a higher overall frequency. Calculating from equ (29), the shift and broadening we expect from the alpha carbon CSA (δ=1.5 kHz, η=1.0 at 7.4 T) is on the order of 40 Hz or less. If we make then make the reasonable assumption that the width of the alpha carbon distribution is dominated by the effects of rf inhomogeneity, we can use it in combination with the calculated shift and broadening of the carboxyl distribution (again, from equ (29)) to model the observed carboxyl rf distribution. The calculated distribution for the carboxyl (δ=6 kHz, η=1.0 at 7.4 T) absent rf-inhomogeneity is shown in Fig (3-4B), and the convolution of this distribution with the alpha-carbon distribution yields an overall curve that closely follows the observed one. The magnitude of the CSA-induced shift ($\approx$0.2 kHz) and broadening ($\approx$0.5 kHz) can be considered typical values for the experimental conditions we use here.

The CSA-induced shift in the precession frequency of a single spin translates directly into a shift in the dipolar resonance conditions in coupled two-spin systems. This is demonstrated in Fig. (3-1), where the (n=1, Σ) resonance condition for the carboxyl resonance in glycine is shifted approximately 0.4 kHz upfield. The glycine carboxyl nutation spectrum in Fig (3-4) was obtained under conditions very similar to the resonance condition in (3-1), so that the measured shift and broadening of the carboxyl nutation frequency can be compared with the observed shift in the resonance condition. For a 2-spin system with a single CSA we expect the shift and broadening in the resonance condition to be identical to what is observed for the nutation frequency of the spin with CSA, scaled by a

Figure 3-4: Slices from standard 2D-nutation experiments showing the distribution of nutation frequencies about the applied rf field for carboxyl and alpha-carbon resonances in natural abundance glycine (ω_r=9kHz).

(A) The alpha-carbon (dotted line) and carboxyl (solid line) frequency distributions were obtained separately, each with the appropriate peak nearly on resonance, and at identical rf field strengths. The carboxyl distribution is broader and centered at a lower frequency; this is due to the Bloch-Siegert-like shift the carboxyl CSA induces on carboxyl nutation frequencies.

(B) Experimentally obtained carboxyl frequency distribution (solid line; identical to result in (A) above) plotted with calculated result based on 1st-order CSA effects described in text (dashed line), and with the convolution of the calculated result with the alpha-carbon distribution (taken as a measure of the rf-inhomogeneity distribution; dotted line).

(A)

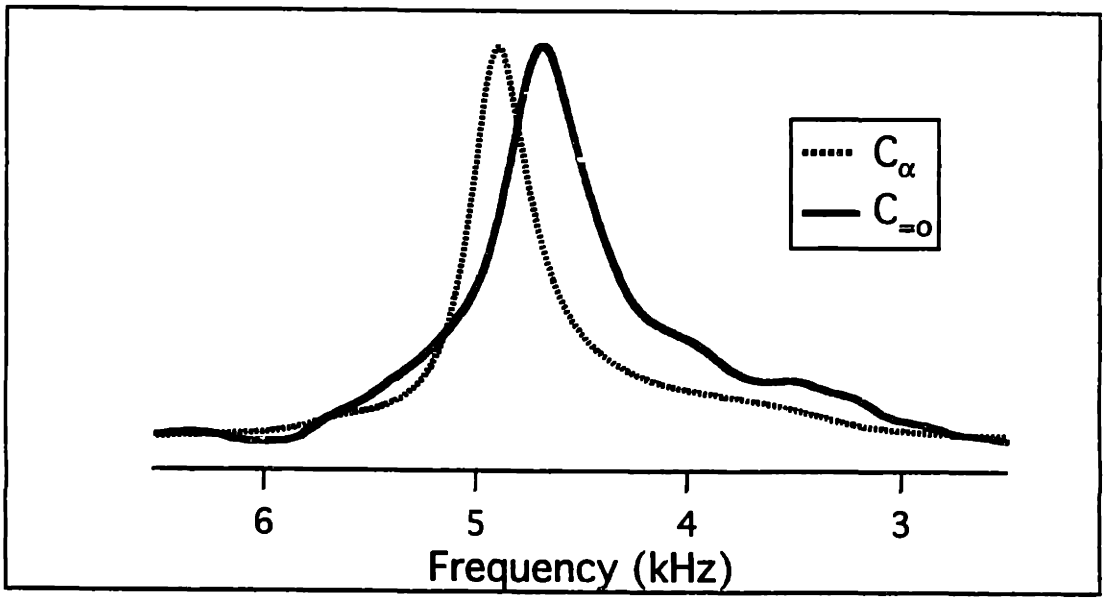
C_α
$C_{=O}$
6
5
4
3
Frequency (kHz)

(B)

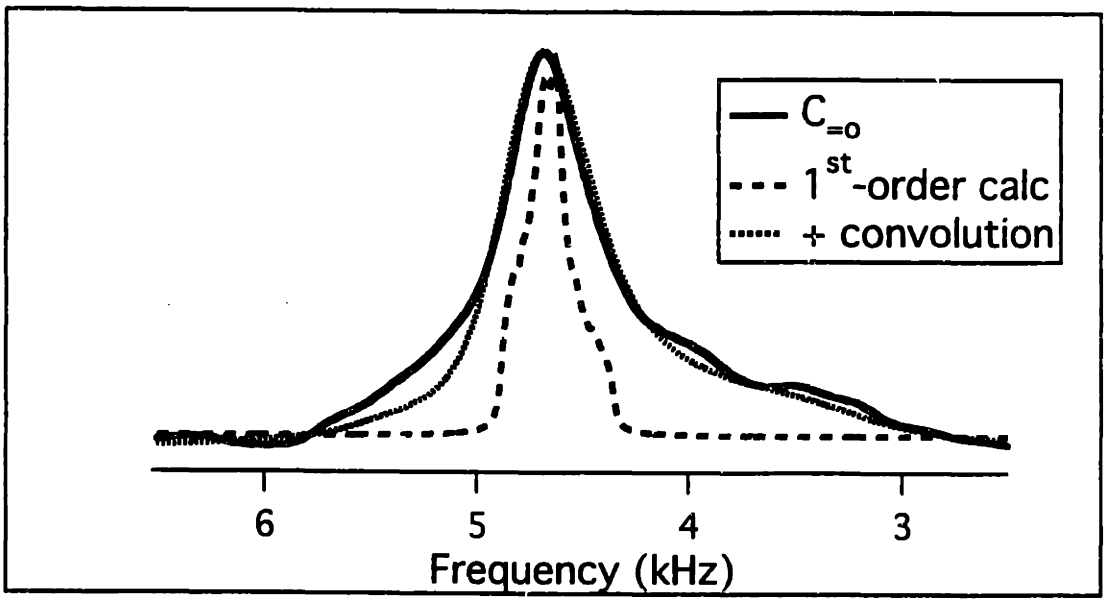
$C_{=O}$
1st-order calc
+ convolution
6
5
4
3
Frequency (kHz)

factor of two (increases in the rf field count twice towards the resonance condition as they affect both spins). For systems with two significant CSA's, such as the (assumed) intermolecular carboxyl pairs giving rise to the dipolar resonance in Fig. (3-1), the shifts from each of the spins will add in an orientation-dependent manner, and (because both shifts are always negative) will always be larger than the shift induced by either CSA alone. The observed shift in the dipolar resonance condition in Fig. (3-1), 0.4kHz, is consistent with the measured shift in the carboxyl precession frequency under similar conditions. Clear evidence of the expected broadening in the dipolar resonance is difficult to discern given the level of rf inhomogeneity in these experiments. In experiments where the rf inhomogeneity has been minimized (for example by packing the sample only in the central section of the rotor), we expect the resonance-broadening effect to become more evident. Application of the HORROR technique to spin-pairs with significant CSA interactions will therefore suffer efficiency reductions due to this broadening that are similar to those suffered in n=1 RR experiments due to chemical shift dispersion, and these reductions can not be compensated for (as rf-inhomogeneity is) by reducing the spatial dimensions of the sample within the coil.

3.2F Alternative Resonance Conditions.

In systems with small chemical shift differences, or large chemical shift differences and symmetric carrier placement, exploitation of all of the dipolar resonance conditions described by equ (14) are blocked - except (n=1, Σ) - by simultaneous recoupling of the CSA interaction. Given large chemical shift differences and asymmetric carrier placement, however, (n=2, Σ) and (n=1,2 Δ) conditions can be matched while avoiding CSA

recoupling. The concept is simple: with the carrier placed asymmetrically (for instance, very close to one resonance in a well-separated two resonance spectrum), the effective fields of the two spins have significantly different magnitude, so that their sum (or difference) can equal ω_r or $2\omega_r$ without either effective field itself having a magnitude approaching those values.

Implicit in this concept is the idea that the effective fields of the two spins - which will have significantly different chemical shift contributions - will generally point in different directions. Consider, for instance, a 2-spin system in which the resonance frequencies of the 2 spins are separated by 10.2 kHz. Diketopiperazine (DKP), with a (1-α2) $^{13}C_2$ labeling scheme ($b_{IS} \approx 0.5$kHz), yields such a spectrum (Fig 3-5). If the carrier frequency is placed near the upfield peak, so that the spins have offsets of +9.8kHz and -0.4kHz, and the spinning speed set to 6.2 kHz, the resonance spectrum displayed in Fig. (3-6A) results. (CP followed by a short period without decoupling was used to selectively excite the carbonyl carbon; the standard longitudinal mixing sequence in Fig. (3-3A) was used to monitor evolution under a series of rf field strengths, with the mixing time fixed at 5ms). Given an rf field of approximately 2.3kHz, the sum of the effective fields (2.3 and 10.1kHz, respectively) equals twice the spinning speed, and recoupling occurs as evident by the dip in the recoupling spectrum. At this condition, the effective field for the carboxyl carbon is approximately longitudinal (tilted away from the z-axis by 13°), while the effective field for the alpha carbon is approximately transverse (tilted out of the plane by 10°). The larger dip at higher field strengths is primarily due to CSA recoupling, when the carboxyl effective field strength approaches twice the spinning speed.

Figure 3-5: Spectrum and effective field diagram for 1-α2 $^{13}C_2$-labeled diketopiperazine (DKP). At 7.4T, the chemical shift difference is approximately 10.2kHz. With the carrier placed near the alpha carbon resonance (at 0kHz), the effective field orientations for rf field magnitudes in the 2-4kHz regime are as shown: the carbonyl effective field is approximately longitudinal, the alpha carbon effective field is approximately transverse.

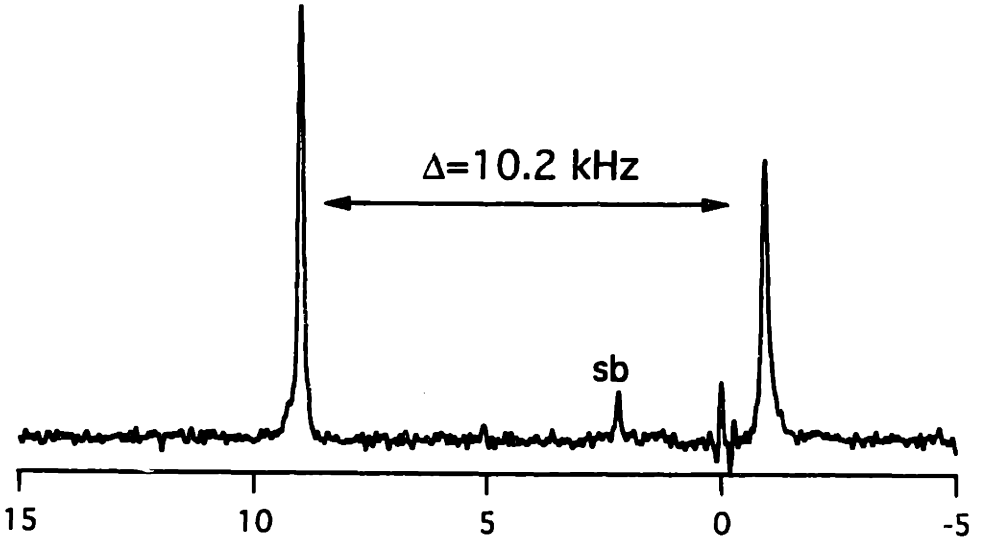
Δ=10.2 kHz
sb
15
10
5
0
-5

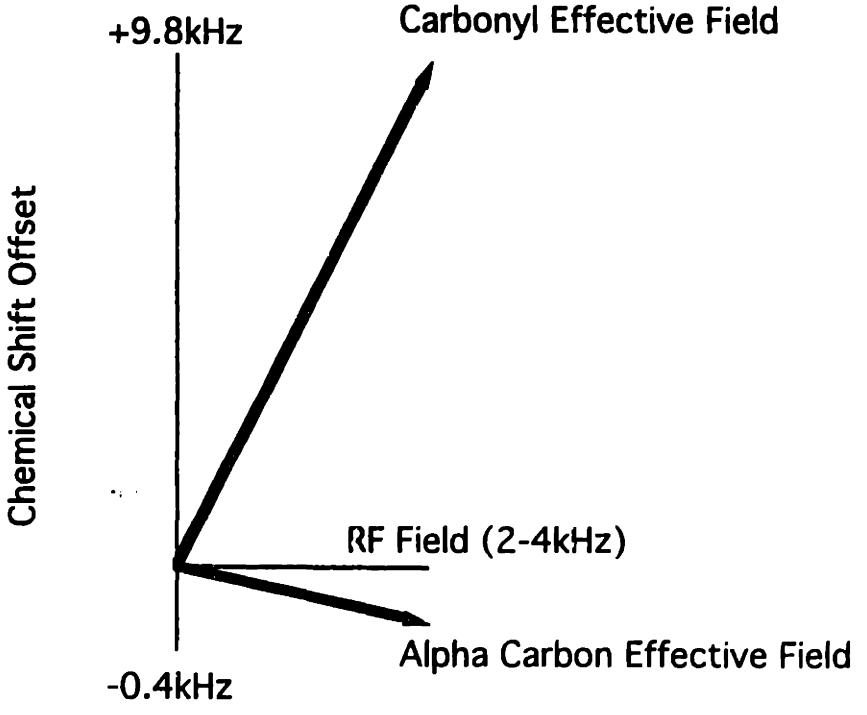
+9.8kHz
Carbonyl Effective Field
Chemical Shift Offset
RF Field (2-4kHz)
Alpha Carbon Effective Field
-0.4kHz

Figure 3-6: Residual carbonyl magnetization after mixing at various rf field strengths for 5ms (pulse sequence diagrammed in Fig. 3-2A):

(A) With ω_r=6.2kHz, an rf field strength of 2.3kHz yields effective field magnitudes that sum to twice the spinning speed, and dipolar recoupling without simultaneous CSA recoupling occurs at the (n=2, Σ) resonance condition. In this and subsequent plots, the large dip at high rf field strength is primarily driven by reintroduction of the carbonyl CSA interaction, when its effective field magnitude equals twice the spinning speed.

(B) With ω_r=6.8kHz, the rf magnitude at which the (n=2, Σ) resonance occurs increases (approx. 3.3kHz), and a dip corresponding to recoupling of the (n=1, Σ) dipolar component appears, as indicated.

(C) At ω_r=7.5kHz, the two dipolar resonance peaks have switched positions.

(A)

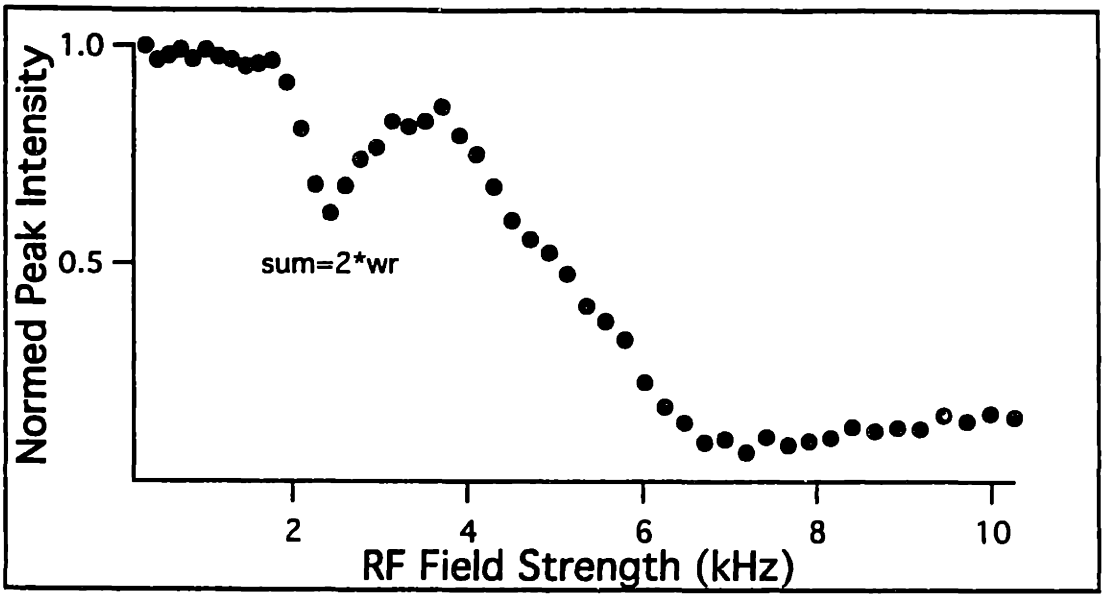
Normed Peak Intensity
1.0
0.5
sum=2*wr
2
4
6
8
10
RF Field Strength (kHz)

(B)

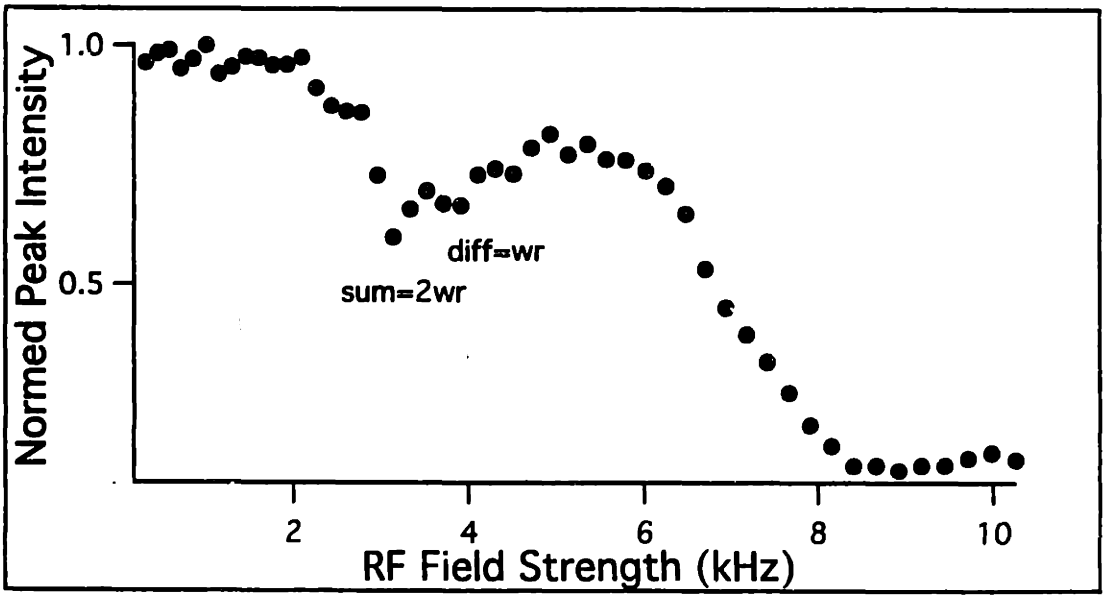
Normed Peak Intensity
1.0
0.5
diff=wr
sum=2wr
2
4
6
8
10
RF Field Strength (kHz)

(C)

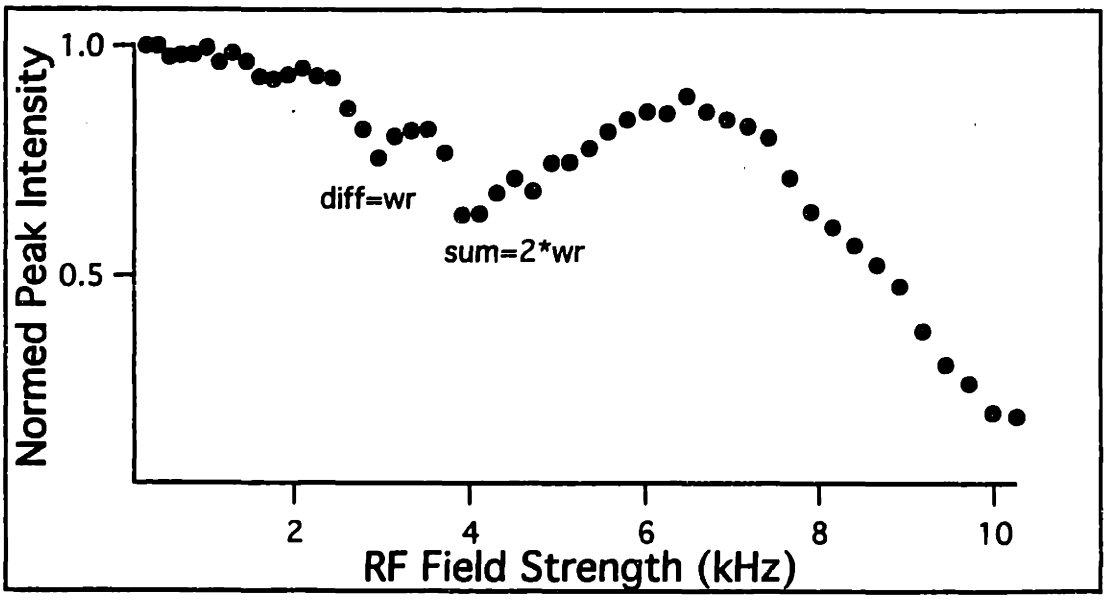
Normed Peak Intensity
1.0
0.5
diff=wr
sum=2*wr
2
4
6
8
10
RF Field Strength (kHz)

Increasing the spinning speed to 6.8kHz yields the recoupling spectrum in Fig. (3-6B). The rf magnitude at which the sum of the magnitudes equals twice the spinning speed has increased (to 3.3 kHz), and the rf magnitude at which the difference equals the spinning speed has moved out from under the large CSA dip, as shown (to 3.7kHz). At even higher spinning speed (7.5kHz, Fig. (3-6C), the two dipolar resonance dips have switched positions.

The usefulness of this type of effect is limited by the magnitude of the recoupled dipolar interaction. The coefficient C_X ($X=\Sigma$ or Δ) appropriate for these cases, calculated from equ (11) above, is on the order of 0.2-0.3, while for comparison the RR value is 0.5 and the 2Q-HORROR value is 0.75. Hence application to weakly-coupled systems is limited, particularly in cases where relaxation effects are significant. For more strongly-coupled systems of the type shown here, however, the effect is observable even at short mixing times. Given this caveat, recoupling using one of the resonance conditions described in this section might have several uses when the strength of the recoupled interaction does not pose a problem. For example: by having one effective field (nearly) longitudinal, and one (nearly) transverse, we expect the dynamics to show RR-like dependence on CSA/dipolar orientation (of the type described at the end of chapter two) only for the CSA of the spin experiencing the longitudinal effective field. And because recoupling can be performed at relatively low frequencies comparable to the magnitude of typical CSA's, we expect the orientation dependence of the dynamics to be significant. Such an experiment might provide an alternative, for instance, to the n=2 RR experiments described at the end of Chapter Two, where the dependence on the alpha carbon CSA is removed, and ramping through the resonance

condition (discussed in later sections of this chapter) reduces dependence on CSD and 2-spin coherence relaxation.

3.3 Ramping Through the Resonance Condition.

3.3A On-Resonance vs. Ramp-Through Spin Dynamics.

RR recoupling experiments are generally performed by placing the system on resonance (i.e. matching spinning speed to chemical shift difference), preparing the appropriate initial condition (e.g. transverse or longitudinal, sum or difference polarization), and then observing the effects of dipolar evolution[2, 18]. The on-resonance dynamics are complicated by the breadth in the resonance condition arising from chemical shift dispersion, and from the effects of relaxation on 2Q coherences created during dipolar evolution. Analogous effects occur in 2Q-HORROR experiments, where the broadening in the resonance condition arises primarily from rf inhomogeneity and the off-resonance CSA effect we have discussed (but does not have a significant contribution from minor variations in chemical shift - i.e. chemical shift dispersion). These effects include reductions in polarization transfer efficiency, and make it difficult to extract accurate distance information without detailed knowledge of the nature of the broadening and relaxation effects. Similar problems occur even in broadband recoupling sequences (e.g. RFDR[12], DRAMA[24], MELODRAMA[13], R/L[25]), where the vigorous manipulation of the low-γ polarization to induce recoupling over a sizable bandwidth is sensitive to rf imperfections, and to the reduction in ^{1}H decoupling efficiency that occurs upon simultaneous application of ^{1}H and low-γ rf. This last effect is of particular concern, because it leads to significant signal loss during extended mixing periods, and so limits the applicability of these sequences in weakly coupled systems (i.e. long distances) unless very high decoupling powers can be applied.

Longitudinal dipolar mixing experiments that use an rf field to induce recoupling at the (n=1, Σ) resonance condition are not strongly sensitive to rf imperfections, and signal loss during mixing for experiments in the RRT regime is often negligible even for long mixing periods (100 ms) at relatively low ^{1}H decoupling power (50-60 kHz). This is primarily due to the small size and constant nature of the rf perturbation, to the fact that the magnetization remains spin-locked during mixing rather than evolving about the effective field, and to the T_1-dominated dependence of the relaxation rate of spin-locked polarization during mixing. Ramping the amplitude of the applied rf such that the system passes through the desired resonance condition(s) can reduce (or even eliminate) the remaining dependence on the resonance broadening influences we have discussed. Consider the time-dependence imposed on the recoupled average Hamiltonian for a spin pair evolving under a linearly ramped rf field (where the ramp rate ($\dot{\omega}_1$) is assumed to be much slower than the spinning speed, so that the average Hamiltonian calculation can be assumed to occur at approximately constant rf power), diagrammed in Fig. (3-7). Far from resonance ($\omega_\Sigma^\epsilon >> \omega_r$) the Hamiltonian is dominated by residual effective field terms and points approximately along the +z axis of the fictitious spin-1/2 space. As the rf amplitude is decreased, the vector representing the Hamiltonian rotates towards and through the transverse plane as resonance is achieved, and then to the -z axis as the system moves away from resonance in the opposite direction ($\omega_\Sigma^\epsilon << \omega_r$). The angular velocity ($d\phi/dt$) of the Hamiltonian rotation for a linear ramp of the rf field strength is:

$$\dot{\phi} = \frac{d\phi}{dt} = \frac{d}{dt}\left(\tan^{-1}\left[\frac{|\tilde{\omega}_d|}{\omega_\Sigma^\epsilon - \omega_r}\right]\right) = \dot{\omega}_\Sigma^\epsilon\left(\frac{|\tilde{\omega}_d|}{\left(\omega_\Sigma^\epsilon - \omega_r\right)^2 + |\tilde{\omega}_d|^2}\right) \qquad (30),$$

Figure 3-7: In the appropriate fictitious spin-1/2 subspace, the vector representing the Hamiltonian consists of resonance mismatch (longitudinal) and recoupled dipolar (transverse) components. When far from resonance ($\omega_\Sigma^\varepsilon >> \omega_r$), the mismatch component dominates and the vector representing the Hamiltonian points nearly along the positive longitudinal axis. As the rf component of the effective fields is reduced to approach resonance, the longitudinal component shrinks and the vector representing the Hamiltonian both shrinks in size and rotates towards the transverse plane. As resonance is matched, and the past, the vector rotates through the transverse plane towards the negative longitudinal axis. As the rf field strength continues to shrink, the system moves farther from resonance and the vector representing the Hamiltonian approaches the negative longitudinal axis. If this process is performed slowly enough (see text) and relaxation effects are minimal, the density operator will follow the Hamiltonian, leading to inversion of sum polarization.

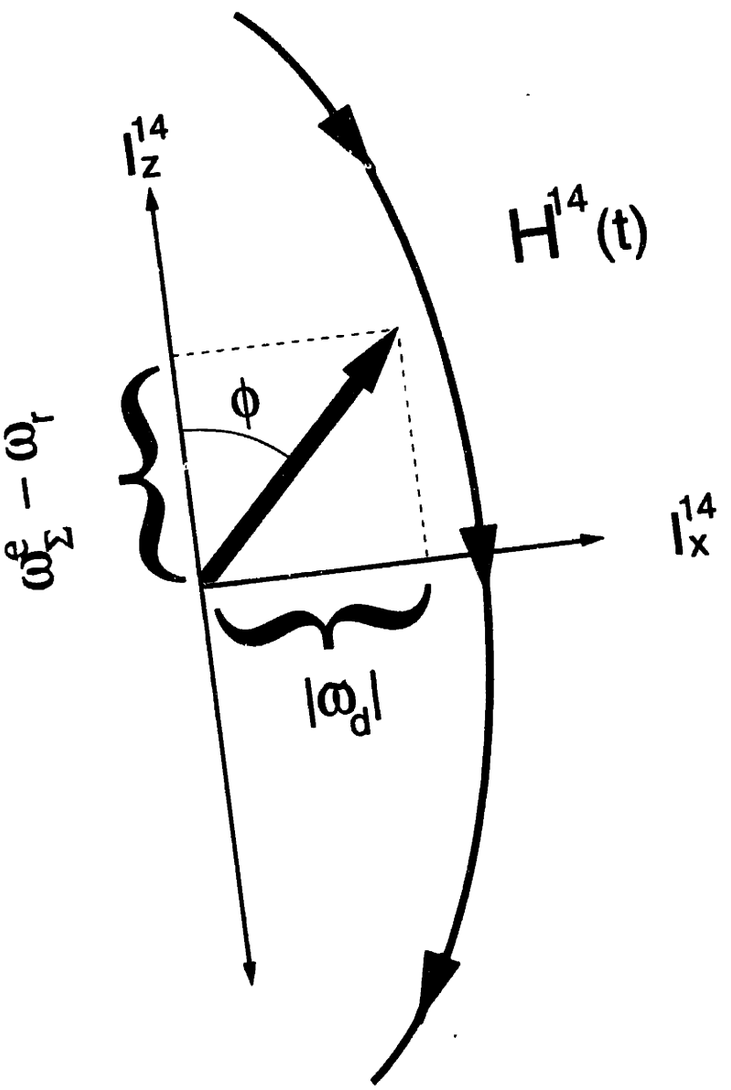
I_z^{14}
$H^{14}(t)$
ϕ
$\omega_\Sigma^e - \omega_r$
I_x^{14}
$|\omega_d|$

where $\dot{\omega}_{\Sigma}^{\varepsilon} = \dot{\omega}_1\left(\alpha_{RF}^{I} + \alpha_{RF}^{S}\right)$. We expect (almost) identical manipulations of the Hamiltonian for spin pairs with slightly different resonance conditions due to broadening influences, as long as the ramp starts far enough to one side of the resonance condition and ramps far enough past the opposite side. Because all spin pairs experience the same rotation of the Hamiltonian (and at identical rates), we expect them to exhibit identical spin dynamics independent of the precise location of their resonance condition within the broader distribution. This is rigorously true for shifts in resonance due to rf inhomogeneity (ignoring edge effects), and approximately true for shifts due to chemical shift dispersion, where resonance occurs at a slightly different rf field strength and hence effective field orientation. In experiments in which quantitation of the coupling is important, measurement of the spin dynamics (e.g. the amount of sum or difference polarization remaining after mixing) as a function of the ramp rate yields a magnetization exchange curve, from which of the magnitude of the dipolar coupling can be extracted.

Linear ramping of the rf magnitude ($\dot{\omega}_1 = \text{constant}$) leads to a linear ramp of the effective field strengths in the 2Q-HORROR regime, and in the RRT regime when the ramp range is small relative to the spinning speed (so that $\alpha_{RF}^{X} \approx \text{constant}$). For linearly changing effective field strengths, however, the angular velocity of the (slowly) rotating Hamiltonian is not constant during the rotation. The angular velocity of the Hamiltonian has a lorentzian distribution (as a function of resonance offset) under this type of rf manipulation, peaked on resonance ($\phi = 90°$), where the magnitude of the Hamiltonian is minimized. The peak in the Hamiltonian rotation rate reduces polarization transfer efficiency, particularly when one is trying to induce adiabatic dynamics.

Adiabatic manipulation of the spin system (changing the Hamiltonian slow enough so that the state of the system follows) requires that the magnitude of the Hamiltonian be much larger than its rate of rotation due to rf manipulation[26]. We can define an adiabatic parameter (AP) as the ratio of these values (magnitude over rotation rate) to characterize the degree to which this condition is satisfied; values much greater than one indicate adiabatic manipulation. For the linear ramp we have discussed, AP is minimized at $\phi = 90°$, and hence conservatively we require

$$AP_{MIN} = \frac{|\tilde{\omega}_d|}{\dot{\phi}_{max}} = \frac{|\tilde{\omega}_d|^2}{\dot{\omega}_\Sigma^e} >> 1 \qquad (31)$$

for adiabatic manipulation of the system. Clearly linear ramps are not optimal for adiabatic experiments because of the peak in the angular velocity. Alternative (non-linear) rf manipulations have much broader angular velocity distributions, allowing shorter overall mixing periods consistent with matching the adiabatic condition throughout the sweep. Meier et al have suggested shapes of the effective field manipulation, in the context of heteronuclear CP, which impart approximately constant angular velocity to the Hamiltonian during the adiabatic sweep[27].

Application of non-linear ramp techniques of this type requires some vaguely defined resonance region where the majority of the spin pairs are approximately on resonance, so that the rf ramp rate can be reduced to compensate in part for the reduction in the magnitude of the Hamiltonian near resonance. For systems in which the breadth in the resonance condition (measured in terms of effective fields) is much larger than the size of the recoupled interaction, this region is not easily defined and the effectiveness of these techniques is reduced. Furthermore, changes in the ramp rate during mixing are not consistent with the needs of experiments

aimed at inducing identical manipulations for all spin pairs within a broadened resonance condition so that the effect of the broadening on the spin dynamics is minimized. Although some modification of the basic linear ramp may be useful in improving the overall efficiency of these experiments without reintroducing broadening-dependent effects, here we use linear ramps to avoid the issue altogether.

3.3B Ramped Rotational Resonance Tickling Applied to Weak Couplings: Accurate Internuclear Distance Measurements.

In experiments where the n=1 RR recoupling technique is being used to induce homonuclear dipolar evolution, the RR tickling (RRT) technique may provide an improved alternative. Spinning the sample slightly faster than dictated by the n=1 resonance condition and then applying a weak rf field to scale up the effective fields and achieve resonance allows experimental control over matching of the resonance condition on short (μs) timescales without sacrificing many of the benefits of standard RR experiments (including chemical shift selectivity, and T_1-dominated relaxation of polarization during mixing). RF control affords several additional benefits, including the ability to extend the effective recoupling bandwidth by ramping the rf over some range. One application is in two-dimensional experiments where chemical shift selectivity combined with recoupling bandwidth can be applied to multiply-labeled systems (discussed in the following chapter). Here we focus on ramping through a broadened resonance condition to reduce the dependence on chemical shift dispersion. Our goal is accurate extraction of the internuclear distance.

The spectrum of doubly ^{13}C-labeled tyrosine ethyl ester (TEE), where the labels are at the $-CH_2-$ of the ester moiety and the 4'-OH aromatic carbon (and the labeled material is diluted 1:10 in natural

abundance), is shown in Fig. (3-8A). The intramolecular internuclear distance is 5.05 Å (from the structure determined by x-ray analysis), yielding a 0.059 kHz coupling constant. At 9.4 T, the chemical shift difference is 9.410 kHz. Spinning at 9.900 kHz (±2 Hz) then necessitates the application of a 1.54 kHz rf field (carrier frequency placed precisely between the two peaks) to achieve resonance. The effective fields in this case are rotated from longitudinal by approximately 18° (Fig. 3-8B). Preparation of sum and difference magnetization along the effective fields followed by mixing at various rf field strengths (pulse sequence in (3-3A)) allows mapping of the recoupling spectrum. The RI (RO) pulse consisted of 50 30μs linear steps from (to) 0 kHz rf power to (from) the appropriate field strength for mixing at each point. Fig. (3-9A) shows the residual sum and difference polarization after 100 ms of mixing at a series of rf field strengths. Selective decay of difference polarization (this refers to the rotating, not tilted, frame) occurs when resonance is matched. Plotting the difference between residual sum and difference polarization (3-9B) yields a closer view of the dipolar resonance (note that the data in 3-9A and B were taken under different conditions). The resonance condition in (3-9B) is shifted slightly upfield from the expected value of 1.54 kHz based on isotropic chemical shifts. The perpendicular components of the CSA interaction are too small here to induce this shift by the mechanism described earlier, so we attribute it to the method by which we characterize the asymmetric rf field distribution that occurs at a given rf power level as a single rf field strength (the peak value of the measured distribution). The inset shows a typical rf field distribution (obtained using the standard nutation technique). The width (FWHM) is approximately 7% (0.10 kHz) of the peak value (1.45 kHz). The rf field strengths as a function of input

Figure 3-8: Relevant parameters for RRT experiments applied to $^{13}C_2$-labeled TEE:

(A) ^{13}C spectrum of TEE sample, obtained at ω_r=9.9kHz. The chemical shift difference at this field strength (9.4T) is 9.41kHz. With the carrier placed between the two resonance, the isotropic chemical shift offsets are equal to ±4.705kHz.

(B) Diagram of the effective field axes and their components. Matching resonance requires each effective field equal 9.9/2=4.95kHz. Given the offsets in TEE, this requires a rf field strength of 1.54kHz. The effective fields in this situation are rotated from longitudinal by 18°.

(A)

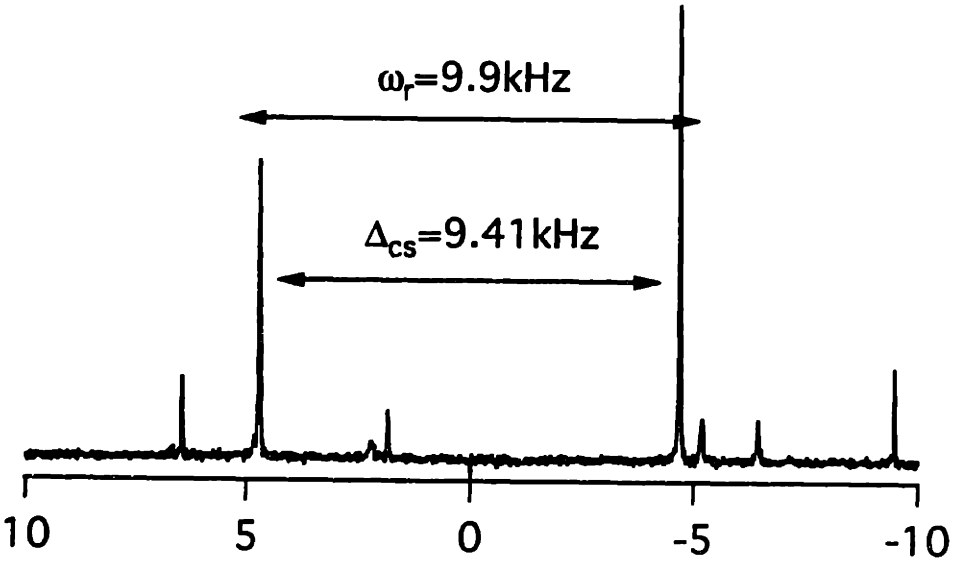
ω_r=9.9kHz
Δ_{cs}=9.41kHz
10
5
0
-5
-10

(B)

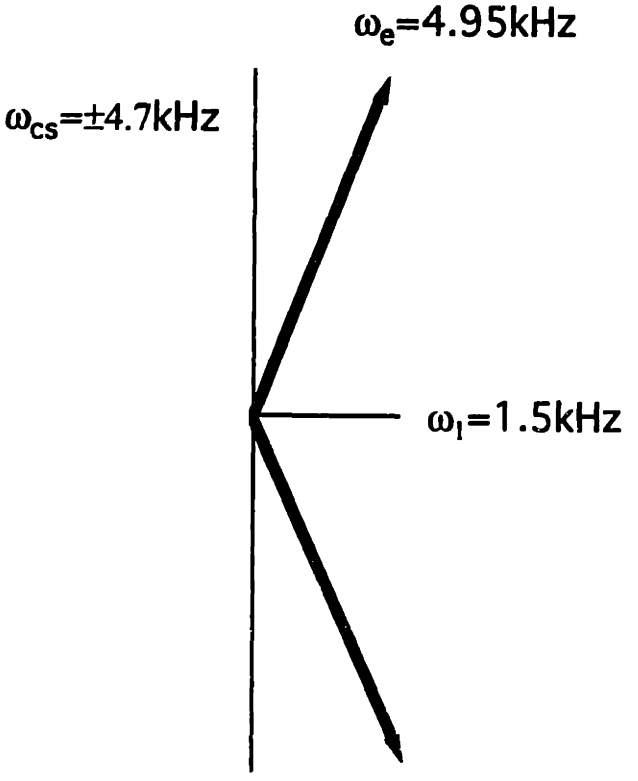
ω_e=4.95kHz
ω_{cs}=±4.7kHz
ω_1=1.5kHz

Figure 3-9: Mapping of the (n=1, Σ) resonance condition in $^{13}C_2$-labeled TEE (100ms mixing time):

(A) "Resonance spectrum" of $^{13}C_2$-labeled TEE (taken at 7.4T, so that the isotropic chemical shift difference was 7.5kHz, and ω_r=8.15kHz). Selective decay of difference polarization (filled circles) at low rf field indicates the dipolar recoupling effect. Decay of both sum (open circles) and difference polarization at higher field indicates CSA recoupling.

(B) A plot of the difference between residual sum and difference polarization (filled circles) at each rf field strength maps out the dipolar resonance condition. Note that this data was taken at 9.4T, under the conditions described in the text. The resonance has a width of approximately 0.4kHz, and is centered at a somewhat higher field than expected from the spinning speed and chemical shift difference. This shift is likely not due to the CSA effect detailed earlier (see text). The level of rf-inhomogeneity is shown in the inset (results of a standard 2D nutation sequence applied to the TEE methylene resonance). Lines under the resonance indicate ramp ranges (see text).

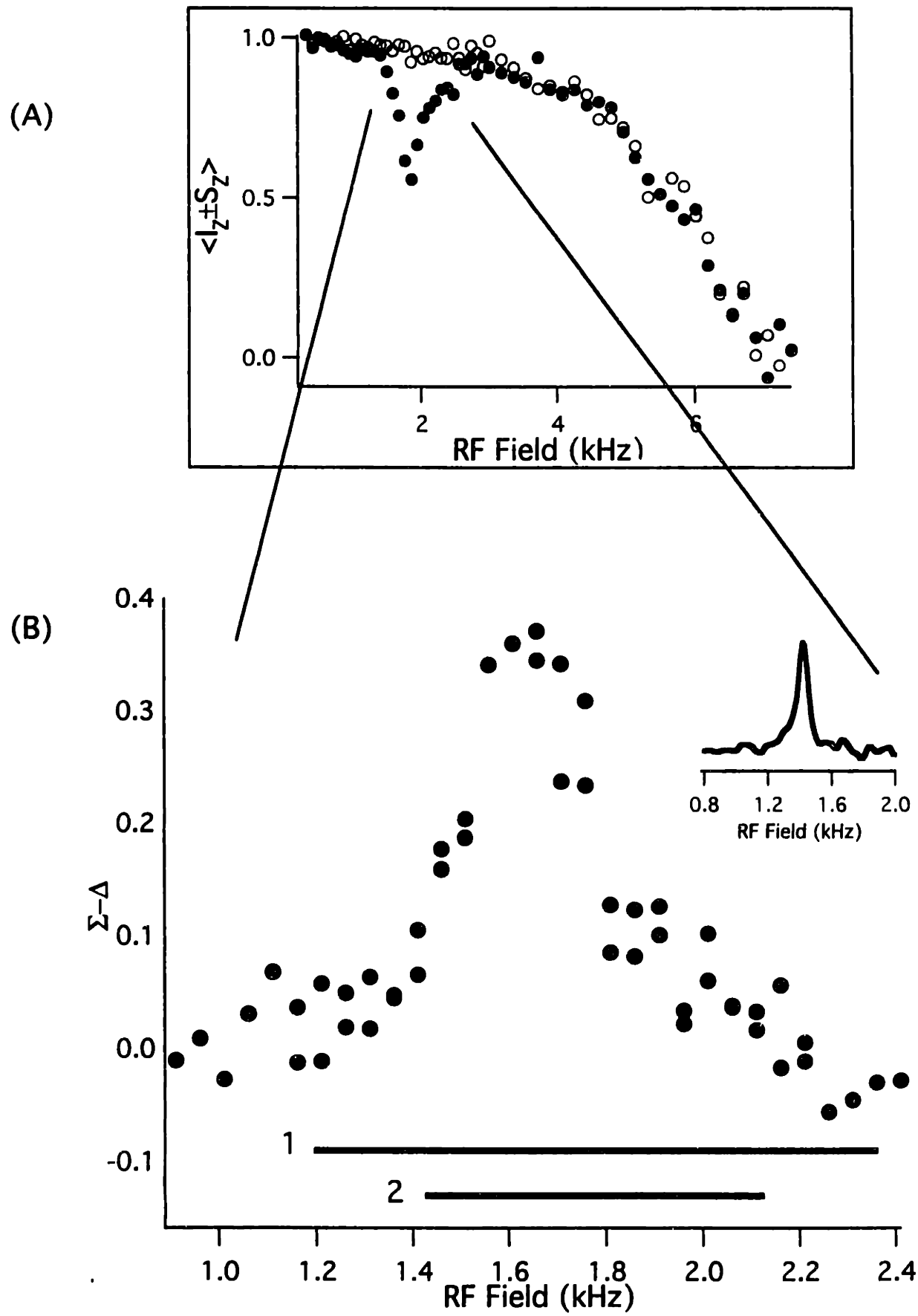
(A)
1.0
0.5
0.0
<I_z±S_z>
2
4
6
RF Field (kHz)
(B)
0.4
0.3
0.2
0.1
0.0
-0.1
Σ-Δ
0.8
1.2
1.6
2.0
RF Field (kHz)
1
2
1.0
1.2
1.4
1.6
1.8
2.0
2.2
2.4
RF Field (kHz)

rf peak-to-peak voltage (ppV) were determined by obtaining 2D nutation spectra[23] at a series of field strengths (≈5) spanning the range of interest (here, approximately 1.0-2.0 kHz), interpreting the peak of the resulting rf distribution in each case as the field strength corresponding to that ppV level, and then fitting the resulting data points to determine the functional relationship between the two. Results in all cases were approximately linear, so that the linear ramps in input ppV induced linear ramps in rf field strength.

The recoupled resonance condition has an rf field width (FWHM) of approximately 0.3 kHz, measured in terms of rf field strength. Translating this into effective field terms ($\times\alpha_{RF}^{x} \approx 0.35$) yields 0.1kHz, this width deriving mainly from the natural width of the recoupling effect combined with the distribution in resonance frequencies arising from chemical shift and, to a lesser extent, rf inhomogeneity. The rf field ranges for the two ramps we applied to this system are indicated by solid lines under the recoupling spectrum (Fig. (3-9)). The first ramp (2.35-1.20 kHz; 1.15 kHz wide) extends significantly beyond both edges of the peak (upfield being more critical than downfield due to the trailing-edge nature of the rf distribution), while the second ramp (2.15-1.45 kHz; 0.70 kHz wide) cuts the edges more closely. These correspond to effective field ramp widths of approximately 0.35 and 0.21 kHz, respectively.

The residual difference polarization after dipolar mixing (corrected for natural abundance background contribution to the detected signal, see Chapter One) is plotted in Fig. (3-10) for the doubly-labeled TEE sample as a function of rf ramp rate. The slowest rates correspond to the longest mixing time, here 100 ms. No detectable decay of sum polarization (±2-4%) was observed for even the longest mixing times (data not shown).

Figure 3-10: Ramped-RRT spin dynamics in $^{13}C_2$-labeled TEE. Experimental data plotted vs. ramp rate for two different ramps (ramp ranges indicated in Fig. (3-9)) and two different ^1H decoupling powers (56 and 76kHz). Solid lines show the results of a simulation using appropriate CSA and dipolar spin Hamiltonian parameters, ignoring relaxation effects. Dotted lines show the results of similar simulations (at 3 different dipolar coupling strengths) which include the effects of 2Q-relaxation (see text). Large variations in the 2Q-relaxation rate (+/- 50%) do not cause significant changes in the simulated curves. In all cases, the data lies along the appropriate (5.05Å) simulation.

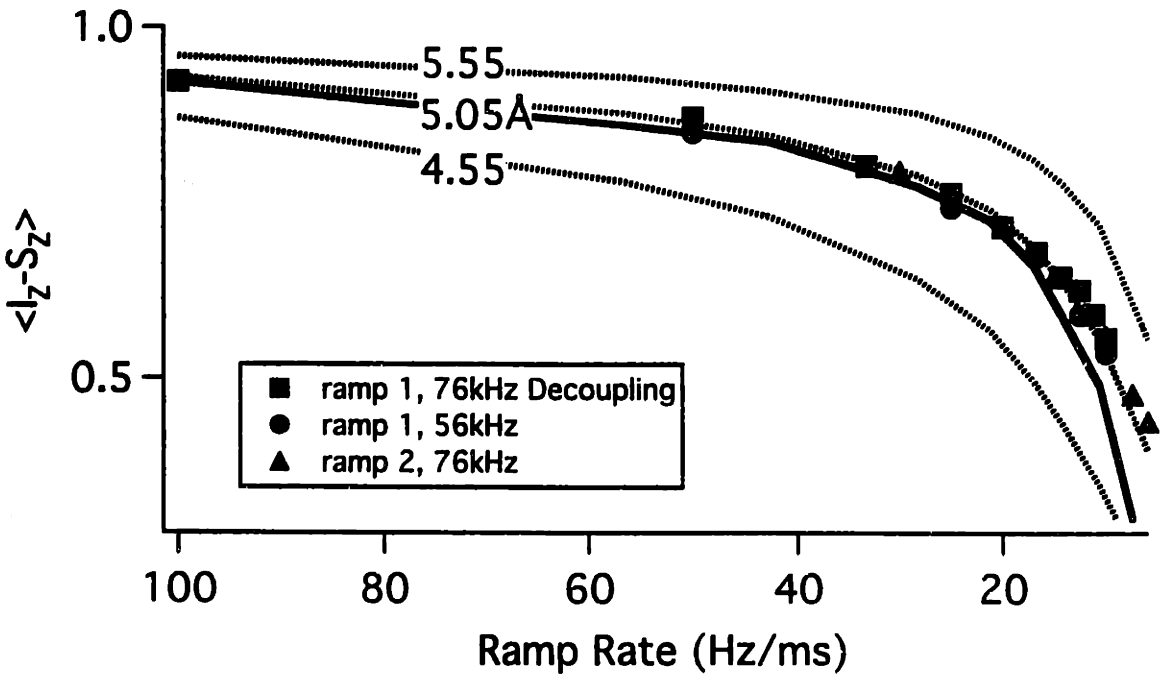
1.0
0.5
<I_z-S_z>
5.55
5.05Å
4.55
ramp 1, 76kHz Decoupling
ramp 1, 56kHz
ramp 2, 76kHz
100
80
60
40
20
Ramp Rate (Hz/ms)

The data obtained using the two different ramps lie on the same curve when plotted as a function of ramp rate - hence the dynamics are not sensitive to the specific details of the ramp. Maximum polarization transfer at the slowest ramp rate is increased by approximately 50% over on-resonance evolution with the same overall mixing time (τ_m=100ms; on-resonance decay of difference polarization at this mixing time can be read from the peak of the resonance condition in Fig. (3-9)). Changes in decoupling power (76 to 56 kHz) do not induce observable changes in the ramp-rate exchange curve, as shown. Simulations of the exchange dynamics using various internuclear distances (by numerical integration of the equations of motion derived from the time-dependent rotating-frame Hamiltonian and explicitly including the effects of RI, mixing, and RO periods) are indicated by solid (no relaxation) or broken (100 Hz relaxation rate for 2-quantum coherences) lines. In the simulated dynamics the 2Q relaxation rate was applied to 2Q coherences relative to the rotating frame rather than the interaction frame, which is not technically correct. The near alignment of the two systems (effective-field tilts from longitudinal no more than 24° during the ramped exchange process), and the small effect relaxation has in these experiments, suggest that this introduces a negligible error.

We want to emphasize three features of the technique evident in the plots we have just described. First, the decay of difference polarization as a function of ramp rate is strongly dependent on the magnitude of the dipolar coupling constant, as indicated by simulation. This verifies the possibility that distance information can be extracted from the observed dynamics. Second, accurate simulation of the dynamics does not require inclusion of the effects of chemical shift dispersion or rf inhomogeneity.

These factors do not affect the spin dynamics, for the reasons we have described. Third, the dependence of the spin dynamics on the rate of 2Q relaxation is reduced relative to RR. The chosen value for the RRT simulations (100 Hz, corresponding to T_2^{zq}=10ms) is a rough estimate; changes by a factor of two in either direction do not significantly affect the result in the regime we show here. Furthermore, changes in the decoupling power which might be expected to result in different 2Q relaxation rates and hence different exchange dynamics have no discernible effect. This is in contrast to data obtained under similar conditions using the n=1 RR technique, shown in Fig. (3-11). Different ^{1}H decoupling power (again, 56 and 76kHz) in this case yields very different dynamics. A simulation of the n=1 RR data using the known internuclear distance and disregarding the effects of chemical shift dispersion and 2Q-relaxation (solid line) does not closely match either of the plotted data sets (it has a minimum (off the bottom of the plot) of approximately -0.5 at 30 ms). Simulations using estimates of the nature of the CSD-broadened resonance condition and the 2Q-relaxation rate at 76kHz ^{1}H decoupling (see Chapter One) provide a better fit (dotted lines), but the sensitivity to small errors in these estimates is indicated by the magnitude of the change induced in the experimental data by changing the ^{1}H decoupling power. The induced change is as large as that expected for a 0.5 Å change in the internuclear distance.

Fig (3-12) illustrates more clearly the reduced 2Q-relaxation rate dependence of the dynamics of the ramped RRT experiment as compared to standard n=1 RR. The simulations in these plots were performed as described above, with changes in relaxation rates and dipolar coupling constants as indicated. Again we point out that the simulated relaxation

Figure 3-11: On-resonance n=1 RR spin dynamics in $^{13}C_2$-labeled TEE. Experimental data plotted vs. mixing time for two different ^1H decoupling powers (56 and 76kHz). Simulation absent relaxation and chemical shift difference distribution effects (solid line), and using the appropriate coupling (corresponding to 5.05Å) is far from the experimental data. Simulations including 2Q-relaxation and difference distribution contributions (performed for 3 values of the dipolar coupling constant; dotted lines) more closely match the 76kHz data, but the decoupling-power induced change in measured exchange curve illustrates the sensitivity of the dynamics to small changes in these parameters.

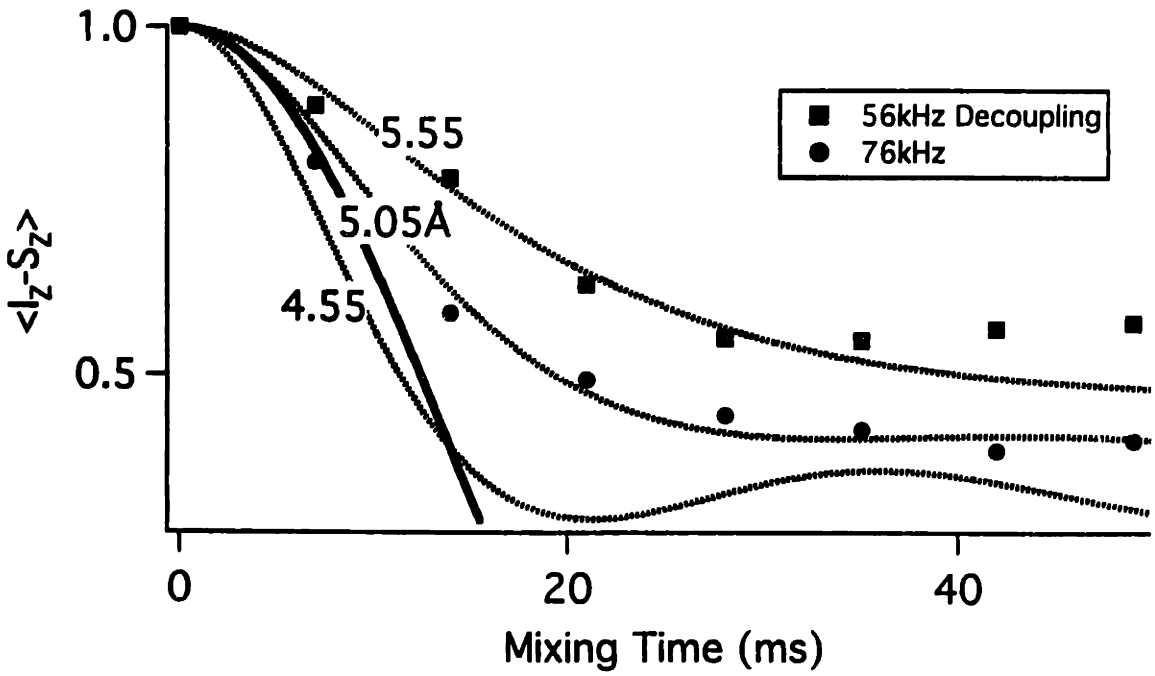
1.0
0.5
<I_z-S_z>
5.55
5.05Å
4.55
56kHz Decoupling
76kHz
0
20
40
Mixing Time (ms)

Figure 3-12: Comparison of 2Q-relaxation rate dependence of on-resonance n=1 RR and ramped-RRT dynamics.

(A) Simulations of n=1 RR dynamics using TEE parameters given in the text, and 2Q-relaxation rates and dipolar coupling constants as indicated. The large plot shows the variation in the dynamics at a fixed coupling strength (corresponding to 5.05Å) and a series of relaxation rates, while the inset shows, for comparison, the variation at a fixed relaxation rate and a series of coupling constants. The changes in both plots look similar, both in magnitude and shape, indicating the difficulty of extracting one parameter (b_{IS}) without accurately knowing the other.

(B) Simulations of ramped-RRT dynamics using parameters as in (A). The changes in the dynamics induced by variation of the 2Q-relaxation rate are much smaller than those induced by changes in the coupling, suggesting the possibility of increased accuracy in cases where zero-quantum relaxation rates are not known accurately.

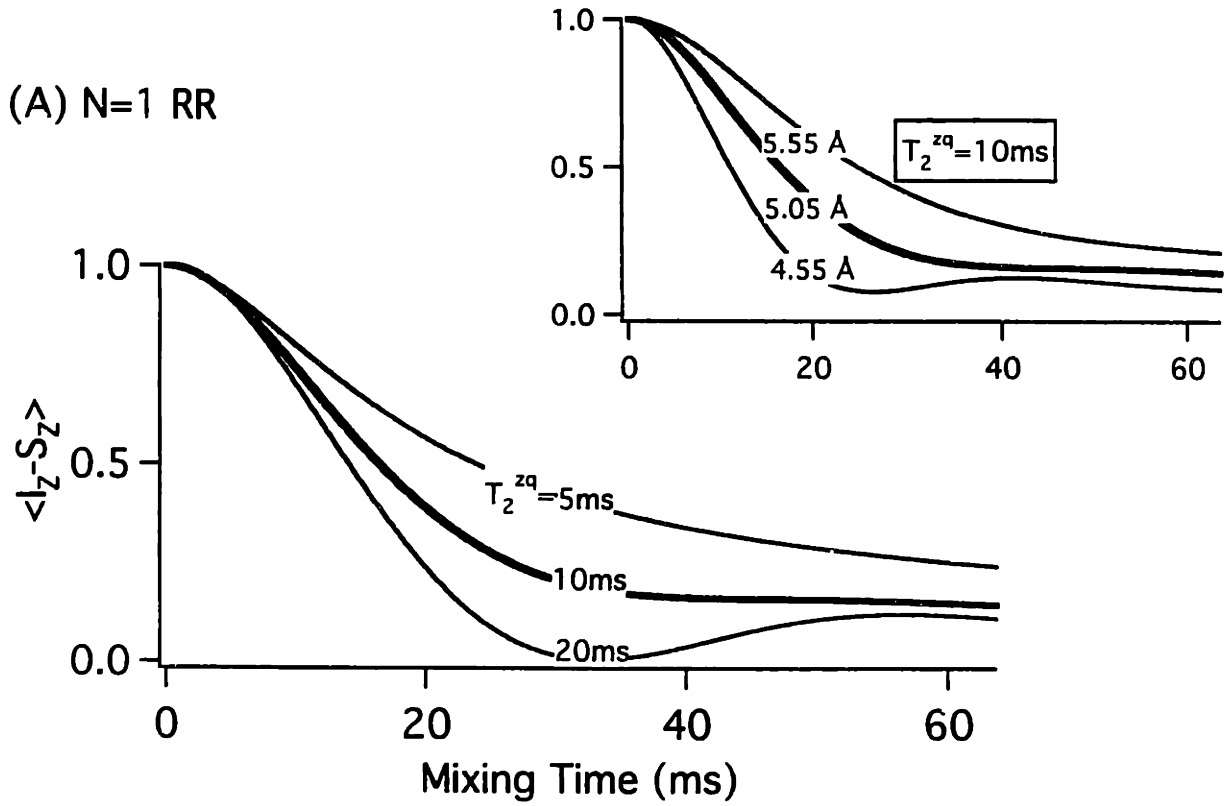
(A) N=1 RR
1.0
0.5
0.0
5.55 Å
5.05 Å
4.55 Å
T_2^{zq}=10ms
0
20
40
60
1.0
0.5
0.0
$\langle I_z\text{-}S_z \rangle$
T_2^{zq}=5ms
10ms
20ms
0
20
40
60
Mixing Time (ms)

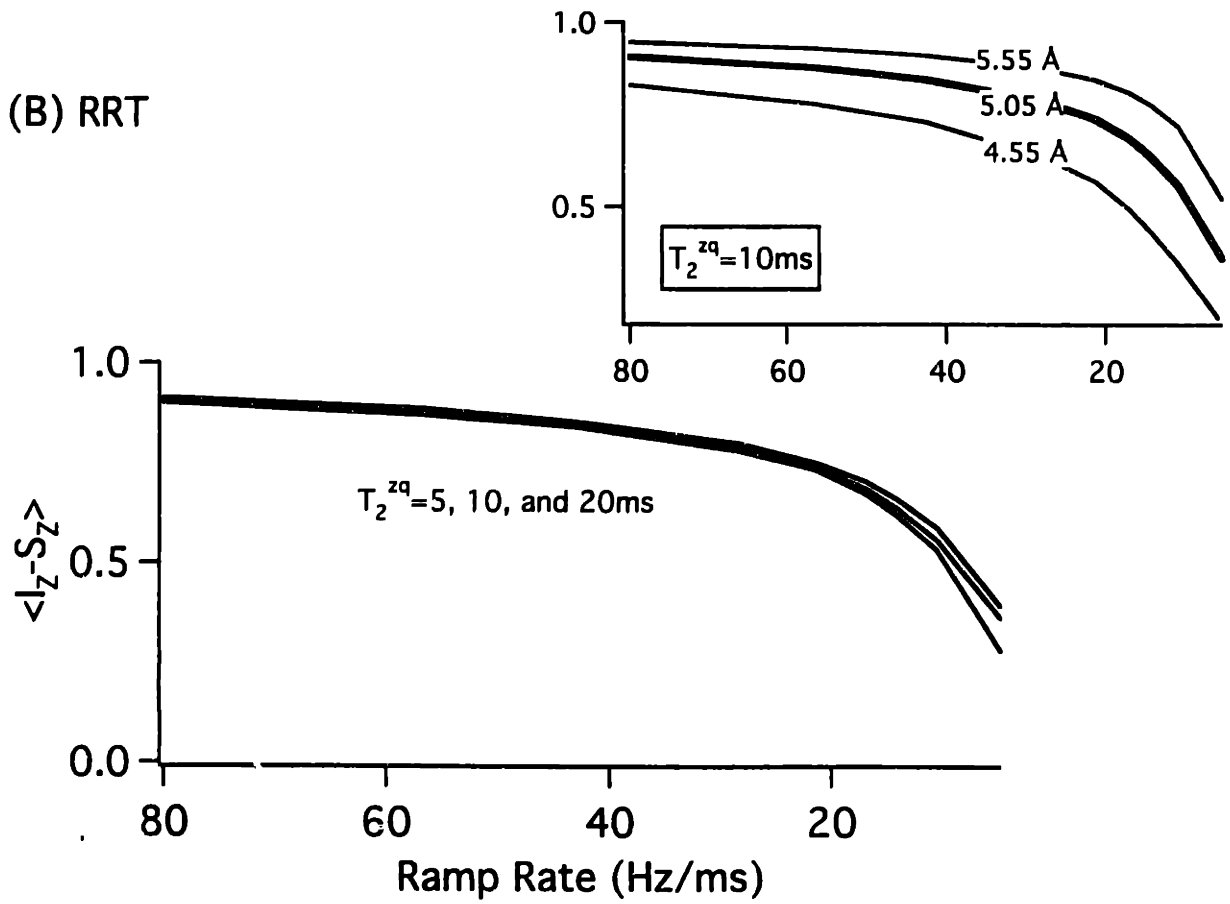
(B) RRT
1.0
0.5
5.55 Å
5.05 Å
4.55 Å
T_2^{zq}=10ms
80
60
40
20
1.0
0.5
0.0
$\langle I_z\text{-}S_z \rangle$
T_2^{zq}=5, 10, and 20ms
80
60
40
20
Ramp Rate (Hz/ms)

behaviour in the RRT calculations is only an approximation due to the lack of alignment of the rotating and tilted frames, but the small degree of tilt makes this reasonable. The large plots (A) and (B) indicate the changes in the dynamics expected for each experiment as a function of changes in the 2Q-relaxation rate. The RRT dynamics show much reduced dependence, particularly as compared to the changes induced in the dynamics as a function of dipolar coupling constant, with relaxation held fixed (inset plots in (A) and (B)). Note that for the slowest ramp rates the RRT dynamics do begin to show a significant relaxation dependence. For rates slow enough to satisfy the adiabatic condition (not now experimentally feasible with linear ramps for weak couplings) simulations (not shown) indicate almost full polarization transfer (>90% efficient) absent relaxation effects, whereas with increasing relaxation rates one observes progressively less efficiency until relaxation dominates, at which point 50% efficiency is observed (corresponding to 0.0 on the $\langle I_Z\text{-}S_Z \rangle$ plots shown here). The reduced relaxation rate dependence in the initial exchange regime may be related to the linear behaviour of the exchange process during fast-passage through the resonance. As described in Chapter One, the shape of of the RR condition changes, in response to changes in 2Q-relaxation rate, in a manner that (approximately) keeps the area encompassed by the resonance constant. If, as we ramp through such a resonance, the exchange that occurs at each point is a linear function of the strength of the resonance at that point (reasonable for fast passage), then the ramp process is effectively an integration of the overall area of the resonance. Because the integrated area of the resonance remains relatively constant for moderate changes in the 2Q-relaxation rate, the overall exchange during fast-passage through

such a resonance should also remain approximately constant for similar changes in relaxation rate.

To the extent that the dynamics become independent of relaxation and inhomogeneity effects, they (the dynamics) become scalable solely as a function of the dipolar coupling constant, and a "universal curve" can be defined which characterizes the dynamics in all situations (although orientation-dependent CSA effects limit the generality). With only reduced dependence on 2Q-relaxation rates, we expect to be able to describe the dynamics using a single curve over some narrowed range of coupling strengths for which the relaxation effects are essentially identical. The adiabatic parameter, for instance, can be used as a universal variable to characterize the time-dependence of the Hamiltonian at a given rf ramp rate and coupling strength. Given no relaxation effects, a single plot of the dynamics as a function of AP would serve to fully characterize time-evolution under ramped RRT for all systems on all time-scales. Given limited relaxation rate dependence, however, the calculation of the dynamics for a particular coupling constant should hold relatively well over some range of coupling strengths bracketing this regime. We then expect that systems with different dipolar couplings (within the bracketed range) will evolve identically if the ramp rate in each case is adjusted so that the AP distribution characterizing the experiments are identical. We demonstrate that this analysis holds in the TEE system we have just presented by plotting the TEE simulations (with relaxation) vs. the calculated value of AP_{MIN} for each simulated data point, yielding the single curve (solid line) in Fig. (3-13). Note that the value of the dipolar interaction that is used in this calculation is not clear, given its distribution across the powder sample. We use a value that is 40% of the dipolar

Figure 3-13: Plot of ramped-RRT dynamics vs. the adiabatic parameter (AP_{MIN}) using equ (31). Plotting the simulated data, calculated using a series of dipolar coupling constant, yields (approximately) a single curve indicated by the solid line. Subsequent plotting of the experimental TEE data, calculating AP_{MIN} using dipolar coupling constants (suitably scaled - see text) corresponding to 4.85 and 5.25Å, respectively, yields the curves indicated by the open triangles. Plotting the experimental TEE data using 5.05Å (filled circles) closely matches simulation, as expected.

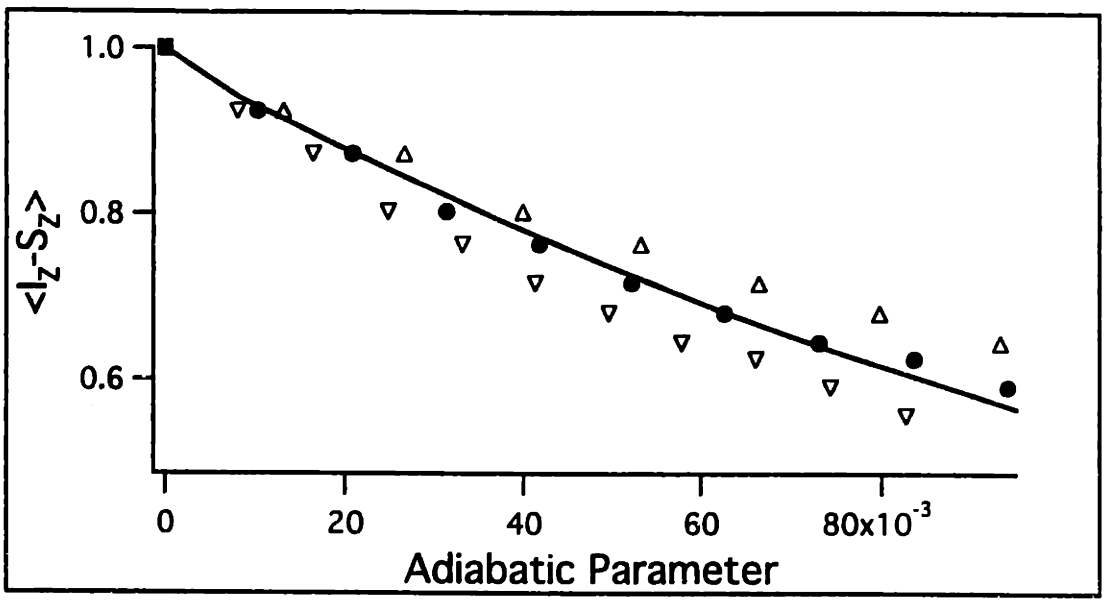
1.0
0.8
0.6
<I_z-S_z>
0
20
40
60
80x10^-3
Adiabatic Parameter

coupling constant, the approximate width of the recoupled dipolar powder pattern, for experiments near RR (a larger value (60% of the width) should be used near 2Q-HORROR to maintain consistency).

Given the (somewhat) universal property of the dynamics, at least during the initial parts of the ramped exchange curve where "fast-passage" is achieved, there is an abbreviated method for extracting the internuclear distance from a given data set when relaxation effects do not dominate. First, perform a single simulation using a dipolar coupling constant that is a rough guess of the expected value, and plot the resulting exchange curve vs. AP_{MIN}. Then put the experimental data on the same plot, adjusting the value of the dipolar coupling constant in the calculation of AP_{MIN} to get the best fit of simulation to experiment. The value of the coupling constant that provides the best fit is the measured value, and error calculation is straightforward. The TEE experimental data is plotted in this way in Fig. (3-13) using coupling constants corresponding to 4.85, 5.05, and 5.25 Å internuclear distances to calculate AP_{MIN}, and indicates that the accuracy of the technique under similar conditions will be better than ±0.2 Å.

3.3D Ramped 2Q-HORROR Applied to a Strong Coupling: Approaching Adiabatic Polarization Transfer in Homonuclear Spin Systems.

The application of ramped techniques to a strongly-coupled spin pair allows access to the regime in which adiabatic manipulations of the polarization become possible. Here we exploit the (n=1, Σ) recoupling effect near the 2Q-HORROR limit to reintroduce the coupling between the directly-bonded α and β carbons in doubly ($^{13}C_\alpha$, $^{13}C_\beta$)-labeled L-alanine (Fig. (3-14)). The internuclear distance is on the order of 1.5 Å, yielding a coupling constant of about 2.2 kHz. The chemical shifts of the two

Figure 3-14: Relevant parameters for ramped 2Q-HORROR experiments applied to ($^{13}C_{\alpha}$,$^{13}C_{\beta}$)-labeled L-alanine:

(A) ^{13}C spectrum of L-alanine sample, obtained at ω_r=13.7kHz. The chemical shift difference at this field strength (9.4T) is 3.0kHz (the peak indicated by the asterisk is from an impurity). With the carrier placed between the two resonances, the isotropic chemical shift offsets are equal to ±1.5kHz.

(B) Diagram of the effective field axes and their components. Matching resonance requires each effective field equal 13.7/2=6.85kHz. Given the offsets in L-alanine, this requires a rf field strength of 6.7kHz. The effective fields in this situation are rotated out of the transverse plane by 13°.

(C) Plot of the difference between residual sum and difference polarization (filled circles) at each rf field strength after 3ms of mixing (see Fig (3-9) for comparison to TEE data). The resonance has a width of approximately 2kHz, and is centered at the expected value (6.7kHz, indicated by arrow). The line under the resonance indicates the ramp range (see text).

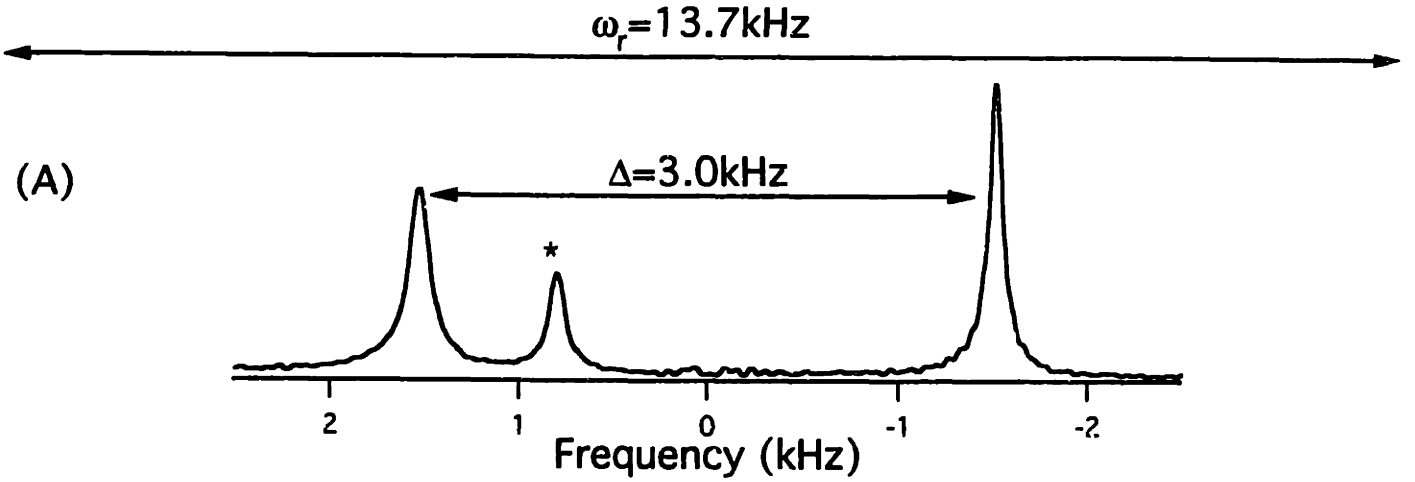
ω_r=13.7kHz
(A)
Δ=3.0kHz
*
2
1
0
-1
-2
Frequency (kHz)

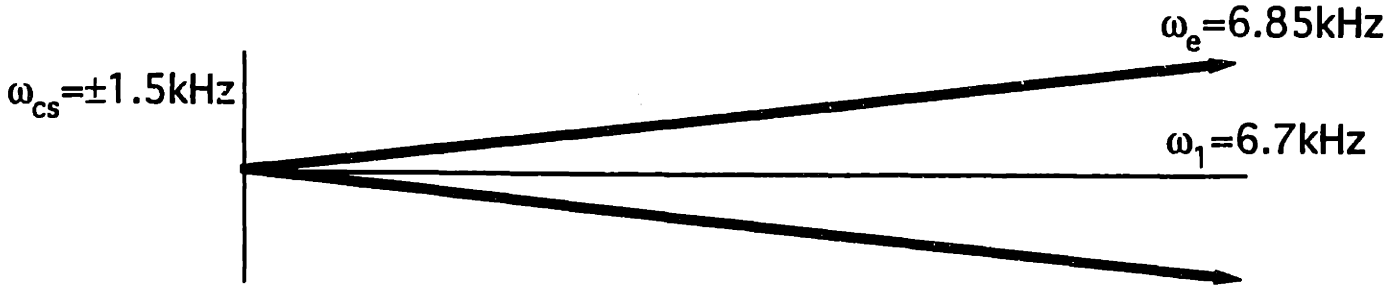
(B)
ω_e=6.85kHz
ω_cs=±1.5kHz
ω_1=6.7kHz

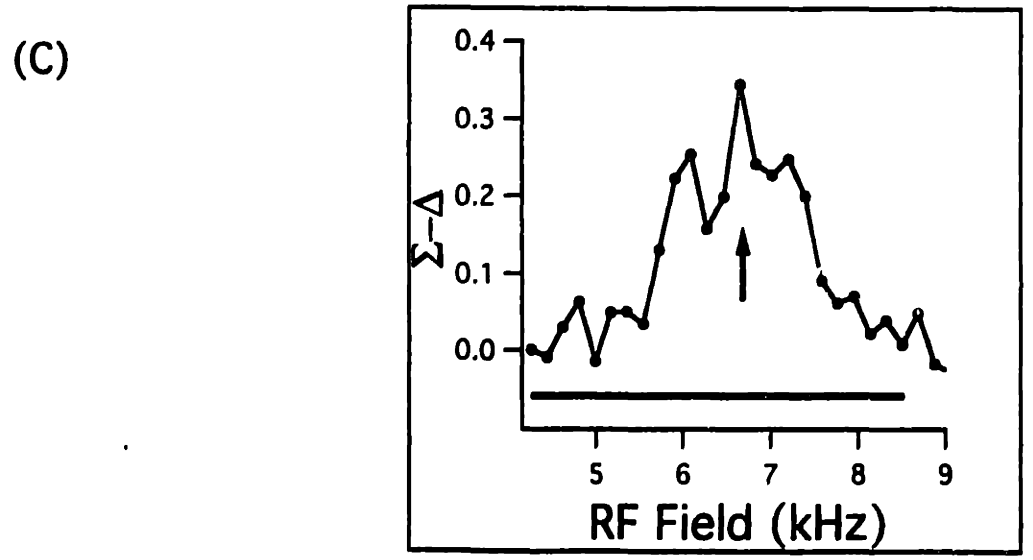
(C)
0.4
0.3
0.2
0.1
0.0
Σ-Δ
5
6
7
8
9
RF Field (kHz)

carbons are relatively close, so that the magnitude of the rf field necessary to match resonance with a 13.7 kHz spinning speed (6.68 kHz) does not deviate much from the "ideal" horror value (13.7/2 = 6.85 kHz). This is reflected in the nearly transverse orientation of the effective fields - rotated out of the transverse plane by 13° (RI/RO pulses were not used in these experiments for this reason). We can map out the resonance condition by observing the selective decay of sum polarization as a function of applied rf power (pulse sequence in Fig. (3-3B), with a dipolar mixing time of 3 ms and no RI/RO pulses); the result is shown in Fig. (3-14C). The resonance is centered about the expected value (the CSA's are too small to induce a shift here), and has a width of approximately 2 kHz. A significant fraction of this width derives from inhomogeneity in the rf, which we expect to be on the order of 0.5 kHz (7% of 6.8 kHz)

The on-resonance evolution (ω_1 constant, = 6.7kHZ) of sum and difference polarization as a function of mixing time is shown in Fig. (3-15A). Absent the broadening effect of rf inhomogeneity, we would expect the sum polarization to show a much deeper initial oscillation and slower damping of the following oscillations, as illustrated by the simulation (calculated by numerical integration as described previously, with no rf-inhomogeneity or relaxation effects included). We can obtain results more closely approximating the ideal case by restricting the sample size to the center of the coil, thus reducing rf-inhomogeneity and so removing the obscuring effects of the more mismatched parts of the sample[4]. The decrease in sample volume, however, means a decrease in S/N that is not desirable. Ramping through the resonance condition provides an alternative method if increasing the efficiency of sum polarization inversion. By ramping through the resonance condition at increasingly

Figure 3-15: On-resonance (A) and ramped (B) 2Q-HORROR dynamics for ($^{13}C_{\alpha}$,$^{13}C_{\beta}$)-labeled L-alanine:

(A) The on-resonance (ω_1=6.7kHz) evolution of sum polarization (filled circles) as a function of mixing time is severely damped as compared to the theoretical calculation (solid line). This is attributed to rf-inhomogeneity (see text). Difference polarization (open circles) decays during mixing, for several reasons described in the text.

(B) The ramped dynamics show much more efficient inversion of sum polarization (filled circles). Ramp range is indicated by line under resonance in Fig. (3-14C) and was kept constant; data is plotted as a function of mixing time.

(A)

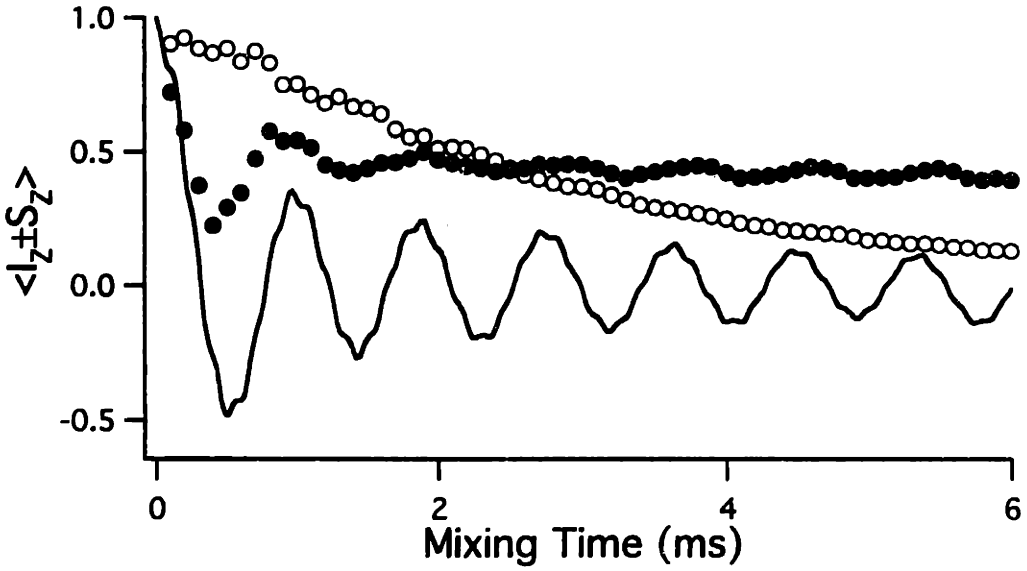
1.0
0.5
0.0
-0.5
<I_z±S_z>
0
2
4
6
Mixing Time (ms)

(B)

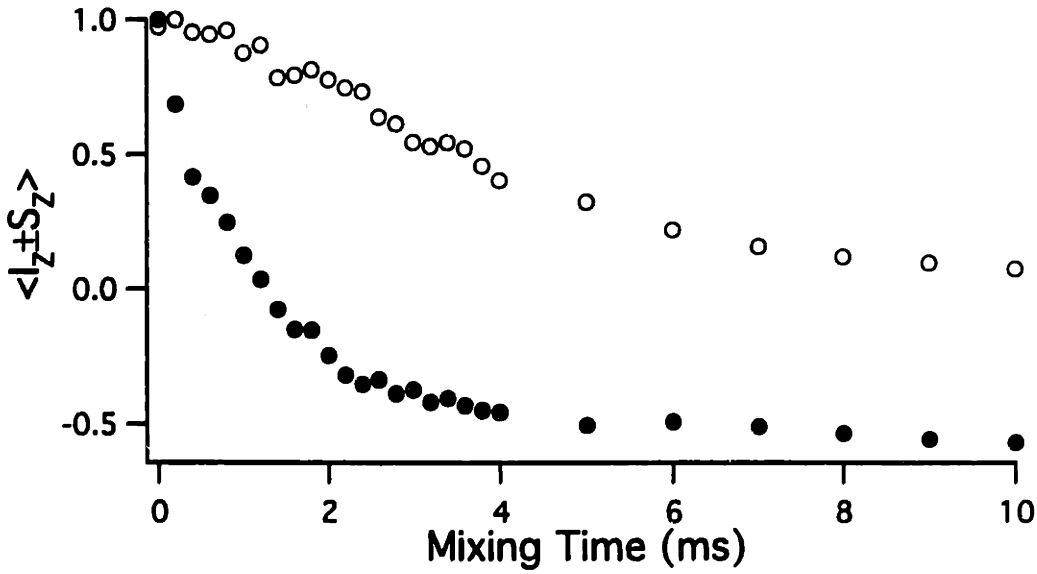
1.0
0.5
0.0
-0.5
<I_z±S_z>
0
2
4
6
8
10
Mixing Time (ms)

slower rates (ramp range indicated by solid line under resonance in Fig. (3-14B), 4.2 kHz width), we can obtain significantly better inversion of sum polarization in the full sample, as indicated in Fig. (3-15B). Here the ramp data are plotted relative to the length of the ramped mixing period; ramp rates are proportional to the inverse of the mixing time. At 5 ms, for example, the effective field ramp rate is ≈1.7 kHz/ms, yielding a value of approximately 1.0 for AP_{MIN}. Although this does not clearly satisfy the conservative adiabaticity condition we have given for linear ramps, it approaches the condition more closely (by an order of magnitude) than the TEE experiments did, and the measured inversion efficiency approaches 80%. Application of non-linear ramp techniques which have a less-peaked angular velocity distribution will yield improved results; simulations (not shown) suggest efficiencies approaching 95% are possible..

That we can get such good inversion with ramped techniques suggests that the damping effects in the on-resonance dynamics arise primarily from rf inhomogeneity, and not from relaxation (which, if significant, would likely have a larger effect on the slower adiabatic process relative to the on-resonance dynamics). In fact, the constant value of spin-locked sum polarization at long ramp times (4-10 ms) indicates that, on this experimental timescale, both (i) the relaxation of spin-locked sum polarization is negligible, and (ii) the 2Q-relaxation rate does not have a major impact on the efficiency of the exchange process.

The decay of difference polarization evident in both the on-resonance and ramped data is not due to the coherent effects of the recoupled dipolar interaction, which has double-quantum character and so commutes with this state of the system. It also does not seem to arise from single-spin relaxation effects, which would be expected to cause decay of

the sum polarization on a similar timescale. Once equilibrium is reach, there is no decay of inverted sum polarization at long times in both ramped and on-resonance data sets. There seems instead to be some type of zero-quantum interaction that we have not yet considered driving the observed evolution of difference polarization. We suggest two possible causes: J-driven evolution and ^{1}H-driven spin diffusion.

Given nearly transverse effective fields, the J-coupling transforms under their effects as follows:

$$I \bullet S \xrightarrow{\omega_I^e I_X + \omega_S^e S_X} I_X S_X + \frac{1}{2}\left(I_+ S_- e^{i\omega_\Delta^e t} + I_- S_+ e^{-i\omega_\Delta^e t}\right) \qquad (32).$$

(where the raising and lowering operators have been defined as linear combinations of the y and z spin operators: $I_+ = I_Y + iI_Z$, etc.). The first term is never averaged, but always commutes with polarization along the effective fields and so should have no effect on the dynamics we describe here. The second term, however, which has zero-quantum (flip-flop) form, can drive the evolution of difference polarization. With symmetric placement of the carrier so that the effective field strengths for the two spins are equal, and nearly transverse effective fields, this term is not averaged, and we expect to observe J-driven evolution (with longitudinal effective fields - near RRT - J-driven evolution of the type described here does not occur). The magnitude of the J-interaction is expected to be on the order of 35 Hz for a ($C\alpha$,$C\beta$) pair[28], and because it is independent of orientation it is particularly effective at driving zero-quantum evolution even given the relatively small size of the interaction. (This effect might be useful in obtaining J-correlated multidimensional spectra when the effective field sum is moved away from the dipolar resonance.) The simulation in Fig (3-16A) indicates the expected evolution of difference polarization under these conditions.

Figure 3-16: Evolution of difference polarization as a function of rf carrier frequency. With the carrier placed precisely between the two resonance peaks, the J-interaction is expected to drive zero-quantum evolution as indicated by the solid line in the plot. Experimental results (open circles) under these conditions show decay, although at a faster rate than predicted by simulation. With the carrier shifted towards the C_α resonance, simulation (dotted line) predicts the elimination of J-driven zero-quantum evolution, however experimental data (open triangles) shows a reduced, but still significant, rate of decay.

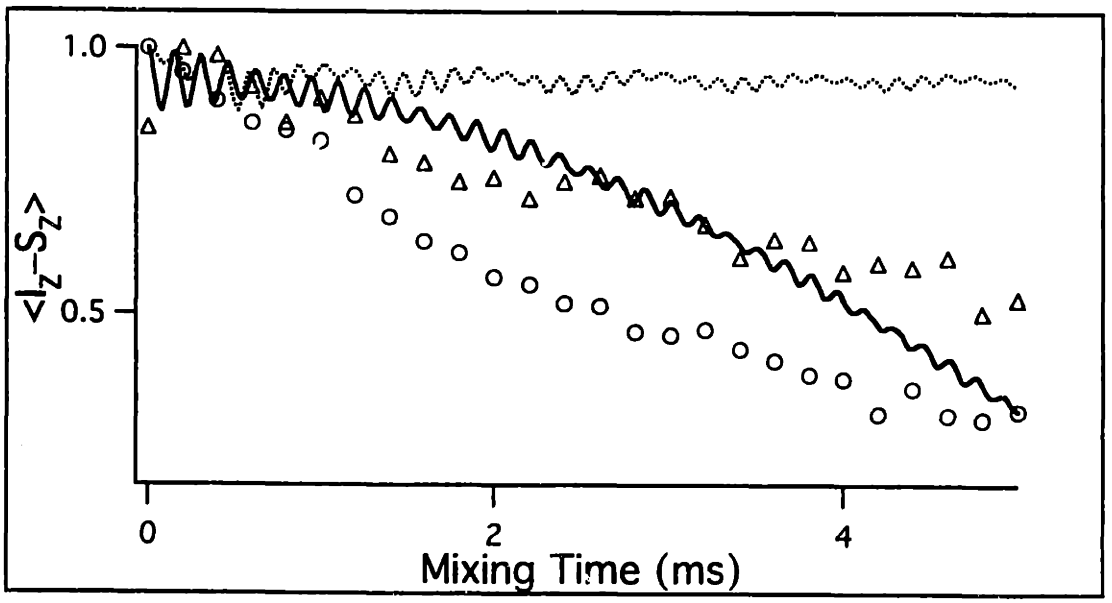
1.0
0.5
$\langle I_z - S_z \rangle$
0
2
4
Mixing Time (ms)

J-driven decay of difference polarization during mixing leads to a reduction in the efficiency of double-quantum, dipolar polarization transfer experiments, which depend on selective decay of sum polarization. The J-driven evolution can be reduced or even eliminated in this sample by asymmetric placement of the carrier, so that the effective fields of the two spins are slightly different. Putting the carrier at the C_α resonance frequency will result in effective field strengths of 6.5 and 7.2 kHz for the C_α and C_β carbons, respectively, when the resonance condition is matched. The 0.7 kHz difference in the two effective field strengths is clearly sufficient to average the 2nd term in the J-interaction, and simulations of the effect support this conclusion (Fig. (3-16)). Experimental data obtained under these conditions, however, indicates that although decay of difference polarization is slowed, it has not been eliminated.

The remaining decay almost certainly is dependent on the presence of the homonuclear coupling between the two spins. Because the effect does not show up in numerical simulations of the two-spin dynamics, however, it must be a product of Hamiltonian terms which we have left out of our analysis. The most likely are the couplings to the ^1H nuclei, which (even under high-power ^1H decoupling) can absorb the excess energy necessary to allow mutual ^{13}C-^{13}C spin flip-flops, and hence zero-quantum polarization transfer. This ^1H-driven relaxation process has been termed "spin diffusion"[29] (a term which is used to label a different process in the following chapter, multiple-step polarization transfer between adjacent low-γ nuclei in uniformly labeled samples under broadband recoupling, essentially ^1H-independent).

3.4 Dipolar Pulse Sequences.

3.4A Dependence of the Magnitude and Phase of the Recoupled Dipolar Interaction on Crystallite Orientation.

The recoupled dipolar interaction in experiments along the (n=1, Σ) continuum has the following form when expressed in terms of the fictitious spin-1/2 operators we have defined (from Chapter One):

$$H_D^{14} = |\tilde{\omega}_D|\left(J_X^{14}\cos(\chi) + J_Y^{14}\sin(\chi)\right) \qquad (33),$$

with $|\tilde{\omega}_D| = C_\Sigma|\omega_1^{(IS)}|$ and $\chi = \tan^{-1}\left(\frac{\mathrm{Im}(\omega_1^{(IS)})}{\mathrm{Re}(\omega_1^{(IS)})}\right)$. Hence both the magnitude and the phase within the transverse plane of the vector representing the dipolar interaction in the fictitious subspace depend on crystallite orientation through the parameter $\omega_1^{(IS)}$. Experiments in which the observable is sum or difference polarization, and where no pulses are applied during the dipolar evolution period to manipulate the coherences, are generally insensitive to the phase dependence. This includes the effective field-locked mixing experiments detailed here: although the phase of the 2Q-coherence created during dipolar mixing depends upon the phase of the recoupled dipolar interaction, the time-dependence of the detected sum or difference polarization does not. The evolution of (interaction frame) sum polarization does, however, show the effects of the dipolar magnitude dependence on crystallite orientation, as we have described. The sinusoidal oscillation between J_Z^{14} and $-J_Z^{14}$ that occurs in a single crystallite is transformed under the powder average into a damped oscillation where full inversion of sum polarization no longer occurs. If we view the dipolar vector as an rf field and the powder distribution of recoupled dipolar coupling strengths as inhomogeneity in the strength of this field, then the

problem of increasing the efficiency of inversion of sum polarization (with all that implies for increased 2Q filtering and polarization transfer efficiency) is one of compensating for dipolar "inhomogeneity".

Experiments which attempt to manipulate the 2Q coherences created during dipolar mixing - 2Q-filtering sequences in particular - are sensitive to the distribution in recoupled dipolar phases in addition to magnitudes. This is because 2Q coherences of different phases do not transform identically upon application of rf pulses. Consider the effect of a 180° pulse on the two components of the 2Q coherences created during a longitudinal mixing experiment:

$$\begin{aligned} J_X^{14} = \quad & I_X S_X - I_Y S_Y \quad \xrightarrow{180^0_{X,\alpha Y}} \quad I_X S_X - I_Y S_Y \quad = J_X^{14} \\ J_Y^{14} = \quad & i(I_X S_Y + I_Y S_X) \quad \xrightarrow{180^0_{X,\alpha Y}} \quad i(-I_X S_Y - I_Y S_X) \quad = -J_Y^{14} \end{aligned} \qquad (34),$$

(spin operators are given relative to the interaction frame axis system). 180° pulses have no effect on the first coherence, but invert the second. In a crystallite oriented such that $\omega_1^{(IS)}$ is purely imaginary (real), only the first (second) coherence is created, and the application of 180° pulses during mixing have no effect on (invert) the 2Q coherence. Clearly the dynamics subsequent to the pulse will be different in the two crystallites. The RR-based MQ filtering sequences that have thus far been proposed depend on appropriate manipulation of the 2Q coherence during mixing, and the inability to do so identically over all crystallites leads to an additional loss (50%) in filtering efficiency above that due to the dipolar powder average. This is described in the Nielsen, et. al.[17] manuscript as the $\bar{\phi}$ effect, where their ϕ corresponds to our χ.

It is thus surprising that in a subsequent manuscript Nielsen, et. al.[4] attribute the increased DQ filtering efficiency of 2Q-HORROR relative to RR as due to the removal of the γ-dependence of the "2Q nutation

frequency under rotational resonance at the n=1 condition", which they claim (in their equ. 3) is proportional to cos(γ) (γ being one of the euler angles (α,β,γ) defining the orientation of the internuclear vector relative to the rotation axis). If we interpret the "2Q nutation frequency" as the rate at which sum polarization rotates into 2Q coherence (i.e. equal to the magnitude of the recoupled dipolar interaction for on-resonance dynamics), then their claim is incorrect. The equations describing the dynamics of the two experiments are identical (within a scale factor) in the appropriate interaction frame, as we have demonstrated, so that the 2Q nutation frequencies have an identical dependence (again, within a scale factor) on the orientation of the internuclear vector that does not include a dependence on the γ angle. The only difference other than the scale factor between the experiments is the orientation of the effective fields; in particular there is no sudden appearance of a γ dependence of the 2Q nutation frequency as one proceeds along the continuum from 2Q-HORROR to N=1 RR.

The phase of the recoupled dipolar interaction, on the other hand, does exhibit a dependence on γ, a dependence which, again, holds across the (n=1, Σ) recoupling continuum and occurs in many similar recoupling techniques (including heteronuclear CP). It is certainly not, as claimed by Nielsen, et al[4], (subsequent to their equ. 15) a "novel feature" of 2Q-HORROR. Writing out the orientation dependence of $\omega_1^{(IS)}$ explicitly:

$$\omega_1^{(IS)} \propto \sin(2\beta)e^{i\gamma} \tag{35}$$

demonstrates that the dipolar phase is completely determined by γ:

$$\chi = \tan^{-1}\left(\frac{\sin\gamma}{\cos\gamma}\right) = \gamma \tag{36},$$

(the magnitude, however, is independent of γ). Crystallites in which the internuclear vectors have identical values for β (i.e. exist within the same "carousel"[30]) but different values for γ will have recoupled dipolar interactions of the same magnitude, but with different phases determined by their γ angles.

3.4B Control of the Phase of the Recoupled Dipolar Interaction.

The phase of the vector representing the recoupled dipolar interaction in the transverse plane of the fictitious subspace is determined by the phase difference between the (linearly-polarized) spatial- and (circularly-polarized) spin-modulations of the recoupled dipolar term before time-averaging. The full time-dependence of the (n=1, Σ) term before averaging is given by ($|m|$=1, Σ term extracted from equ (16))

$$\begin{aligned} H(|m|=1,\Sigma) &= |\omega_1^{(IS)}| \sum_{m=-1,1} e^{im(\omega_r t+\gamma)}\left(I_+S_+e^{i\omega_\Sigma t}+I_-S_-e^{-i\omega_\Sigma t}\right) \\ &= |\omega_1^{(IS)}|\cos(\omega_r t+\gamma)\left(J_X^{14}\cos(\omega_\Sigma t)+J_Y^{14}\sin(\omega_\Sigma t)\right) \end{aligned} \qquad (37).$$

On resonance ($\omega_\Sigma = \omega_r$), whether the zero-order average consists of a J_X^{14} or a J_Y^{14} term (or some linear combination of the two) depends on which spin term (or linear combination of terms) has a phase matching that of the spatial modulation (γ=0° yields J_X^{14}; γ=90°, yields J_Y^{14}). A similar effect is expected to occur in any recoupling experiment in which the frequency of a MAS-induced oscillation of the spatial part of one term in the Hamiltonian is matched to the magnitude of another, non-commuting static term. This includes the homonuclear dipolar recoupling experiments we have discussed here, the heteronuclear analogue (CP), and CSA-recoupling experiments.

Techniques which abruptly alter the relative phases of the MAS- and spin operator-induced oscillations also alter the phase of the recoupled

interaction, thus allowing rf-like control over the phase of the interaction during subsequent mixing periods. The uses of these techniques include the creation of dipolar echos (from a 180° dipolar phase shift) and more complex dipolar pulse sequences that incorporate the idea of composite pulses to compensate, for example, for the dipolar "inhomogeneity" that we have discussed. These techniques should be applicable, both within the dipolar recoupling framework we present here, and in the related experiments.

We will describe two ways to control the phase of the recoupled interaction by abruptly altering the relative phases of the two oscillations (pulse sequences shown in Fig. (3-17)). The first of these (3-17A) involves "freezing" spin evolution during some fraction of a rotor cycle. While the effective-field-induced modulation of the spin part of the dipolar term is thus interrupted, the continuing rotation of the rotor will lead to phase accumulation in the spatial part of the interaction. When recoupling begins again after the interruption, the relative phase of the two oscillations will have changed, and this will be reflected in the phase of the recoupled interaction during the subsequent mixing period. The change in phase induced by a freeze period lasting a time Δt is:

$$\Delta\gamma = \frac{2\pi(\Delta t)}{\tau_r} \qquad (38),$$

($\tau_r = \frac{2\pi}{\omega_r}$ is the rotor period). Therefore, to change the phase of the interaction by 90° between two dipolar mixing periods (analogous to switching the phase of applied rf from x during one period to y during the next) requires placing a freeze sequence, $\Delta t = \tau_r/4$ in length, between the two periods. (Note that equ (38) assumes a "1st" order resonance, i.e. recoupling of a dipolar spin component modulated at the spinning speed.

Figure 3-17: 'Freeze' (A) and 'Jump' (B) methods for inducing changes in the phase of the recoupled dipolar interaction between two mixing periods:

(A) Freeze: During the first mixing period, the resonant spin and spatial terms have the same phase, yielding a recoupled dipolar interaction with phase labeled 'X' (bottom of figure). During the freeze period, chemical shift evolution is canceled for a fraction of the rotor cycle (here by application of high-power rf (with phase inverted halfway through the freeze period to eliminate rf-dependent evolution)). Subsequent to the freeze period, the spin and spatial terms are again in resonance, but the spatial term has gained 90° on the spin term, leading to a recoupled dipolar interaction with phase +Y during the second mixing period. (During the first and second mixing periods, application of rf (as diagrammed) is only required if necessary to match resonance.)

(B) Jump: After the first mixing period (characterized by dipolar phase 'X'), the effective fields for both spins are increased (or decreased) in magnitude so that the spin term oscillates at a frequency significantly larger (or smaller) than the MAS-induced oscillation of the relevant spatial term. On return to resonance, the spin and spatial terms will differ in phase depending on the length and magnitude of the jump. Here we diagram a spatial term lag of 90°, leading to a recoupled dipolar phase of -Y during the second mixing period.

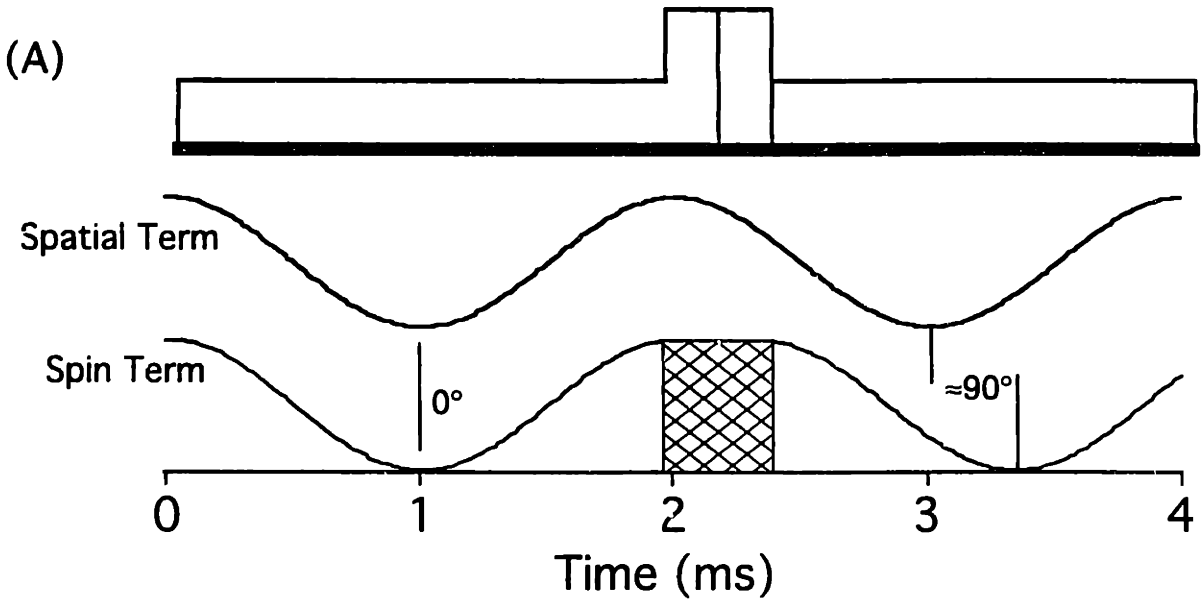
(A)
Spatial Term
Spin Term
0°
≈90°
0
1
2
3
4
Time (ms)

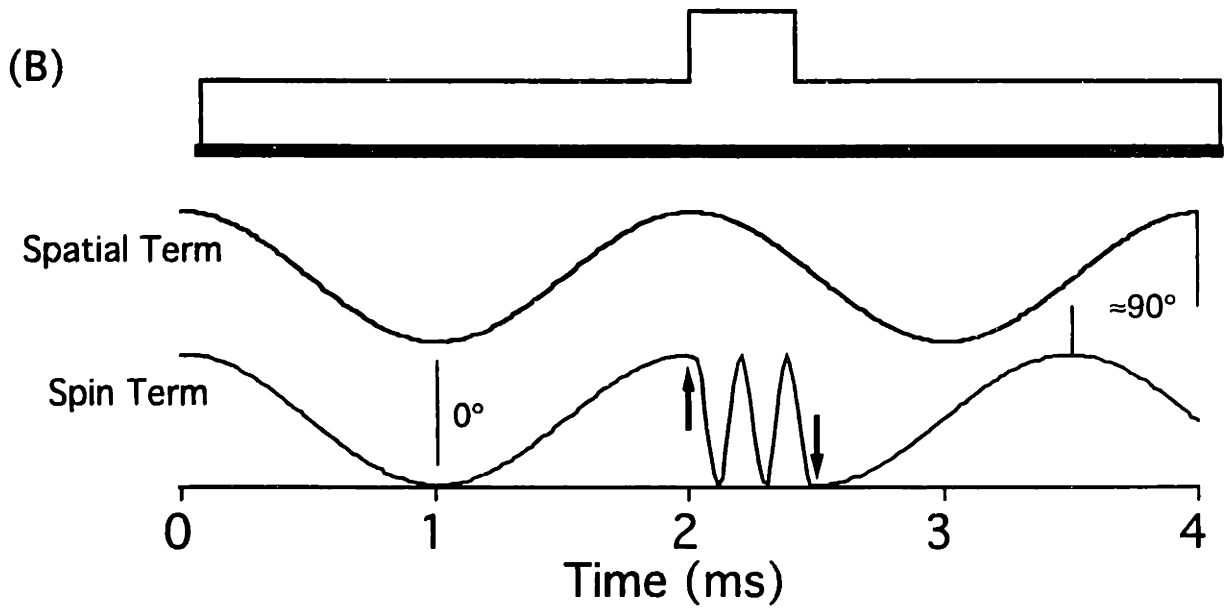
(B)
Spatial Term
Spin Term
0°
≈90°
0
1
2
3
4
Time (ms)

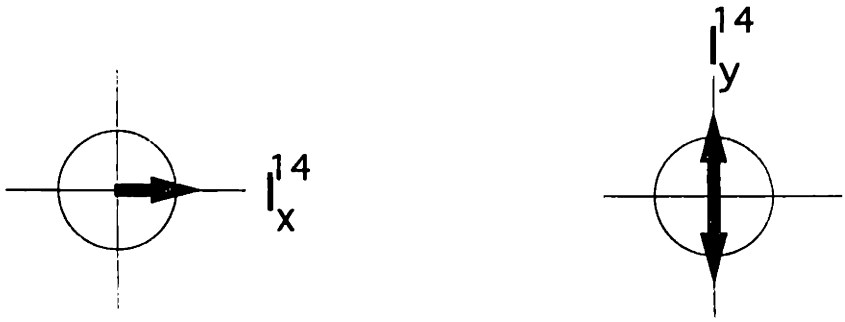
I_x^{14}
I_y^{14}

In experiments where a dipolar terms modulated at a frequency n times the spinning speed (for instance, and n-order rotational resonance), equ (38) must also be multiplied by n.)

Several alternatives exist for freezing spin evolution for short periods. The crucial property of such sequences is the removal of chemical shift (offset and CSA) evolution during the period without introduction of rf-driven evolution. Although in principle dipolar evolution should also be removed during the freeze period, the relatively small size of typical dipolar interactions relative to the spinning speed implies that their effect during freeze periods that are fractions of a rotor period will be minimal. The $X\bar{X}$ method (application of strong x-phase rf for half the period, followed by strong $\bar{x}$-phase rf for the second half), which is used in the SELTICS sequence to "interrupt" chemical shift evolution for short periods[31], is one alternative that has proven to be effective. A second method involves application of a series of 180° rf pulses, with short interpulse spacings, bracketed by a pair of 90° pulses of opposite phases, the entire sequence lasting the length of the freeze period.

The second method by which the relative phases of the spin- and space- oscillations can quickly be changed involves moving the system away from resonance for short periods (Fig. (3-17B)). If we consider a system evolving on-resonance, the interaction-frame dynamics will be driven solely by the transverse, recoupled dipolar vector (of whatever phase). A sudden jump in the effective field strengths far from resonance introduces a large longitudinal component to the average Hamiltonian in this interaction frame. The time-dependence imposed by this component can be imposed on the density matrix, or we can transform to the equivalent of the standard toggling frame and describe the effect by placing this time

dependence on the on-resonance Hamiltonian. Using the second picture, the longitudinal component rotates the dipolar Hamiltonian in the transverse plane by some angle determined by the distance from resonance and the length of the period (a dipolar z-pulse). On subsequent return to resonance, the dynamics will again be driven solely by the dipolar vector, but now of altered phase.

We can alternatively examine the effect of the sudden jump from resonance by considering the time-dependence of the relative phases of the spin- and space modulations of the recoupled term in the dipolar Hamiltonian. Assuming we are on resonance, during the first mixing period the phase difference remains constant and the dipolar vector has a single, fixed phase. During the period away from resonance, the spin term in the Hamiltonian oscillates at a frequency that is much larger or smaller than the spatial oscillation, gaining or losing phase relative to it. On subsequent return to resonance, there will be a new phase difference between the two oscillations that depends on the length and magnitude of the jump from resonance, and which determines the phase of the dipolar vector during the next mixing period. Given a jump x kHz away from resonance (so that $\omega_\Sigma^\varepsilon = \omega_r$ goes to $\omega_\Sigma^\varepsilon = \omega_r + x$) lasting a time Δt, the change in dipolar phase will be:

$$\Delta\gamma = 2\pi(\Delta t)x \qquad (39).$$

For a system in which resonance occurs with the effective field sum equal to 10 kHz (e.g. an ideal 2Q-HORROR experiment with ω_r=10kHz, ω_1=5kHz), shifting the sum to 60 kHz (ω_1=30kHz) for 10μs induces a 180° rotation of the dipolar vector in the transverse plane.

3.4C Dipolar Pulse Sequences.

One of the simplest applications of the phase-control technique is the creation of dipolar "echos" by switching the phase of the recoupled dipolar interaction from one mixing period to the next by 180°. We demonstrate the effect in the context of an n=1 RR experiment in Fig. (3-18) for the directly-bonded C_α, $C_{=O}$ spin pair in doubly ^{13}C-labeled glycine. The sample spinning speed was set to 10.49 kHz to match the isotropic chemical shift difference (at a field strength of 9.4T). After creation of longitudinal difference magnetization (relative to the rotating frame) using our standard RRT preparation sequence (and omitting the RI pulse), the initial dipolar mixing period begins with a dipolar phase in each crystallite we label 'X' (although different crystallite have different phases, the absolute phase makes no difference in this experiment). After some mixing time, we apply a freeze sequence lasting for one-half the rotor cycle (48μs). The freeze sequence consists of a pair of 90° pulses of opposite phases bracketing a set of 4 180° pulses, with an interpulse spacing of approximately 1.0μs (the ^{13}C rf field strength was 58 kHz). After the freeze sequence, a second mixing period ensues where evolution is driven by a dipolar vector whose phase is shifted by 180° ($\bar{X}$), which we expect will refocus the evolution of the first mixing period. Detection is performed using the standard RRT detection sequence, again omitting the RO pulse.

The exchange curves obtained with no freeze sequence (closed circles), and with freeze sequences applied after 0.3, 0.5, or 1.0 ms (open symbols) are shown in Fig. (3-18B). The time scale refers to the overall running time in each experiment (freeze time excluded), with freeze application occurring where indicated by the arrows for each

Figure 3-18: n=1 RR echo results from $^{13}C_2$-labeled glycine:

(A) Pulse Sequence: The spinning speed is set equal to the chemical shift difference (10.49kHz) and longitudinal difference polarization was initially prepared (sequence not shown), so that zero-quantum dipolar evolution occurred during the first mixing period. A freeze period was then applied, lasting half of a rotor cycle, so that the spatial term gained 180° of phase on the spin term, and during the subsequent mixing period the dipolar phase was inverted. After the second mixing period, a 90° pulse (not shown) was applied to create transverse polarization for detection.

(B) Time dependence of difference magnetization without freeze period (filled circles) and with freeze period (open symbols), applied where indicated by arrows.

(C) Shifting the raw echo data (in (B)) to the left by twice the echo period and scaling appropriately yields (nearly) overlapping curves, demonstrating that the evolution after the freeze sequence is an echo.

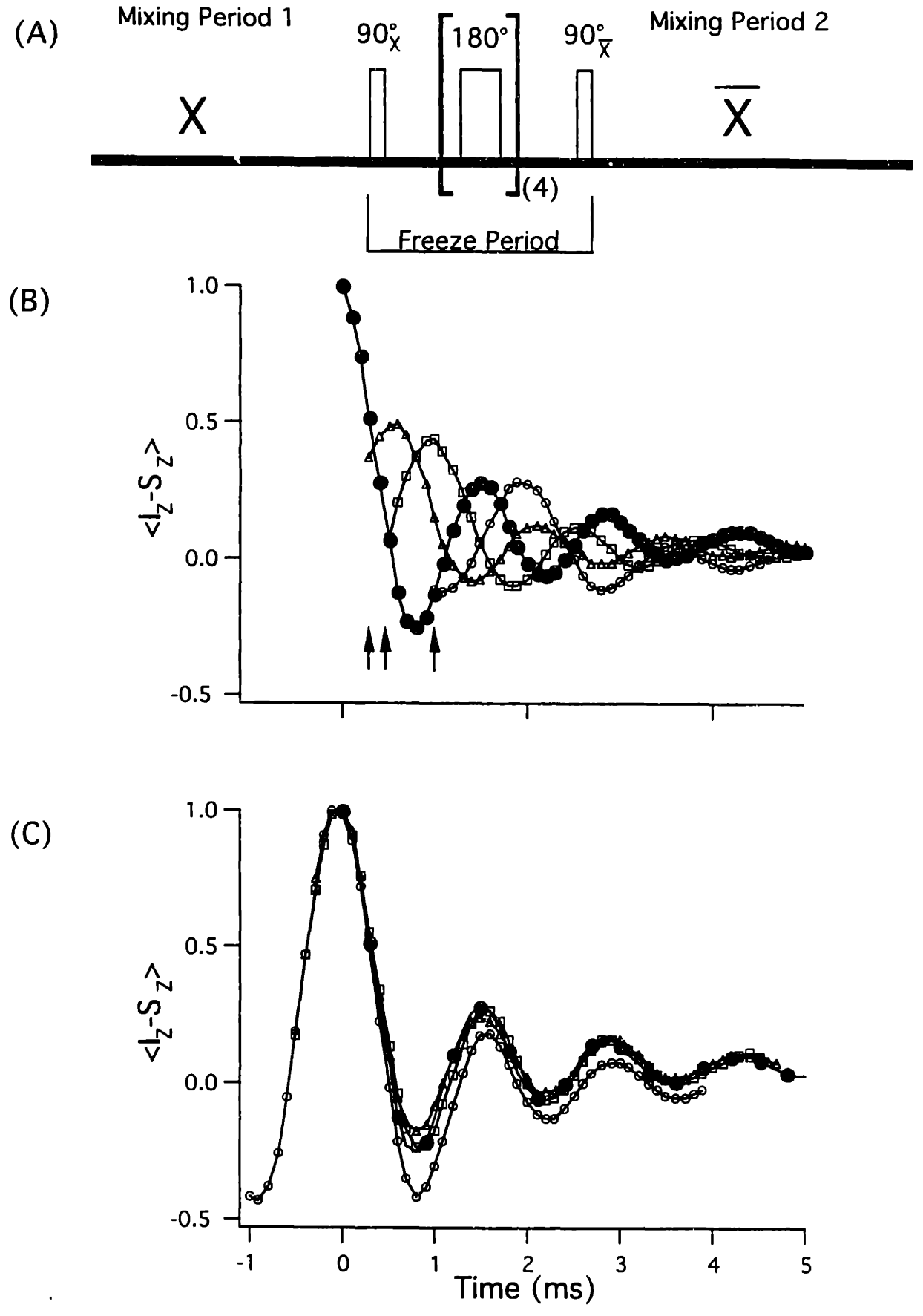
(A)
Mixing Period 1
90°x
180°
90°x̄
Mixing Period 2
X
X̄
(4)
Freeze Period
(B)
1.0
0.5
0.0
-0.5
<Iz-Sz>
(C)
1.0
0.5
0.0
-0.5
<Iz-Sz>
-1
0
1
2
3
4
5
Time (ms)

experiment. Fig. (3-18C) shows the data with each curve shifted to the left (negative time) and scaled so that the echo maxima align. The time shift in each case was the expected value - twice the length of the mixing period before freeze. The fact that the shifted curves align so well indicates that the change in the dipolar phase that we are attempting to produce is occurring with some accuracy. The relative intensities of the successive echo maxima are (1.0, 0.49, 0.43, 0.28) corresponding to echo times of (0, 0.6, 1.0, 2.0) ms. The drop in intensity of the echo peak maxima relative to the initial intensity may be due to several factors. It does not seem to arise from signal loss during the actual freeze process, as the first point of each echo curve in (A, middle), after freeze, falls on top of the equivalent time point on the no-freeze curve (this is in spite of the fact that the ^{13}C and ^{1}H decoupling field strengths were not significantly different). There certainly is a 2Q-relaxation effect, particularly given the strength of the decoupling field (65 kHz), and the rate at which such a strong coupling creates fast-relaxing 2Q-coherence. If this effect dominates, and if we have some estimate of the coupling strength, then we can extract a good estimate of the 2Q relaxation rate from this data. Applied generally, echo experiments of this type might allow separation of "homogeneous" (2Q-relaxation) and "inhomogeneous" (dipolar powder average) contributions to the damping of the dipolar exchange curve.

Another effect that can make a significant contribution to the observed signal loss is mismatch from resonance. If we are not precisely at resonance, then the Hamiltonian will have a longitudinal component that remains the same in both evolution periods independent of the freeze sequence. This lack of full inversion of the Hamiltonian between the two periods reduces our ability to fully refocus the evolution during the second

period, to an extent determined by the relative sizes of the recoupled interaction and the resonance mismatch. Given the large size of the coupling in the experiments we describe here, it seems unlikely that this plays a significant role in the observed dynamics. In systems with weaker couplings and significant chemical shift dispersion, where accurate estimate of the 2Q-relaxation rate can be crucial to extracting accurate distance information, some method of fully inverting the Hamiltonian is necessary to apply this echo method to extract the 2Q-relaxation rate.

Dipolar pulse sequences that are more complex than the simple $\phi_X - \phi_{\bar{X}}$ "echo" (ϕ represents the angle of rotation about the dipolar vector; $X / \bar{X}$ represents the phase of the vector during the rotation, with the initial phase arbitrarily labeled X in all crystallites) are possible. A composite dipolar 180° pulse sequence, designed to compensate for dipolar inhomogeneity and resonance mismatch, can be created based on composite rf sequences[32] designed to compensate for the rf-analogous effects: rf inhomogeneity and chemical shift offset, respectively. Here we demonstrate the effectiveness of a very simple example, the $90^0_X - 180^0_Y - 90^0_X$ sequence, and use the second phase control technique (jumps away from resonance) to implement it. The corresponding dipolar pulse sequence has five distinct periods (Fig. (3-19A)): (i) an initial on-resonance dipolar evolution period (with phase X) timed to last long enough for sum polarization to rotate approximately 90° about the recoupled interaction, (a dipolar 90°, phase X) (ii) a jump in the magnitude of the effective fields away from resonance long enough to induce a 90°z rotation of the dipolar vector in the interaction frame, (iii) a second evolution period at resonance lasting approximately twice as long as the first (a dipolar 180°, now with phase Y), (iv) a second jump away from resonance to induce a 270°z

Figure 3-18: $90°_X$-$180°_Y$-$90°_X$ composite dipolar pulse sequence applied to $^{13}C_\alpha$, $^{13}C_\beta$ labeled L-alanine:

(A) The pulse sequence has five periods: (i) initial evolution on-resonance for a period approximating 90° evolution about the dipole (a dipolar $90°_X$ pulse); (ii) a jump away from resonance timed to induce a 90° shift in the phase of the recoupled interaction - from X to Y; (iii) on-resonance evolution lasting approximately twice as long as the initial period (a dipolar $180°_Y$ pulse); (iv) a second jump from resonance timed to induce a 270° phase shift - from Y back to X; (v) a final on-resonance evolution period, lasting approximately as long as the first (a dipolar $90°_X$ pulse).

(B) Evolution of sum (filled symbols) and difference (open symbols) as a function of mixing time. Standard on-resonance evolution (circles) of sum polarization shows the severely damped evolution previously described. Application of the dipolar pulse sequence (squares) induces more complicated dynamics, eventually yielding 50% greater sum-polarization inversion efficiency. (Jumps away from resonance indicated by arrows.) The evolution of difference polarization in both cases is approximately identical.

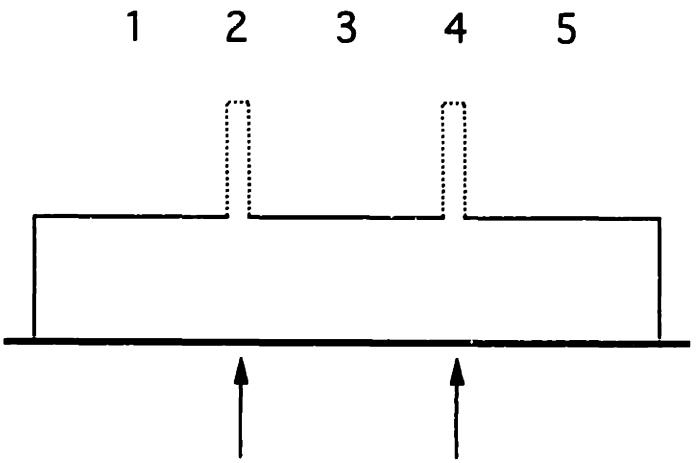
1
2
3
4
5

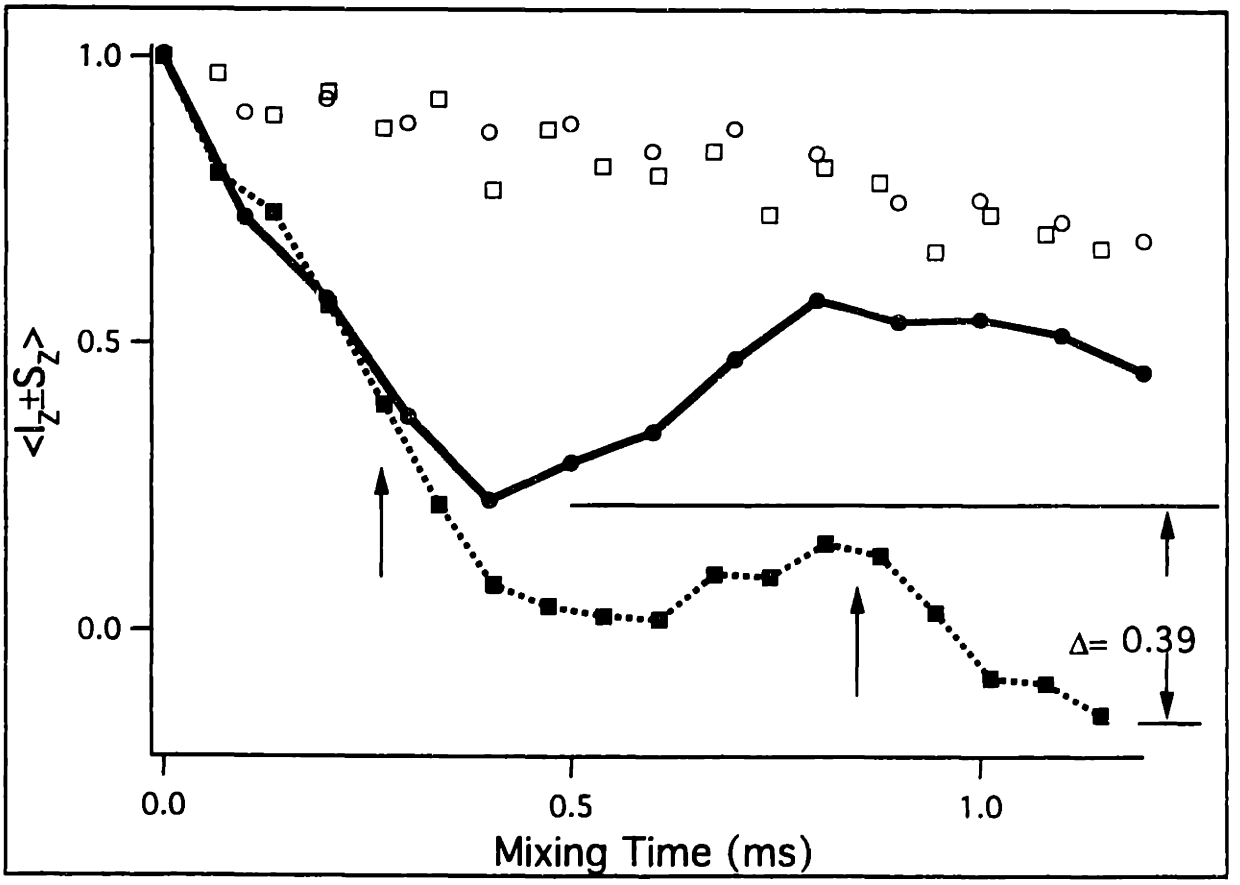
1.0
0.5
0.0
$\langle I_z \pm S_z \rangle$
Δ= 0.39
0.0
0.5
1.0
Mixing Time (ms)

rotation of the dipolar vector, and (v) a final evolution period at resonance (a dipolar 90°, phase X). Throughout this process, the magnetization remains locked along the effective fields - there is no change in the phase of the applied rf, only in its magnitude. Given systems where the sudden jump away from resonance may require a significant change in the effective field orientations (such as sudden application of RF to n=1 RR experiments, where the effective fields may rotate significantly away from longitudinal during the jump), it may be necessary to ramp to and from the off-resonance point so that magnetization remains locked along the effective field.

We demonstrate the implementation of this sequence on the directly-bonded $^{13}C_\alpha$, $^{13}C_\beta$ spin pair in doubly $^{13}C_2$-labeled alanine in Fig. (3-19B). The conditions were identical to those in which the previously described ramped 2Q-HORROR experiments were performed: the spinning speed was set at 13.7 kHz, the carrier was placed directly between the two resonances (offsets ±1.5 kHz) and a 6.7 kHz rf field was used to induce resonance. During each jump away from resonance, the rf field was changed to (and from) 31 kHz in a single step (the first period away from resonance lasted 12μs (90°z); 36μs for the second (270°z)) (note that these jumps away from resonance are somewhat longer than one would calculate; this may be due to pulse imperfections in the "jump" process). The first dipolar mixing period (dipolar 90°x) was 300μs; the second was 600μs, and the third, 300μs. First we show for comparison the standard on-resonance dynamics, acquired as described in the previous section. This plot shows severe damping that leads to an overall efficiency of inversion of the sum polarization (40%) that is significantly lower than the theoretical maximum (≈75%). We have attributed this primarily to resonance mismatch effects,

specifically from the rf-inhomogeneity in the coil. The composite dipolar 180° sequence seems to partially compensate for this effect, achieving an inversion efficiency of 60%. That the difference polarization in the two experiments (on-resonance and jump-induced composite dipolar sequence) evolve almost identically, and that the sum polarization actually goes negative when the dipolar pulse sequence is applied, indicate that the reduced size of the detected sum polarization signal after application of the compensated dipolar pulse is due to further inversion, and not from some type of signal loss induced by the sudden jumps from resonance. Simulation results (not shown) indicate that when mismatch effects are small and dipolar inhomogeneity is the limiting factor, this sequence can achieve efficiencies >90%.

We expect that more complex pulse sequences, with better overall compensation, can achieve significantly better results than we have demonstrated here, even in systems dominated by large resonance mismatch effects. Alternative pulse sequences might also be useful in other applications, for instance composite 90° dipolar pulses may be useful in creating high-efficiency DQ-filtering sequences.

3.5 References.

1. Levitt, M.H., D.P. Raleigh, F. Creuzet, R.G. Griffin. *J. Chem. Phys.* **92**, 6347-6364 (1990).
2. Raleigh, D.P., F. Creuzet, S.K. Das Gupta, M.H. Levitt, R.G. Griffin. *J. Amer. Chem. Soc.* **111**, 4502-4503 (1989).
3. Bennett, A.E., R.G. Griffin, S. Vega. in *NMR Basic Principles and Progress* (eds. Diehl, P., E. Fluck, H. Gunther, R. Kosfeld, J. Seelig) 1-77 (Springer-Verlag, Berlin, 1994).
4. Nielsen, N.C., H. Bildsoe, H.J. Jakobsen. *J. Chem. Phys.* **101**, 1805-1812 (1994).
5. Takegoshi, K., K. Nomura, T. Terao. *Chem. Phys. Lett.* **232**, 424 (1995).
6. Pines, A., M.G. Gibby, J.S. Waugh. *J. Chem. Phys.* **59**, 569-590 (1973).
7. Levitt, M.H., T.G. Oas, R.G. Griffin. *Isr. J. Chem.* **28**, 271 (1988).
8. Spiess, H.W. in *Dynamic NMR Spectroscopy* (eds. Diehl, P., E. Fluck, R. Kosfeld) 58-214 (Springer-Verlag, Berlin, 1978).
9. Waugh, J.S., U. Haeberlen. *Phys. Rev.* **175**, 453-467 (1968).
10. Mehring, M. *Principles of High Resolution NMR in Solids* (Springer-Verlag, Berlin, 1983).
11. Gan, Z.-H., D.M. Grant. *Chem. Phys. Lett.* **168**, 304 (1990).
12. Bennett, A.E., J.H. Ok, R.G. Griffin. *J. Chem. Phys.* **96**, 8624-8627 (1992).
13. Sun, B.-Q., P.R. Costa, D. Kocisko, P.T. Lansbury, Jr., R.G. Griffin. *J. Chem. Phys.* **102**, 702 (1995).

14. Levitt, M.H., D. Suter, R.R. Ernst. *J. Chem. Phys.* **84**, 4243-4255 (1986).
15. Gullion, T., S. Vega. *Chem. Phys. Lett.* **194**, 423 (1992).
16. Weintraub, O., S. Vega, C. Hoelger, H.H. Limbach. *J. Magn. Res. A* **110**, 12-18 (1994).
17. Nielsen, N.C., F. Creuzet, R.G. Griffin. *J. Chem. Phys.* **96**, 5668-5677 (1992).
18. Raleigh, D.P., M.H. Levitt, R.G. Griffin. *Chem. Phys. Lett.* **146**, 71-76 (1988).
19. Morris, G.A., R. Freeman. *J. Magn. Res.* **29**, 433-462 (1977).
20. Bloch, F., A. Siegert. *Phys. Rev.* **57**, 552 (1940).
21. Shirley, J.M. *Phys. Rev. B* **138**, 979 (1965).
22. Zur, Y., M.H. Levitt, S. Vega. *J. Chem. Phys.* **78**, 5293 (1983).
23. Bax, A. *Two-Dimensional Nuclear Magnetic Resonance in Liquids* (Delft University Press, Dordrecht, Holland, 1980).
24. Tycko, R., G. Dabbagh. *Chem. Phys. Lett.* **173**, 461 (1990).
25. Baldus, M., M. Tomaselli, B.H. Meier, R.R. Ernst. *Chem. Phys. Lett.* **230**, 329-336 (1994).
26. Slichter, C.P. *Principles of Magnetic Resonance* (Springer-Verlag, Berlin, 1989).
27. Hediger, S., B.H. Meier, R.R. Ernst. *Chem. Phys. Lett.* **240**, 449 (1995).
28. Cavanagh, J., W.J. Fairbrother, A.G. Palmer III, N.J. Skelton. *Protein NMR Spectroscopy: Principles and Practice* (Academic Press, Inc., San Diego, 1996).
29. Suter, D., R.R. Ernst. *Phys. Rev. B* **25**, 6038-6041 (1982).
30. Levitt, M.H. *J. Magn. Res.* **82**, 427 (1989).

31. Hong, J., G.S. Harbison. *J. Magn. Res. A* **105**, 128-136 (1993).

32. Levitt, M.H. *Progress in NMR Spectroscopy* **18**, 61-122 (1986).

Chapter 4

Polarization Transfer Between Weakly-Coupled Homonuclear Spin-Pairs in a Strongly-Coupled Spin Matrix.

4.1 Introduction.

Dipolar recoupling in two-spin systems is achieved by appropriately manipulating the spin terms in the Hamiltonian so that the average Hamiltonian (over a cycle time τ_c) is essentially dipolar in character. Measurement of the rate of exchange of magnetization between the recoupled sites then gives an estimate of the magnitude of the recoupled dipolar Hamiltonian, and hence the internuclear distance. In larger spin systems, broadbanded recoupling techniques allow the simultaneous reintroduction of many couplings, and one would hope to be able to simultaneously extract numerous distance constraints by mapping out the rates of polarization transfer among the various coupling pathways using standard multidimensional NMR techniques[1]. Such a transition has been made in solution NMR, from observation of two-spin NOE effects which yield a single internuclear distance, to standard 2D (or as 2D slices of ND) ^{1}H-^{1}H NOESY spectra which yield sufficient distance constraints (upwards of 10^3[2]) to accurately determine the structure of small proteins[3].

The transition from homonuclear two-spin to multispin systems in solids has been more difficult for at least two reasons. The first that we will consider is the coherent nature of the polarization transfer process driven by recoupled dipolar interactions in spinning solids. In solution, polarization transfer induced by the Nuclear Overhauser Effect (NOE) is incoherent, in the sense that it is a relaxation process that depends on random motional correlations to allow dipole-driven spin diffusion that would otherwise not occur[4]. Hence the effect is second-order, and its strength has a $1/r^6$ distance dependence. Of particular importance is the fact that polarization transfer between pairs of spins sharing a common partner (spin I coupled to J coupled to K, J being the common partner) occurs independently, except to the extent that each transfer pathway affects the polarization of the common nucleus (this idea is implicit, for instance, in the QUIET-NOESY technique of Bodenhausen, *et. al.*[5], where manipulation of polarization levels allows (approximate) cancellation of polarization transfer through selected pathways in multispin networks). In solids, the recoupled dipolar interaction between I and J (generally) does not commute with that between J and K, with the result that the dynamics show significant dependence on the relative magnitudes of the couplings. In particular, when one coupling dominates, the smaller coupling will be "truncated", and hence have little observable effect on the spin dynamics. Extrapolated to larger spin systems, this effect suggests that it will be difficult to observe significant polarization transfer through weak couplings (e.g. corresponding to 4-5Å internuclear distances) in the strongly-coupled spin system presented by a uniformly-labeled sample using broadband dipolar recoupling techniques. And without transfer of

this type, it will be difficult to extract useful structural information (at least using methods built up from the two-spin case).

The second problem we will consider is polarization transfer between distant spins by a series of transfers through a chain of strongly coupled spins lying between them (loosely termed "spin diffusion"[3]). Because we wish to extract the internuclear distance between a pair of spins by relating the measured rate of polarization transfer between them to the strength of their internuclear coupling, transfer between the two which proceeds by pathways other than the direct one introduces errors in the rate measurement and hence the extracted distance. In solution NMR, ^{1}H-^{1}H NOESY mixing times are kept short enough so that the overall level of polarization transfer between even strongly-coupled ^{1}H nuclei remains small (<10%)[6]. For the more weakly-coupled spin pairs whose internuclear distances are particularly useful in determining structure (3-5Å), these mixing times yield transfer on the order of 0.1-1%. S/N is usually high enough to allow accurate detection and quantitation of such small transfer amounts, even in large biological molecules. In solids the problem is worse for two reasons. First, the difference between the transfer rates for the strongest couplings and the weaker, structurally-useful couplings (1.5Å and 4-5Å, respectively for ^{13}C) may span a larger range in solids (2-3, rather than 1-2, orders of magnitude), yielding smaller levels of polarization transfer through the structurally-useful weak couplings when the overall transfer is kept low (this is in spite of the $1/r^3$ dependence of the dipolar effect in solids). Second, S/N is generally worse in solids, and usually is not sufficient to allow dependable identification and quantitation of polarization transfer levels of 1% or below in most biological molecules of interest. Hence the results of experiments

performed with mixing times which are long enough to allow detection of polarization transfer (if any) between weakly-coupled spin pairs generally show evidence of substantial transfer through weak couplings, allowing for significant spin diffusion effects.

One approach in solids to avoid these problems is to reduce the overall density of the multispin network. If, for instance, ^{13}C labeled samples are synthesized with an enrichment significantly below 100%, and with a random (or other known) distribution of the ^{13}C nuclei, the resulting coupled spin network upon application of broadband recoupling techniques will have a reduced number of pathways for spin diffusion and increased numbers of isolated spin pairs, from whose interaction useful structural information can be extracted (a similar approach has been used in obtaining high-resolution ^{1}H spectra of organic solids[7]). A major drawback of such a scheme is the drop in S/N implicit in label dilution: for a 20% randomly-labeled sample, we expect 4% of the molecules to have a copy of each spin pair, dropping S/N for observing this interaction roughly by a factor of 25.

An alternative approach to reducing recoupled spin density is to use a recoupling technique that does not fully recouple all of the spin pairs in the sample. The rotational resonance (RR) technique[8], for example, recouples only those spin pairs whose chemical shift difference matches a (small) integer multiple of the spinning speed; other couplings are truncated according to their distance from resonance. Given a favorable chemical shift distribution in a uniformly-labeled sample, this allows us to select those spin pairs we recouple, an effect we can exploit to observe the dynamics between weakly coupled spin pairs and hence extract useful structural information. A modification of the RR technique - RR tickling

(RRT) - is useful in a multidimensional framework where selective recoupling over some bandwidth is desired. Alternative chemical shift-dependent recoupling techniques with different resonance conditions can be exploited similarly.

A summary of this chapter is as follows. In the next (second) section we focus on the simplest spin system in which dipolar truncation and spin diffusion effects become evident (3 spins), demonstrating both theoretically. We also consider the effects of the J-interaction, and demonstrate that they can be significant on the >5-10ms timescales necessary to drive polarization between relatively distant spins. In the third section we present experimental results confirming dipolar truncation in a model 3-spin system, under the RFDR[9] and MELODRAMA[10] pulse sequences, and describe additional features of the dynamics. In the fourth section, we use numerical simulation to extrapolate the truncation and diffusion effects to larger spin systems, showing the appearance of "interference" effects for dipolar truncation in 4 spin systems and considering the conformation-dependence of the polarization transfer dynamics expected for a 4-spin system modeled on a segment of molecular backbone. In the final section, we describe the concept of selective recoupling, and demonstrate the use of both RRT and ramped 2Q-HORROR[11] in this context.

4.2 Theoretical Considerations for 3 Spins.

4.2A Non-Commutation of Recoupled Dipolar Interactions.

The zero-order average Hamiltonian calculation for the RFDR dipolar recoupling pulse sequence, given in Bennett, et al[9], for a homonuclear two-spin system (absent CSA), can be generalized to an N-spin system. The internal Hamiltonian for the N-spin system is given by:

$$H = \sum_{n=1}^{N} \omega_n I_Z^{(n)} + \sum_{n=1}^{N}\sum_{m=1}^{n} \omega_{nm}^{(D)}\left(3I_Z^{(n)}I_Z^{(m)} - \vec{I}^{(n)} \bullet \vec{I}^{(m)}\right) \qquad (1).$$

The 180° rf pulses in the standard sequence (placed at the center of each rotor period) do not affect the dipolar terms in the Hamiltonian (ignoring finite pulse effects), but induce a step-wise time-dependence on the chemical shift terms when transformed to the standard toggling frame:

$$\tilde{H} = \sum_{n=1}^{N} f(t)\omega_n I_Z^{(n)} + \sum_{n=1}^{N}\sum_{m=1}^{n} \omega_{nm}^{(D)}\left(3I_Z^{(n)}I_Z^{(m)} - \vec{I}^{(n)} \bullet \vec{I}^{(m)}\right) \qquad (2),$$

where

$$f(t) = \begin{cases} +1 & \text{for } t < \tau_r/2 \\ -1 & \text{for } t \geq \tau_r/2 \end{cases} \qquad (3)$$

for a single rotor period (this assumes delta-function pulses). Subsequent transformation to an interaction frame defined by the (toggled) chemical shift terms:

$$U_{int} = \exp\left(-i\sum_{n=1}^{N} \omega_n I_Z^{(n)} \int f(t)dt\right) \qquad (4),$$

yields

$$\tilde{\tilde{H}} = \sum_{n=1}^{N}\sum_{m=1}^{n} \exp\left[-i\Delta_{nm}\int f(t)dt\left(I_Z^{(n)} - I_Z^{(m)}\right)/2\right] H_{nm}^{(D)} \exp\left[+i\Delta_{nm}\int f(t)dt\left(I_Z^{(n)} - I_Z^{(m)}\right)/2\right] \qquad (5),$$

where we have used $\Delta_{nm} = \omega_n - \omega_m$ and $H_{nm}^{(D)} = \omega_{nm}^{(D)}\left(3I_Z^{(n)}I_Z^{(m)} - \vec{I}^{(n)} \bullet \vec{I}^{(m)}\right)$, the commutation relation:

$$\left[I_Z^{(s)}, H_{nm}^{(D)}\right] = 0 \quad \text{if} \quad s \neq n,m \qquad (6),$$

and the fact that

$$e^{-i\left(\omega_n I_Z^{(n)} + \omega_m I_Z^{(m)}\right)} H_{nm}^{(D)} e^{+i\left(\omega_n I_Z^{(n)} + \omega_m I_Z^{(m)}\right)} = e^{-i\left(\Delta_{nm}\left(I_Z^{(n)} - I_Z^{(m)}\right)/2\right)} H_{nm}^{(D)} e^{+i\left(\Delta_{nm}\left(I_Z^{(n)} - I_Z^{(m)}\right)/2\right)} \quad (7).$$

Connection to the two-spin calculation from this point is clear, each separate dipolar term in (5) having the same form as the single dipolar term in the analogous two-spin derivation. Calculation of the zero-order average then yields

$$\bar{\tilde{H}}^{(0)} = \sum_{n=1}^{N} \sum_{m=1}^{n} \bar{H}_{nm}^{(D)} \quad (8),$$

with (from (Bennett et al[9])):

$$\bar{H}_{nm}^{(D)} = c_{nm}^{RFDR}\left(I_X^{(n)} I_X^{(m)} + I_Y^{(n)} I_Y^{(m)}\right) = \frac{c_{nm}^{RFDR}}{2}\left(I_+^{(n)} I_-^{(m)} + I_-^{(n)} I_+^{(m)}\right) \quad (9),$$

and with $c_{nm}^{RFDR}(\beta,\gamma)$ a function of several variables including dipolar orientation. Note that there is an additional complication in interpreting the validity of the average Hamiltonian (8), due to the noncommutation of the various dipolar terms in the N-spin Hamiltonian. Because the assumption that the spinning speed is much larger than the coupling is implicit even in the two spin case, the more general assumption that the spinning speed dominates all relevant couplings in the system should be sufficient to assure the acceptability of the zero-order approximation in the multispin case.

Generalization of the 2-spin MELODRAMA[10] average Hamiltonian calculation proceeds in a more direct manner from the N-spin internal Hamiltonian (1) above, because the appropriate interaction frame in which the average Hamiltonian is calculated is fully defined by the applied rf fields. Hence no relations of the type in equs (6) and (7) are necessary to demonstrate that the zero-order average for each pair-wise dipolar term

can be calculated separately, the result being (with the rf magnitude a even multiple of the spinning speed):

$$\bar{H}^{(0)} = \sum_{n=1}^{N}\sum_{m=1}^{n} \bar{H}_{nm}^{(D)} \qquad (10),$$

with

$$\bar{H}_{nm}^{(D)} = c_{nm}^{MD}\left(I_X^{(n)}I_X^{(m)} - I_Y^{(n)}I_Y^{(m)}\right) = \frac{c_{nm}^{MD}}{2}\left(I_+^{(n)}I_+^{(m)} + I_-^{(n)}I_-^{(m)}\right) \qquad (11),$$

and again $c_{nm}^{MD}(\beta,\gamma)$ is a function of several variables including the dipolar orientation.

The form of the Hamiltonians in equs (9) and (11) indicate that the RFDR and MELODRAMA pulse sequences yield recoupled dipolar Hamiltonians with zero- and double-quantum character, respectively. In a two-spin system (energy level diagram in Fig. (4-1A)), the RFDR sequence drives "flip-flop" transitions $[(+-)\leftrightarrow(-+)]$ between the central two states (indicated in the 2-spin energy-level diagram by dashed line), while the MELODRAMA sequence drives "flip-flip" transitions $[(++)\leftrightarrow(--)]$ between the outer two states (solid line). The coupling in either case can be represented by the appropriate fictitious spin-1/2 operator as shown. Moving to larger spin systems, the trends evident in this limiting case will hold: dipolar terms with zero-quantum character will, because they induce flip-flop processes that conserve total polarization, drive transitions between levels with the same total polarization. And because dipolar terms with double quantum character induce flip-flip processes that change total polarization by ±2 quanta, they will drive transitions between levels separated by this amount. From the standard energy level diagram for a 3 spin system in Fig. (4-1B, left), we can draw in the appropriate MELODRAMA-recoupled (4-1B, middle) or RFDR-recoupled (4-1B, right) 3-spin transitions by simply connecting all pairs of levels that satisfy

Figure 4-1: Energy level diagrams for 2- and 3-spin (1/2) systems, with couplings induced by zero- and double-quantum recoupling sequences drawn in (dashed and solid lines, respectively). Note that the energy level splittings are arbitrarily assigned, and in most recoupling sequences these splittings are suppressed, so that the coupled levels become degenerate.

(A) 2-spin system. Application of either zero- or double-quantum recoupling sequences couple a pair of levels as shown. This yields a (usually) degenerate two-level system with a coupling term that can be represented using the appropriate fictitious spin-1/2 operator.

(B) 3-spin system. Typical energy level diagram on the right, with the recoupled networks for double- (middle) and zero-quantum (right) recoupling sequences, as shown.

(A)

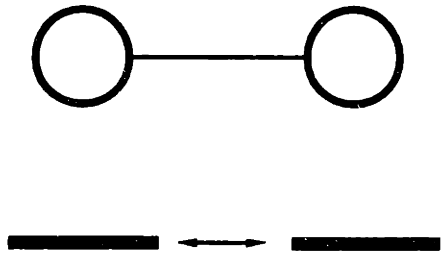

$J_x^{(ab)}$

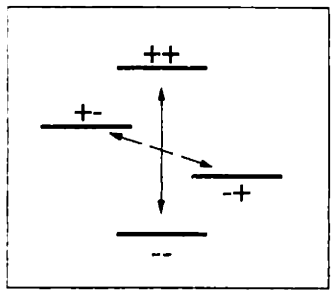

(B)

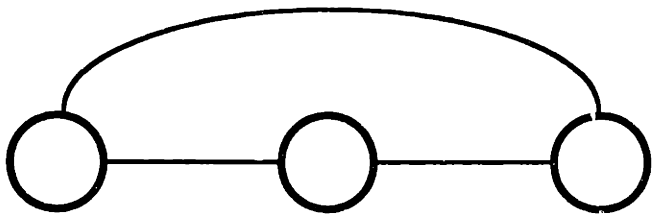

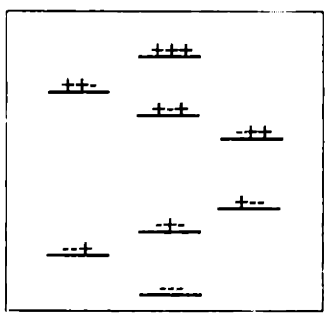

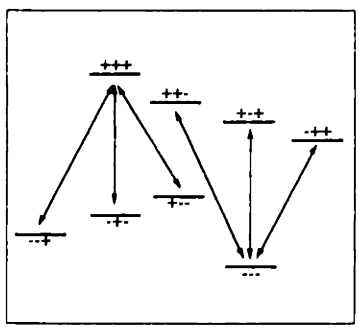

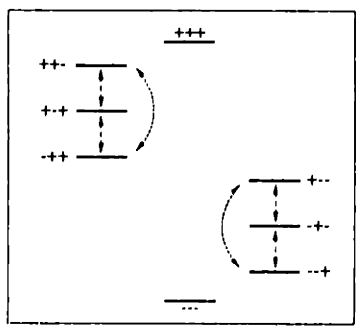

the given constraint for each case (note that the rate at which transitions occur between the connected levels depends on the strength of the recoupled interaction, so that some of the transitions indicated in (4-1B) may not apply to a particular case where one or more of the couplings is negligibly small).

The pattern of connectivity among the energy levels coupled by each type of technique in a 3-spin system is significantly different. Both techniques yield a coupling scheme that has two copies of a single, unique pattern of connectivity, but where the pattern under the RFDR (or other zero-quantum) sequence consists of transitions between all pairs of a 3-level set, the MELODRAMA (or other double-quantum) sequence induces transitions separately from 3 different levels to a single common one. The differences between the two sequences are not central to the line of reasoning we are following here, and are considered in a later section. For now, we want to emphasize the similarities between them. If we eliminate one coupling in the spin system, for instance the coupling between the 1st and 3rd spins (e.g. transitions between $(+\pm-)$ and $(-\pm+)$ for RFDR, and between $(+\pm+)$ and $(-\pm-)$ for MELODRAMA), then one transition in each unique coupled network of energy levels is eliminated. The pattern of connectivity under the RFDR and MELODRAMA sequences becomes identical, each with two different levels separately coupled to a single common level (Fig. (4-2)), and the recoupled Hamiltonian can now be expressed as a sum of the appropriate fictitious spin-1/2 operators from two different spaces which share a common level (as shown).

Expressing the unique block of the Hamiltonian in matrix form (in the appropriate interaction frame, as described above in the derivation of each average Hamiltonian) further emphasizes their similarity. For both

Figure 4-2: Eliminating one of the dipolar interactions in a 3-spin (1/2) system yields similar energy level coupling networks under zero- and double-quantum recoupling, with two levels coupled to a common one. The average dipolar Hamiltonian in this case is a sum of the appropriate fictitious spin-1/2 operators from two different subspaces which share a common level.

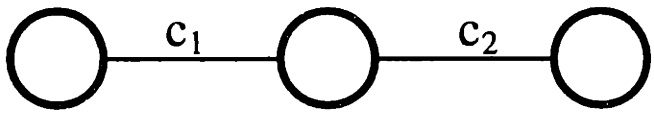
c_1
c_2

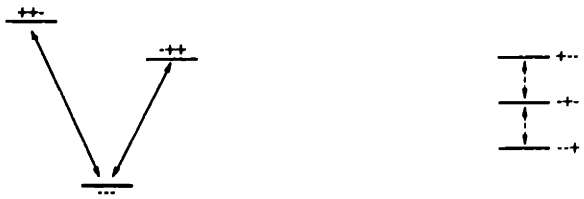


$c_1 J_x^{(ab)}$
$c_2 J_x^{(bc)}$

sequences, we can represent the unique block of the Hamiltonian as:

$$H = \begin{array}{c|ccc} & \langle 1| & \langle 2| & \langle 3| \\ \hline |1\rangle & 0 & c_1 & c_2 \\ |2\rangle & c_1 & 0 & 0 \\ |3\rangle & c_2 & 0 & 0 \end{array} \qquad (12),$$

where for MELODRAMA $|1\rangle = |+++\rangle, |2\rangle = |--+\rangle, |3\rangle = |+--\rangle$ and for RFDR, $|1\rangle = |+-+\rangle, |2\rangle = |-++\rangle, |3\rangle = |++-\rangle$. The constants c_1 and c_2 represent (half) the magnitudes of the couplings between the 1st and 2nd, and 2nd and 3rd, spins, respectively (as indicated in Fig (4-2)). The general form for the propagator derived from this Hamiltonian is

$$U(0,t) = \left[\begin{array}{c|c|c} \cos(\omega t) & -i\frac{c_1}{\omega}\sin(\omega t) & -i\frac{c_2}{\omega}\sin(\omega t) \\ \hline -i\frac{c_1}{\omega}\sin(\omega t) & \frac{c_2^2}{\omega^2}+\frac{c_1^2}{\omega^2}\cos(\omega t) & \frac{c_1 c_2}{\omega^2}(\cos(\omega t)-1)^2 \\ \hline -i\frac{c_2}{\omega}\sin(\omega t) & \frac{c_1 c_2}{\omega^2}(\cos(\omega t)-1)^2 & \frac{c_1^2}{\omega^2}+\frac{c_2^2}{\omega^2}\cos(\omega t) \end{array}\right] \qquad (13),$$

with $\omega = \sqrt{c_1^2 + c_2^2}$. The time-dependence of any observable can then be calculated using the standard equation:

$$\langle O\rangle(t) = Tr[O\rho(t)] = Tr\left[OU_{int}U(0,t)\rho(0)U^{-1}U_{int}^{-1}(0,t)\right] \qquad (14)$$

(Note that the contribution of the non-evolving blocks of the density matrix to the trace calculation must also be included; also U_{int} is generally equal to the identity matrix or a 180° inversion pulse over multiples of a rotor cycle).

Exchange is calculated by assuming initial z-magnetization on one site ($\rho(0) = I_z, J_z$, or K_z), and then determining the time-dependence of z-magnetization on the other sites ($O = I_z, J_z$, or K_z) (odd-order MELODRAMA experiments require a different initial condition ($\rho(0) = I_y, J_y$, or K_y), but yield identical dynamics[10]; hence this distinction is ignored). Given these initial conditions, the interaction frame transformation involves multiplication by the identity matrix with positive

sign (even-order MELODRAMA) or alternative positive and negative sign (RFDR) after successive rotor cycles. The resulting functions are directly interpretable as the expected cross-peak intensities in a standard two-dimensional correlation experiment. The matrix forms for the longitudinal spin operators are diagonal in both bases defined above, with the I_z and K_z operators having identical representations in both RFDR and MELODRAMA bases (the I_z diagonal elements are +-+ (top left to bottom right); for K_z, ++-). The J_z operator is represented by a diagonal matrix with elements (+--) in the MELODRAMA basis, and the negative of this (-++) in the RFDR basis. For MELODRAMA, the general result is:

with $\rho(0) = I_z$:

$$\begin{aligned} \langle I_z \rangle(t) &= c_1'^4 \cos^2(\omega t) + c_2'^2\left(2c_1'^2 \cos(\omega t) + c_2'^2\right) \\ \langle J_z \rangle(t) &= -\left(c_1'^4 + c_1'^2 c_2'^2\right)\sin^2(\omega t) \\ \langle K_z \rangle(t) &= c_1'^2 c_2'^2\left[-\sin^2(\omega t) + 2\left(1-\cos(\omega t)\right)\right] \end{aligned} \qquad \text{(15A-C)},$$

and

with $\rho(0) = J_z$:

$$\begin{aligned} \langle I_z \rangle(t) &= -\left(c_1'^4 + c_1'^2 c_2'^2\right)\sin^2(\omega t) \\ \langle J_z \rangle(t) &= \left(c_1'^4 + 2c_1'^2 c_2'^2 + c_2'^4\right)\cos^2(\omega t) \\ \langle K_z \rangle(t) &= -\left(c_2'^4 + c_1'^2 c_2'^2\right)\sin^2(\omega t) \end{aligned} \qquad \text{(16A-C)},$$

where we have defined $\omega = \sqrt{c_1^2 + c_2^2}$ and $c_x' = c_x/\omega$ (x=1 or 2) (the equations for polarization starting on the K spin can be derived by switching the I and K spins, and the c_1 and c_2 couplings, in equs (15A-C)). The general result for RFDR follows directly from the above equations by taking into account the factor of -1 relating the J_z matrices from the two bases: multiply by a negative one the expectation values which involve a single J_z (e.g. polarization starting on J_z and ending up on I_z or K_z, or polarization starting on I_z or K_z and ending up on J_z), but not the expectation values which involve zero or two J_z's (e.g. polarization starting and remaining on J_z, or polarization starting and ending up on I_z or K_z).

From these general equations, specific cases can be extracted by imposing the appropriate conditions on c_1 and c_2. For example, setting one of the couplings (c_2, e.g. the coupling between J and K) to zero and examining the evolution of polarization initially on the I spin yields the much simplified equations:

with $\rho(0) = I_z$:

$$\begin{aligned} \langle I_z \rangle(t) &= \cos^2(\omega t) &&= \left(\cos(2c_1 t) + 1\right)/2 \\ \langle J_z \rangle(t) &= -\sin^2(\omega t) &&= \left(\cos(2c_1 t) - 1\right)/2 \\ \langle K_z \rangle(t) &= 0 \end{aligned} \qquad \text{(17A-C).}$$

Magnetization that originates on one spin will oscillate to the other spin, and back again, with a frequency given by $2c_2$ (Fig. (4-3A)). Note that magnetization will fully exchange between the sites (i.e. 100% transfer efficiency, at $t = \frac{n\pi}{2c_2}$, n=1,2..) independent of the size of c_2, although for smaller c_2 it will take longer (this neglects relaxation effects, which generally limit transfer efficiency in systems where they dominate to 50%).

The more relevant situation for our purposes is when one coupling dominates the other, for instance $c_2 >> c_1$. The equations this assumption yields, for polarization starting on the I (weakly-coupled spin), are:

with $\rho(0) = I_z$:

$$\begin{aligned} \langle I_z \rangle(t) &= \left[1 - 2x^2(1 - \cos(\omega t))\right] \\ \langle J_z \rangle(t) &= -x^2 \sin^2(\omega t) \\ \langle K_z \rangle(t) &= x^2\left[-\sin^2(\omega t) + 2(1 - \cos(\omega t))\right] \end{aligned} \qquad \text{(18A-C),}$$

where $x = \frac{c_1}{c_2} << 1$, and we have dropped terms of $O(x^4)$ and higher. The maximum transfer (and hence the cross-peak intensity) between the weakly-coupled spin-pair I and J depends on the parameter x and hence scales with the (I,J) coupling, c_1; hence decreases in c_1 that lead to decreased magnetization transfer for a given mixing time can not be fully compensated by longer mixing times (in contrast to the two-spin case).

Figure 4-3: Calculated polarization transfer for a weakly-coupled I-J spin pair (coupling given by c_1) without (A) and with (B) J-spin strongly-coupled to a third spin, K (coupling given by c_2):

(A) In the isolated 2-spin system, unit polarization starting on I fully oscillates to J and back again at a frequency determined by the magnitude of the coupling (see text).

(B) When the effects of a strong coupling are added, two changes occur to the polarization transfer process between the weakly coupled spin pair (I,J). First, the maximum polarization transfer scales as the square of the ratio of the weak to the strong coupling (here we show results for a factor of 20 difference). Second, the oscillation frequency changes from c_1 to c_2, that is, the oscillation frequency for the weak coupling is now determined by the strong coupling.

(A)

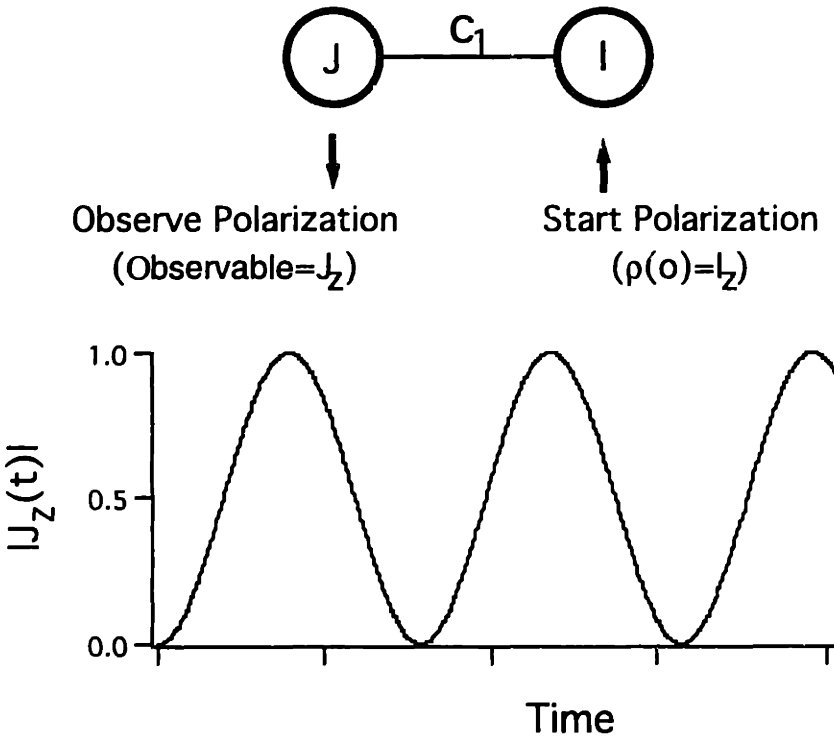
J
C1
I
Observe Polarization
(Observable=Jz)
Start Polarization
(ρ(o)=Iz)
1.0
0.5
0.0
|Jz(t)|
Time

(B)

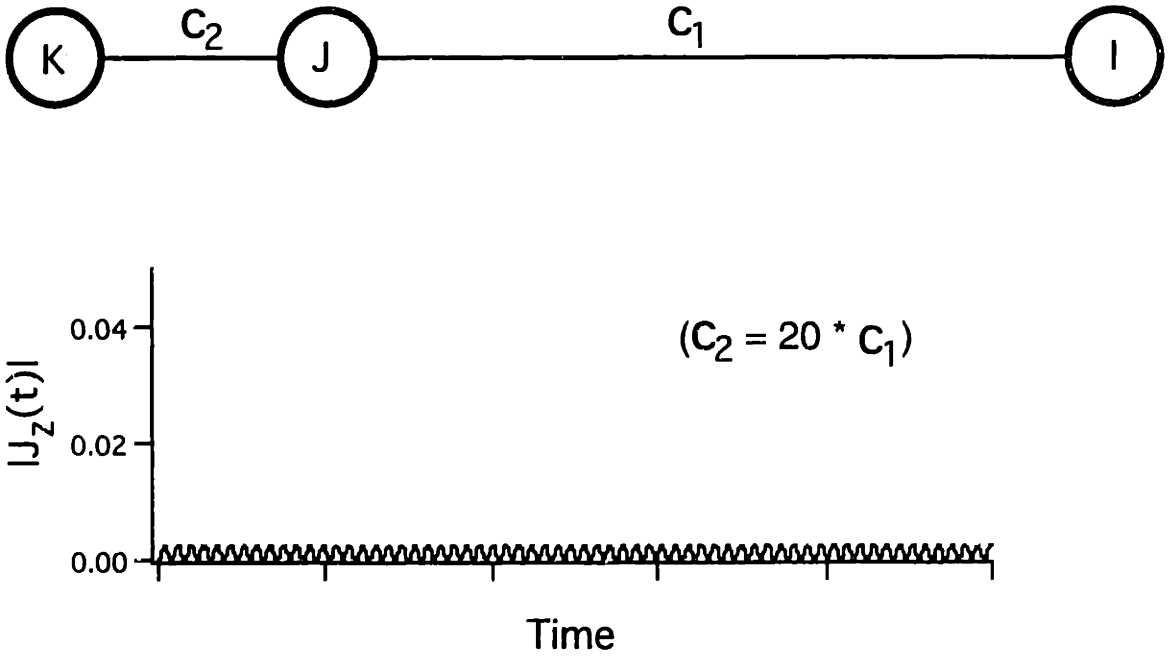
K
C2
J
C1
I
0.04
0.02
0.00
|Jz(t)|
(C2 = 20 * C1)
Time

Furthermore, if the (J,K) coupling arises from a directly bonded interaction (internuclear distance ca. 1.5 Å, corresponding dipolar coupling constant ca. 2.2 kHz) and the (I,J) coupling is on the order of 100Hz (corresponding to an internuclear distance ca. 4.2 Å) then the ratio given in equ. (11) is on the order of 1/400, i.e. a maximum of approximately 0.25% of the magnetization that originates on spin I will be detectable on spin J (Fig. (4-3B); note that this ignores orientational effects discussed below). Maximum transfer on the order of 1% requires that the weak coupling be approximately $1/10^{th}$ of the strong (200 Hz ignoring orientational effects, corresponding to an internuclear distance ca. 3.35 Å).

The discussion to this point considers only a single orientation of the three-spin system relative to the fixed reference frame, i.e. a single crystallite in the polycrystalline sample. That is, the efficiency of dipolar recoupling (and hence the constants c_1 and c_2 in the analysis above) under any of the existing methods depends on the orientation of the internuclear vector connecting the recoupled nuclei relative to the rotor. For MELODRAMA, the orientation dependence is given by $\sin(2\beta)\cos(\gamma)$, where ß is the angle between the dipolar vector and the rotor axis and γ is the initial (t=0) angle around the rotor axis[10]. This means that the magnitude of the recoupled dipolar coupling is given by

$$c_x = \frac{c}{r^3}\sin(2\beta)\cos(\gamma) \qquad (19)$$

where c is an orientation- and internuclear distance-independent constant, r is the internuclear distance, and ß and γ describe the orientation of the dipolar vector relative to the initial rotor frame as described above. The magnetization exchange observed for a polycrystalline sample is a sum of the exchange occurring in each crystallite, hence a powder average is

required (see Chapter One). Consider as an example the extension of the results for the two-spin case given in equs (17A-C) to the exchange observed in a polycrystalline sample: each crystallite-embedded two-spin system shows oscillatory magnetization exchange with a characteristic frequency ($2c_1$) that depends on (i) the internuclear distance (the same in all crystallites), and (ii) the orientation of the dipolar vector relative to the rotor (different in different crystallites). The observed exchange is a sum of oscillations of different frequencies that interfere with each other and lead to a rapid damping of the observed signal. Ignoring relaxation, oscillatory exchange is still occurring in each crystallite, even in the damped region of the observed exchange curve, but because of the powder average we don't see it.

The effect this orientation dependence has on the 3 spin case is harder to analyze generally, because allowing for the dipolar orientation dependence introduces a new variable - the relative angle between the two coupling vectors. If the 3 nuclei are collinear, then the crystallite orientation dependence will be the same for both couplings and, although the absolute magnitudes of the couplings will change over the powder average, their ratio will not. Thus the observed signal will be a sum of single crystallite signals that differ only in frequency but not in amplitude, as in the two-spin case, and the 3 spin analysis given above for one orientation will hold for all orientations. If, however, they are not collinear, then the ratio of the couplings will change as a function of orientation. In particular there will be some molecular orientations in which the strong coupling is not recoupled at all, so that evolution of the system proceeds as in a two-spin system under the weak coupling alone and significant magnetization transfer between J and K can occur (in this class

of crystallites). For a strong coupling of 2.2kHz and a weak coupling of 0.1kHz, a series of numerical simulations that explicitly include the effects of the powder average indicate that maximum polarization transfer approaching 5% is possible when the 3 spin configuration deviates significantly from collinearity (Fig. (4-4A)).

Relaxation can also affect the result, as shown in Fig. (4-4B). The simulations yielding this data were identical to those shown in Fig. (4-4A), except that they also include MQ-relaxation (calculated from a single-quantum rate of 75Hz, although no SQ relaxation was included). Relaxation reduces the ability of the strong couplings to completely refocus the effects of the weak, so that over long times some transfer can occur (although the rate still remains slow). Some method of increasing relaxation rates during mixing (without increasing signal loss) may be one approach to driving polarization transfer between weakly-coupled spins in a strongly-coupled matrix.

4.2B Multistep Polarization Transfer along Strongly-Coupled Pathways.

The presence of strong couplings reduces our ability to measure weak couplings, particularly those of the second type (i.e. those between nuclei separated by 3 to (approximately) 5 bonds - see Chapter One), in another way: magnetization exchange between the spin pair may proceed either directly through the weak coupling connecting them, or through a series of exchange processes between the intervening, strongly-coupled nuclei. Due to the relative sizes of the relevant couplings and the truncating effect we have discussed, in most cases we expect the second pathway to dominate. This will make it difficult to measure the magnitude of exchange (if any) through the first, direct pathway, from which the

Figure 4-4: Numerical simulations of polarization transfer in a 3-spin (1/2), 2 coupling system (as diagrammed). The MELODRAMA pulse sequence was used in the simulation (40kHz rf field, with ω_r=10kHz), chemical shift terms were set to zero, and the two dipolar couplings were assigned as illustrated.

(A) Top plot shows evolution of longitudinal I, J, and K polarization under the MELODRAMA sequence, with unit polarization beginning on the I spin (and a 0° dipolar orientation). Fast transfer between the strongly-coupled J and K spins occurs, but even over long timescales no polarization is transferred to the weakly-coupled I spin. In the bottom left plot, the time-dependence of the I spin is plotted as a function of dipolar orientation; in some orientations, transfer approaching 5% is possible.

(B) Bottom right plot displays same calculations as bottom left, but with 2Q-relaxation (r=150Hz) included. Oscillations are damped, and transfer approaching 8% is possible on this timescale.

(A)

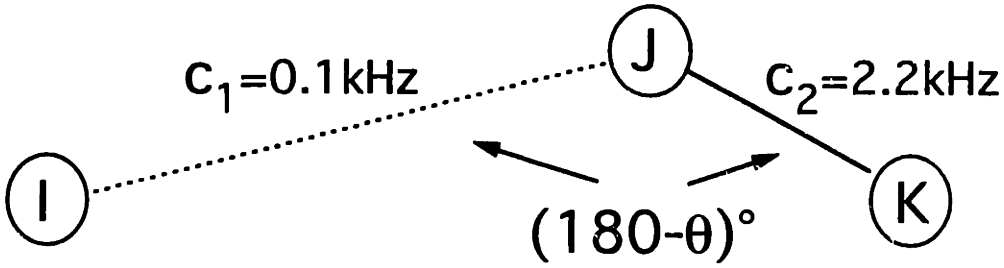
c_1=0.1kHz
J
c_2=2.2kHz
I
K
(180-θ)°

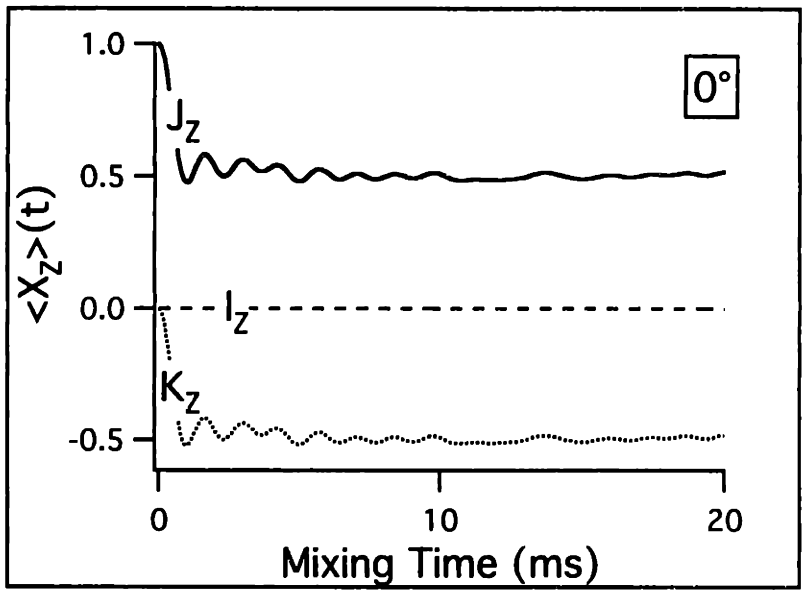
1.0
0.5
0.0
-0.5
0°
J_z
I_z
K_z
<X_z>(t)
0
10
20
Mixing Time (ms)

(B)

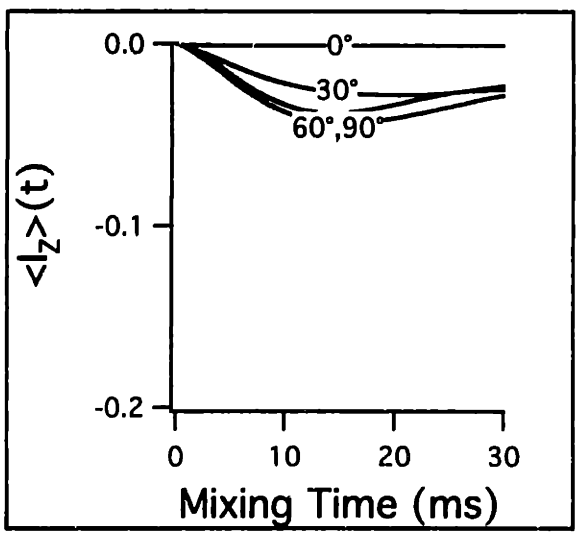
0.0
-0.1
-0.2
0°
30°
60°,90°
<I_z>(t)
0
10
20
30
Mixing Time (ms)

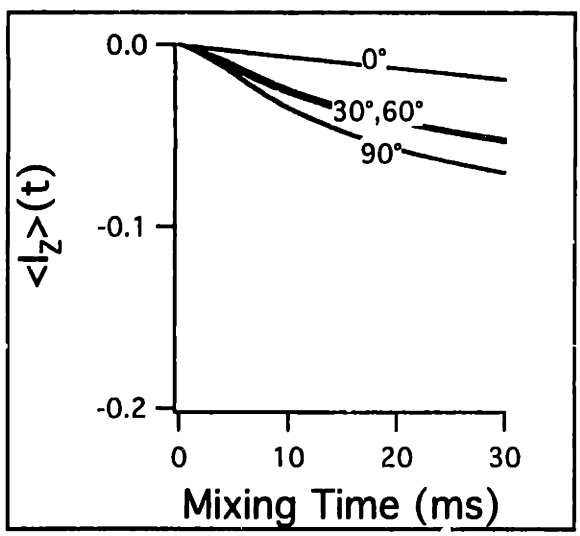
0.0
-0.1
-0.2
0°
30°,60°
90°
<I_z>(t)
0
10
20
30
Mixing Time (ms)

internuclear distance is generally estimated. As an example of the effect, consider the rate at which polarization starting on the I spin appears on the K spin in the 3-spin, 2-coupling system we have previously discussed, where both couplings are equal:

with $\rho(0) = I_z$:

$$\langle K_z \rangle(t) = \frac{1}{4}\left[-\sin^2\left(\sqrt{2}ct\right) + 2\left(1 - \cos\left(\sqrt{2}ct\right)\right)\right] \qquad (24)$$

(adapted from equ (15C), where c represents the magnitude of the directly-bonded dipolar interaction). Two-bond polarization transfer occurs at a frequency determined by the magnitude of the directly-bonded interaction, and almost as quickly as one-bond transfer. Even ignoring the truncating effects of the strong couplings on the weaker, through-space I-K coupling, the transfer rate through the direct path between I and K should be lower by a factor of approximately 4 based solely on the smaller size of the coupling. The exact solution for the MELODRAMA case which includes both the effects of the directly-bonded I-J and J-K couplings and the weaker I-K coupling (set equal to 1/4 the directly-bonded interaction, appropriate for the 3-nuclei geometry of alanine, for example), is:

with $\rho(0) = I_z$:

$$\langle K_z \rangle(t) = \frac{16^2}{33^2}\left[-\sin^2\left(\sqrt{2}ct\right) + 2\left(1 - \cos\left(\sqrt{2}ct\right)\right)\right] - \frac{1}{33}\sin^2\left(\sqrt{2}ct\right) \qquad (24).$$

The first term (in brackets) is identical to (24) above (scaled by ≈5%) and the additional term has very little magnitude. The general conclusion is that the polarization transfer process between the I and K spins is primarily driven by a 2-step transfer, from I to J and then to K, rather than through the I-K coupling itself. (In the 3-spin, 3-coupling case the unique blocks of the RFDR and MELODRAMA Hamiltonians are no longer identical, so that the RFDR equivalent to (24) is not directly derivable from the given MELODRAMA result. The conclusion is the same however: polarization

transfer between the I and K spins in this model system is primarily driven by the two directly-bonded interactions.). Although the powder average increases the effects of the weaker coupling somewhat, for reasons similar to those given in the previous section, the system remains dominated by the strong couplings.

One feature of the MELODRAMA (and other double-quantum recoupling) sequence that is useful in detecting multistep transfer of this type is the dependence of the sign of the cross-peak on the number of transfer steps it arises from[10]. For an isolated spin pair, it is clear from equs (17A-B) that the sign of the cross-peak is negative under MELODRAMA (and positive under RFDR or other zero-quantum recoupling sequence). In the 3-spin, 2-coupling system we have described previously, polarization transfer from the I spin to the J spin yields the expected negative crosspeak (equ (15B)). Subsequent transfer of this polarization to the K spin, however, yields a positive cross-peak (equ (15C)). (Note that in both cases RFDR yields a positive cross-peak). The trend continues for successive transfers of the same polarization; so that in general we expect the cross-peak arising from N successive transfers to have a sign determined by $(-1)^N$.

A draw-back of this feature of double-quantum recoupling sequences is the lack of polarization conservation during mixing, even absent single-quantum relaxation effects. In RFDR (or other zero-quantum techniques) each flip-flop transfer conserves overall polarization, so that the total polarization in a 2D-spectrum, for instance, remains constant for arbitrarily large spin systems with essentially any coupling network (that this is clear for 3 spins can be demonstrated by adding the RFDR-modified equations for I, J, and K polarization in any of the cases described above).

In MELODRAMA, each transfer does not conserve polarization, but in isolated 2-spin systems the sum of the absolute value of the polarization on each spin (positive diagonal peak intensity minus negative cross-peak intensity in a 2D, for instance) is conserved - hence in an important sense the total signal remains constant. This continues to hold for MELODRAMA in the 3-spin, 2-coupling case (which we expect because of its close similarity to the RFDR case), but fails as soon as we add the third coupling to the system (which also ends the similarity with RFDR). In the latter system there are two different pathways, for instance, from the I to the K spin, one through two successive transfers (mediated by the J spin) and yielding a positive crosspeak, and one directly through the I-K coupling that yields a negative cross-peak. Polarization transferred through the two pathways cancels, and so reduces overall polarization in the system. Calculation of the general dynamics under the MELODRAMA pulse sequence for a 3-spin, 3-coupling system yields:
with $\rho(0) = I_z$:

$$\begin{aligned}
\langle I_z\rangle(t) &= \left[\left(c_1'^2 + c_3'^2\right)\cos(\omega t)\right]^2 + c_2'^2\left[2\left(c_1'^2 + c_3'^2\right)\cos(\omega t) + c_2'^2\right] \\
\langle J_z\rangle(t) &= -\left(c_1'^4 + c_1'^2c_2'^2 + c_1'^2c_3'^2 + c_2'^2c_3'^2\right)\sin^2(\omega t) + 2c_2'^2c_3'^2\left(1-\cos(\omega t)\right) \\
\langle K_z\rangle(t) &= -\left(c_3'^4 + c_1'^2c_2'^2 + c_1'^2c_3'^2 + c_2'^2c_3'^2\right)\sin^2(\omega t) + 2c_1'^2c_2'^2\left(1-\cos(\omega t)\right)
\end{aligned} \qquad \text{(25A-C)},$$

with all other cases derivable from this result by appropriate permutation of spin labels and couplings. For a (non-physical) system in which all three couplings are equal ($c_1=c_2=c_3=c$), a plot of the absolute value of the three components indicates that, as polarization oscillates back and forth among the spins, periodically all polarization completely disappears from the system (when $ct = \frac{2\pi}{3}$ or $\frac{4\pi}{3}$ + 2πn). For a more physically reasonable system in which one coupling is approximately a quarter of the magnitude of the other two ($c_1=c_2=c$; $c_3=c/4$), the periodic drop in total absolute

polarization shows a minimum near 80% - that is, approximately 20% of the polarization periodically disappears due to the presence of the weak I-K coupling. Taking into account a powder average, the periodic decay of absolute polarization is damped, and quickly comes to equilibrium with approximately 10% of the polarization lost over the first 1-2ms (Fig. (4-5A)).

The limited amount of decay (10%) in the this case is due to the relatively limited amount of polarization transfer that occurs through the weaker I-K coupling. If one adds multiple-quantum relaxation parameters to the system, the ability of the strong couplings to refocus (and hence attenuate) the I-K driven evolution is reduced (as described previously), and overall signal loss by this mechanism is increased. Assuming a 20Hz homogeneous linewidth for each spin (and MQ relaxation rates that are the sum of the appropriate single-quantum rates), the decay of polarization introduced by the presence of the weak third coupling increases significantly with time, as shown in Fig. (4-5B). Note that absent the third coupling, absolute polarization is conserved regardless of the multiple-quantum relaxation rate.

The simulations so far presented for a 3 spin system suggest that a significant, but modest, signal loss on the order of 10-20% will occur during the first few ms of dipolar mixing with double-quantum type recoupling sequences, independent of more direct single-quantum signal loss processes (e.g. from pulse imperfections, T_2 relaxation). In larger spin systems where a larger number of competing odd/even pathways between spin pairs occurs, we might increased signal loss. This is supported by 4-spin calculations presented in Section 5.4. Recent experimental results show evidence of rapid initial signal loss of this type,

Figure 4-5: Numerical simulations of polarization transfer in a 3-spin (1/2), 3 coupling system under the MELODRAMA pulse sequence (40kHz rf field, with ω_r=10kHz; chemical shift terms were set to zero, and the dipolar couplings were assigned as illustrated to mimic those in U-$^{13}C_3$ labeled alanine).

(A) Evolution of longitudinal I (solid line), J (dotted line), and K (dashed line) polarization as a function of mixing time, starting with unit polarization on the I spin. Fast transfer from I to J to K occurs, as expected (K evolution is shown w/ and w/o the weaker c/4 coupling (two dashed lines); their similarity emphasizes the fact that the strong couplings primarily drive evolution). If the absolute values of the polarization on the three spins is added, one obtains the top (solid, thick) line. There is a (small) initial dip signaling loss on the order of 10% of the initial polarization over the first 1-2ms.

(B) Plot of (absolute) sum polarization for 3 cases: (i) c/4 coupling neglected (top, solid, thick line), no signal loss occurs; (ii) c/4 coupling included, no relaxation (solid thin line) reproduced from (A) above shows the expected initial 10% signal loss followed by equilibrium; and (iii) with MQ relaxation (r=150Hz for DQ coherence), signal loss does not come to equilibrium, and increases with mixing time. Simulations without the c/4 coupling, but including relaxation, show no signal loss.

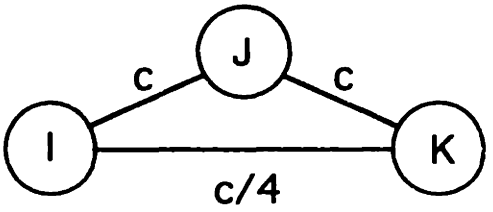
J
c
c
I
K
c/4

(A)

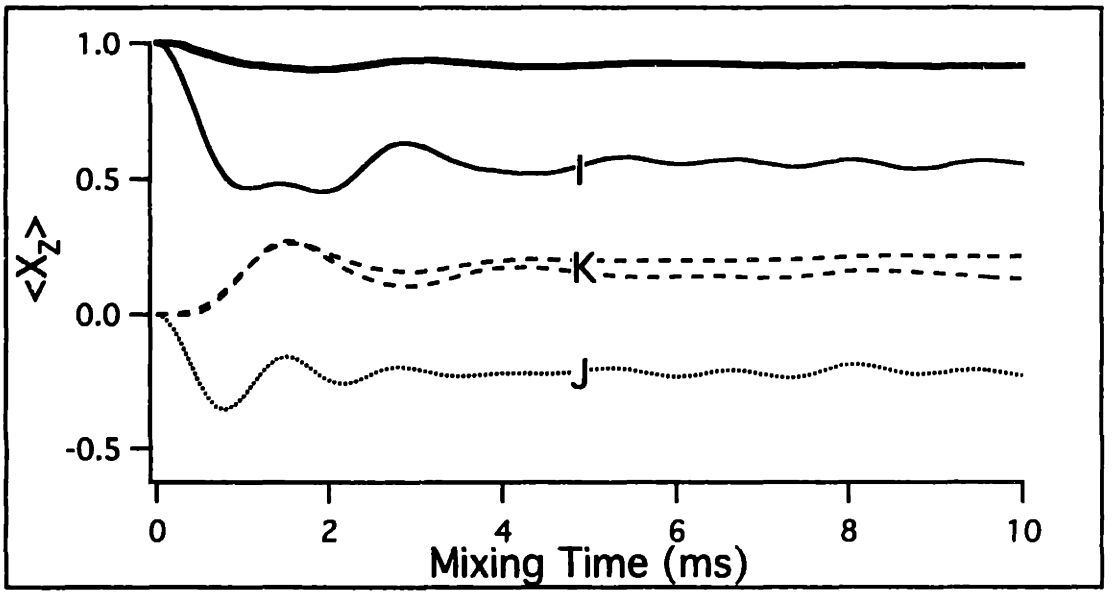
1.0
0.5
0.0
-0.5
<X_Z>
I
K
J
0
2
4
6
8
10
Mixing Time (ms)

(B)

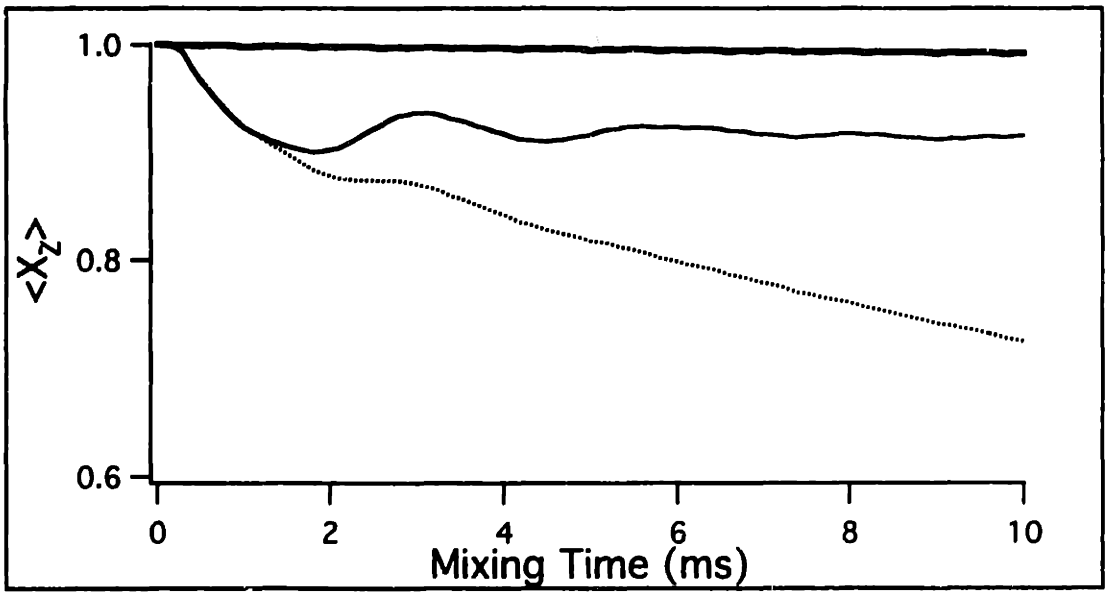
1.0
0.8
0.6
<X_Z>
0
2
4
6
8
10
Mixing Time (ms)

but it is difficult to separate out the various contributions to the overall decay. Efforts to reduce overall signal loss, primarily by improved ^{1}H decoupling efficiency, will also aid in reducing signal loss through this mechanism, but an important point is the fact that some significant amount of loss seems likely to remain in double-quantum recoupling experiments, regardless of the success of these efforts.

4.2C Some Effects of J-Couplings in Recoupling Experiments.

The electron-mediated J-interaction is often ignored in calculating dipolar-recoupled spin dynamics because of its relatively small size, particularly as compared to the magnitude of the dipolar interaction (50Hz vs. 2kHz for directly-bonded ^{13}C nuclei). This is even though the averaged J-interaction (after considering the effects of the dipolar pulse sequence) in many experiments is such that it will drive evolution of the initial state, sometimes in a manner directly competing with the desired dipolar evolution (see below). For the very short mixing times (ca. 1-3 ms) that are commonly used to obtain correlation spectra (from uniformly ^{13}C-labeled samples) with cross-peaks indicating 1- and 2-bond correlations, the assumption that J-driven evolution is minimal is essentially accurate. But because recoupled dipolar interactions are scaled from their static value (by factors on the order of 50-80%), and because the recoupled dipolar interaction magnitude is also scaled by orientation effects, the relative speed with which the J-interaction and the recoupled dipolar interaction drive spin dynamics is not as disparate as the 2kHz vs. 40/50Hz comparison might suggest. For mixing times on the order of 5-10ms applied to samples with directly-bonded ^{13}C spin pairs, significant J-driven evolution occurs in many cases, and for longer mixing times, its effects may

dominate the observed polarization transfer. This presents an additional factor in quantifying polarization transfer between weakly-coupled spin-pairs in strongly-coupled spin networks because of the relatively long mixing times necessary to see the effects of the weak couplings.

The J-interaction (in the rotating frame) between a pair of spins I and S is isotropic in both its spatial and spin components:

$$H = (2\pi J)\tilde{I} \bullet \tilde{S} \qquad (26),$$

where J (in Hz) represents the magnitude of the interaction. For directly-bonded ^{13}C nuclei, J ranges between approx. 40 to 50Hz[12], depending on the intervening bond torsion angle. (^{13}C spins separated by 2 bonds have J-interactions on the order of 3-5Hz; hence at least in this case the J-interaction seems to drop with increasing nuclear separation more quickly than the dipolar interaction, and for isolated spin pairs separated by several bonds the assumption that the J-interaction has no effect on the experiment should become increasingly accurate.) In the presence of chemical shift differences significantly larger than J (which we will assume is always the case, given the small size of J), this is truncated to the "weak coupling" form:

$$H = (2\pi J)I_z S_z \qquad (27).$$

We will consider the effects of two types of RF manipulations on the J-interaction, the first being the series of rotor-synchronized π-pulses applied in the standard RFDR[9] experiment. Because the π-pulses effectively remove the effects of chemical shift truncation of the J-coupling for spin pairs whose shift difference is much smaller than the spinning speed (assuming 1 π pulse per rotor cycle), the form of the effective J-interaction for these pairs under this sequence will be the untruncated, "strong coupling" form in equ (26). This Hamiltonian drives TOCSY-

like[13] isotropic mixing, transferring magnetization of whatever orientation (x-, y-, or z-) from one spin to magnetization of the same orientation on the coupled spin. Hence for the longitudinal initial state used in RFDR, the J-interaction will mimic the RFDR-driven, zero-quantum polarization transfer between directly-bonded spin pairs with $\Delta_{cs} << \omega_r$. And since RFDR recoupling depends on there being a chemical shift difference on the order of the spinning speed (or larger), the directly-bonded spin pairs between which the J-interaction is most effective will also be those whose RFDR recoupling is least efficient. The relative rates of the two interactions in transfering polarization between directly-bonded spin pairs is illustrated in Fig (4-6A). Spin pairs with large chemical shift differences (top) fully exchange polarization through the recoupled dipolar interaction in 1-2ms, and the presence or absence of the J-coupling has no effect on the observed dynamics. For spin pairs with small shift differences (such as might appear in the CH_n region of a peptide spectrum), however, the exchange is much slower (full exchange requiring 6-8ms), and has a significant J-driven component. In the limit of no chemical shift difference (and identical CSA's including orientation), the exchange dynamics are fully determined by the J-interaction. Plotting the dynamics in this case (bottom) provides an estimate of the upper-limit on the rate of J-driven transfer. The effects of 2Q-relaxation on the exchange process, usually minimal in strongly-recoupled systems, may be significant for both dipolar- and J-driven transfer when the chemical shift differences are small relative to the spinning speed, so that rates of transfer are slow. The rate of J-driven transfer in the presence of a typical 2Q-relaxation rate is illustrated in the bottom plot.

Figure 4-6: Numerical simulations of polarization transfer in a 2-spin (1/2) system under the RFDR pulse sequence (40kHz rf field, with ω_r=5kHz; chemical shift terms were set as indicated below, the dipolar coupling constant was 2kHz, and a 40Hz J-interaction was included).

(top) Chemical shift terms set for a $C_{=O}/CH_n$ spin pair (isotropic difference=12kHz, CSA parameters from glycine). Evolution of longitudinal I (solid line) and S (dotted line) polarization as a function of mixing time, starting with unit polarization on the I spin. Fast transfer from I to S occurs over the first 1-2ms; simulations absent the J-interaction (not shown) are identical.

(middle) Chemical shift terms set for a CH_n/CH_n spin pair (isotropic difference=1kHz, CSA parameters from alanine). Evolution of longitudinal I (solid line) and S (dotted line) polarization as a function of mixing time, starting with unit polarization on the I spin. Slower transfer from I to S takes 6-8ms, and simulations absent the J-interaction show that is makes a large contribution to the overall transfer. In experiments with a larger spinning speed to chemical shift difference ratio, we expect the dipolar contribution to drop, and the J-contribution to remain constant.

(bottom) Chemical shift terms set to zero, so that transfer can only proceed through the J-interaction. Simulations with and without relaxation indicate typical J-transfer rates.

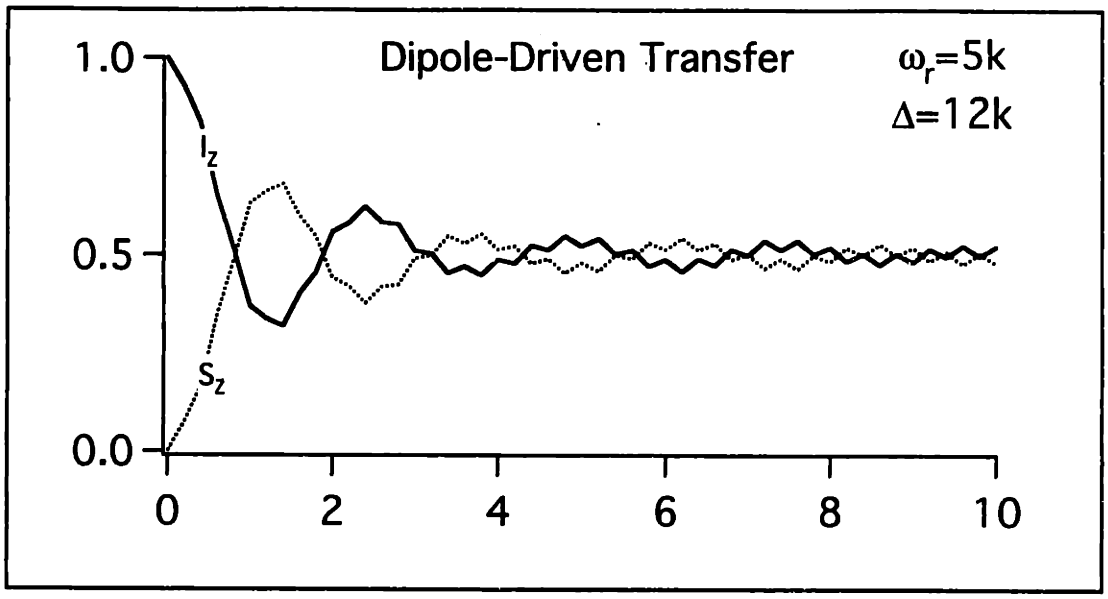
Dipole-Driven Transfer
ω_r=5k
Δ=12k
1.0
0.5
0.0
I_z
S_z
0
2
4
6
8
10

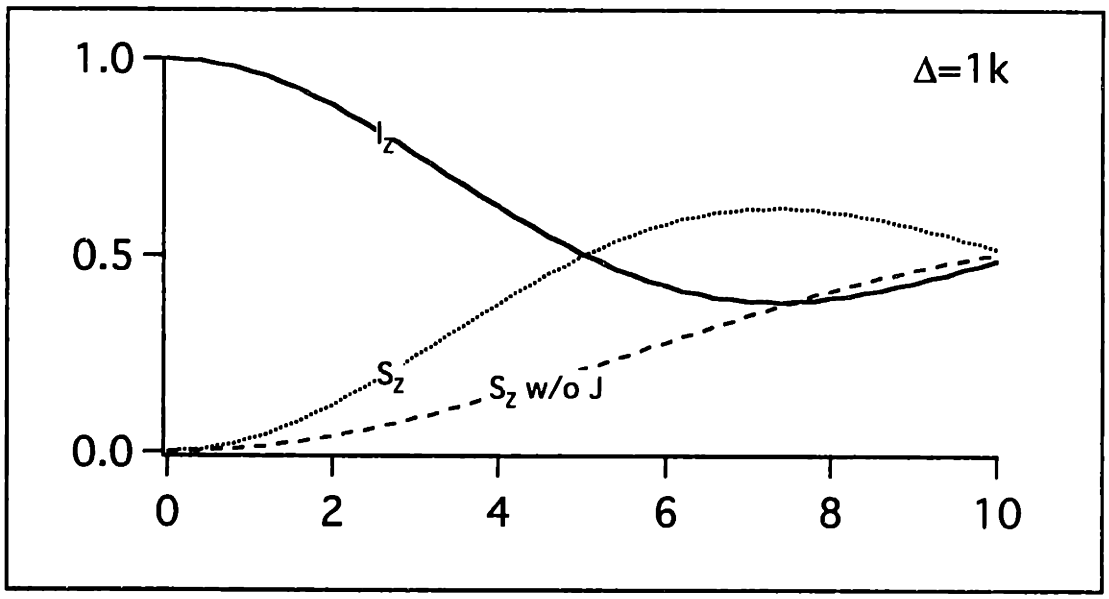
Δ=1k
1.0
0.5
0.0
I_z
S_z
S_z w/o J
0
2
4
6
8
10

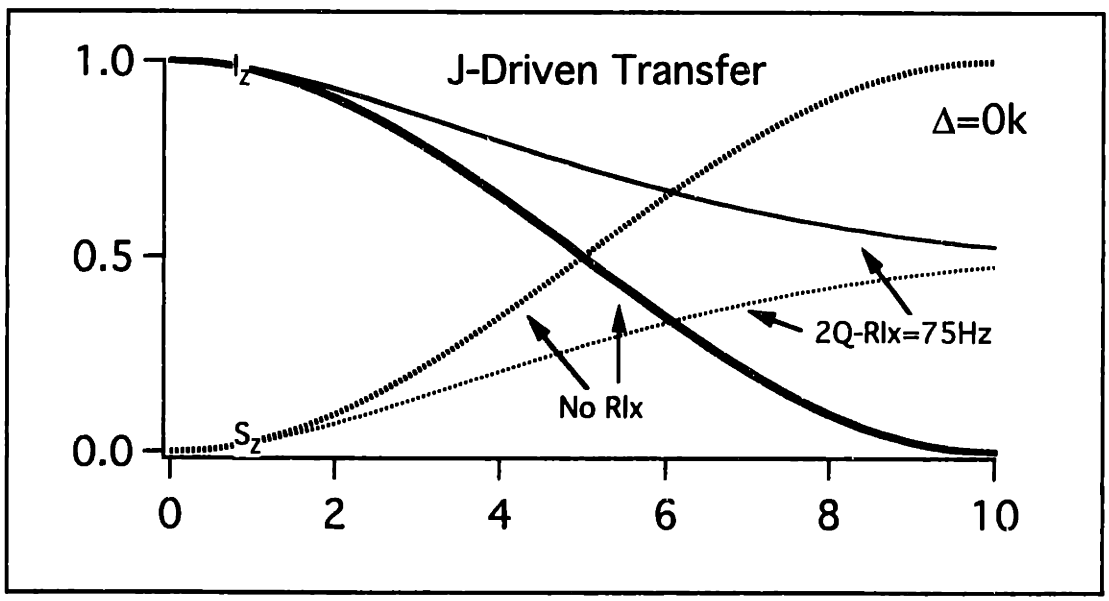
J-Driven Transfer
Δ=0k
1.0
0.5
0.0
I_z
S_z
2Q-Rlx=75Hz
No Rlx
0
2
4
6
8
10

The second type of rf-manipulation of the J-coupling we will consider is the application of continuous bursts of irradiation, as in several "windowless" recoupling sequences, particularly as relevant to the MELODRAMA sequence. Given strong enough irradiation, the chemical shift differences are effectively eliminated, and again the J-interaction regains its strong form of equ (26). Subsequent shifts in the phase of the irradiation should, in principle, have little additional effect on the form of the J-interaction. The reasoning is as follows. The J-interaction initially has the form of a dot product, and dot products are invariant to rotation. Chemical shift differences, which correspond (in the appropriate interaction frame) to different rotations of the I and S spin spaces, do not constitute a single overall rotation and hence do not leave the dot product invariant, instead imparting a time-dependence that leads (upon averaging) to the weak form of equ (27). Application of a strong RF field induces an overall rotation of the spin system that is identical in the two spin spaces to the extent that the rf truncates the chemical shift difference terms in the Hamiltonian. Because the dot product is insensitive to the overall rotation as long as it is identical in both spin spaces, the phase of the applied rf should not matter. To the extent that shifts in the phase of the rf compensate for (or exacerbate) incomplete chemical-shift truncation by the rf field, there may be higher-order effects which affect the extent to which the strong J-interaction is reintroduced.

The "strong" form of the J-interaction under CW rf drives TOCSY-like isotropic mixing, as we have discussed. In the framework of a typical N=4 MELODRAMA experiment in which the polarization is initially longitudinal to maximize the effectiveness of the recoupled dipolar interaction, the J-interaction will again mimic RFDR-like zero-quantum

polarization transfer between directly-bonded spins. In this case, however, the J-driven polarization transfer interferes with the double-quantum, dipolar-driven transfer, with the result that at longer mixing times the effects of the two can cancel out. Consider the dynamics in a strongly-coupled spin pair with a small chemical shift difference (2kHz), Fig. (4-7): although initially (1-2ms) the transferred polarization is negative, indicating dipolar transfer, at longer mixing times (4-10ms) the J-interaction begins to dominate, eventually driving the transferred polarization positive. The data shown for simulations absent the J-interaction confirm that it is responsible for this longer-time effect. In systems with larger chemical shift differences (10kHz), the rf truncation of the chemical shifts is not as complete, and J-driven evolution is reduced (bottom). In both cases, the effects of 2Q-relaxation are expected to have a larger damping effect on the J-driven component, due to its smaller rate.

Figure 4-7: Numerical simulations of polarization transfer in a 2-spin (1/2) system under the MELODRAMA pulse sequence (40kHz rf field, with ω_r=10kHz; chemical shift difference set to 3kHz, and the dipolar coupling constant was 2kHz).

(top) No J-interaction included. Evolution of longitudinal I (solid line) and S (dotted line) polarization as a function of mixing time, starting with unit polarization on the I spin. Fast transfer from I to S occurs over the first 1-2ms, signalled by a drop in I spin intensity and appearance of negative S spin intensity. Equilibrium is reached with positive polarization on the I spin and negative on the S spin.

(bottom) J-interaction included. Initial transfer period yields negative polarization on the S spin, but over the subsequent 5-10ms the S-spin polarization turns positive as the J-interaction drives zero-quantum transitions.

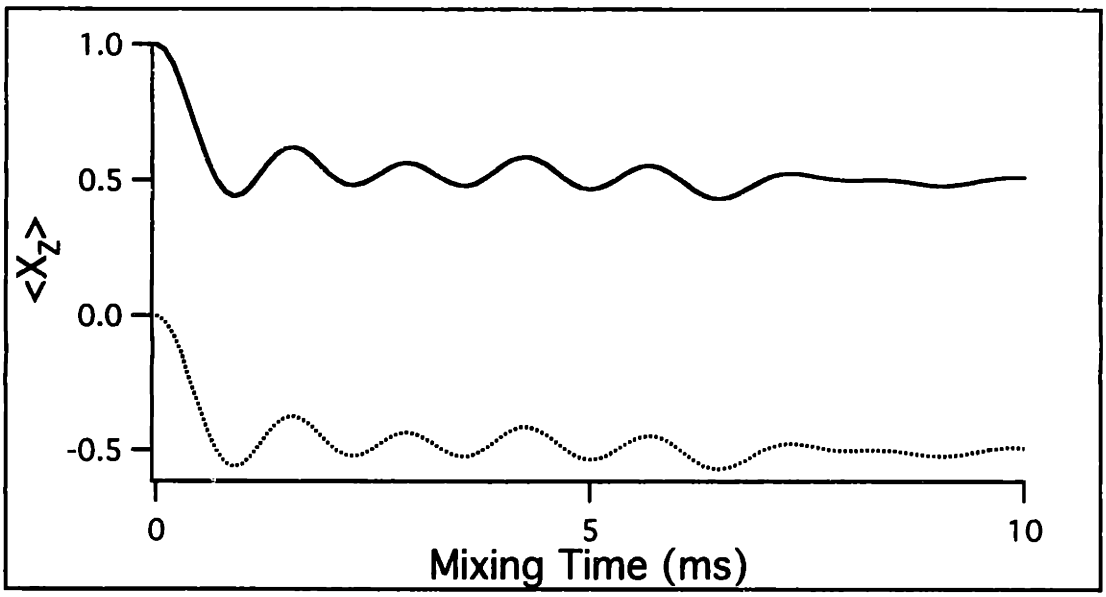
1.0
0.5
0.0
-0.5
<Xz>
0
5
10
Mixing Time (ms)

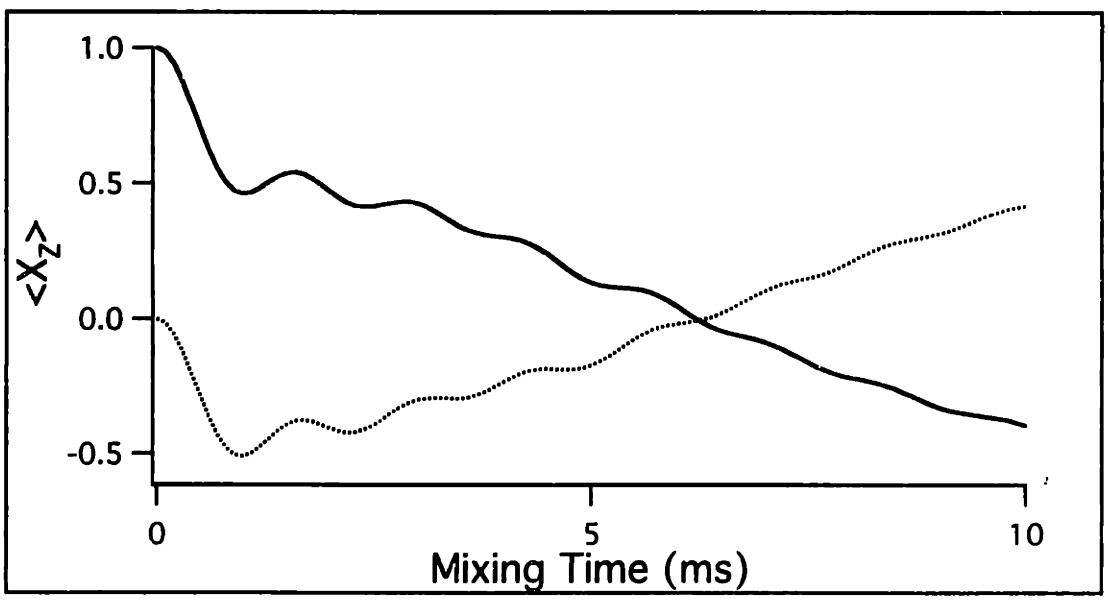
1.0
0.5
0.0
-0.5
<Xz>
0
5
10
Mixing Time (ms)

4.3 Experimental Results for Broadband Dipolar Recoupling Sequences Applied to a Model 3-spin System.

4.3A Model 3-Spin System.

That polarization transfer occurs between well-separated (e.g. 3-5, or more, intervening bonds) ^{13}C nuclei in uniformly ^{13}C-labeled compounds during application of any one of the many broadbanded dipolar recoupling sequences (given a sufficiently long mixing time, e.g. 10-30ms) is not at issue: both published results[14]and results that we have obtained from a series of such compounds (L-Ala, L-Leu, L-Arg, L-Tyr) demonstrate conclusively that this is the case. The calculations presented in the previous section, however, suggest that much of this transfer, in many cases, is due to a series of 1- and 2-bond transfers along the molecular backbone ("through-bond" transfer), rather than directly through the much weaker coupling between the distant spins themselves ("through-space" transfer). If this is the case, then the rate of polarization transfer between well-separated spins no longer has a clear dependence (if any) on the internuclear distance (except as this varies in an overall way with the number of intervening bonds), and extraction of such distance information in the standard manner from measurement of the polarization transfer rate becomes difficult or impossible. Furthermore, we expect little polarization transfer between spin pairs well-separated in the primary sequence, regardless of their spatial proximity (but see section 5.4 for interference effects that limit the validity of this statement).

Before proceeding, I would like to make several qualifying statements relevant to the claims made in the previous paragraph. First, the "dipolar truncation" and "spin diffusion" effects upon which much of

this argument rests depend upon efficient dipolar recoupling of the entire spin network, so that every spin is strongly recoupled to a close (1- or 2-bond) neighbor. Certain sequences which are not fully broadbanded, when applied to samples with particular chemical shift distributions, may not fully recouple the spin matrix, leaving isolated, weakly-coupled spin pairs that then yield a structurally useful cross-peak. The RFDR effect applied to U-^{13}C chlorophyll provides an example: because RFDR most efficiently recouples spin pairs whose chemical shift difference is comparable to or larger than (a small multiple of) the spinning speed, the technique applied to samples (such as chlorophyll) with many neighboring spins with similar chemical shifts (and hence small chemical shift differences) will not efficiently recouple numerous spin pairs in the sample, particular under fast-spinning (ω_r=10k) conditions. The gaps this leaves in the recoupled spin-network may, as stated, leave certain pairs of well-separated spins isolated, so that (if efficiently recoupled themselves) they can exchange significant polarization directly through the coupling between them. This is an example of 'fortuitous' selective recoupling, a more directed form of which is described in a subsequent section. (Note that the presence of a crosspeak between closely-spaced resonances corresponding to a directly-bonded spin pair under RFDR does not necessarily signal effective recoupling of the dipolar interaction (and hence the lack of a 'gap' in the recoupled network), as the J-interaction can drive such transfer in these cases - see previous section.)

Second, interference effects in dipolar truncation will allow detectable levels of polarization transfer between weakly-coupled spin pairs when the relevant strong couplings have the appropriate spatial orientation

(see section 5.4); however the rate of transfer will be strongly dependent on the relative orientations of the couplings.

Third, it may be that the pattern of crosspeak intensities in a standard 2D homonuclear chemical shift correlation experiment, obtained using a broadbanded recoupling technique, still contains useful structural information, even if the polarization transfer processes yielding the crosspeaks were dominated by 1- and 2-bond transfers. One reason this might be the case is because the rate of successive short transfers yielding a crosspeak between relatively distant spins will have some dependence on the relative orientations of the successive couplings. Analysis of this, or some other, effect might allow extraction of useful structural information from these spectra (see following section). The point we want to emphasize here is that the direct relation between internuclear distance and polarization transfer rate that holds in two-spin systems most likely does not hold generally for weakly-coupled spin pairs in a strongly-coupled spin matrix, making it difficult to apply the methods which have been used to extract information in the two spin case (quantitation of polarization transfer rate and direct relation to distance) in the multispin case.

Direct experimental confirmation of these claims is not easily made by examining the polarization transfer dynamics in small (and hence easily obtainable), uniformly ^{13}C-labeled molecules such as amino acids. Although, as stated, experimental results indicate polarization transfer between even the most distant spin pairs often occurs in these samples (given a sufficiently long mixing time), the relatively small number of intervening bonds between such spins allows for the possibility that the overall transfer is primarily due to a series of 1- and 2-bond transfers. Furthermore, separation of through-bond and through-space transfer has

proven difficult for well-separated spins (not withstanding the crosspeak sign-inversion property of double-quantum recoupling experiments like MELODRAMA). Application of the experiment to significantly larger, uniformly-labeled samples, with sufficient overall structure such that nuclei far apart in the primary sequence are relatively close in space, would provide one method to test the validity of these claims. Because through-bond transfer would be effectively eliminated by the large number of intervening bonds between certain pairs of spins, any observed polarization transfer between such spins could be attributed to the through-space interaction with some confidence. Uniformly ^{13}C-labeled Lys-Tyr dipeptide, which crystallizes in a "hairpin" conformation such that the Lys and Tyr sidechains parallel each other, is an example of the type of sample where this effect might be visible: exchange between the ^{13}C nuclei at the ends of the two sidechains under application of standard broadband recoupling sequences would provide a measure of the effectiveness of dipolar truncation in eliminating transfer through weak couplings in this system. Difficulties in synthesizing this sample have blocked such an approach.

Specifically labeling two (spatially) neighboring regions of a molecule, leaving the nuclei between the two regions (in the primary sequence) unlabeled, provides an alternative approach which does not place constraints on the structure of the chosen molecule. Polarization transfer between the two regions must be "through-space" because of the lack of a continuous pathway of strongly-coupled spins between them. Hence if the two labeled regions contain strongly-coupled spin pairs, then measurement of the polarization transfer rate through the weak couplings between the two regions provides a method to examine the dipolar truncation effect.

The labeling scheme most closely matching the 3-spin systems described in the previous sections of this chapter requires one region consisting of a directly-bonded spin pair, and a second region consisting of a single, isolated spin. Using the tripeptide glycylglycylvaline (GGV; natural abundance ^{13}C spectrum in Fig (4-8A)) as our matrix, we have synthesized such a sample by labeling the alpha and carbonyl carbons of the central glycine residue, and the carboxyl carbon of the terminal valine (Fig (4-8B)). A doubly $^{13}C_2$-labeled version of this sample (alpha carbon of the central glycine and terminal carboxyl) has also been synthesized as a control (Fig. (4-8C)).

Analysis of the published crystal structure[15] yields the following values (magnitude and orientation) for the relevant dipolar tensors in GGV:

Coupling	distance (Å)	b_{IS} (kHz)	Orientation*
$G_\alpha(2)$-$G_\omega(2)$	1.51	2.38	(0°,0°,0°)
$G_\alpha(2)$-$V_\omega(3)$	4.52	0.089	(0°,-21°,0°)
$G_\omega(2)$-$V_\omega(3)$	3.16	0.26	(0°,-31°,0°)

(*relative to a coordinate system with z-axis along the $G_\alpha(2)$-$G_\omega(2)$ bond, and y-axis perpendicular to the plane formed by the 3 labeled nuclei).

Experimental: Specifically ^{13}C-labeled variants of the tripeptide glycylglycyl(L-)valine were synthesized stepwise on solid-phase support using standard Fmoc chemistry.

First, specifically ^{13}C-labeled Fmoc-amino acids were synthesized from their labeled amino acid precursors (obtained from CIL) as follows (method from D. Kocisko[16]): (i) mix 2mmol amino acid (dissolved in 8ml warm, aq. 10% (w/v) Na_2CO_3) with 2.5mmol FMOC-O-Su (dissolved in 5ml 1,4 dioxane); (ii) stir 24-72hr, adding 1mmol FMOC-O-Su

Figure 4-8: ^{13}C spectra of the tripeptide glycylglycyl(L-)valine, with various labeling schemes (ω_r=8kHz; ^{1}H decoupling power 80-90kHz):

(A) Natural abundance compound; peaks assigned using information from specifically ^{13}C-labeled compounds listed below, and by reference to tabulated chemical shift data.

(B) $^{13}C_3$-labeled compound, with both carbons of the central glycine and the carboxyl of the terminal valine labeled. Note the broadening of the directly-bonded 13C spin pair due primarily to the J-interaction.

(C) $^{13}C_2$-labeled compound, with the alpha carbon of the central glycine and the carboxyl of the terminal valine labeled.

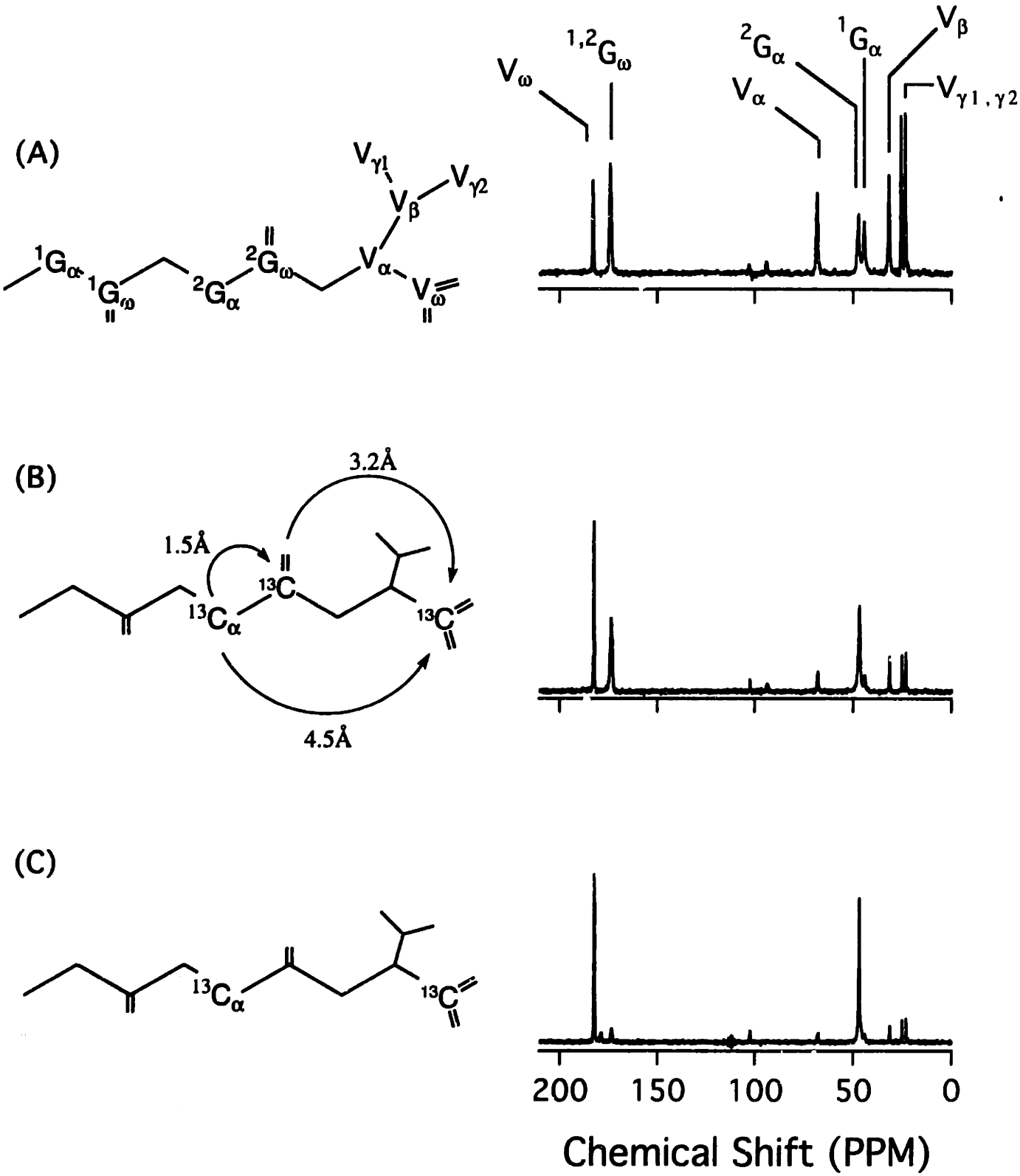
(A)
$V_{\gamma 1}$
$V_{\gamma 2}$
V_β
$^1G_\alpha$
$^1G_\omega$
$^2G_\omega$
$^2G_\alpha$
V_α
V_ω
$^{1,2}G_\omega$
$^2G_\alpha$
$^1G_\alpha$
V_β
V_ω
V_α
$V_{\gamma 1,\gamma 2}$
(B)
3.2Å
1.5Å
^{13}C
$^{13}C_\alpha$
^{13}C
4.5Å
(C)
$^{13}C_\alpha$
^{13}C
200
150
100
50
0
Chemical Shift (PPM)

approximately halfway through this period; (iii) dilute reaction with 30ml H_2O, and extract 3X with ethyl ether (keeping aq. layer); (iv) add 50ml ethyl acetate to aq. solution, and reduce pH to 2 with concentrated HCl (=5ml); (v) extract solution 2X with 1N HCl, 2X with H_2O; (vi) dry with $MgSO_4$, filter, and rotovap off solvent, yielding FMOC-amino acid crystals. Verify purity by TLC (using 10:1 toluene:acetic acid). The expected yield is 60-80%. (Natural abundance Fmoc-amino acids were obtained commercially.)

Second, the c-terminal (valine) residue was coupled to the resin (p-benzyloxybenzyl alcohol, "Wang", resin) following the method of Sieber[17] (dry reagents are crucial): (i) dissolve resin and 2 equivalents (eq; calculated from resin substitution level) of Fmoc-amino acid in minimal DMF (in reaction vessel) and shake 15 minutes; (ii) add 3.3eq pyridine and 2eq 2,6 dichlorobenzoylchloride successively, and shake 15-20hr; (iii) wash (2X DMF); (iv) cap with 5eq benzoyl chloride, 10eq pyridine (shake 10-15min); (v) wash. The expected yield is 40-50% (calculated as a percentage of resin "sites" coupled to amino acid).

Third, successive residues were coupled to the first (working c-terminal to n-terminal) as follows (method from T. Ashburn, K. Halverson[18]): (i) remove Fmoc (deprotect) by adding 50% piperdine/DMF and shaking 15-20min; (ii) wash 2X DMF, 2X methanol, 2X DCM; (iii) confirm deprotection by Kaiser test; (iv) wash 2X DMF; (v) couple next residue by adding 3eq Fmoc-amino acid, 3eq PyBOP, 3eq HOBt, and 4.5eq DIEA, shaking for 2-4hr; (vi) confirm coupling by Kaiser test; (vii) acetylate with 10eq acetic anhydride, 5eq DIEA, shaking 10-15min; (viii) wash 2X DMF, 2X DCM; repeat for additional residues.

Fourth, the completed peptide was removed from the resin as follows: (i) deprotect; (ii) wash 2X DCM, dry resin under vacuum; (iii) cleave peptide by shaking 2-3hr with reagent K[19] (10ml per 1g resin): 82.5% TFA, 5% phenol, 5% H_2O, 5% thioanisole, 2.5% ethane dithiol.(% by volume); (iv) filter solution and rotovap off solvent, yielding an oil; (v) pipet oil into ether, centrifuge mixture and keep solid (this is peptide).

Fifth, the peptide was purified by HPLC. With H_2O (0.1% TFA) as the mobile phase on a C4 column, the GGV peptide comes off after 4min. A subsequent ramp to 80% H2O/20% acetonitrile (maintaining 0.1% TFA) over 5 minutes washes off impurities. Rotovapping off solvent from the GGV peak yielded an oil, and solution NMR (^1H and ^{13}C) analysis of this material confirmed identity and purity.

Crystalline material was obtained as follows (method from BACHEM Bioscience Inc., Philadelphia, PA[20]): (i) dissolve peptide (oil) in water, and add approx 5-10eq of natural abundance material obtained from BACHEM (so that intermolecular spin-spin effects are minimzied in the NMR experiments); (ii) rotovap off excess water to saturate solution; (iii) add isopropyl alcohol to approximately triple overall volume; (iv) store <0°C for 12-24hr. Yields white crystalline material suspended in solution which can be isolated by filtration (wash filtrate 2X with isopropyl alcohol, 2X acetone). ^{13}C NMR spectra of solid material thus obtained show narrow peaks (20-50 Hz (FWHM) at 9.4T), indicating high crystallinity, and with peak positions identical to those observed in the natural abundance material, Fig (4-X). (Note that the resonance peaks arising from the directly-bonded spin pair in the $^{13}C_3$-labeled GGV variant are broadened by the J-interaction.) The spectra in this figure were

obtained using standard CP/MAS techniques, with a spinning speed of 8kHz and ^{1}H decoupling power of 80-90kHz.

4.3B RFDR Results.

RF-driven dipolar recoupling, RFDR[9] (or equivalently broadband dipolar recoupling, BDR[21]), involves the application of rotor-synchronized π-pulses to broaden rotational resonance conditions, providing a less chemical-shift dependent ("broadband") recoupling technique. Recoupling under the RFDR sequence is generally most efficient when the spinning speed is near a rotational resonance condition (i.e. equal to a (sub)multiple of the chemical shift difference for the relevant spin pair), but because of the broadening effects of the π-pulses a significant recoupling effect is still seen when the spinning speed lies between conditions, independent of the size of the coupling. When the spinning speed greatly exceeds the chemical shift difference, however, there are no nearby rotational resonance conditions, and recoupling efficiency drops dramatically. Hence the RFDR sequence is not fully "broadbanded" in the sense that spin pairs with small chemical shift differences relative to the spinning speed (such as might exist in the aliphatic region of a typical peptide spectrum) will not be efficiently recoupled. This effect can be exploited to reduce the density of the recoupled spin network in uniformly labeled samples, reducing spin diffusion and dipolar truncation and hence allowing extraction of more accurate internuclear distance information in the 3-5Å range (Andrew Bennett has suggested applying fewer π-pulses (e.g. 1 every 2 or 3 rotor cycles) to reduce the broadening of the rotational resonance condition[22] and hence increase the chemical shift-dependence of the technique even

further, with the limit of no π-pulses equivalent to the standard rotational resonance experiment.).

Of practical importance in the application of the RFDR technique is the loss of signal that occurs during application of the pulse sequence to a typical spin system. The signal loss occurs for several reasons, including rf imperfections (inhomogeneity, mis-set pulses, etc.), and chemical shift offset effects. A π-pulse train with a specific phase alternation pattern for adjacent pulses (the XY-16, $XYXY\,YXYX\,\overline{X}\overline{Y}\overline{X}\overline{Y}\,\overline{Y}X\overline{Y}X$, pattern, where each letter X or Y represents the phase of the corresponding 180° pulse, is particularly effective), compensates for many of these effects, although not without the presence of a residual transverse component of the spin polarization throughout the experiment (the relaxation of which - according to T_2 - leads to signal loss). Higher-power rf pulses can reduce signal loss of this type, particularly in systems with significant chemical shift offsets.

A second effect that leads to signal loss is the decreased efficiency of ^{1}H decoupling that occurs upon simultaneous application of rf on both the low-γ (e.g. ^{13}C) and ^{1}H channels (^{1}H decoupling is applied throughout the experiment to remove the effects of the strong ^{1}H-low-γ dipolar interactions on the evolution of the low-γ nuclei). An average Hamiltonian calculation of this effect, first by Bennett[23] and subsequently by Terao[24], et al, suggests that the signal loss is minimized by maximizing the ratio of the ^{1}H to low-γ rf power, with a ratio approaching 3 being sufficient to eliminate most signal loss. This can present something of a problem, because maximizing the low-γ rf power to minimize signal losses of the type described in the previous paragraph can lead to unacceptably high ^{1}H power levels necessary to satisfy the "ratio-of-3" rule just

mentioned. In such cases, a some compromise is necessary which minimizes overall signal loss.

Signal loss during mixing is a problem common to almost all dipolar recoupling sequences, which require vigorous rf manipulation of the low-γ spin polarization to achieve recoupling (rotational resonance (and variants - e.g. RRT) is a notable exception, as (little or) no rf is applied during dipolar mixing). As stated, contributions to this effect come from both low-γ rf imperfections (and interactions with chemical shift), and from reduced ^{1}H decoupling efficiency. The result is that very high ^{1}H decoupling power is necessary to allow sufficient low-γ rf power to minimize signal losses of the 1st type while still satisfying the "ratio-of-3" rule. When high enough ^{1}H decoupling power is not available (this has, at least until recently, been the case in our lab), one must live with signal losses that can be prohibitively large, particularly when one wants to mix for the 10's of ms necessary to see significant effects from weak couplings (see, for instance, the published results for the C7 sequence[25]).

We have applied the RFDR pulse sequence (with 1 π-pulse per rotor cycle) to the doubly $^{13}C_2$-labeled GGV sample (described in the previous section) to demonstrate the effectiveness of the technique, and to provide a control for subsequent 3-spin experiments. The pulse sequence is diagrammed in Fig. (4-9A): after standard cross-polarization (and subsequent decoupling on the ^{1}H channel), a period of transverse evolution occurs on the low-γ channel, either to allow for inversion (see chapter one), or for the incremented t_1 period necessary for a 2D spectrum. A 90° pulse then creates longitudinal polarization for mixing, and the rotor-synchronized π-pulse train (multiples of XY-16) is applied to create the RFDR effect. After mixing, a 90° pulse creates transverse polarization for

Figure 4-9: RFDR pulse sequence (A) and results (B) from $^{13}C_2$-labeled GGV:

(A) The RFDR mixing sequence (π-pulses at the center of each rotor period) is placed within the framework of a standard longitudinal mixing experiment (see Chapter One) to drive longitudinal polarization transfer. Free evolution after CP but before the first ^{13}C 90° can either be used for inversion, or as an incremented chemical shift evolution period for 2D acquisitions.

(B) Plot of residual sum (Σ) and difference (Δ) polarization as a function of mixing under the RFDR sequence (experimental parameters given in text). The large decay of difference polarization shows the effects of the recoupled interaction, however the decay of sum polarization indicates overall signal loss during mixing. The solid lines are approximate fits to the data (see text).

(C) 1D slices extracted from the 2D spectra, selected to pass through the glycine C_α diagonal. At zero mixing time, all of the intensity lies in the diagonal; at subsequent mixing times a crosspeak to the weakly-coupled valine C_ω appears. This confirms the 1D mixing curve results.

(A)

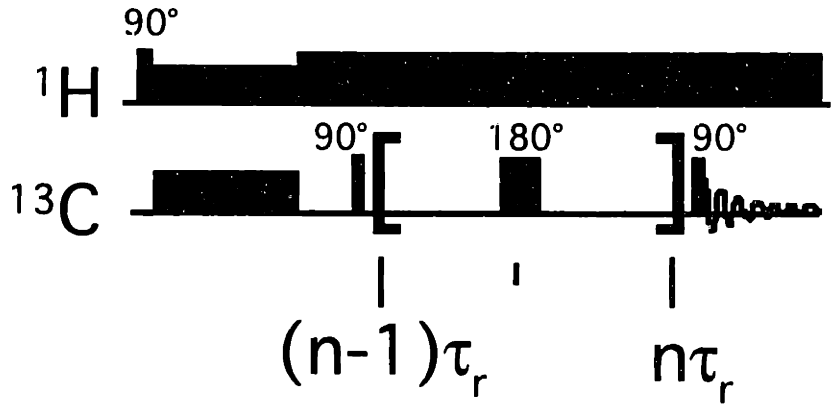
90°
^{1}H
90°
180°
90°
^{13}C
(n-1)τ_r
nτ_r

(B)

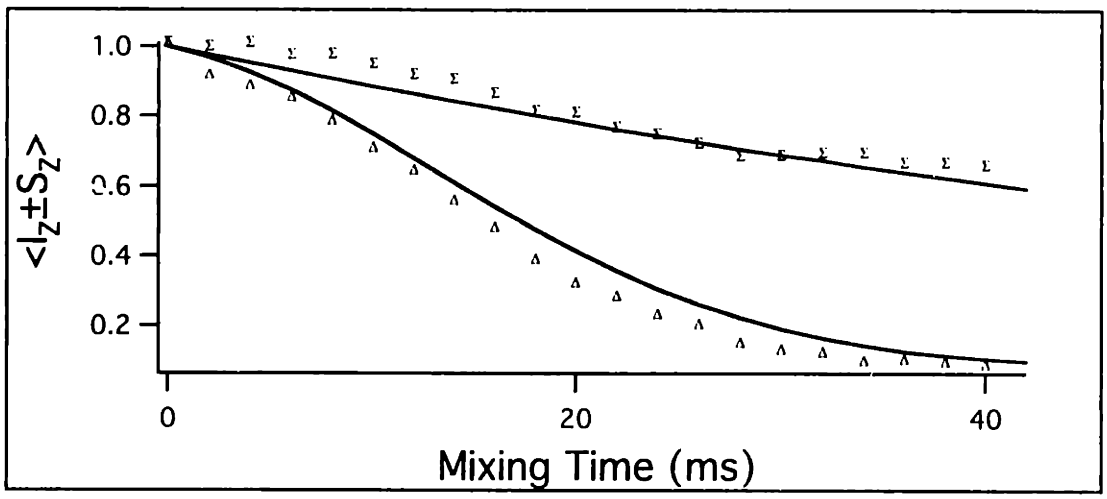
1.0
0.8
0.6
0.4
0.2
<$I_z \pm S_z$>
0
20
40
Mixing Time (ms)

(C)

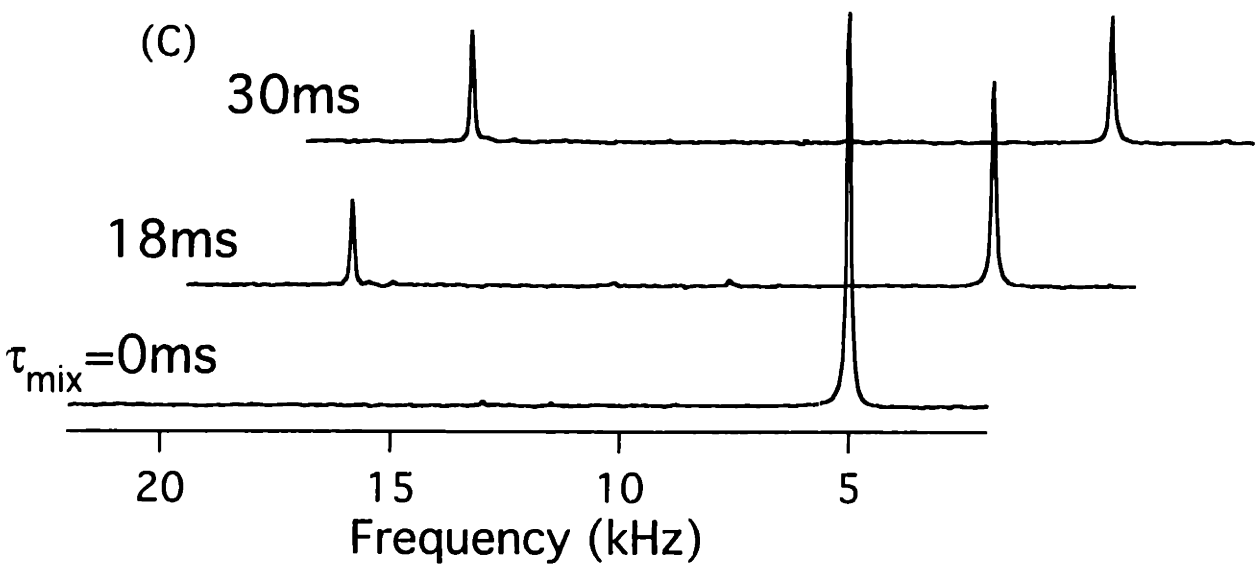
30ms
18ms
τ_{mix}=0ms
20
15
10
5
Frequency (kHz)

detection. In the experiments described here, the spinning speed was set equal to 8kHz (τ_r=0.125ms), and the mixing time was set to an integer multiple of 2ms to allow for full XY-16 cycling of the 180° pulses (16*0.125ms=2ms) at each point. In a 2-spin system, monitoring the evolution of both sum and difference polarization under the mixing sequence allows separation of dipolar-driven polarization transfer and signal-loss effects: because the recoupled Hamiltonian has zero-quantum character, only difference polarization will evolve under the recoupled Hamiltonian, and any decay of sum polarization can be attributed to non-ideal signal losses of the type just described (some of which may be dipolar-dependent). (Note that the difference between the intensity of these two states after mixing can be directly related to the magnitude of the crosspeak in the analogous 2D experiment.)

A plot of the evolution under RFDR mixing for sum and difference polarization is shown in Fig. (4-9B). The carrier frequency was placed directly between the two spins; for sum polarization, the initial transverse evolution period was set to zero length, while for difference polarization it was set to one-quarter of the inverse of the chemical shift difference (see Chapter One). The much faster decay of difference polarization indicates the effects of the dipolar coupling between the two spins, recoupled efficiently even though the spinning speed (8kHz) is between the n=1 and n=2 rotational resonance conditions (chemical shift difference = 13.2kHz). Decay of sum polarization also occurs, however, demonstrating the signal loss effects described in the previous sections (the ^{1}H decoupling power was approx. 100kHz (2.5μs 90° pulse), and the ^{13}C rf power for the 180° pulses was set to 31kHz (8μs 90° pulse)). The amount of signal loss during mixing - approximately 30% of total polarization by 30-40ms - is not

prohibitive, and suggests that experiments performed at these power levels are applicable to systems where S/N is not as high. Accurate extraction of distance information from data of this type has required fitting several signal loss and relaxation parameters in addition to the coupling strength. Simulation of the dynamics absent relaxation effects, and inclusion of signal loss (evident in sum decay) as an overall damping term, here yields an approximate fit roughly confirming the expected dynamics.

Two-dimensional experiments, where the polarization on each spin is initially "labeled" with the frequency of that spin by an initial transverse evolution period, allow mapping out of polarization transfer pathways in more complicated spin systems[1]. This precludes the need to prepare a series of initial states by selective manipulation of spin polarization to achieve the same end. To facilitate direct comparison with the three-spin experiments where 2D methods were used, we have performed analogous experiments in the 2-spin system. The t_1 dwell time was set to 100μs (yielding a 10kHz spectral window in the ν_1 dimension and hence folding of the resonance peaks), and 96 t_1 points were acquired. The data was zero-filled to 512x1024, and 20Hz of exponential broadening was used in both dimensions during processing. Rather than displaying the entire 2D spectrum for each mixing time, 1D "slices" of the 2D spectra (constant ν_1 selected to pass through the glycine alpha resonance) are shown in Fig. (4-9C). With the mixing time set equal to zero, all of the polarization lies in the diagonal peak at the glycine alpha resonance frequency. At longer mixing times, polarization transfer is signaled by the appearance of a crosspeak at the valine carboxyl frequency. The evolution evident in the 2D spectra approximately matches that predicted by the 1D mixing curve

Figure 4-10: Polarization transfer by application of RFDR to $^{13}C_3$-labeled GGV (ω_r=8kHz):

(A) Plot of the intensities of the glycine C_α diagonal and crosspeaks between it and the other two carbons as a function of mixing time. There is no significant transfer to the weakly-coupled valine C_ω, and the overall signal intensity drops rapidly during mixing.

(B) 1D slices extracted from the 2D spectra, selected to pass through the glycine C_α diagonal. At zero mixing time, all of the intensity lies in the diagonal; at subsequent mixing times a crosspeak to the strongly-coupled glycine C_ω appears. Again, very little transfer to the valine C_ω occurs.

(A)

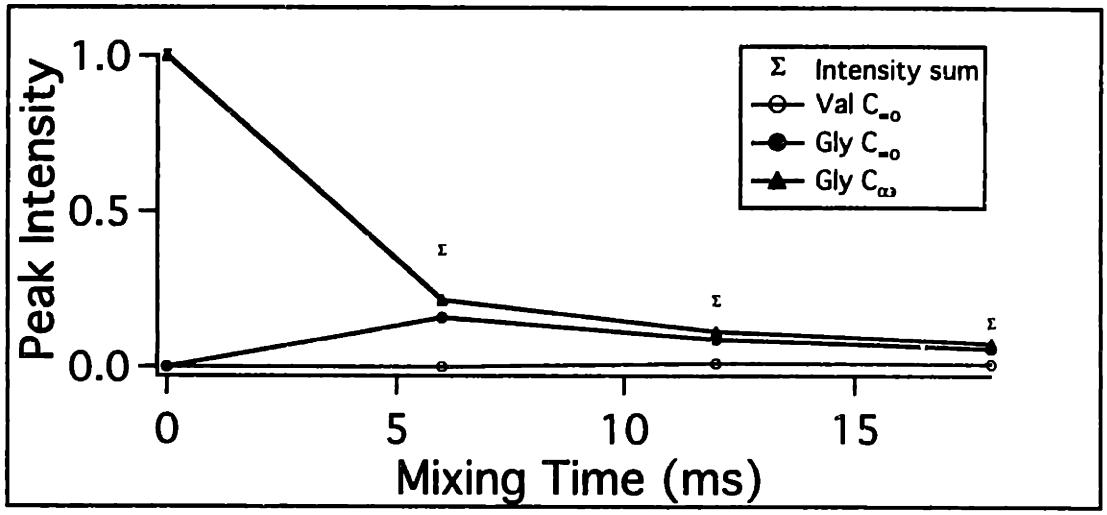
Peak Intensity
1.0
0.5
0.0
0
5
10
15
Mixing Time (ms)
Σ Intensity sum
Val C=O
Gly C=O
Gly Cα

(B)

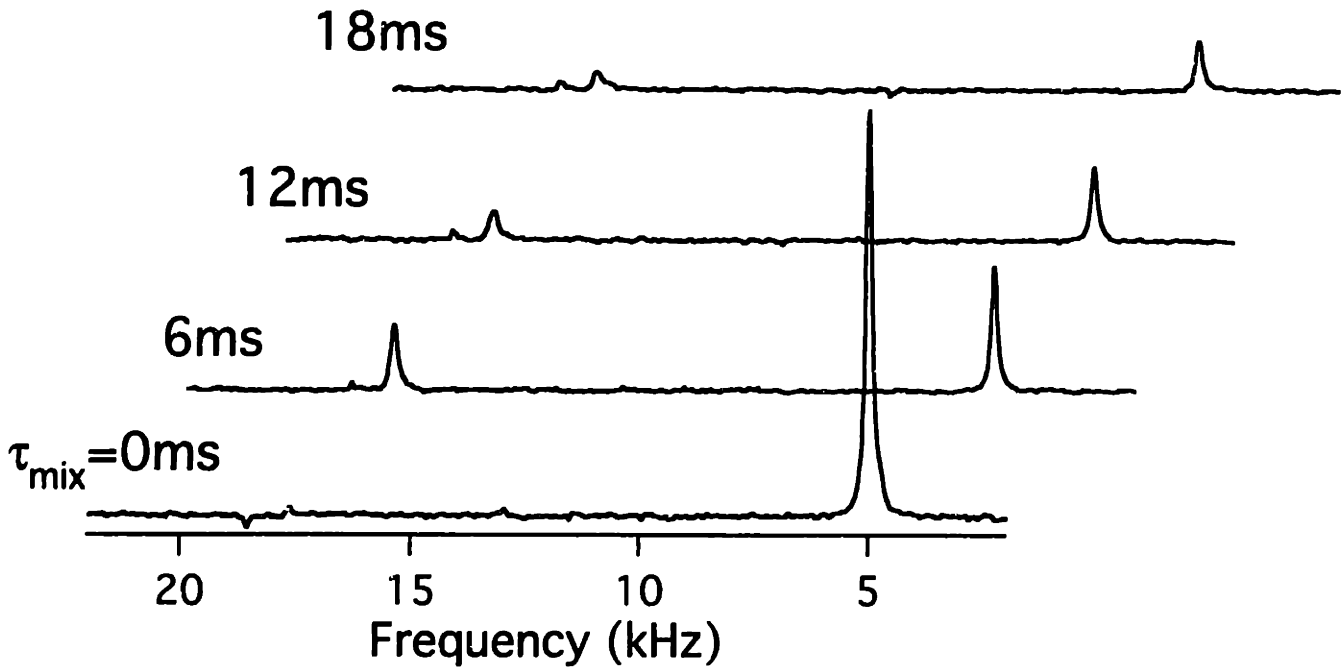
18ms
12ms
6ms
τmix=0ms
20
15
10
5
Frequency (kHz)

previously shown, as expected (this data was acquired under conditions identical to those previously described).

Application of the identical 2D experiment to the 3-spin sample (with mixing times adjusted as shown) yields the results shown in Fig. (4-10). There are several clear changes in the evolution of the spin system attributable to the introduction of the strong coupling between the glycine alpha and carbonyl carbons. First and foremost, very little polarization transfer to the weakly-coupled valine carboxyl carbon occurs (at the longest mixing times - approaching 18ms - a small crosspeak that represents less than 1% polarization transfer is visible). This is approximately as predicted in the previous sections for theoretical models of 3-spin systems (note that RFDR does not efficiently recouple the glycine carbonyl/valine carboxyl interaction because of the small shift difference between them, so that under this sequence the system most closely matches the 3-spin, 2 coupling model). Second, significant polarization transfer between the directly bonded spin pair does occur at short mixing times, indicated by the presence of the sizable glycine carbonyl crosspeak. Third, signal loss during mixing in this sample is greatly accelerated, and by 18ms most of the polarization has disappeared from the spectrum. This last effect is at least in part from increased relaxation of residual transverse polarization in the strongly coupled spin pair due to the presence of the strong coupling, and can be reduced only by increasing the low-γ rf power, and at the expense of reducing ^{1}H decoupling efficiency. Simulations of this type of effect (which do not require the presence of any relaxation terms as the signal loss is driven solely by the presence of the coupling) indicate that, for chemical shift offsets of the size in this system, low-γ rf

Figure 4-11: Polarization transfer by application of RFDR to $^{13}C_3$-labeled GGV (ω_r=3kHz):

(A) Plot of the intensities of the glycine C_α diagonal and crosspeaks between it and the other two carbons as a function of mixing time. There is small but detectable transfer to the weakly-coupled valine C_ω; overall signal intensity drops as indicated during mixing. (Symbols are assigned as in Fig. (4-10).)

(B) 1D slices extracted from the 2D spectra, selected to pass through the glycine C_α diagonal.

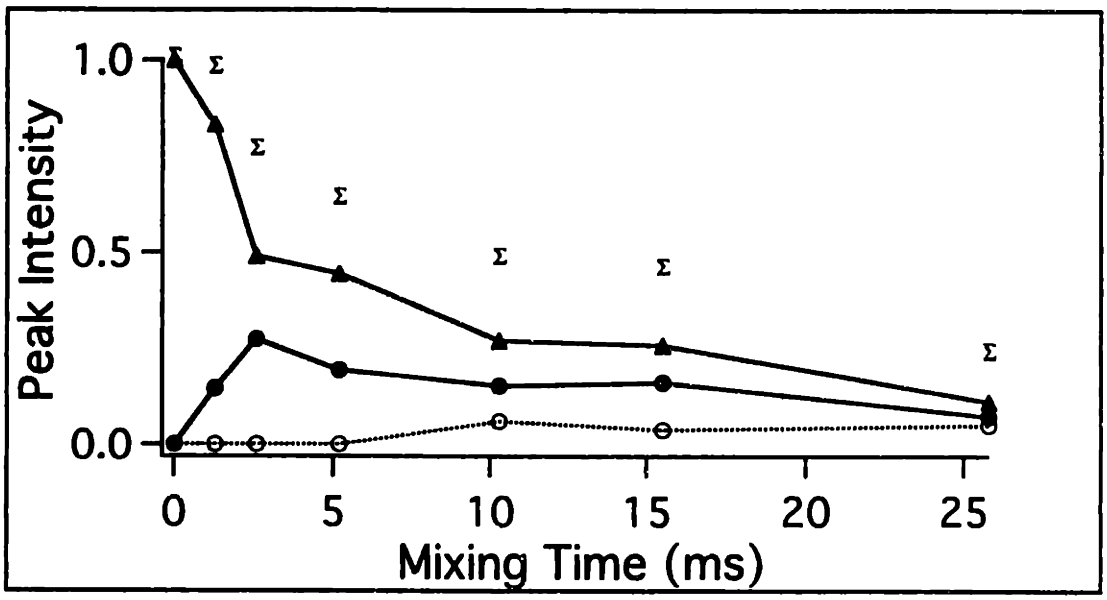
1.0
0.5
0.0
Peak Intensity
Σ
Σ
Σ
Σ
Σ
Σ
0
5
10
15
20
25
Mixing Time (ms)

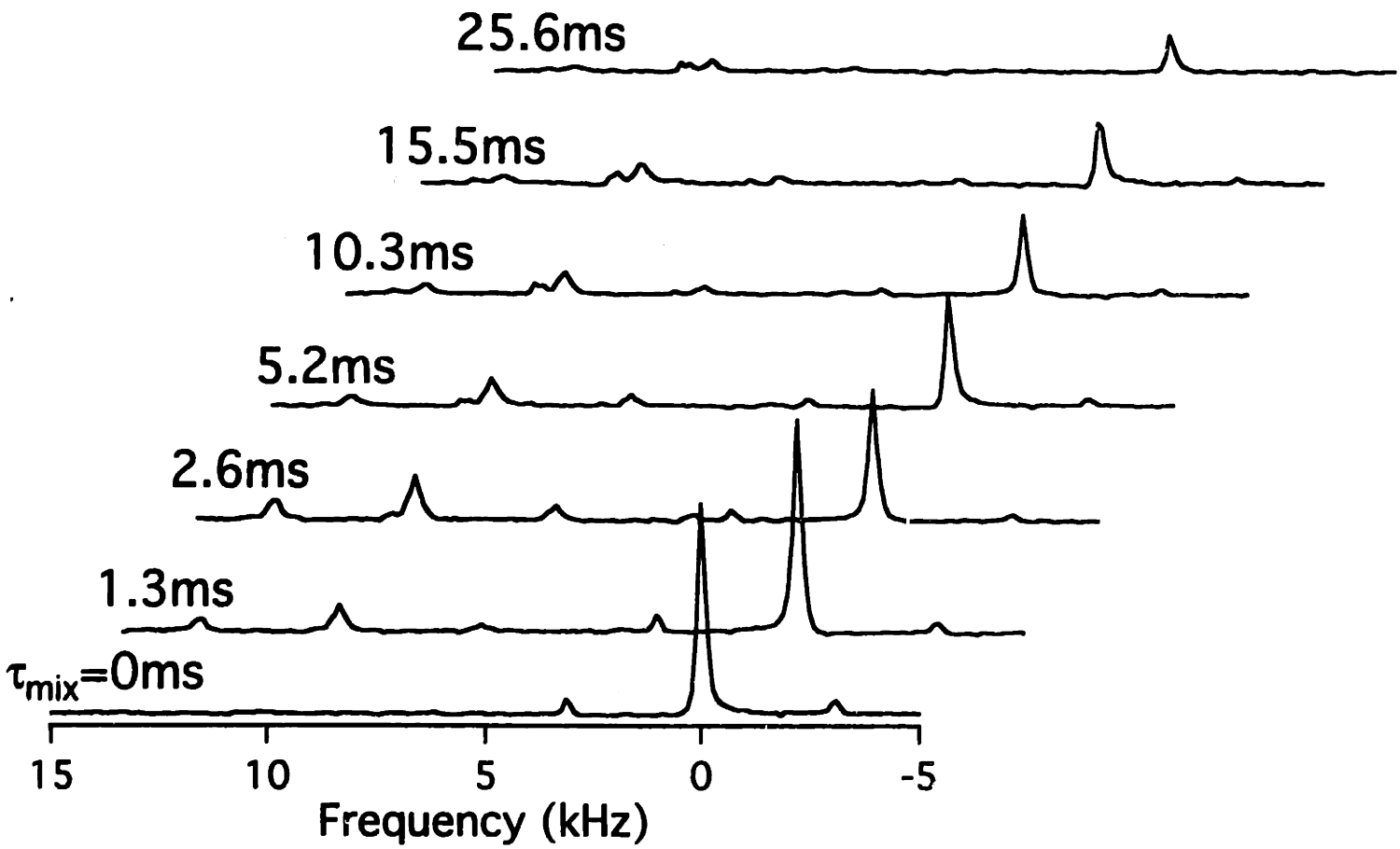
25.6ms
15.5ms
10.3ms
5.2ms
2.6ms
1.3ms
τmix=0ms
15
10
5
0
-5
Frequency (kHz)

field magnitudes approaching 50-60kHz are necessary to minimize this effect.

Performing the same experiment at a much lower spinning speed (3kHz) shows slightly higher levels of polarization transfer (approaching 5%) to the weakly-coupled spin and slower overall signal loss, Fig (4-11). Because the recoupling effect at such a low speed relative to the chemical shift differences results from high-order rotational resonances (order 2-4) which are CSA-dependent, the orientation dependence of the recoupling effect in this case is increased (as the overall recoupling efficiency is decreased), and more orientations of the 3-spin system yield efficient recoupling of the weak interaction without efficient recoupling of the strong coupling. This is one example of using the spinning-speed dependence of the RFDR effect to reduce dipolar truncation effects.

One additional note - displaying 2D spectra without normalizing them relative to the initial signal intensity can be misleading in terms of the implied polarization transfer efficiency between pairs of spins, particularly because of the rapid decay of polarization in strongly-coupled spin pairs. Expanding the 18ms slice from the 8kHz 3-spin system, for instance, yields a spectrum where the cross-peak to the weakly-coupled valine carboxyl looks significant compared to the diagonal peak. Shown relative to the zero-mixing spectrum, however, it is clear that very little polarization transfer has occurred. In systems with very high S/N, detection of such small crosspeaks is clearly feasible, although extraction of relatively accurate distance information would seem difficult (in many cases, however, mere knowledge of proximity between certain spin pairs can be very useful).

4.3C MELODRAMA Results.

The RFDR sequence represents only one alternative for (relatively) broadbanded dipolar recoupling, one that depends on broadening rotational resonances. The MELODRAMA sequence[10] represents an even more broadbanded technique which focuses primarily on direct manipulation of the dipolar interaction to interfere with dipolar averaging. It is based on the DRAMA sequence[26], but uses an applied rf field to both truncate and play the role of the chemical shift terms in the Hamiltonian, so that 90° shifts in the phase of the applied rf at the appropriate points in the rotor cycle replicate the DRAMA dipolar recoupling effect, and with much reduced chemical shift dependence. The basic sequence is illustrated in figure (4-12A): within the standard longitudinal mixing framework, the dipolar mixing period consists of a continuous burst of rf power of fixed magnitude and frequency, but with changes in phase occurring periodically during the rotor cycle. During the first rotor cycle, the rf phase is set to X for the first quarter of the rotor period, to Y during the middle half, and back to X during the final quarter. Calling this basic sequence 'R', the rf applied over 16 contiguous rotor cycles is represented $RR\bar{R}\bar{R}\ \bar{R}RR\bar{R}\ \bar{R}\bar{R}RR\ R\bar{R}\bar{R}R$, where '$\bar{R}$' represents a cycle in which the rf phase is set to $\bar{X}$, $\bar{Y}$, $\bar{X}$. This "supercycling" of the overall rf phase follows symmetry principles and leads to cancellation of higher-order terms in the average Hamiltonian that would otherwise interfere with dipolar evolution.

Dipolar recoupling and rf truncation of chemical shift effects, particularly CSA, require that the magnitude of the applied rf be an integer multiple of the spinning speed, preferably of 4 or higher. For even multiples, longitudinal mixing experiments maximize dipolar-driven

Figure 4-12: Polarization transfer by application of MELODRAMA to $^{13}C_2$- and $^{13}C_3$-labeled GGV (ω_r=5kHz):

(A) Diagram of the MELODRAMA pulse sequence within a longitudinal mixing framework. The mixing sequence itself consists of continuous RF, with phase X for the first quarter of the rotor cycle, phase Y for the middle half, and phase X for the final quarter. The overall phase from rotor cycle to rotor cycle is periodically inverted as described in the text.

(B) The evolution of sum and difference polarization in the two-spin system. Larger decay of sum polarization (Σ) indicates dipolar evolution (the recoupled Hamiltonian has double-quantum character), but difference polarization (Δ) also shows decay indicating rapid signal loss during mixing. Solid lines represent approximate fits to the data, as described in the text.

(C) 1D slices extracted from the 2D spectra, selected to pass through the glycine C_α diagonal. At zero mixing time, all of the intensity lies in the diagonal for both 2- and 3-spin experiments. At a long mixing time (25.6ms) in the 2-spin sample, a dectable crosspeak appears to the weakly-coupled valine C_ω, and overall signal loss is substantial, as expected from the 1D mixing curves. In the 3-spin sample, signal loss is even greater, and at this mixing time the diagonal peak has decayed by a large amount and no crosspeaks are evident. (Both t=25.6ms slices are normed to the single t=0 slice.)

(A)

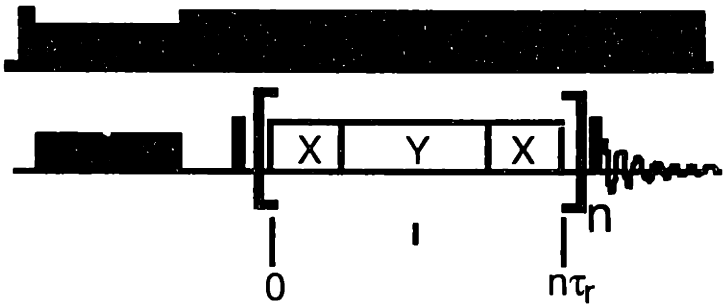
X
Y
X
n
0
nτr

(B)

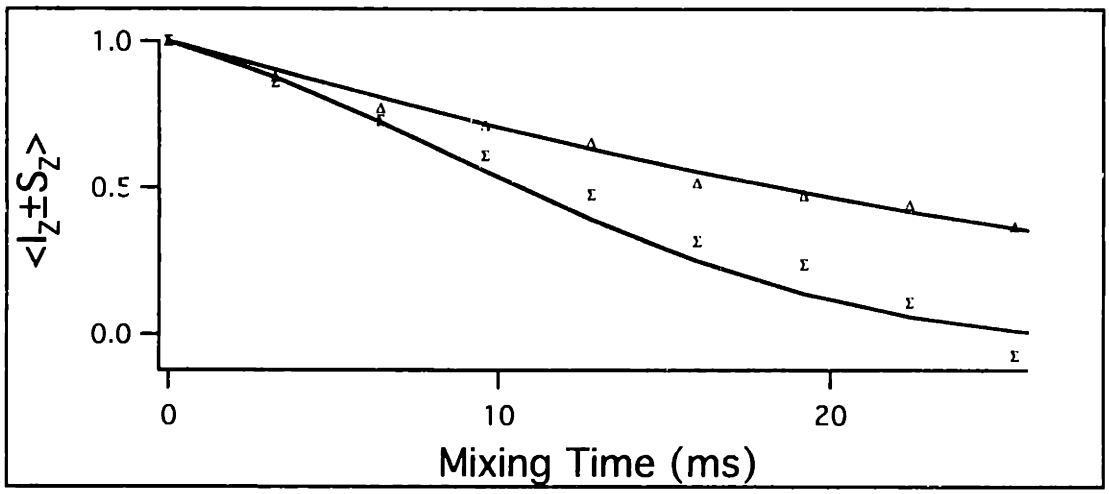
1.0
0.5
0.0
<IZ±SZ>
0
10
20
Mixing Time (ms)

(C)

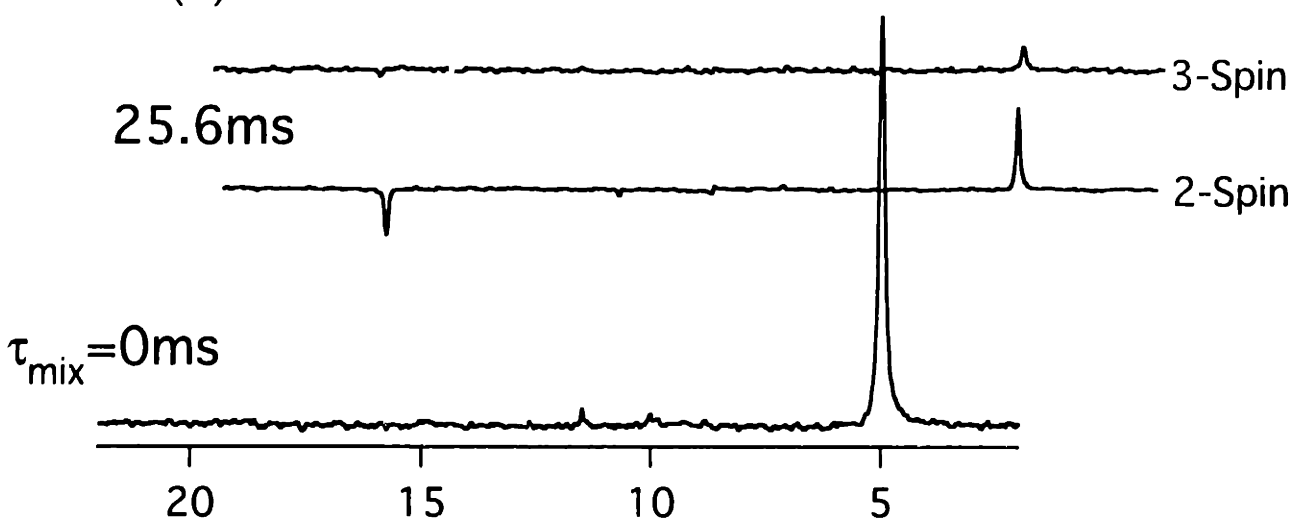
3-Spin
25.6ms
2-Spin
τmix=0ms
20
15
10
5

evolution, while for odd multiples transverse evolution (with the initial state of the polarization 90° out of phase with the initial burst of MELODRAMA rf, i.e. initial polarization along Y for the sequence given above). Here we demonstrate the technique on the doubly $^{13}C_2$-labeled GGV sample, with a spinning speed of 5kHz and a ^{13}C rf field of 25kHz (an odd multiple of the spinning speed, hence transverse mixing was used). The ^{1}H decoupling power was set to approximately 100kHz. Data points were acquired every 3.2ms of mixing to allow for complete supercycling of the overall phase of the ^{13}C rf, as described above. The results are shown in Fig. (4-12B). Because of the double-quantum nature of the recoupled interaction in this case, we expect sum polarization to show the effects of dipolar evolution, with difference polarization (ideally) showing no decay. We do see more decay of sum vs. difference polarization, indicating the presence of the recoupled interaction, however overall signal loss (as evident in the decay of difference polarization) is significant. Again, extraction of accurate distance information would require simulations including a variety of relaxation and signal-loss effects; here we use numerical simulations of the "ideal" evolution (i.e. absent any relaxation or signal-loss effects, but include appropriate spin-system and rf parameters), damped according to the decay of difference polarization, as a rough estimate of the expected dynamics, and achieve an approximate fit.

2D experiments were performed on both the 2- and 3-spin GGV samples to allow direct comparison. The results, presented as slices through the glycine alpha resonance (see previous section), are illustrated in Fig. (4-12C). Both sets of spectra are normed to the same t=0 slice. Comparison of zero-mix and 25ms mix times clearly shows evidence of

significant polarization transfer in the 2-spin, but not the 3-spin sample, and both data sets show significant signal loss.

4.4 Theoretical Extrapolation to Larger Spin Systems.

4.4A Interference in Dipolar Truncation: the Interaction Between a Pair of Strongly-Coupled Spin Pairs.

Extrapolation of the three spin results we have presented to larger spin systems requires taking into account the simultaneous effects that several strong couplings will have on each weak one. In the 3-spin, 2-coupling case the average Hamiltonian (on application of the appropriate recoupling sequence) consists of two non-commuting terms:

$$\overline{H} = c_1 J_x^{ab} + c_2 J_x^{bc} \qquad (28).$$

When one term dominates, we can use the standard AHT approach[27] to approximate the effects - transform to an interaction from defined by the dominant coupling, and then average over the appropriate cycle time. Applied to (28), the transformation before averaging yields ($c_2 >> c_1$):

$$\tilde{\overline{H}} = J_X^{(ab)} \cos(c_2 t/2) + J_Y^{(ac)} \sin(c_2 t/2) \qquad (29),$$

where we have used[28, 29]

$$\begin{aligned} \left[J_X^{(ij)}, J_X^{(ik)}\right] &= \frac{i}{2} J_Y^{(jk)} \\ \left[J_Y^{(jk)}, J_X^{(ij)}\right] &= \frac{i}{2} J_X^{(ik)} \end{aligned} \qquad (30).$$

In this frame, the large coupling imparts a time-dependence on the weak one, and subsequent averaging yields an average Hamiltonian in which the weak coupling is absent. The effect is similar to chemical-shift truncation of dipolar couplings in 2-spin systems: transforming to an interaction frame defined by the dominant chemical-shift difference term imparts a time-dependence on the dipolar flip-flop term, and hence averaging of that term of the coupling.

Given the presence of numerous couplings in a large multispin system, we expect that weak interactions might be simultaneously

modulated in the manner just described by more than one large, non-commuting dipolar coupling. In this case, it is possible that the different modulations will interfere, leaving some residual component of the weak coupling that is not modulated and so is not truncated. This is similar to the dipolar recoupling effect itself, where two different modulations (of spin and spatial terms) of the single coupling in a two-spin system interfere, leaving a residual unmodulated component that can then drive polarization transfer. In this multispin system all of the modulations of the weak coupling occur in spin space, however the interference effect is still possible. The details of the effect will depend critically on the relative sizes of the recoupled interactions, and so on the orientation of the internuclear vectors in the multispin system. As a demonstration of the effect, we show the results of numerical simulations for the 4-spin system diagrammed in Fig. (4-13). The (I,J) and (K,L) spin pairs are strongly-coupled (2.2kHz coupling constant), and a weak coupling (0.1kHz) exists between J and K. (The MELODRAMA sequence was used in the simulations, with chemical shifts set to zero, a 10kHz spinning speed, and a 40kHz rf field). In Fig. (4-13A) we show the evolution of longitudinal polarization of all four spins in a collinear arrangement, given initial unit polarization on the I spin. Rapid transfer between I and J occurs, which is followed by reasonably fast transfer through the weak (J,K) coupling; subsequent transfer to L is rapid. Clearly the interference effect is active here, leaving a significant component of the weak coupling unmodulated, and so able to transfer polarization.

The orientation-dependence of the effect is shown in Fig. (4-13B). When the two strong couplings are no longer collinear, their recoupled magnitudes will differ in the same crystalline, so that they will apply

Figure 4-13: Numerical simulations of polarization transfer in a 4-spin system (aligned as diagrammed). The thick lines represent strong (2.2kHz) couplings, the thin dashed line represents a weak (0.1kHz) coupling. Calculations were performed using the MELODRAMA pulse sequence.

(A) Evolution of longitudinal I, J, K, and L polarization, starting with unit polarization on the I spin, for a collinear arrangement of the spins. Reasonable transfer occurs through the weak coupling, indicating that (in this alignment) the truncating effects of the two strong couplings on the weak one interfere, leaving a residual component that can effectively transfer polarization.

(B) Plot of K-spin polarization as a function of mixing time for a series of 4-spin arrangements as indicated. When the two strong couplings are no longer parallel, there interference is reduced, and dipolar truncation remains in force.

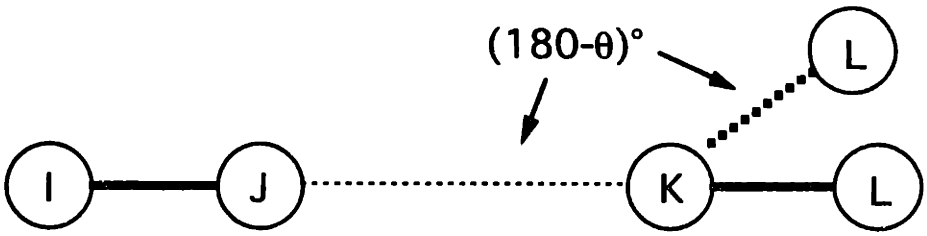
(180-θ)°
L
I
J
K
L

(A)

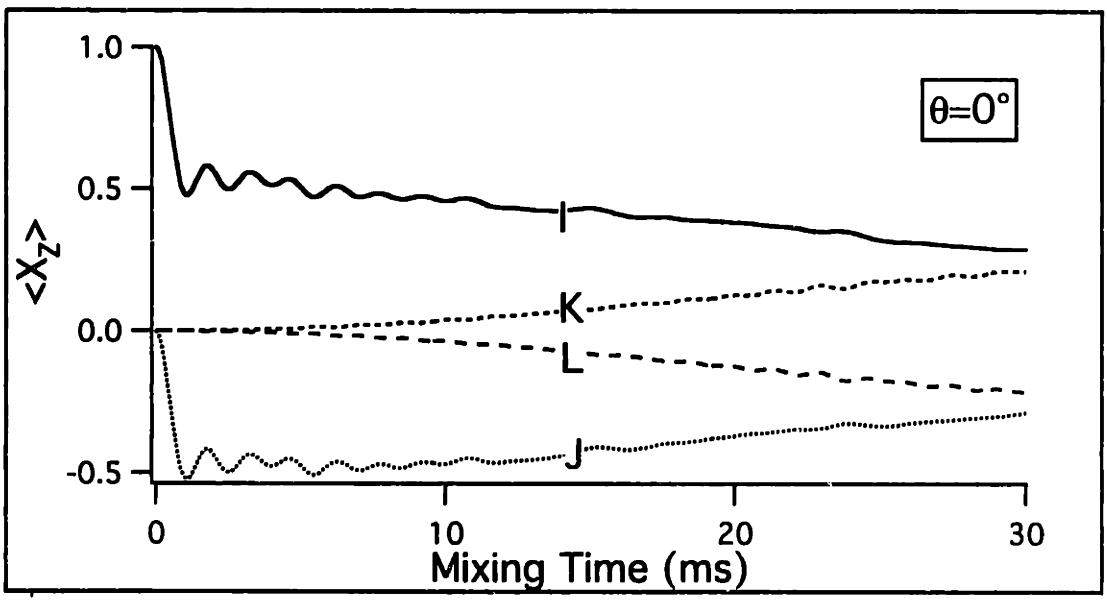
1.0
0.5
0.0
-0.5
<Xz>
θ=0°
I
K
L
J
0
10
20
30
Mixing Time (ms)

(B)

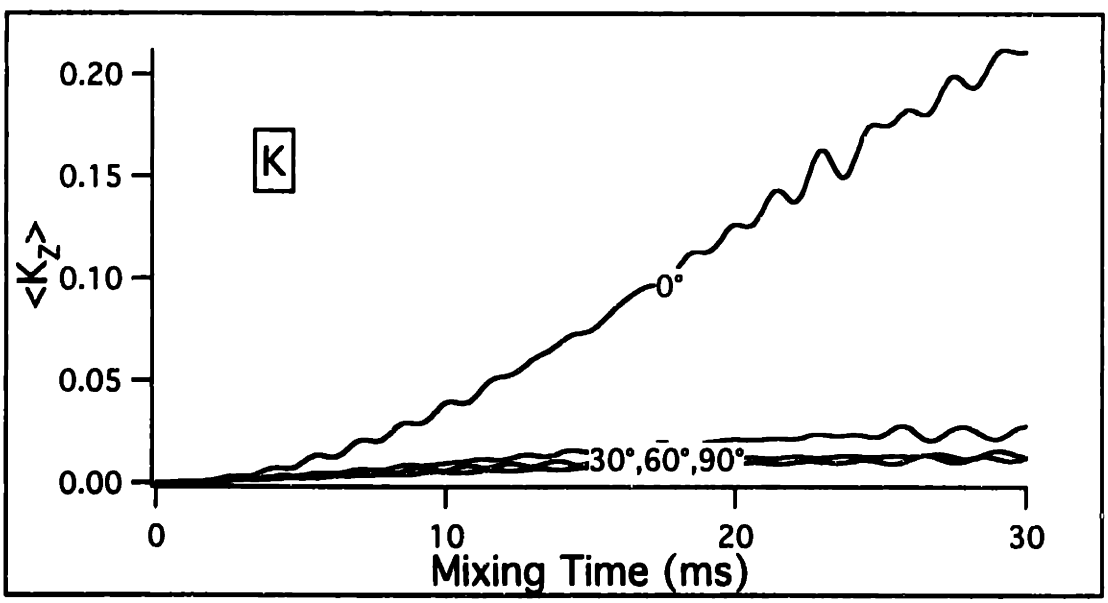
0.20
0.15
0.10
0.05
0.00
<Kz>
K
0°
30°,60°,90°
0
10
20
30
Mixing Time (ms)

modulations of different frequencies to the weak coupling. The result is that interference is no longer effective, and dipolar truncation occurs. This is evident in the lack of significant transfer to the K spin for 30°-90° orientations. (Simulations (not shown) which alter the orientation of both strong couplings relative to the weak one support the conclusion that the crucial parameter in determining the effectiveness of dipolar truncation in this model is whether the strong couplings are parallel or not: when they are, interference occurs and the effectiveness of truncation is reduced. Deviations from parallel on the order of 15° are more are sufficient for truncation to occur.)

4.4B Simulating the Polarization Transfer Dynamics for a 4-Spin Segment of Molecular Backbone.

The possibility that interference effects may allow significant transfer through weak couplings in a strongly-coupled matrix is an interesting one that deserves investigation. Here we present simulations of the polarization transfer dynamics in a 4-spin system arranged in a manner that models 4 successive atoms along a molecular backbone (i.e. with three intervening bonds). Simulations were performed for both *cis* (A) and *trans* (B) conformations (Fig. (4-14)), and both with and without the weak (I,L) coupling. In all four cases, the results are almost identical. This suggests that (i) because the presence or absence of the (I,L) coupling has no effect, little transfer occurs along this pathway; (ii) transfer through the strong couplings is not strongly orientation dependent, as suggested in an earlier section. In this case, there is not a great deal of structural information encoded in the crosspeak pattern. (Numerical calculations were done using the MELODRAMA pulse sequence, with chemical shifts set to zero, a spinning speed of 10kHz and an rf field strength of 40kHz. The dipolar

Figure 4-14: Numerical simulations of polarization transfer in a 4-spin system modeled on a segment of molecular backbone, for both *trans* and *cis* conformations, with the *trans* conformation shown. The couplings were assigned as indicated (in *cis*, the I,L coupling constant was 0.3kHz).

(A) Evolution of longitudinal I, J, K, and L polarization, starting with unit polarization on the I spin, for the *trans* conformation. Rapid transfer from I to the other 3 spins occurs, and it is not clear whether the weak coupling contributes. Simulations (not shown) neglecting the weak coupling yield identical dynamics, suggesting that it has no effect. The sum of absolute polarization shows a very large drop (approaching 50%) over the first 3-5ms, due to cancellation effects in double-quantum transfer by competing odd and even pathways (see earlier section). No relaxation effects are included.

(B) Evolution of longitudinal I, J, K, and L polarization, starting with unit polarization on the I spin, for the *cis* conformation. Results closely match (A), although some differences are apparent. These differences are not due to the weak (I,L) coupling, however, as simulations without it are identical. Again, overall signal loss during mixing is rapid.

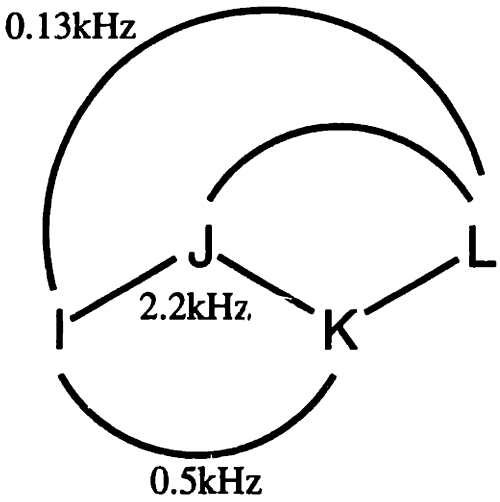
0.13kHz
J
L
2.2kHz
I
K
0.5kHz

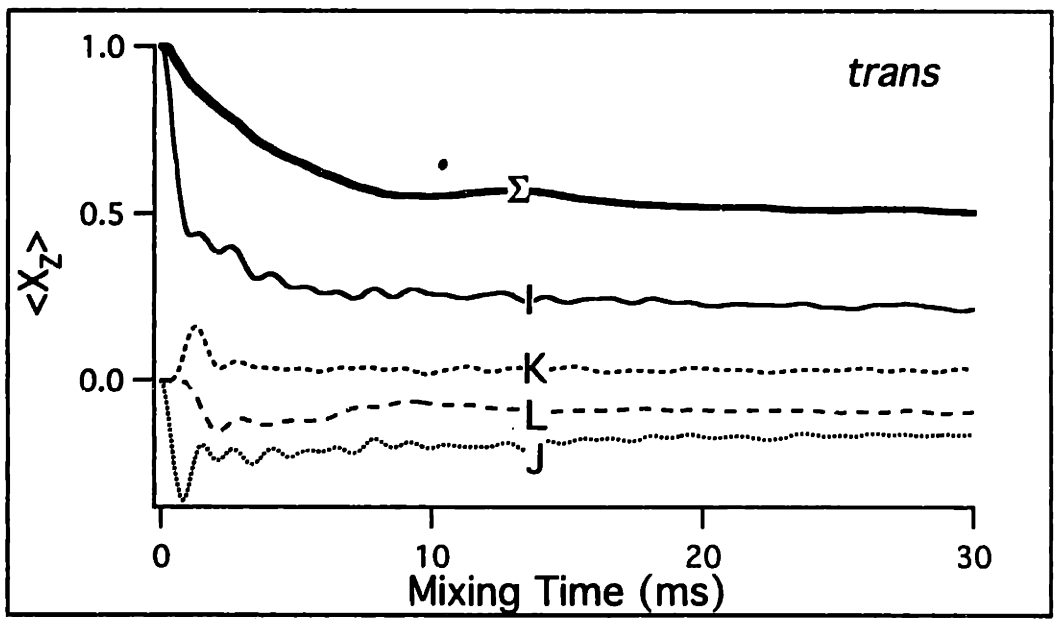
trans
1.0
0.5
0.0
<Xz>
Σ
I
K
L
J
0
10
20
30
Mixing Time (ms)

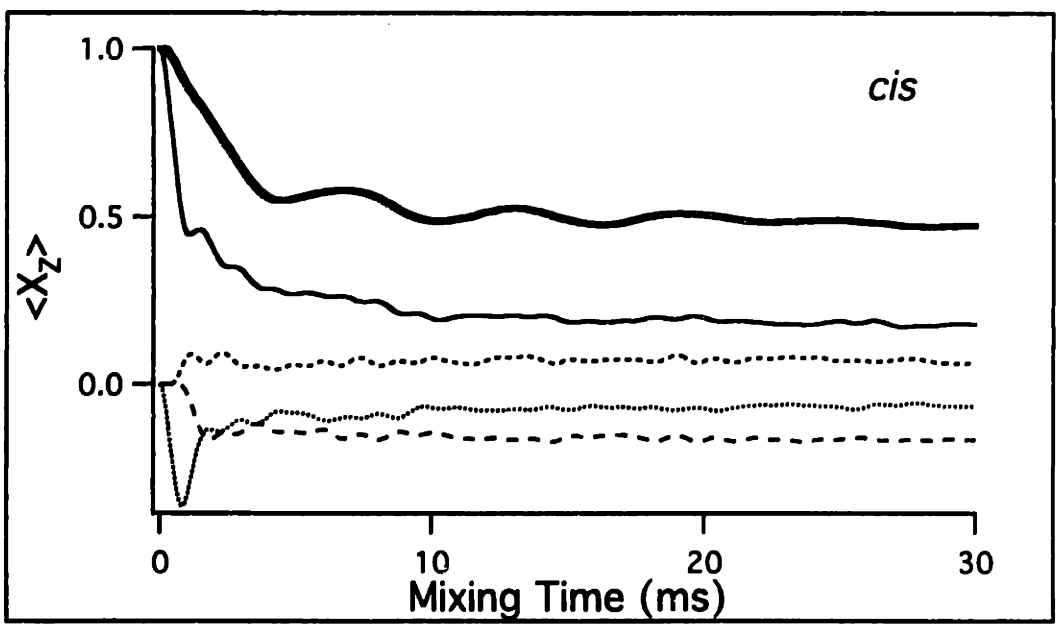
cis
1.0
0.5
0.0
<Xz>
0
10
20
30
Mixing Time (ms)

coupling were assigned (both magnitude and orientation) as indicated in the figure. Because the RFDR sequence has significant dependence on chemical shift, calculations based on it as the recoupling sequence would yield results strongly dependent on the chemical shifts assigned to the successive nuclei. As described previously, this property of RFDR may in many cases lead to reduced overall recoupling efficiency, with gaps in the network that then allow transfer through weak couplings.)

An additional effect evident in these simulations is the large loss of signal that occurs during mixing (and absent any relaxation effects). This signal loss occurs because of the double quantum nature of the interaction, and was described relative to a 3-spin system in an earlier section of this chapter. The signal loss in this case (approaching 50% over the first 3-5ms) is much larger than that for the 3-spin system, and this is the case that more closely approximates most uniformly labeled samples.

4.5 Selective Polarization Transfer.

4.5A Concept.

Where broadbanded recoupling techniques applied to multiply labeled samples induce dynamics that are primarily driven by the strong couplings, extraction of useful structural information will be difficult. Given a favourable distribution of chemical shifts, however, we can apply selective recoupling techniques - ones which recouple only those spin pairs whose chemical shifts match some resonance condition - to selectively reintroduce the coupling between weakly-coupled spin pairs of interest, and extract structural information from the subsequent evolution. Here we discuss two alternatives.

The selectivity of the rotational resonance effect is well-known[8]: spin pairs whose chemical shift difference does not match the spinning speed (or a submultiple of it) are less efficiently recoupled by an amount roughly determined by the ratio of the magnitude of the coupling to the size of the resonance mismatch. In two-spin experiments this is of (minor) benefit because it reduces the effects background (natural abundance) spins have on the dynamics. In multiply-labeled compounds, where the "background" contribution is much higher, RR selectivity is expected to be more beneficial for the same reasons, and performing standard longitudinal mixing experiments for a selected spin pair in a multiply-labeled sample is possible given the appropriate chemical shift distribution (subject to all of the errors in standard 2-spin RR experiments - see Chapter One). Application of the technique in a multidimensional framework, however, is of little utility, because its narrow bandwidth will drive polarization transfer over only a small region of the spectrum.

Rotational resonance tickling (RRT), because of the rf-component of the effective fields, allows ramping through a series of resonance conditions. In inhomogeneously-broadened two-spin systems, this is useful in reducing the effects of the broadening on the dipole-driven dynamics. In multiply-labeled samples, however, it suggests the additional possibility of ramping through a series of resonance conditions corresponding to different spin pairs in succession in a single experiment. During passage through each condition, the corresponding spin pair will be selectively recoupled (to the extent that chemical shifts truncate all other couplings), so that we will maintain the desired selectivity while increasing the overall bandwidth. This technique is applicable over any (relatively contiguous) range of the zero-quantum spectrum where n=1 RR is applicable. In peptide spectra, for instance, one would be able to obtain 2D spectra using this technique which showed correlations from the $C_{=O}$ region of the spectrum to specific sections of the CH_n region of the spectrum.

2Q-HORROR represents a second alternative. Although this technique is ostensibly chemical-shift "insensitive", this is only true over some limited range of chemical shifts. For larger chemical shift differences (approaching the spinning speed), the technique become selective. Hence applied to a specific region of the spectrum of a multiply labeled compound where no strong couplings exist, this technique allows selective recoupling of all weakly-coupled spin pairs within that region. For instance, the $C_{=O}$ region of typical peptide spectra is an isolated region that contains no strongly-coupled spin pairs: application of 2Q-HORROR to this region will selectively recouple all $C_{=O}$ spin pairs, and because they are all weakly-coupled, will allow extraction of useful structural information to the extent that dipolar evolution can be observed and quantified (because

$C_{=O}$ resonances often overlap, this technique would likely have to be some part of a multidimensional experiment in which, for instance, ^{15}N-^{13}C correlation allows separation of the $C_{=O}$ resonances).

In what follows we provide examples of each.

4.5B Using RRT.

RRT techniques are only applicable where n=1 RR experiments are possible: where the chemical shift difference is large enough so that matching the spinning speed to that frequency is feasible in terms of sideband intensities, etc., but not so large that spinning somewhat faster than the chemical shift difference is not possible. In multiply-labeled systems where a number of spin pairs have closely-lying chemical shift differences (within a range that is on the order of 10-25% of the spinning speed), spinning faster than the largest chemical shift difference, and then applying an rf field at the approximate center of the spectrum with a ramped magnitude that brings each spin pair through its resonance condition in succession, allows selective recoupling over some significant spectral bandwidth.

The application of this technique to the $^{13}C_3$-labeled GGV sample (discussed in earlier sections) is shown in Fig. (4-15). As compared to the results from the broadband recoupling experiments, two differences are apparent: first, significant transfer to the weakly-coupled valine C_ω occurs (this is to be expected given the selective nature of RR-based experiments); second, signal loss during even very long mixing periods is not severe. In this experiment, the spinning speed was set to 13.7kHz, and the applied rf was ramped from 0.8-1.3kHz as shown. This range passes through the resonance condition for the weakly-coupled valine C_ω/glycine C_α pair, but

Figure 4-15: Rotational resonance tickling experiment applied to 13C3-labeled GGV sample. The spinning speed was set larger than the largest chemical shift difference (13.2kHz for the valine C_ω/glycine C_α; 12.7kHz for the glycine C_ω/C_α), and the rf magnitude (carrier set in the middle of the spectrum) was ramped from 0.8-1.3kHz over the mixing times shown. RI/RO pulses of 300ms duration were applied before/after dipolar mixing. A plot of the intensity of the glycine C_α diagonal peak and its crosspeaks to the other two carbons indicates effective polarization transfer through the weak coupling, and a low level of signal loss during mixing. The 1D slices (see previous figures) illustrate the effect: at longer mixing times a sizeable crosspeak to the valine C_ω appears. (Reduced S/N is due to a smaller rotor and less signal averaging, not to any differences in the sample (other than size).)

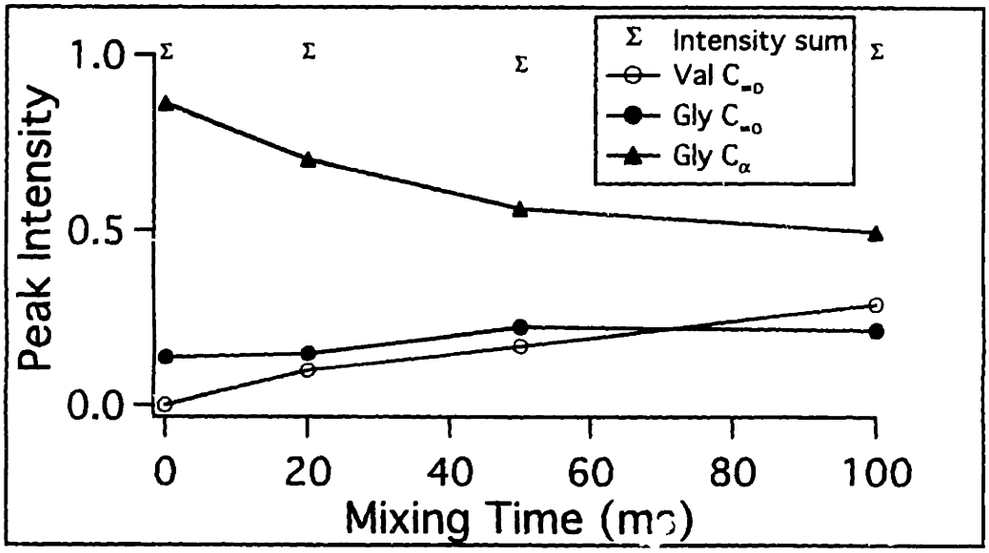
Σ Intensity sum
Val C=O
Gly C=O
Gly Cα
Σ
Σ
Σ
Σ
1.0
0.5
0.0
Peak Intensity
0
20
40
60
80
100
Mixing Time (ms)

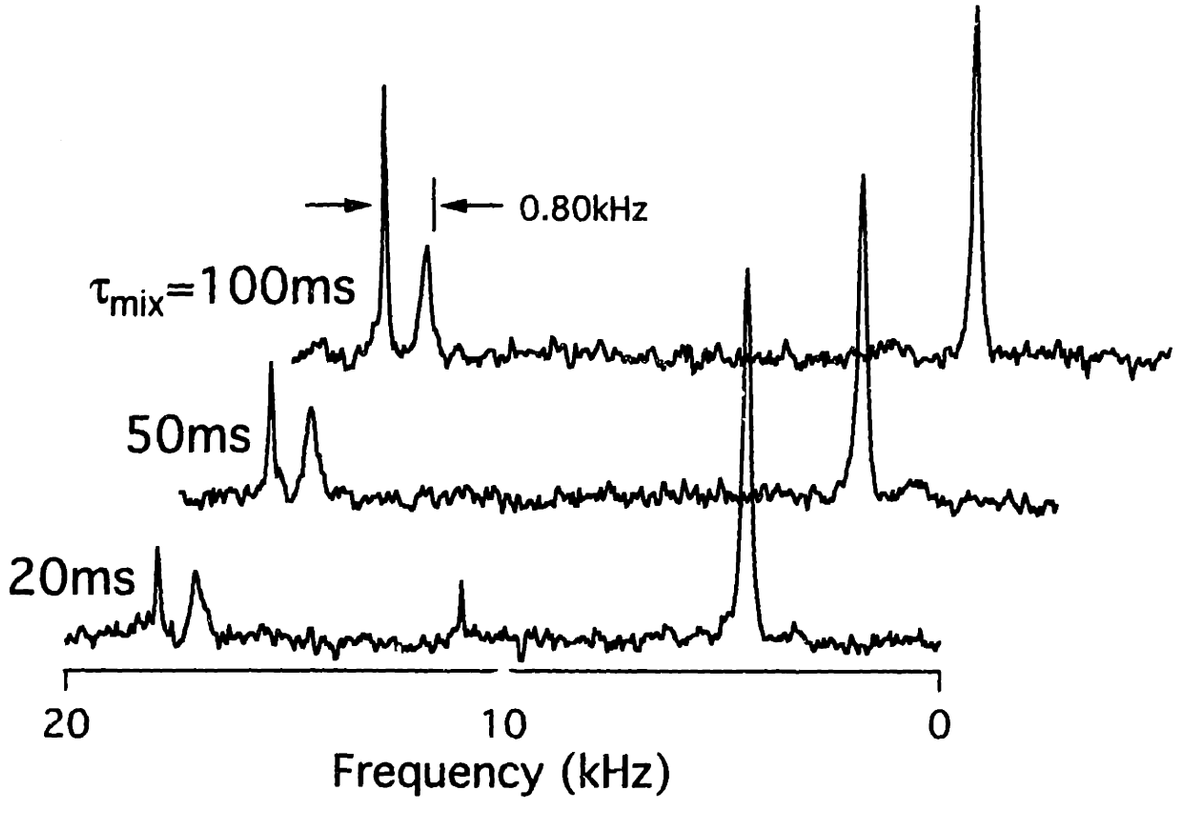
0.80kHz
τmix=100ms
50ms
20ms
20
10
0
Frequency (kHz)

does not pass through the strongly-coupled glycine C_α/C_ω resonance. Nevertheless, detectable transfer through the strong coupling does occur, through a combination of off-resonance and relaxation effects. Several points: first, increasing the ramp range to pass through successive resonances requires increasing the ramp rate, and hence reducing the transfer between each pair. This limits the bandwidth of the tecnnique significantly. Second, if resonance conditions containing a common spin are ramped through successively, the polarization level of that spin will have changed from the first to the second pass, and this effect may complicate analysis of the dynamics. Third, the RI and RO sequences must be particularly quick in strongly-coupled samples to reduce dipolar evolution during there application. In the experiments shown here, 300-500μs RI and RO pulses were not sufficient to fully eliminate all evidence of dipolar evolution during their application.

4.6 References.

1. Ernst, R.R., G. Bodenhausen, A. Wokaun. *Principles of Nuclear Magnetic Resonance in One and Two Dimensions* (Oxford University Press, Oxford, 1987).
2. Clore, G.M., A.M. Gronenborn. *Science* **252**, 1390-1399 (1991).
3. Williamson, M.P., D. Neuhaus. *The Nuclear Overhauser Effect in Structural and Conformational Analysis* (VCH Publishers, Inc., New York, 1989).
4. Abragam, A. *The Principles of Nuclear Magnetism* (Oxford University Press, Inc., Oxford, 1961).
5. Zwahlen, C., S.J.F. Vincent, L. DiBari, M.H. Levitt, G. Bodenhausen. *J. Amer. Chem. Soc.* **116**, (1994).
6. Turner, C.J. (1996).
7. Maus, D.C. *Molecular and Spin Dynamics in Solid State Nuclear Magnetic Resonance Spectroscopy* (MIT, 1996).
8. Raleigh, D.P., M.H. Levitt, R.G. Griffin. *Chem. Phys. Lett.* **146**, 71-76 (1988).
9. Bennett, A.E., J.H. Ok, R.G. Griffin. *J. Chem. Phys.* **96**, 8624-8627 (1992).
10. Sun, B.-Q., P.R. Costa, D. Kocisko, P.T. Lansbury, Jr., R.G. Griffin. *J. Chem. Phys.* **102**, 702 (1995).
11. Nielsen, N.C., H. Bildsoe, H.J. Jakobsen. *J. Chem. Phys.* **101**, 1805-1812 (1994).

12. Cavanagh, J., W.J. Fairbrother, A.G. Palmer III, N.J. Skelton. *Protein NMR Spectroscopy: Principles and Practice* (Academic Press, Inc., San Diego, 1996).
13. Braunschweiler, L., R.R. Ernst. *J. Magn. Res.* **53**, 521 (1983).
14. Boender, G.J., J. Raap, S. Prytulla, H. Oschkinat, H.J.M. deGroot. *Chem. Phys. Lett.* **237**, 502-508 (1995).
15. Lalitha, V., E. Subramanian, J. Bordner. *Int. J. Peptide Protein Res.* **24**, 437-441 (1984).
16. Kocisko, D. (1994).
17. Sieber, P. *Tet. Lett.* **28**, 6147-6150 (1987).
18. Ashburn, T.T., K.J. Halverson. (1992).
19. King, e.a. *Int. J. Peptide Protein Res.* **182**, 225 (1990).
20. Bioscience, B. (1996).
21. Sodickson, D.K., M.H. Levitt, S. Vega, R.G. Griffin. *J. Chem. Phys.* **98**, (1993).
22. Bennett, A. (1993).
23. Bennett, A. (MIT, 1995).
24. Ishii, Y., J. Ashida, T. Terao. *Chem. Phys. Lett.* **246**, 439-445 (1995).
25. Lee, Y.K., N.D. Kurur, M. Helmle, O.G. Johannessen, N.C. Nielsen, M.H. Levitt. *Chem. Phys. Lett.* **242**, 304-309 (1995).
26. Tycko, R., G. Dabbagh. *Chem. Phys. Lett.* **173**, 461 (1990).
27. Haeberlen, U. *High Resolution NMR in Solids* (Academic Press, New York, 1976).
28. Wokaun, A., R.R. Ernst. *J. Chem. Phys.* **67**, (1977).
29. Vega, S. *J. Chem. Phys.* **68**, 5518 (1978).